Nanomaterials for Application in Medicine and Biology

NATO Science for Peace and Security Series

This Series presents the results of scientific meetings supported under the NATO Programme: Science for Peace and Security (SPS).

The NATO SPS Programme supports meetings in the following Key Priority areas: (1) Defence Against Terrorism; (2) Countering other Threats to Security and (3) NATO, Partner and Mediterranean Dialogue Country Priorities. The types of meeting supported are generally "Advanced Study Institutes" and "Advanced Research Workshops". The NATO SPS Series collects together the results of these meetings. The meetings are coorganized by scientists from NATO countries and scientists from NATO's "Partner" or "Mediterranean Dialogue" countries. The observations and recommendations made at the meetings, as well as the contents of the volumes in the Series, reflect those of participants and contributors only; they should not necessarily be regarded as reflecting NATO views or policy.

Advanced Study Institutes (ASI) are high-level tutorial courses intended to convey the latest developments in a subject to an advanced-level audience

Advanced Research Workshops (ARW) are expert meetings where an intense but informal exchange of views at the frontiers of a subject aims at identifying directions for future action

Following a transformation of the programme in 2006 the Series has been re-named and re-organised. Recent volumes on topics not related to security, which result from meetings supported under the programme earlier, may be found in the NATO Science Series.

The Series is published by IOS Press, Amsterdam, and Springer, Dordrecht, in conjunction with the NATO Public Diplomacy Division.

Sub-Series

A.	Chemistry and Biology	Springer
B.	Physics and Biophysics	Springer
C.	Environmental Security	Springer
D.	Information and Communication Security	IOS Press
E.	Human and Societal Dynamics	IOS Press

http://www.nato.int/science
http://www.springer.com
http://www.iospress.nl

Series B: Physics and Biophysics

Nanomaterials for Application in Medicine and Biology

edited by

Michael Giersig
center of advanced european studies and research (caesar)
Bonn, Germany

and

Gennady B. Khomutov
Moscow State University
Moscow, Russia

Springer

Proceedings of the NATO Advanced Research Workshop on
Nanomaterials for Application in Medicine and Biology
Bonn, Germany
4–6 October 2006

A C.I.P. Catalogue record for this book is available from the Library of Congress.

ISBN 978-1-4020-6828-7 (PB)
ISBN 978-1-4020-6827-0 (HB)
ISBN 978-1-4020-6829-4 (e-book)

Published by Springer,
P.O. Box 17, 3300 AA Dordrecht, The Netherlands.

www.springer.com

Printed on acid-free paper

CONTENTS

PREFACE

This volume contains research reports presented during the NATO Advanced Research Workshop (ARW) “Materials for Application in Medicine and Biology” held in Bonn, Germany, from October 4 to 6, 2006 at the center of advanced european studies and research (caesar).

The application of nanomaterials in medicine and biology can be understood as the gathering and use of our current knowledge on nanoscale features of biological systems in order to learn how to design nanodevices for biomedical uses. The success of this approach, known as nano-engineering, will allow scientists to devise strategies for the design and construction of nanodevices to be used in clinical trials (diagnosis and therapeutic monitoring), as well as to develop products with potential applications in regenerative medicine.

One goal of this conference was to bring together researchers from Eastern and Western countries, offering them a platform to meet and discuss results of their research work. Thus, the aim of this conference was not only to present the advancements in research achieved during the past years, but it had also been conceived as a concerted European effort where expertise, technologies, and ideas were broadly shared to accelerate this progress. The conference provided an interactive forum with more than 100 participants from 15 countries.

The 15 selected papers cover the following topics: (1) nanodevices for biomedical applications; (2) DNA-nanoparticle conjugates; (3) transmembrane delivery of macromolecules by nanomaterials and/or polyelectrolytes; (4) glyconanoparticles for biomedical purposes; (5) optical properties of gold nanoparticles and biosensing; (6) magnetic behavior of S-capped gold nanoparticles; (7) quantum dots for biological tagging; (8) polymer-based capsules; (9) theoretical approaches to nanoparticles.

The conference was organized by the Department of Nanoparticle Technology at the center of advanced european studies and research (caesar), with Professor Dr. Giersig as head-organizer, and Professor Dr. Khomutov from Moscow State University as co-organizer, in full cooperation with caesar, and generous financial support by NATO.

We would especially like to thank the NATO Science Programme for providing a generous grant for the realization of this conference. We would also like to acknowledge and thank all those who participated in this event including those who provided expertise through the presentation of their research as well as everyone who engaged in discussions and contributed to the organization and planning of the conference – in short, all who helped to make the NATO Advanced Research Workshop 2006 a success.

CONTRIBUTORS

Daria Afanasieva
Dept. of Molecular Biophysics, Faculty of Physics,
St. Petersburg State University, Uluanovskaya St. 1, Petrodvorets, St.
Petersburg, 198504, Russia

David Alcántara
Laboratory of Glyconanotechnology, CIC biomaGUNE and
CIBER-BBN Networking Centre on Bioengineering, Biomaterials
and Nanomedicine, Paseo Miramón 182, Parque Tecnológico
de San Sebastián, 20009 San Sebastián, Spain

Daria V. Andreeva
Max Planck Institute of Colloids and Interfaces, Am Muehlenberg 1,
14476 Golm/Potsdam, Germany

Susan Andreko
Molecular Biosensor and Imaging Center, Mellon Institute, Carnegie
Mellon University, 4400 Fifth Avenue, Pittsburgh, PA 15213, USA

Valeria Andronova
D.I. Ivanovsky Institute of Virology, Russian Academy of Medical
Sciences, Gamaleya Str. 16, Moscow, 123098, Russia

Natalia A. Arkharova
Institute of Crystallography, Russian Academy of Sciences,
Leninsky pr. 59, Moscow, 119333, Russia

Yulia G. Baklagina
Institute of Macromolecular Compounds, Russian Academy of
Sciences, Bolshoi pr. 31, St. Petersburg, 199004, Russia

Byron Ballou
Molecular Biosensor and Imaging Center/Department of Biological
Sciences, Mellon Institute, Carnegie Mellon University, 4400 Fifth
Avenue, Pittsburgh, PA 15213, USA

África G. Barrientos
Laboratory of Glyconanotechnology, CIC biomaGUNE and
CIBER-BBN Networking Centre on Bioengineering, Biomaterials
and Nanomedicine, Paseo Miramón 182, Parque Tecnológico
de San Sebastián, 20009 San Sebastián, Spain

Ludmila N. Borovikova
Institute of Macromolecular Compounds, Russian Academy of
Sciences, Bolshoi pr. 31, St. Petersburg, 199004, Russia

Marcel P. Bruchez
Molecular Biosensor and Imaging Center/Department of Chemistry,
Mellon Institute, Carnegie Mellon University, 4400 Fifth Avenue,
Pittsburgh, PA 15213, USA

Oliver Brüstle
Institute of Reconstructive Neurobiology, Life and Brain Center,
University of Bonn, Sigmund-Freud-Str. 25, 53127 Bonn,
Germany

Dong Cai
Department of Biology, Boston College, 140 Commonwealth Avenue,
Chestnut Hill, MA 02467, USA/NanoLab, Inc., Newton, MA 02458,
USA

David Carnahan
NanoLab, Inc., Newton, MA 02458, USA

Thomas C. Chiles
Department of Biology, Boston College, 140 Commonwealth Avenue,
Chestnut Hill, MA 02467, USA

Caroline Clavel
Laboratory of Glyconanotechnology, CIC biomaGUNE and
CIBER-BBN Networking Centre on Bioengineering, Biomaterials
and Nanomedicine, Paseo Miramón 182, Parque Tecnológico
de San Sebastián, 20009 San Sebastián, Spain

Lauren A. Ernst
Molecular Biosensor and Imaging Center, Mellon Institute, Carnegie
Mellon University, 4400 Fifth Avenue, Pittsburgh, PA 15213, USA

Izabela Firkowska
center of advanced european studies and research (caesar),
Nanoparticle Technology Dept., Ludwig-Erhard-Allee 2,
53175 Bonn, Germany

Jesus M. de la Fuente
Laboratory of Glyconanotechnology, CIC biomaGUNE and
CIBER-BBN Networking Centre on Bioengineering, Biomaterials
and Nanomedicine, Paseo Miramón 182, Parque Tecnológico
de San Sebastián, 20009 San Sebastián, Spain

Georgy Galegov
D.I. Ivanovsky Institute of Virology, Russian Academy of Medical
Sciences, Gamaleya Str. 16, Moscow, 123098, Russia

Suna Giannona
center of advanced european studies and research (caesar),
Nanoparticle Technology Dept., Ludwig-Erhard-Allee 2,
53175 Bonn, Germany

Michael Giersig
center of advanced european studies and research (caesar),
Nanoparticle Technology Dept., Ludwig-Erhard-Allee 2,
53175 Bonn, Germany

Sergey Grokhovsky
V.A. Engelhardt Institute of Molecular Biology, Russian Academy
of Sciences, Vavilov Str. 32, Moscow, 119991, Russia

Georgy Gursky
V.A. Engelhardt Institute of Molecular Biology, Russian Academy
of Sciences, Vavilov Str. 32, Moscow, 119991, Russia

Nina Kasyanenko
Dept. of Molecular Biophysics, Faculty of Physics, St. Petersburg
State University, Uluanovskaya St. 1, Petrodvorets, St. Petersburg,
198504, Russia

Krzysztof Kempa
Department of Physics, Boston College, 140 Commonwealth Avenue,
Chestnut Hill, MA 02467, USA

Gennady B. Khomutov
Faculty of Physics, Moscow State University, Leninskie Gory 1,
119992 Moscow, Russia

Albert K. Khripunov
Institute of Macromolecular Compounds, Russian Academy of
Sciences, Bolshoi pr. 31, St. Petersburg, 199004, Russia

Marina V. Kitaeva
School of Chemistry, M.V. Lomonosov Moscow State University,
Leninskie Gory, Moscow, 119899, Russia

Vera V. Klechkovskaya
Institute of Crystallography, Russian Academy of Sciences,
Leninsky pr. 59, Moscow, 119333, Russia

B. Christoffer Lagerholm
Molecular Biosensor and Imaging Center, Mellon Institute,
Carnegie Mellon University, 4400 Fifth Avenue, Pittsburgh,
PA 15213, USA
Present address: Memphys, Physics Department, University
of Southern Denmark, Campusvej 55, 5230 Odense, Denmark

Luis M. Liz-Marzán
Departamento de Química Física, and Unidad Asociada
CSIC- Universidade de Vigo, 36310 Vigo, Spain

M. Arturo López-Quintela
Laboratory of Magnetism and Nanotechnology, Institute of
Technological Research, Departments of Physical Chemistry
and Applied Physics, University of Santiago de Compostela,
Edificio da Imprenta, 15782 Santiago de Compostela, Spain

Klaus Luecke
GILUPI Nanomedicine GmbH, Am Muehlenberg 11, 14476 Golm,
Germany

Olga Martínez-Ávila
Laboratory of Glyconanotechnology, CIC biomaGUNE and
CIBER-BBN Networking Centre on Bioengineering, Biomaterials
and Nanomedicine, Paseo Miramón 182, Parque Tecnológico
de San Sebastián, 20009 San Sebastián, Spain

Nikolay S. Melik-Nubarov
School of Chemistry, M.V. Lomonosov Moscow State University,
Leninskie Gory, Moscow, 119899, Russia

Frederic M. Menger
Department of Chemistry, Emory University, Atlanta, GA 30322,
USA

Antonio Mouriño Mosquera
Department of Organic Chemistry, CSIC Associated Unit,
University of Santiago de Compostela, Spain

Dmitry Nechipurenko
Department of Physics, Moscow State University, Leninskie Gory,
Moscow, 119992, Russia

Yury Nechipurenko
Engelhardt Institute of Molecular Biology, Russian Academy
of Sciences, Vavilov Str. 32, Moscow, 119991, Russia

Alexei Nikitin
V.A. Engelhardt Institute of Molecular Biology, Russian Academy
of Sciences, Vavilov Str. 32, Moscow, 119991, Russia

Isabel Pastoriza-Santos
Departamento de Química Física, and Unidad Asociada CSIC-
Universidade de Vigo, 36310 Vigo, Spain

Soledad Penadés
Laboratory of Glyconanotechnology, CIC biomaGUNE and
CIBER-BBN Networking Centre on Bioengineering, Biomaterials
and Nanomedicine, Paseo Miramón 182, Parque Tecnológico
de San Sebastián, 20009 San Sebastián, Spain

Jorge Pérez-Juste
Departamento de Química Física, and Unidad Asociada CSIC-
Universidade de Vigo, 36310 Vigo, Spain

Robert Polozov
Institute for Theoretical and Experimental Biophysics, Moscow
Region, Institutskaya Str. 3, Puschino, 142290, Russia

Zhifeng Ren
Department of Physics, Boston College, Chestnut Hill, MA 02467,
USA

José Rivas
Laboratory of Magnetism and Nanotechnology, Institute of
Technological Research, Departments of Physical Chemistry
and Applied Physics, University of Santiago de Compostela,
Edificio da Imprenta, 15782 Santiago de Compostela, Spain

María J. Rodríguez Vázquez
Laboratory of Magnetism and Nanotechnology, Institute of
Technological Research, Departments of Physical Chemistry and
Applied Physics, University of Santiago de Compostela, Edificio da
Imprenta, 15782 Santiago de Compostela, Spain

José A. Rojas-Chapana
center of advanced european studies and research (caesar),
Nanoparticle Technology Dept., Ludwig-Erhard-Allee 2, 53175 Bonn,
Germany

Eleonora V. Shtykova
Institute of Crystallography, Russian Academy of Sciences,
Leninsky pr. 59, Moscow, 119333, Russia

Ruslan Yu. Smyslov
Institute of Macromolecular Compounds, Russian Academy
of Sciences, Bolshoi pr. 31, St. Petersburg, 199004, Russia

Gleb B. Sukhorukov
Department of Materials, Queen Mary, University of London,
Mile End Road, E1 4NS, London, United Kingdom

Anna Surovaya
V.A. Engelhardt Institute of Molecular Biology, Russian Academy
of Sciences, Vavilov Str. 32, Moscow, 119991, Russia

Albina A. Tkachenko
St. Petersburg State University, Universitetskaya nab. 7-9,
St. Petersburg, 199034, Russia

Mercedes Torneiro
Department of Organic Chemistry, CSIC Associated Unit,
University of Santiago de Compostela, Spain

Vladimir V. Volkov
Institute of Crystallography, Russian Academy of Sciences,
Leninsky pr. 59, Moscow, 119333, Russia

Alan S. Waggoner
Molecular Biosensor and Imaging Center/Department of Biological
Sciences, Mellon Institute, Carnegie Mellon University, 4400 Fifth
Avenue, Pittsburgh, PA 15213, USA

Alexander A. Yaroslavov
School of Chemistry, M.V. Lomonosov Moscow State University,
Leninskie Gory, Moscow, 119899, Russia

Yuri M. Yevdokimov
Engelhardt Institute of Molecular Biology of the Russian Academy
of Sciences, Vavilov Str. 32, Moscow, 119991, Russia

Biocompatible Nanomaterials and Nanodevices Promising for Biomedical Applications

Izabela Firkowska[1], Suna Giannona[1], José A. Rojas-Chapana[1], Klaus Luecke[2], Oliver Brüstle[3], and Michael Giersig[1,*]

Abstract Nanotechnology applied to biology requires a thorough understanding of how molecules, sub-cellular entities, cells, tissues, and organs function and how they are structured. The merging of nanomaterials and life science into hybrids of controlled organization and function is possible, assuming that biology is nanostructured, and therefore man-made nano-materials can structurally mimic nature and complement each other. By taking advantage of their special properties, nanomaterials can stimulate, respond to and interact with target cells and tissues in controlled ways to induce desired physiological responses with a minimum of undesirable effects. To fulfill this goal the fabrication of nano-engineered materials and devices has to consider the design of natural systems. Thus, engineered micro-nano-featured systems can be applied to biology and biomedicine to enable new functionalities and new devices. These include, among others, nanostructured implants providing many advantages over existing, conventional ones, nanodevices for cell manipulation, and nanosensors that would provide reliable information on biological processes and functions.

Keywords Nanotechnology, carbon nanotubes, gold nanoparticles, nanoporation, tissue engineering, biosensing

1 Introduction

Nanotechnology poses a new frontier in science and technology. The essence of nanotechnology is the ability to work at the atomic and molecular levels, to create novel structures or devices with fundamentally new molecular organization.

---

[1] center of advanced european studies and research (caesar), Nanoparticle Technology Department, Ludwig-Erhard-Allee 2, 53175 Bonn, Germany

[2] GILUPI Nanomedicine GmbH, Am Muehlenberg 11, 14476 Golm, Germany

[3] Institute of Reconstructive Neurobiology, Life and Brain Center, University of Bonn, Sigmund-Freud-Str. 25, 53127 Bonn, Germany

[*] To whom correspondence should be addressed. E-mail: giersig@caesar.de

M. Giersig and G. B. Khomutov (eds.),
Nanomaterials for Application in Medicine and Biology

Novel materials engineered at the nanometer scale (nanomaterials) are indispensable elements on the whole field of nanotechnology. They can be considered as the most important crossing between basic research and marketable products and processes. Nanomaterials show great market potential, e.g. by substituting other materials or by making available new functionalities and thus enabling new products. The fact that the dimensions of nanomaterials are analogous to those of natural biological structures such as proteins and DNA allows for the direct integration of nanomaterials into biological systems. Last, it offers a platform for the emerging research field of bio-nanotechnology. Bio-nanotechnology can be viewed as an attempt to reproduce cellular basic building blocks or molecular design principles by means of highly organized structures based on nanomaterials. This enables scientists and engineers to create bio-inspired nanodevices with life-science applications. This challenge requires an interdisciplinary research effort that can be translated directly into new technologies and products for biomedical applications.

We have recently started working with carbon nanotubes and gold nanoparticles for their application in the field of biomedical devices. Carbon nanotubes – discovered by Sumio Iijima[1] (1991) – are among the technologically most interesting nanoscale materials currently under investigation for medical application.[2–5] Carbon nanotubes being mechanically tough, chemically inert, and highly conductive make them very attractive tools for bio-interfacial engineering, ultra-sensitive biosensing, single-cell experimentation, and drug delivery.

On the other hand, arrays of noble-metal nano-islands are promising as new platforms for low-cost and rapid biosensing. This becomes possible as a result of changes in the electro-optical properties of the metal nanoparticles, which are induced by simple target attachment. As a result, this class of metal nano-sensors provided with a very sensitive biofunctionalization is able to rapidly report the presence of specific substances in a fluid or in the air. In particular, we show that periodic arrays of gold nanoparticles can work as nanosensors due to the wavelength-specific plasmonic-resonance phenomena between lights and the gold surface.

2 Results

The following results reflect recent findings and future prospects of nanotechnology applications in life science. The nanomaterials used have made it possible to study interfacial phenomena encountered in biological systems. The results emerging from these studies create an exciting focus for research in the bioengineering field. On the other hand, recent results obtained on nanosensory include the development of biosensing-chips for the recognition, trapping, and immobilization of rare cells types in peripheral blood. The biosensing-chip relies on gold nano-islands combined with an antigen-antibody reaction. Our ultimate goal is to design chip-sensors for diagnostic and patient monitoring.

2.1 Carbon Nanotubes and Nanoporation

Initial experiments probing the usefulness of nanostructures for cell manipulation were conducted in bacterial cells. First, we demonstrated the interaction of carbon nanotubes and silica-coated gold nanoparticles with biological membranes in *Acidothiobacillus ferrooxidans*.[6] In this study we predicted that, when exposed to short microwave-pulses, carbon nanotubes would undergo spontaneous polarization leading to dipole-like oscillation able to disrupt the cell envelope of bacterial cells. Published in late 2004, the prediction was later verified in experiments with DNA. Here, we provided details of highly reproducible and facile integration of plasmids into bacterial cells by an electromagnetic procedure based on employing nanotubes as needle-like devices.[7] As a result, carbon nanotubes exposed to a short microwave (mw) pulse (2–4 sec) become polarized in the direction of an electromagnetic field, thereby interacting directly with charges on cell surfaces (see Fig. 1).

As the nanotubes remain polarized while being attached to the cell surfaces, the membrane disrupts gradually, and thereby the particles/plasmids are physically acted upon and subsequently incorporated into the cells. This finding opens up the path to a new system for cell electroporation which uses nanotubes as electroporative devices. Several attempts to reproduce these results on eukaryotic cells have been unsuccessful. Transformation of *Saccharomyces cerevisiae* by mw-activated carbon nanotubes resulted in transient expression of plasmid DNA, but not in a transfer to the progeny after cell division. A similar phenomenon was observed in mammalian cells by using plasmid DNA covalently bound to carbon nanofibres and centrifugation.[8] We are currently working on modifying the surface of nanotubes and nanowires to improve – under the conditions of our experiments – the nanoporation

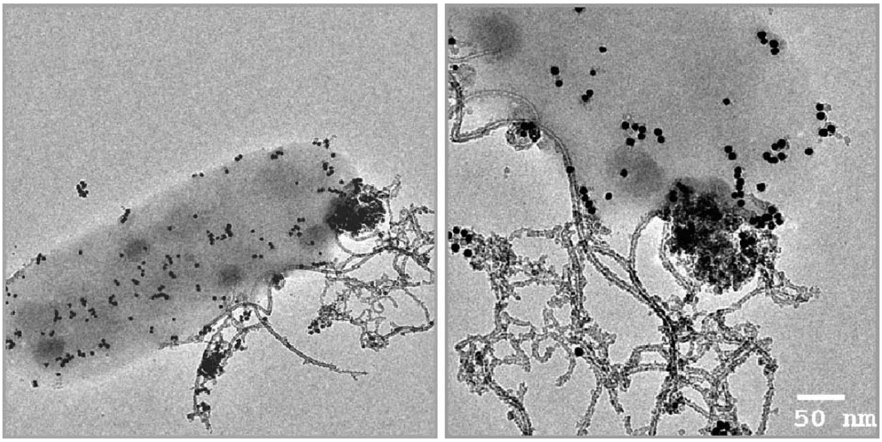

Fig. 1 TEM images depicting an *Acidothiobacillus ferrooxidans* bacterium interacting with water-dispersible multiwalled carbon nanotubes and silica-coated gold nanoparticles

of these cells. In this context, the mechanical penetration of cell membranes by carbon nanotubes and gene transfer under a magnetic driving field (spearing) has been reported.[9] This technique lends itself as an alternative method for effective cell poration and requires no time-consuming operations. Prato et al.[10] show that Hela cells incubated in solutions containing ammonium-functionalized single-walled carbon nanotubes and DNA increase gene expression with increasing incubation times. Likewise, Gao et al. obtain similar results with positively charged nanotubes.[11] In both cases, the mechanism of cellular uptake so far remains unclear. Kam et al. proposed an energy-dependent endocytosis mechanism for the intracellular transport of carbon nanotubes and gene expression.[12] Unlike our approach, in these three examples, cells were incubated for at least 1 h in concentrated solutions of functionalized carbon nanotubes. Thus, each of these approaches is time-consuming and not free from contamination with nanotubes, but a valuable source of information describing cellular uptake of cell-penetrating carbon nanotubes.

Transient contact of cells with an array of aligned carbon nanotubes may solve this problem. Vertically aligned nanotube arrays can be applied in multiple parallel processes as nano-needle-chips (see Fig. 2). In this case, under a short electromagnetic pulse or centrifugation, all aligned carbon nanotubes contacting living cells would simultaneously position themselves across the cell membrane, thus leading to a highly improved introduction of foreign material into cells, thereby preserving the integrity and cleanness of the samples.[8,13]

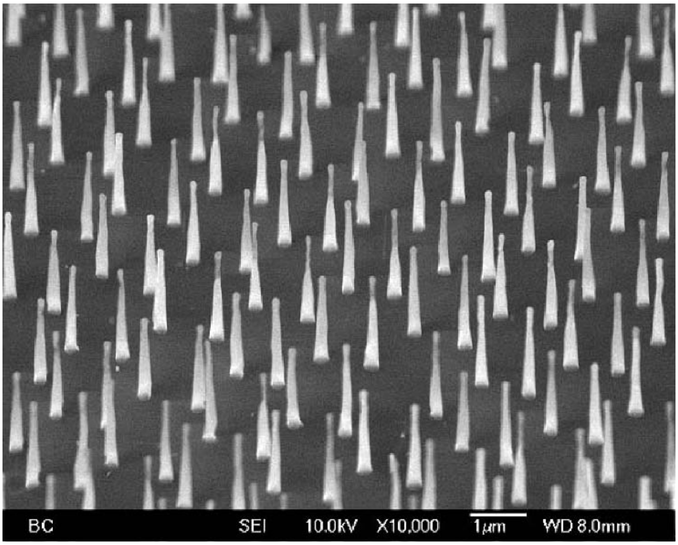

Fig. 2 SEM image showing an array of aligned carbon nanotubes intended for delivering foreign material into cells quickly and efficiently. In this case, the nanotubes will leave the cells clean and unharmed

Taking into account that carbon nanotubes are hollow cylinders, they can store active substances, thus the same nano-electroporative approach may be used for localized drug delivery. In contrast to conventional micro-pipettes widely used for patch-clamp electrophysiology, ionophoretic stimulation, and single-cell injections, nanoscaled minimal-invasive nanotubes are advantageous for studies involving gentle membrane permeabilization and subsequent ejection of molecules from the internal lumen of a nanotube into the cytosol.[14]

2.2 Carbon Nanotubes for Bone Tissue Engineering

Previously we showed that mouse fibroblast cells were able to grow onto nanopatterned substrates made up of intercrossed carbon nanotubes.[15] In a recent set of experiments, we have also demonstrated that a substrate provided with a periodic nano-pattern can significantly influence cellular behavior.[16] These results show that highly ordered arrays of carbon nanotubes may be used for guiding and controlling the growth of mammalian cells. On the other hand, the effects of nanoscale substrate topography (texture and roughness) on the behavior of human cells can be explored by substrates prepared by nanosphere lithography (NSL) combined with layer-by-layer deposition (LBL). We possess in-depth expertise in these techniques and they have been successfully used to prepare nanohybrids with enhanced mechanical properties mimicking the unique features of the extracellular matrix (ECM).[17]

2.2.1 Periodic Array of Aligned Carbon Nanotubes

Our current studies have focused on manipulating the growth of osteoblast-like cells with periodic arrays of aligned carbon nanotubes.[16] This perfectly controlled chemical environment and the spacing of these nanotubes in a nanometer range dramatically enhance cell surface activity. Cell-culture assays on these substrates reveal that the high number of attachment sites (nanotubes) promotes cell-attachment via cell extensions much better than non-nanostructured substrates (Fig. 3). The formation of cell extensions is closely associated with biomechanical forces exerted by cells on individual nanotubes (Fig. 4). These interfacial reactions at the nanoscale definitely lead to cell shape alterations and influence the direction of their movement. To explore whether a distortion of the periodic carbon nanotube-pattern might result in a change in the onset of cell adhesions, the wafer surface was scratched with a diamond knife. The results show a lack of cell growth onto the naked underlying wafer surface (Fig. 5). Similar findings have recently been reported by Cavalcanti-Adam et al.[18] who describe the development of thin, tube-like membrane tethers as being dependent on the surface nanopatterning and its density. We can assume that the observed substrate preference is exclusively due to the presence of hydrophobic carbon nanotubes. These results allow us to conclude that osteoblast cells are able to “sense” the nano-geometry of their surrounding

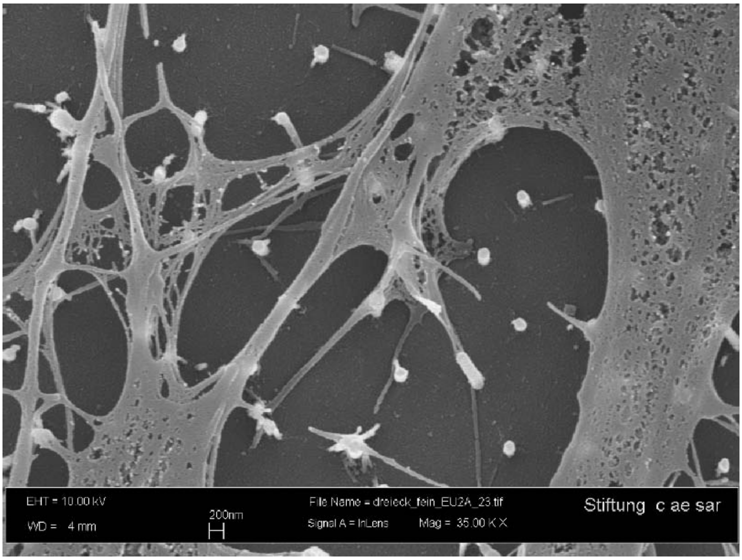

Fig. 3 SEM image depicting the growth of osteoblast-like cells on a periodic array of carbon nanotubes. Remarkably, the cell extensions are consistent with the dimension and distribution of aligned nanotubes

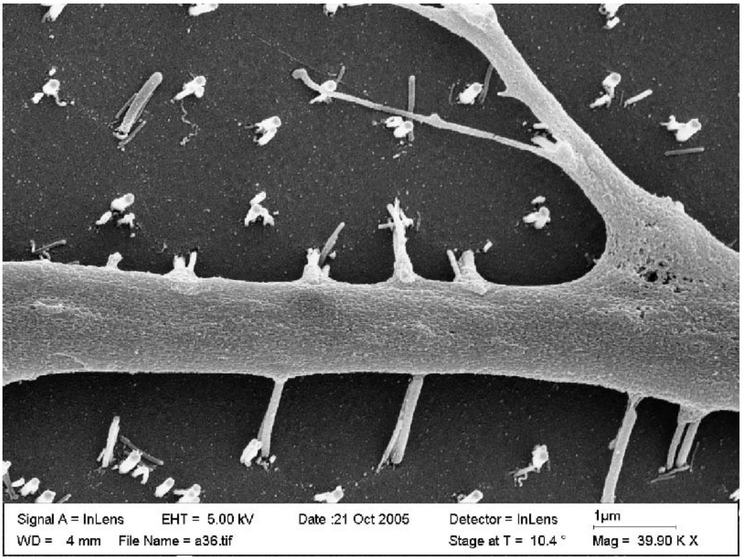

Fig. 4 SEM image depicting cell extensions of osteoblast-like cells exerting traction forces against the nanotubes

Fig. 5 SEM image showing the lack of growth effect by a nanotube-free area of the nanopatterned substrate

environment. Further, the periodic distribution of the nanotubes directly controls how and where osteoblast-like cells will grow. Carbon nanotubes mimicking morphological nano-features of the native ECM reveal new “smart tools” by which bone cells can be patterned during development. This could be a beneficial effect regarding tissue regeneration.[19,20]

2.2.2 Fabrication of Highly Ordered Nanostructured Layers and Their Impact on Cell Growth

As aforementioned, the NSL technique combined with the layer-by-layer (LBL) assembly process was employed to reproduce at least partially, both the exceptional nanotopography and nanochemistry presented on the extracellular matrix (ECM) of bone. In particular, we aim to create architectures and topographies that mimic native bone tissue (Fig. 6). The complete network architecture consists of successive layers of cross-linked carbon nanotubes that self-assemble into orderly structures. The method allows for controlled shaping and guarantees the considerable chemical and mechanical stability of the self-assembled monolayers, allowing for high reproducibility in manufacturing. The films – as free-standing substrates – are characterized by controlled geometry, surface topography, and chemical composition.[17] The films can be impregnated with macromolecules such as collagen and fibronectin, and dotted with bioactive materials, including hydroxyapatite and metal nanoparticles.

To address the role of nano-sized features in complex nanostructured substrates, both texture and surface roughness of free-standing films were tested for their ability

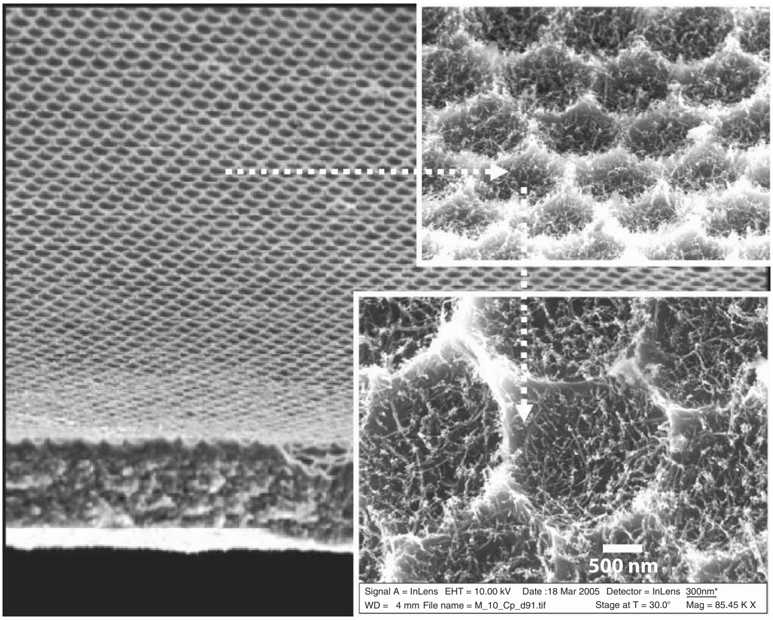

Fig. 6 SEM image showing a bioinspired free-standing substrate made up of carbon nanotubes arranged in a regular network of micro-cavities

to promote cell growth. Thin free-standing films are extremely interesting substrates in examining how cell growth, proliferation, and differentiation may be controlled by nanosized features. Therefore, the design and characterisation of bioinspired nanoscaled-featured constructs constitute a major part of our research. In order to design a suitable cell scaffold the following are required: carbon nanotubes as the chosen material must be biocompatible, non-toxic, of sufficient strength to support cell growth, geometrically appropriate and favorable to cell proliferation. Moreover, the same scaffolds as free-standing films have to be provided with highly interconnected pores to allow the diffusion of liquid medium for nutrient supply and waste removal. Taken together, all of these properties define optimal culturing conditions.

For these experiments, osteoblast-like cells were seeded onto nanostructured films to evaluate cell viability and proliferation. Standard tissue culture plastic was used as a control. The results demonstrate that the cells respond to a surface nanotopography with excellent adhesion and spreading (Fig. 7). The cells respond differently depending on the configuration of the micro- and nanotopographical cues present on the substrates. Furthermore, the cell patterns on the substrates reveal that the nanotubes do influence the organization of the cells. This aspect suggests that nanoscale biomechanics of cell attachment and migration may be steered by man-made nanoscaled features. The latter will contribute to a better understanding of the central role that cell mechanics plays in sensing a nanoenvironment comparable to cell substructures. These findings offer the possibility of enhancing cell growth by using multiple nano-architectures and various chemical and physical stimuli. This promising approach promotes the fabrication of nanostructured substrates that can

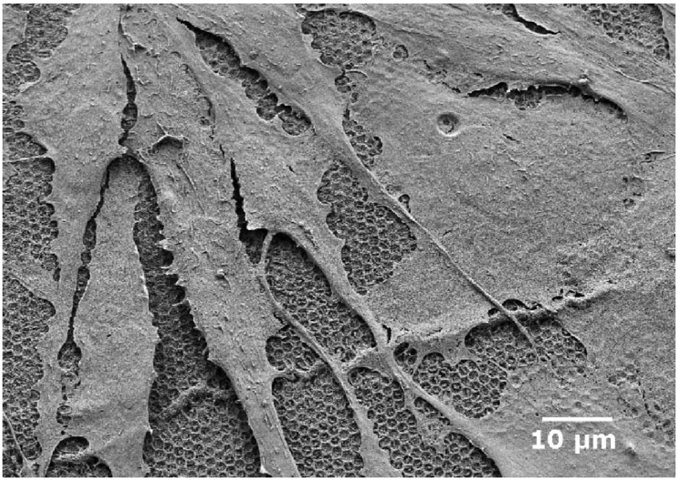

Fig. 7 SEM image depicting cell growth of osteoblast-like cells on bioinspired CNT-based substrates

mimic the extracellular matrix so that cell adhesion, growth and proliferation can be manipulated for future implant technologies.[21,22]

2.3 Nanotechnology Approaches in Enhancing Axon Regeneration

Though there have been a number of developments in neural prosthetics at the nanoscale by using carbon nanotubes[23–26] and semiconductor nanoparticles,[27] the engineering of functional and stable neural/electronic interfaces remains a crucial research area. The major challenge for the engineering and application of neuroprosthetic implants constitutes the establishment of a bi-directional flow of information between a conductive nanomaterial and the neural systems.[28,29]

Based on the premise that nanostructures might influence axonal repair – the gap between severed nerves – nanoscale-featured substrates made up of multi-walled carbon nanotubes and neuronal cells will be tested in collaboration with the Institute of Reconstructive Neurobiology in Bonn. Carbon nanotubes are strong, electrically conductive, and hollow structures of pure carbon that might conduct electrical signals to neurons, thereby acting as a "scaffolding" device to stimulate nerve cells to elongate and repair damage, and create new axons.[30,31] These new axons would take over for the damaged ones, reconnecting with the damaged nerves' counterparts. The elucidation how these phenomena may be manipulated and exploited when carbon nanotubes are assembled into a neural network has not been explored yet. Carbon nanotubes would represent a means of presenting axons with an attractive hollow structure provided with unique conductive electrical properties, which can be used for highly-controlled local stimulation. Much experimental work remains to be done in this regard. Our working hypothesis is that carbon nanotube-based substrates,

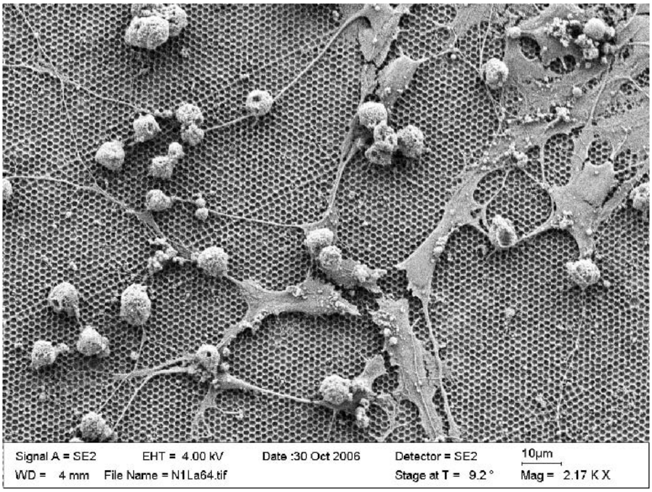

Fig. 8 SEM image depicting a bioinspired CNT-based substrate promoting the growth of neural cells

provided with multiple growth-promoting cues, will induce positive stimulation of axon regeneration. The ultimate goal behind this project is to develop nano-featured substrates that can actively communicate with neural cells.[30,31] Initial results show neuronal cells growing onto nanostructured substrates (Fig. 8).

2.4 Hexagonal Array of Gold Nanoparticles and Biosensing

Another component of our studies is the design of nanostructured sensor devices having promising properties for medical diagnostics. This research is mainly focused on the detection of metabolites by means of bioactive interfaces (nanosensors) designed at the nanoscale. Our goal is to create minimal-invasive interfaces that allow fast diagnosis of organics and cells with a high specificity and sensitivity. This includes the preparation and biofunctionalization of metal nanoparticles as detection devices. Here, we describe a novel biosensing system that comprises biological receptor molecules (i.e., antibodies for target recognition) attached to sensitive optical nano-transducers. It is conceived to detect the presence of a substance on the metal surface by determining changes in light absorption in the sample. Specifically, the nanosensor is based on the tunability of the localized surface plasmon resonance (LSPR) of arrays of noble-metal nanoparticles.[32,33] The nanosensor operates on the principle that small changes in the refractive index at or near a noble metal nanoparticle can be used to detect the binding of substances at very low concentrations.

Our nanobiosensor design essentially consists of a periodic array of gold nano-"islands" prepared by means of nanosphere lithography (NSL). The NSL uses a sacrificial mask of polymer nanospheres for subsequent processing steps. The NSL combined with chemical vapour deposition (CVD) results in an array of periodic

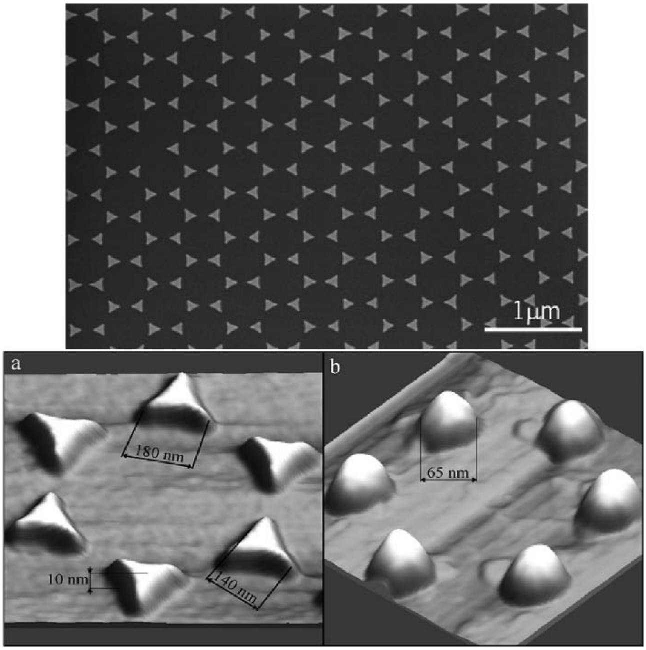

Fig. 9 (Upper part) Scanning electron microscope (SEM) image of an ordered array of nanoparticles generated from a polystyrene nanosphere mask after gold deposition and removal of the mask. (a) SEM micrograph displaying the typical morphology of the hexagonal array seen in the upper image. It consists of homogeneous triangular-shaped gold nanoparticles, which, after a sintering process, can undergo a morphological change from triangles to spheres (b)

nanostructures on a substrate (see upper part of Fig. 9). The nano-islands obtained via this method have a width ranging from 50 to 150 nm and a thickness of ca. 10 nm (see Fig. 9). Both the size and the interparticle spacing of the gold arrays can be tuned by the colloidal particles in the mask. Though NSL is a complex and costly technique, one advantage of this method in its application to bio-sensing is the high-throughput sensing and the potential of simultaneously monitoring many targets in one substrate, which is essential in biosensing technology. In addition, being bound to a substrate (wafer) greatly increases the efficacy of these nano-islands for use in bio-sensing applications. However, the efficacy of the nano-islands as nanosensors is strongly influenced or even governed by the inactivity of the surface area around the nano-islands. The latter presupposes the avoidance of the non-specific attachment caused by random collisions between the targets and the nanostructured substrate. Thus, the nano-islands of the present approach are designed towards specific interactions, and therefore to allow a specific measurement which relies exclusively upon the special properties and periodicity of the metal nano-islands.

To address the functionalization of the gold array, we follow previously-established procedures.[34,35] The nano-islands were provided with heterofunctional linkers, which

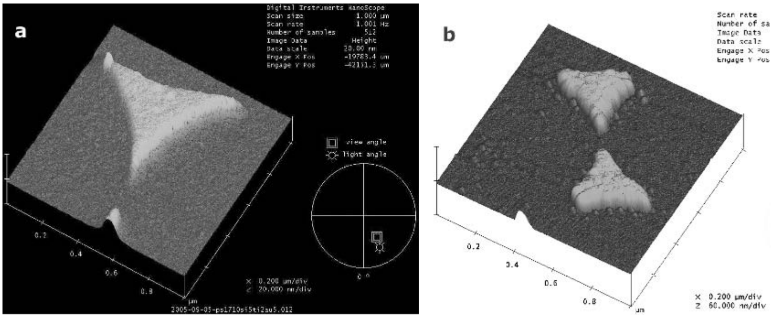

Fig. 10 Atomic-force-microscope (AFM) images displaying gold nano-islands. (a) Single gold nano-island before functionalization. (b) Two islands after biochemical functionalization with streptavidine (0.1 mM), which can be inferred indirectly from the roughness of the treated gold surface

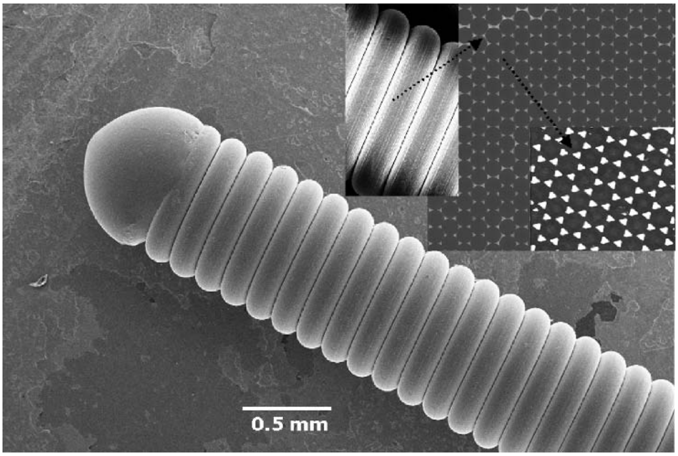

Fig. 11 SEM micrograph displaying a conventional catheter – for both intravenous and intra-arterial insertion – provided with a nanostructured pattern for analyte and cell marker detection (see inset)

anchor to the gold islands. Basically, the linker possesses a thiol tail that covalently bonds to the gold islands and a carboxylate group pointing upwards from the surface, to which a macromolecule (e.g., human IgG) can be attached (see Fig 10).

We chose gold as the substrate material for three reasons: (1) it is stable in a physiological environment, (2) its well-known surface plasmon resonance (SPR) activity, and (3) our experience with gold thiol chemistry and nanosphere lithography. Depending on the desired target, the application, and the type of sensing technique to be used, the sensor can take on any number of configurations – from non-invasive chips to minimal-invasive catheter/needles (see Fig. 11).

As we stated previously, our current research focus is nano-biotechnology with a major emphasis on nano-biomedicine. Since a significant part of tomorrow's medicine will be based on the non-invasive and painless early detection of diseases, a priority will be placed on technologies that emphasize miniaturization of the current laboratory techniques. Figure 11 shows the surface of a catheter provided with a nanoscale-featured pattern corresponding to periodic hexagonal gold-nano-island arrays (see inset) that can be functionalized for early diagnosis of diseases, including other disease forms for which specific markers are known. We are currently using the chips for prenatal diagnosis at early pregnancy by trapping fetal cells in the maternal circulation.

3 Summary

The technologies presented in this report turned out to be ideal for the development of prototypes that have been conceived as a both innovative and marketable choice in the emerging field of nanomedicine. Our concept is to start out from individual nanocomponents that are either useful in themselves, i.e., acting as individual, highly sensitive devices, or assemble themselves into precisely structured building blocks, or serve as templates for constructing other structures. Ultimately, the objective is to develop innovative technologies that can help solve healthcare problems. Concerning cell manipulation, the central idea is to provide cells with a favorable environment dotted with spatial, nanoscaled features, which can induce cell growth and proliferation. In particular, we expect that adding such features to severed neural cells would encourage axonal regeneration and recovery. On the other hand, the aforementioned immuno-nanoassays based on highly sensitive arrays of gold nano-particles will without a doubt be one of the most crucial and versatile analytical tools for the field of clinical diagnostics and environmental science. All these technologies demanded great interdisciplinary efforts, high-risk approaches, access to state-of-the-art facilities, and corresponding financial support. One example of this was the successful interaction of scientists from many disciplines working together on the design of a nano-sensor prototype intended for the detection of disease markers in human sera. This prototype has been successfully tested for rare fetal cell trapping from peripheral maternal blood. The further development of this nano-sensor technology is currently being supported by venture funds. We hope that technology knowledge platforms will emerge from research activities in the fields of biology, biomedicine, and environmental sciences through the application of nanoscience and nanotechnology approaches. They will encourage scientists and companies to work together on income-generating projects to support rapid product and market development.

Acknowledgements We gratefully acknowledge NanoLab company (hwww.nano-lab.com/) for kindly supplying us with nanotubes and nanotube-substrates. We would also like to acknowledge the extensive cooperation provided by GILUPI Nanotechnologies (www.gilupi.com) and its project staff in the design and performance of the nanosensors.

References

1. S. Iijima, Helical microtubules of graphitic carbon, *Nature* 354, 56–58 (1991).
2. L. Lacerda, A. Bianco, M. Prato, and K. Kostarelos, Carbon nanotubes as nanomedicines: from toxicology to pharmacology, *Adv. Drug Deliv. Rev*. 58(14), 1460–1470 (2006).
3. S. Polizu, O. Savadogo, P. Poulin, and L. Yahia, Applications of carbon nanotubes-based biomaterials in biomedical nanotechnology, *J. Nanosci. Nanotechnol*. 6(7), 1883–1904 (2006).
4. N. Sinha and J. T. W. Yeow, Carbon nanotubes for biomedical applications, *EEE Trans Nanobiosci*. 4(2), 180–195 (2005).
5. J. A. Rojas-Chapana and M. Giersig, Multi walled carbon nanotubes and metallic nanoparticles and their application in biomedicine, *J. Nanosci. Nanotechnol*. 6, 316–321 (2006).
6. J. A. Rojas-Chapana, M. A. Correa-Duarte, Z. Ren, K. Kempa, and M. Giersig, Enhanced introduction of gold nanoparticles into vital acidothiobacillus ferrooxidans by carbon nanotube-based microwave electroporation, *Nano Lett*. 4(5), 985–988 (2004).
7. J. A. Rojas-Chapana, J. Troszczynska, I. Firkowska, C. Morsczeck and M. Giersig, Multi-walled carbon nanotubes for plasmid delivery into Escherichia coli cells, *Lab. Chip* 5(5), 536–539 (2005).
8. T. E. McKnight, A. V. Melechko, G. D. Griffin, M. A. Guillorn, V. I. Merkulov, F. Serna, D. K. Hensley, M. J. Doktycz, D. H. Lowndes, and M. L. Simpson, Intracellular integration of synthetic nanostructures with viable cells for controlled biochemical manipulation, *Nanotechnology* 14(5), 551–556 (2003).
9. D. Cai, J. M. Mataraza, Z. H. Qin, Z. Huang, J. Huang, T. C. Chiles, D. Carnahan, K. Kempa, and Z. Ren, Highly efficient molecular delivery into mammalian cells using carbon nanotube spearing, *Nat. Methods* 2, 449–454 (2005).
10. M. Prato, K. Kostarelos, A. Bianco, D. Pantarotto, R. Singh, D. McCarthy, M. Erhardt, and J. P. Briand, Functionalized carbon nanotubes for plasmid DNA gene delivery, *Angew. Chem. Int. Ed. Engl*. 43(39), 5242–5246 (2004).
11. L. Gao, L. Nie, T. Wang, Y. Qin, Z. Guo, D. Yang, and X. Yan, Carbon nanotube delivery of the GFP gene into mammalian cells, *ChemBioChem* 7(2), 239–242 (2006).
12. N. W. Kam, Z. Liu, and H. Dai, Carbon nanotubes as intracellular transporters for proteins and DNA: an investigation of the uptake mechanism and pathway, *Angew. Chem. Int. Ed. Engl*. 45(4), 577–581 (2006).
13. J. D. Yantzi and J. T. W. Yeow, Carbon nanotube enhanced pulse electric field electroporation for biomedical applications, *Proceeding of the IEEE International Conference on Mechatronics & Automation*, Niagara Falls, Canada, July 2005.
14. N. A. Kouklin, W. E. Kim, A. D. Lazareck, and J. M. Xu, Carbon nanotube probes for single-cell experimentation and assays, *Appl. Phys. Lett*. 87, 173901–173901–3 (2005).
15. M. A. Correa-Duarte, N. Wagner, J. A. Rojas-Chapana, C. Morsczeck, M. Thie, and M. Giersig, Fabrication and biocompatibility of carbon nanotube-based 3D networks as scaffolds for cell seeding and growth, *Nano Lett*. 4(11), 2233–2236 (2004).
16. S. Giannona, I. Firkowska, J. A. Rojas-Chapana, and M. Giersig, Vertically aligned carbon nanotubes as cytocompatible material for enhanced adhesion and proliferation of osteoblast-like cells, *J. Nanosci. Nanotechnol*. 7, 1679–1683 (2007).
17. I. Firkowska, M. Olek, N. Pazos-Perez, J. A. Rojas-Chapana, and M. Giersig, Highly ordered MWNT-based matrixes: topography at the nanoscale conceived for tissue engineering, *Langmuir* 22(12), 5427–5434 (2006).
18. E. A. Cavalcanti-Adam, T. Volberg, A. Micoulet, H. Kessler, B. Geiger, and J. P. Spatz, Cell Spreading and focal adhesion dynamics are regulated by spacing of integrin ligands, *Biophys. J*. 92(8), 2964–29 (2007).
19. B. S. Harrison and A. Atala, Carbon nanotube applications for tissue engineering, *Biomaterials* 28(2), 344–53 (2007).
20. X. Shi, J. L. Hudson, P. P. Spicer, J. M. Tour, R. Krishnamoorti, and A. G. Mikos, Injectable nanocomposites of single-walled carbon nanotubes and biodegradable polymers for bone tissue engineering, *Biomacromolecules* 7(7), 2237–2242 (2006).

21. T. J. Webster and E. S. Ahn, Nanostructured biomaterials for tissue engineering bone, *Adv. Biochem. Eng. Biotechnol.* 103, 275–308 (2007).
22. L. P. Zanello, B. Zhao, H. Hu, and R. C. Haddon, Bone cell proliferation on carbon nanotubes, *Nano Lett.* 6(3), 562–567 (2006).
23. B. Nguyen-Vu, H. Chen, A. M. Cassell, R. Andrews, M. Meyyappan, and J. Li, Vertically aligned carbon nanofiber arrays: an advance toward electrical-neural interfaces, *Small* 2(1), 89–94 (2006).
24. V. Lovat, D. Pantarotto, L. Lagostena, B. Cacciari, M. Grandolfo, M. Righi, G. Spalluto, M. Prato, and L. Ballerini, Carbon nanotube substrates boost neuronal electrical signalling, *Nano Lett.* 5(6), 1107–1110 (2005).
25. T. J. Webster, Nano-biotechnology: carbon nanofibres as improved neural and orthopaedic implants, *Nanotechnology* 15, 48–54 (2004).
26. M. P. Mattson, R. C. Haddon, and A. M. Rao, Molecular functionalization of carbon nanotubes and use as substrates for neuronal growth, *Mol. Neurosci.* 14(3), 175–182 (2000).
27. T. C. Pappas, W. M. S. Wickramanyake, E. Jan, M. Motamedi, M. Brodwick, and N. A. Kotov, Nanoscale engineering of a cellular interface with semiconductor nanoparticle films for photoelectric stimulation of neurons, *Nano Lett.* 7(2), 513–519 (2007).
28. F. Patolsky, B. P. Timko, G. Yu, Y. Fang, A. B. Greytak, G. Zheng, and C. B. Lieber, Detection, stimulation, and inhibition of neuronal signals with high-density nanowire transistor array, *Science* 313, 110–1104 (2006).
29. G. A. Silva, Nanotechnology approaches for the regeneration and neuroprotection of the central nervous system, *Surg. Neurol.* 63, 301– 306 (2005).
30. M. K. Gheith, T. C. Pappas, A. V. Liopo, V. A. Sinani, B. S. Shim, M. Motamedi, J. P. Wicksted, and N. A. Kotov, Stimulation of neural cells by lateral currents in conductive layer-by-layer films of single-walled carbon nanotubes, *Adv. Mater.* 18(22), 2975–2979 (2006).
31. M. K. Gheith, V. A. Sinani, J. P. Wicksted, R. L. Matts, and N. A. Kotov, Single-walled carbon nanotube polyelectrolyte multilayers and freestanding films as a biocompatible platform for neuroprosthetic implants, *Adv. Mater.* 17(22), 2663–2670 (2005).
32. K. A. Willets and R. P. Van Duyne, Localized surface plasmon resonance spectroscopy and sensing, *Annu. Rev. Phys. Chem.* 58, 267–297 (2007).
33. A. J. Haes and R. P. Van Duyne, A nanoscale optical biosensor: sensitivity and selectivity of an approach based on the localized surface plasmon resonance spectroscopy of triangular silver nanoparticles, *J. Am. Chem. Soc.* 124(35), 10596–10604 (2002).
34. S. Kanno, Y. Yanagida, T. Haruyama, E. Kobatake, and M. Aizawa, Assembling of engineered IgG-binding protein on gold surface for highly oriented antibody immobilization, *J Biotechnol.* 76, 207–214 (2000).
35. D. Shenoy, W. Fu, J. Li, C. Crasto, G. Jones, C. Dimarzio, S. Sridhar, and M. Amiji, Surface functionalization of gold nanoparticles using hetero-bifunctional poly(ethylene glycol) spacer for intracellular tracking and delivery, *Int. J. Nanomed.* 1(1), 51–58 (2006).

This page intentionally blank

Isohelical DNA-Binding Oligomers: Antiviral Activity and Application for the Design of Nanostructured Devices

Georgy Gursky[1,*], Alexei Nikitin[1], Anna Surovaya[1], Sergey Grokhovsky[1], Valeria Andronova[2], and Georgy Galegov[2]

Abstract We performed a systematic search for new structural motifs isohelical to double-stranded DNA and found five motifs that can be used for the design and synthesis of new DNA-binding oligomers. Some of the DNA-binding oligomers can be equipped with fluorescence chromophores and metal-chelating groups and may serve as conductive wires in nano-scaled electric circuits. A series of new DNA-binding ligands were synthesized by a modular assembly of pyrrole carboxamides and novel pseudopeptides of the form (XY)n. Here, Y is a glycine residue; n is the degree of polymerization. X is an unusual amino acid residue containing a five-membered aromatic ring. Antiviral activity of bis-linked netropsin derivatives is studied. Bis-netropsins containing 15 and 31 lysine residues at the N-termini inhibit most effectively reproduction of the herpes virus type 1 in the Vero cell culture, including virus variants resistant to acyclovir and its analogues. Antiviral activity of bis-linked netropsin derivatives is correlated with their ability to interact with long clusters of AT-base pairs in the origin of replication of the viral DNA.

Keywords Isohelical DNA-binding oligomers, conductive polymers, nano-structured devices, DNA sequence recognition, antiviral activity

1 Introduction

In the past decade, great progress has been achieved in the design and synthesis of compounds that can bind to DNA at selected sites. Most of the synthesized sequence-specific DNA-binding ligands are constructed on the basis of derivatives

---

[1] V.A. Engelhardt Institute of Molecular Biology, Russian Academy of Sciences,
Vavilov Str. 32, Moscow, 119991, Russia

[2] D.I. Ivanovsky Institute of Virology, Russian Academy of Medical Sciences,
Gamaleya Str. 16, Moscow, 123098, Russia

* To whom correspondence should be addressed. e-mail: gursky@eimb.ru

M. Giersig and G. B. Khomutov (eds.),
Nanomaterials for Application in Medicine and Biology

of the antitumor antibiotics netropsin and distamycin A (for a review, see Bailly and Chaires[1]). X-ray[2–4] and NMR[5] studies show that these two antibiotics bind in the minor DNA groove at runs of four or five AT-base pairs. Their binding specificity derives from specific hydrogen-bonding interactions between the amide NH groups of the antibiotic molecule and the thymine O_2 and adenine N_3 atoms, van-der-Waals forces, and electrostatic interactions.

An obvious way to enhance the binding specificity shown by these antibiotics is to synthesize dimer compounds (bis-netropsins and bis-distamycins) in which two monomers are linked by flexible linkers in head-to-head, head-to-tail, and tail-to-tail orientations. Since the first communications on the synthesis and DNA-binding properties of the compounds of this class,[6,7] considerable progress has been achieved.[8–26] It was shown that some of these compounds exhibit a high binding specificity and selectively inhibit initiation of transcription directed by certain procaryotic and eukaryotic promoters.[7,25] Bis-linked netropsin derivatives inhibit the activity of topoisomerases I and II,[16,17] HIV-1 reverse transcriptase[18] and integrase.[19]

It is also shown that bis-netropsins containing a two-stranded antiparallel peptide motif can recognize DNA sites with mixed sequences of AT- and GC-base pairs.[13] NMR and x-ray studies showed that two distamycin (lexitropsin) molecules can be packed in an antiparallel side-by-side manner in the minor DNA groove.[2,10,15] The side-by-side dimer motif was used by Dervan and coworkers for the design of covalently linked polyamide dimers containing N-methylpyrrole- and N-methylimidazole-carboxamide units.[11,14] These ligands in hairpin form can recognize a broad category of nucleotide sequences on DNA. DNA recognition depends on side-by-side amino acids pairing in the minor groove. Antiparallel pairing of imidazole (Im) opposite pyrrole (Py) corresponds to a GC base pair, whereas a Py–Py combination recognizes either AT- or TA-base pair.[23] In addition, pairs Py–Hp and Hp–Py (Hp is a 3-hydroxypyrrole) recognize AT- and TA-base pairs, respectively.[24] Further progress in the design and synthesis of sequence-specific DNA-binding ligands is limited by the failure of pyrrole(imidazole) carboxamides containing five contiguous pyrrole (imidazole) rings to be in register with DNA base pairs. This is attributed to the fact that the helical parameters of pyrrolecarboxamide oligomers and DNA are different.[27,28] Incorporation of flexible amino acid residues (such as β-alanine) into polyamides can improve the match between the helical parameters of polyamide and DNA. However, this design strategy can be only moderately successful in targeting long DNA sequences (> six base pairs), due to a loss of binding affinity and the formation of complexes with different sequence preferences.

In the present work, we performed a systematic search for new structural motifs isohelical to double-stranded DNA. We found five motifs that can be used for the design and synthesis of new DNA-binding oligomers and polymers. Some of these motifs can be used for the design of nano-structured devices. A series of new DNA-binding ligands were synthesized by a modular assembly of pyrrole carboxamides and novel pseudopeptides of the form (XY)n. Here, Y is a glycine residue; n is the degree of polymerization. X is an unusual amino acid residue containing a five-membered aromatic ring. The DNA-binding properties and antiviral activity of bis-linked netropsin derivatives were studied.

2 Structural Motifs Isohelical to DNA

Analogues of the pyrrolecarboxamide antibiotics netropsin and distamycin and the bis-benzimidazole dye Hoechst 33258 are widely used as building blocks in the synthesis of sequence-specific DNA-binding ligands. These compounds contain a structural motif in which five-membered aromatic cycles are linked via two sp^2-hybridised atoms (Fig. 1). This structural motif will be referred to as motif I.[29]

In order to search for new polymer structures isohelical to DNA, we used software that makes it possible to determine whether a given polymer chain takes up a helical conformation with the specified parameter values. A model of the polymer chain in the corresponding conformation can then be built. A search for new structural motifs was carried out by Goodsell and Dickerson.[28] We considered a broader range of chemical structures[29] and used other criteria to select the structures with the required parameters. Using the SMOG software,[30] we generated all possible graphs for the monomeric units containing a specified number of carbon atoms and then transformed them into three-dimensional models of the monomer using special software.[29,30] It is assumed that the monomeric units are rigid and that conformation changes in the oligomer occur only by rotation around the bonds connecting successive monomer units with one another. We also excluded structures containing triple bonds in each monomer unit. Taking these restrictions into account, we considered all possible carbohydrates containing three to six carbon atoms. In addition,

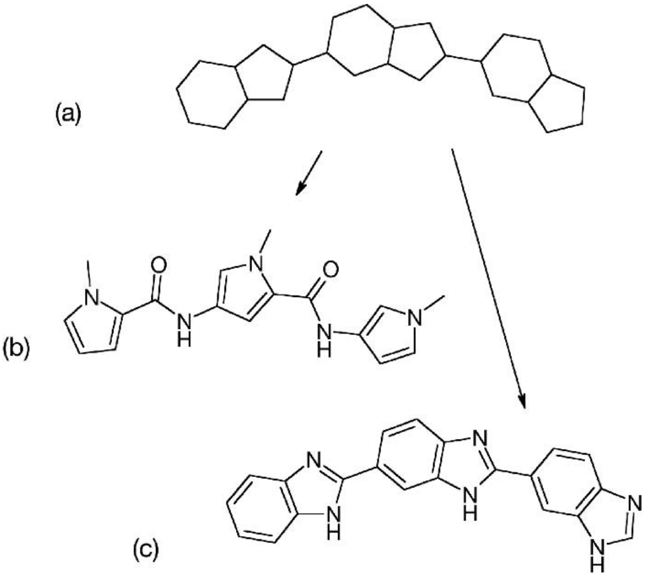

Fig. 1 Structural motif I containing the repeating units of the antibiotic distamycin (b) and the dye Hoechst 33258 (c)

we modified the structure of known DNA-binding compounds and constructed new compounds from fragments of DNA-binding antibiotics and dyes directly in the minor DNA groove. Ligands that could serve as DNA binders were inserted into the minor DNA groove and optimization in the MMFF94[31] as well as in Florent'ev's molecular-mechanical force fields was carried out and we found a number of new structural motifs.

Motif II is built on the basis of a polyacetylene chain (Fig. 2a).

Although polyacetylene is a linear polymer, systematic change of the torsion angles (approximately 20°) makes it possible to form a helix with the appropriate parameters. A replacement of double bonds with amide bonds and aliphatic rings makes it possible to obtain chemical structures for a wide variety of compounds which are built on the basis of this motif (Fig. 2b, c). Figure 2d shows the projections of the helical structure of the oligomer (see Fig. 2c) on the horizontal plane perpendicular to the helix axis and on the vertical plane passing through the helix axis.

Structural motif III contains only one sp2-hybridized atom linking five-membered rings (Fig. 3a).

An important feature of this motif is that it may be directly (without a linker) connected to a fragment of motif I to form an oligomer that can be wrapped around the minor groove of DNA. The compounds built on the basis of motif III were coined isolexins by Goodsell and Dickerson.[28] The helical structure built on the basis of a combination of motifs I and III is shown in Fig. 3d. Motif IV contains cyclohexane residues linked at the first and fourth positions in an axial conformation (Fig. 3e).

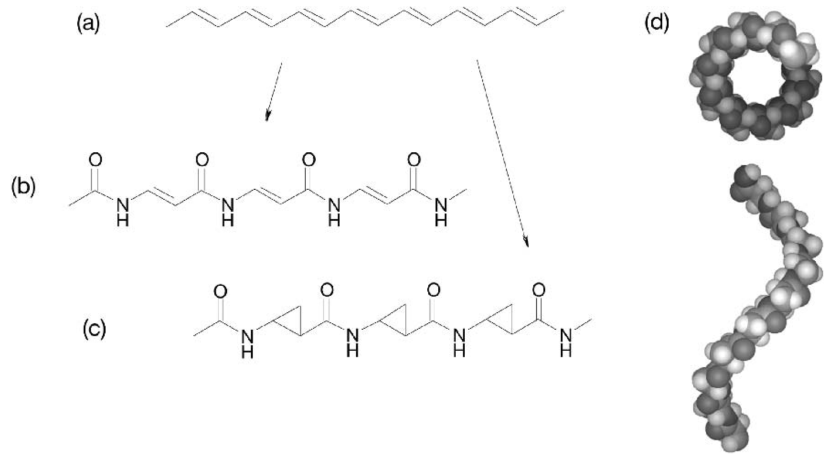

Fig. 2 Structural motif II containing a polyacetylene chain (-CH = CH)$_n$ (a) twisted in a right-handed manner to form the helix isogeometrical to DNA. Projections of the oligomer helix (b) on the vertical and horizontal plane perpendicular to the helix axis are shown (d)

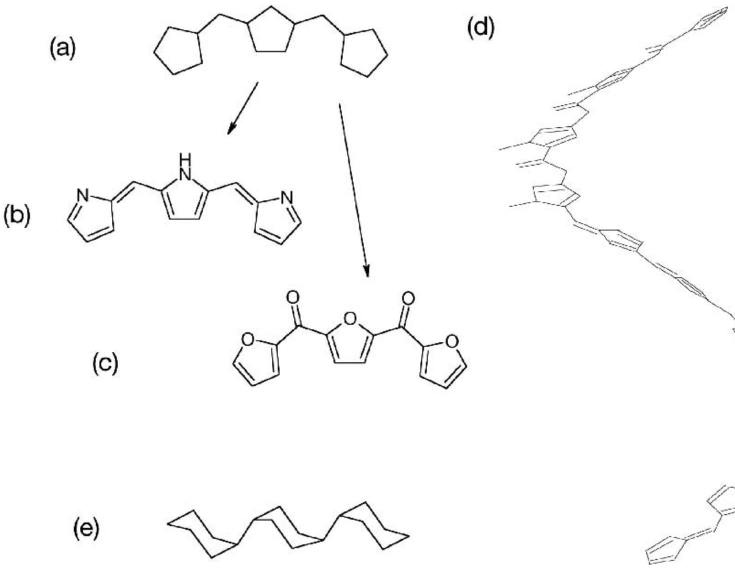

Fig. 3 Structural motifs III (a-c) and IV (e) and the structure of a helix built on the basis of motifs I and III (d)

Structural motif V (Fig. 4) exhibits very interesting features. Its repeating unit consists of two amino acid residues: an α-amino acid residue and an unusual amino acid residue containing a five-membered aromatic ring.

Examples are 5-aminomethylfuran-2-carboxylic acid residue (Fig. 4b) or its analogues containing five-membered heterocycles, such as thiazole (Fig. 4c), oxazole (Fig. 4d), N-methylhydroxypyrrole (Fig. 4e), N-methylimidazole, oxadiazole and triazole. The amino acid residues of this type occur frequently in biologically active compounds.[32] Interestingly, the oxazole- and thiazole-containing peptide antibiotic microcin B17 contains structural elements relevant to motif V.[33] It inhibits activity of DNA gyrase. On the basis of motif V, very long sequence-specific DNA-binding oligomers can be constructed with helix-generating parameters identical to those of DNA in B form. Molecular modeling studies show that thiazole-containing oligomers can be well accomodated in the minor DNA groove of the poly(dG) poly(dC) duplex. The oligomer containing six repeating units occupies twelve DNA base pairs upon binding. In the complex, the nitrogen of the thiazole ring and the carbonyl oxygen of glycine in each repeating unit are hydrogen-bonded to the guanine 2-amino groups of two successive GC-pairs. Replacement of thiazole by N-methyl hydroxypyrrole leads to a sterical clash caused by repulsive interaction between the guanine 2-amino group and the

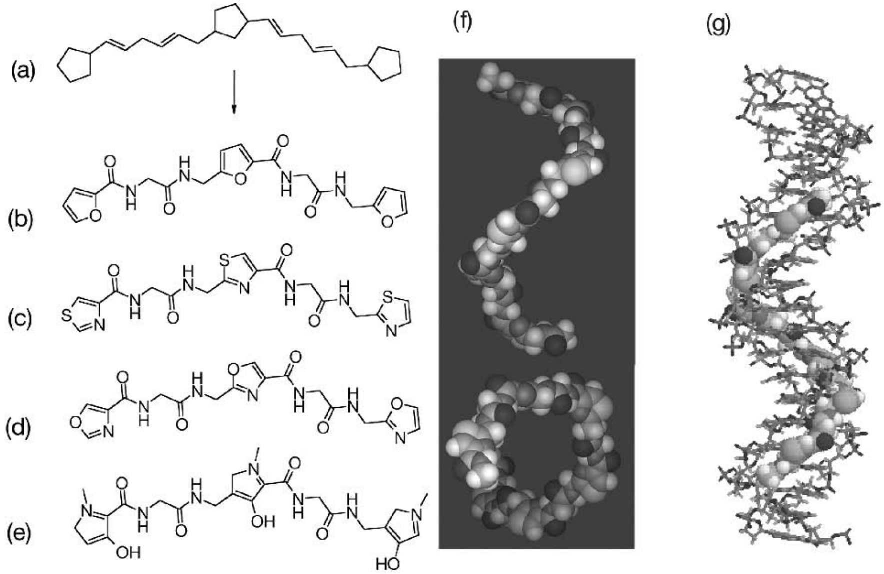

Fig. 4 Structural motif V (a-e) and structure of the complex formed by thiazole-containing oligomer with poly(dG) poly(dC) (g). Projections of the helical structure of the thiazole containing oligomer on the vertical and horizontal planes are shown in panel f

hydroxyl group in position 3 of the pyrrole ring (Fig. 4e). One may suggest that a heteropolymer built on the basis of motif V and containing hydroxypyrrole and thiazole rings binds in the minor DNA groove in such a way that hydroxypyrrole residues interact with AT-base pairs and avoid GC-pairs, whereas glycine and 4-aminomethylthiazole-2-carboxylic acid residues are tolerant to the presence of GC-pairs. Molecular modeling studies show that the hydroxyl group of the hydroxypyrrole can be hydrogen-bonded to the O2 atom of thymine or N3 atom of adenine. This type of hydrogen bonding is observed for N-methyl hydroxypyrrole residues incorporated in motif I.[34]

On the basis of motifs I and V, we constructed a DNA-binding ligand in which two netropsin fragments (motif I) are covalently linked via the pseudopeptide containing glycine, 5-aminomethylfuran-2-carboxylic acid and malonic acid residues (Fig. 5). As revealed by CD spectroscopy studies, the bis-linked netropsin derivative binds in the extended conformation to the DNA oligomer with the sequence 5′-CCTTTTAATTAAAACC-3′ with a stoichiometry of 1:1.[35] The molar dichroism value at 320 nm (121 ± 3) is consistent with simultaneous bonding of the netropsin-like fragments (motif I) and the pseudopeptide linker (motif V) to DNA. The bound ligand occupies 12 AT-base pairs upon binding to poly(dA)′poly(dT). It does not form hairpins upon binding to the DNA oligomers harboring the sequences 5′-CCTTTTTAAAAACC-3′ and 5′- CCTTTTAAAACC-3′ and forms monodentate complexes with these duplexes.[35]

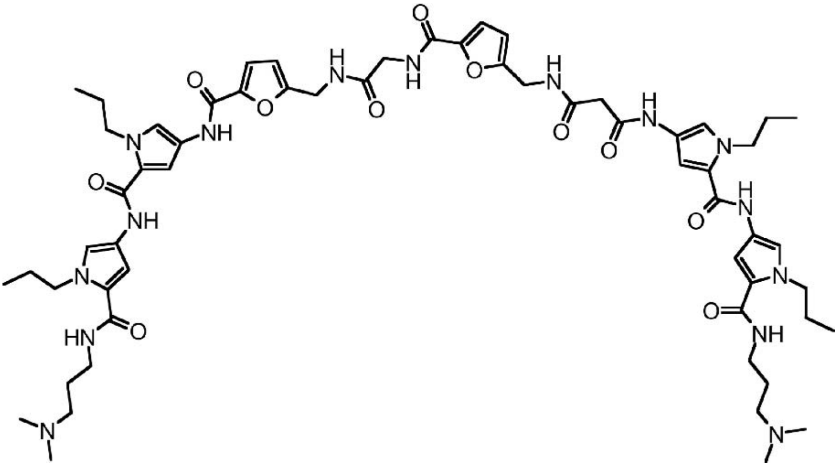

Fig. 5 Sequence-specific DNA-binding ligand constructed on the basis of motifs I and V

In contrast to this, bis-netropsins in which monomers are connected by flexible aliphatic tethers bind to these duplexes both in the extended conformation and in hairpin form.[16,18] Our experiments show that motif V exhibits rigidity sufficient for preventing the hairpin formation upon binding of the ligand to DNA. On the other hand, motif V displays a greater conformational plasticity than motif I. A combination of motifs I and V can be used for constructing DNA-binding ligands capable of reading long DNA sequences. The failure of pyrrole (imidazole) carboxamides with five or more pyrrole (imidazole) rings to be in register with the corresponding base pairs of the target site can be overcome by the use of shorter pyrrole (imidazole) carboxamides connected by isohelical tethers built on the basis of motif V. A combination of rigid netropsin-like fragments and isohelical pseudopeptides improves the match between pyrrolecarboxamide binding modules of the ligand and DNA base pairs. Conjugates of this type may represent new lead structures for the development of antiviral and antitumor agents.

2.1 Application for the Construction of Nanoscaled Devices

Isohelical DNA-binding oligomers can be equipped with metal-chelating groups, semiconductor crystals (q-dots) and fluorescent dyes to create a family of fibers with unusual electric, magnetic, and optical properties. In motif V, glycine residues can be replaced by lysine or glutamic acid residues whose side chains may serve as attachment points for covalent bonding to fluorescent dyes and chemical groups capable of chelating metal ions. Oligoacetylenes (motif II) and isolexines (motif III) possess conjugated π electron systems. The extended π electron systems of oligoacetylene or oligopyrrole are highly sensitive to chemical or electrochemical oxidation or reduction. Injection or removal of electrons from the π system of these oligomers (doping) dramatically increases their conductivity and alters their optical properties.[36] Since these reactions are reversible, it is possible to control the electrical and optical properties of these oligomers with a great deal of precision. Bound ligands are allowed to interact with the adjacent bound ligands to form long conductive associates. The electrical and optical properties of conjugated oligomers depend on the molecular structure of their repeating units. In particular, the electrical properties of oligoacetylene can be changed when a pair of carbon atoms connected by a double bond are replaced by carbon and nitrogen atoms linked by the amide bond (Fig. 2b). A transient conversion from the semiconducting state to a metal-type conductive state can also be induced upon light irradiation (photodoping). Oligodiacetylene can be obtained by polymerization of diacetylene building blocks upon UV–irradiation.[37] A template-assistant photopolymerization of diacetylene–nucleoside conjugates bound to a stretched single-stranded DNA fragment is observed.[38]

There are two possible applications of DNA as a structural material for the construction of nano-structured devices. Metallization of DNA was invented as a perspective method for the construction of conductive wires for nano-scaled electrical circuits.[39,40] Braun and coworkers connected micrometer-sized gold electrodes by single molecule of double-stranded DNA which was metallized with silver.[40]

The DNA can also be used as a scaffold for the clumping of DNA-binding ligands that possess appropriate electrical, optical, and magnetic properties. Template-assistant organic synthesis and photopolymerization can be used to generate very long oligomers. An obvious advantage of this approach is that DNA is accessible for modification and manipulation with the aid of different enzymes.

2.2 *Antiviral Activity of Bis-Linked Netropsin Derivatives*

The current strategy of suppressing infection caused by the human herpes virus is based on the selective inhibition of the activity of viral DNA polymerase by modified nucleosides such as acyclovir, ganciclovir, and famciclovir. The search for new antiviral drugs among non-nucleoside compounds is of great interest, because herpes virus variants are isolated which are resistant to treatment with acyclovir and its analogues. The group of De Clercq and Lown studied the antiviral activity of bis-netropsins in which monomers are covalently bound via aliphatic linkers of different length. The high activity of bis-netropsins against the vaccinia virus was revealed, whereas the inhibiting activities against infections caused by herpes viruses of type 1 and 2 were observed at the level of subtoxic concentrations.[9] We studied the antiviral activity of bis-netropsins, in which two netropsin fragments are attached in tail-to-head and tail-to-tail manners via triglycine and cis-diammine Pt(II) residues.[41–43] Bis-netropsins containing 15 and 31 lysine residues at the N-terminus of the bis-netropsin molecule inhibit reproduction of the herpes virus type 1 in the Vero cell culture, including virus variants resistant to acyclovir and its analogues.[42] The antiviral activity of these compounds was correlated with their ability to interact selectively with long clusters of AT-base pairs on DNA.

We also compared DNA-binding properties and antiviral activities of two bis-netropsins containing cis-diammine Pt(II) groups attached to each netropsin-like fragment via one (Pt-bis-Nt) or two (Pt-(2G)-bis-Nt) glycine residues.[43] Our observations show that Pt-bis-Nt and Pt(2G)-bis-Nt bind selectively to AT-rich regions on DNA. However, Pt(2G)-bis-Nt exhibits practically no antiviral activity in Vero cell culture experiments, whereas Pt-bis-Nt strongly inhibits reproduction of herpes simplex virus type 1 with the selectivity index equalling 60.[43] The possible target sites for the binding of Pt-bis-Nt and Pt(2G)-bis-Nt are long AT-tracks in the origin of replication (OriS and OriL) of the viral DNA. Flanking the AT-cluster in the OriS are the recognition sites for the origin-binding protein (OBP) encoded by the UL9 gene of the herpes virus. Specific and cooperative binding of OBP dimers to these sites leads to a destabilization of the AT-cluster.[44] In the presence of ATP and another viral protein ICP8 (single-stranded DNA-binding protein) OBP induces the unwinding of the minimal OriS duplex (80 bp). Interaction of the bis-netropsin with the AT-track may prevent its destabilization and may interfere with the assembly and normal functioning of the viral proteins UL9 and ICP8.

Interaction of Pt-bis-Nt and Pt(2G)-bis-Nt with the fragment of OriS was studied by DNase I footprinting and CD spectroscopy. The CD data show that Pt(2G)-bis-Nt interacts with the AT-track predominantly in the extended conformation and self-associated dimer form. In contrast, Pt-bis-Nt binds to this fragment in the extended conformation and in hairpin form. The footprints produced by Pt-bis-Nt and Pt(2G)-bis-Nt at the same concentration level are different. Pt-bis-Nt protects a longer DNA region from DNase I cleavage as compared with the footprint size generated in the presence of Pt(2G)-bis-Nt.[43] This protection effect is observed at a three times lower concentration. It is also worth noting that Pt-bis-Nt strongly protects a DNA site with the sequence 5′-TATAGGTATA-3′ from cleavage, whereas in the presence of Pt(2G)-bis-Nt, no protection in this DNA region is detected.[43] It is also known that Pt-bis-Nt in the parallel-stranded hairpin form binds most strongly to the DNA site with the sequence 5′-TATAT-3′[18] which is present in the OriS AT-track. These observations indicate that DNA binding properties and antiviral activities of these bis-netropsins are correlated.

3 Conclusion

Using a systematic computational search, new structural motifs isohelical to double-stranded DNA are found. These motifs can be used for the design and synthesis of new generations of sequence-specific DNA-binding ligands. Some of them possess unusual electrical, optical, and magnetic properties. Oligoacetylenes and related molecules (motif II) as well as isolexins (motif III) and their conjugates with oligobisbenzimidazoles (motif I) possess conjugated π electron systems and may serve as conductive wires in nano-scaled electrical circuits. On the basis of motif V or a combination of motifs I and V very long DNA-binding oligomers can be constructed with helix-generating parameters identical to those of DNA in the B-form. These molecules can be equipped with metal-chelating groups and fluorescent chromophores and used for the design of DNA-based nano-structured devices. Some of these ligands are cell-permeable and bind to DNA with high affinity and specificity in the context of chromatin. Sequence-specific binding of these ligands to their target sites on DNA may inhibit activity of some transcription factors and DNA-binding enzymes and may also affect global structural features of protein–DNA assemblies implicated in replication and/ or transcription processes. We found that some bis-oligopyrrolecarboxamides act as efficient inhibitors of herpes simplex virus type 1 reproduction in cell culture experiments. Their antiviral activities appear to be correlated with their ability to bind selectively to the origin of replication of the viral DNA and to inhibit activity and normal functioning of the viral proteins UL9 and ICP8.

Acknowledgements We are grateful to V. L. Florent'ev who kindly permitted us to use the molecular-mechanic force field developed by him for calculations, to S. A. Rodin and V. F. Pismensky for participation in the CD measurements. We also thank Chemical Computing Group Inc. that kindly provided the MOE software.

This study was supported by the Program of the Presidium of the Russian Academy of Sciences on Molecular and Cell Biology and the Russian Foundation for Basic Research (projects nos. 04-04-49364 and 07-04-01031).

References

1. C. Bailly and J. B. Chaires, Sequence-specific DNA minor groove binders. Design and synthesis of netropsin and distamycin analogues, *Bioconjug. Chem.* 9(5), 513–538 (1998).
2. M. L. Kopka, C. Yoon, D. Goodsell, P. Pjura, and R. E. Dickerson, The molecular origin of DNA-drug specificity in netropsin and distamycin, *Proc. Natl. Acad. Sci. USA*. 82(5), 1376–1380 (1985).
3. M. Coll, C. A. Frederick, A. H. Wang, and A. Rich, A bifurcated hydrogen bonded conformation in the d(AT) base pairs of the DNA dodecamer d(CGCAAATTTGCG) and its complex with distamycin, *Proc. Natl. Acad. Sci. USA*. 84(23), 8385–8389 (1987).
4. R. E. Dickerson, Helix structures and molecular recognition by B-DNA, in: *Oxford Handbook of Nucleic Acid Structure*, S. Neidle (ed.) (Oxford University Press, New York, 2001), pp. 145–197.
5. R. E. Klevit, D. E. Wemmer, and B. R. Reid, 1H NMR studies on the interaction between distamycin A and a symmetrical DNA dodecamer, *Biochemistry* 25(11), 3296–3303 (1986).
6. A. A. Khorlin, A. S. Krylov, S. L. Grokhovsky, A. L. Zhuze, A. S. Zasedatelev, G. V. Gursky, and B. P. Gottikh, A new type of AT-specific ligand constructed of two netropsin-like molecules, *FEBS Lett.* 118(2), 311–314 (1980).
7. G. V. Gursky, A. S. Zasedatelev, A. L. Zhuze, A. A. Khorlin, S. L. Grokhovsky, S. A. Streltsov, A. N. Surovaya, A. M. Nikitin, A. S. Krylov, V. O. Retchinsky, R. S. Beabealashvili, and B. P. Gottikh, Synthetic sequence-specific ligands, *Cold Spring Harbor Symp. Quant. Biol.* 47, 367–378 (1983).
8. J. W. Lown, K. Krowicki, U. G. Bhat, A. Skorobogaty, B. Ward, and J. C. Dabrowiak, Molecular recognition between oligopeptides and nucleic acids – novel imidazole-containing oligopeptides related to netropsin that exhibit altered DNA-sequence specificity, *Biochemistry* 25(23), 7408–7416 (1986).

9. J. W. Lown, K. Krowicki, J. Balzarini, R. A. Newman, and E. De Clerk, Novel linked antiviral and antitumor agents related to netropsin and distamycin: synthesis and biological evaluation, *J. Med. Chem.* 32(10), 2368–2375 (1989).
10. J. G. Pelton and D. E. Wemmer, Structural characterization of a 2:1 distamycin A d(CGCAAATTGGC) complex by two-dimensional NMR, *Proc. Natl. Acad. Sci.* 86(15), 5723–5727 (1989).
11. M. Mrksich, M. E. Parks, and P. B. Dervan, Hairpin peptide motif, A new class of oligopeptides for sequence-specific recognition in the minor groove of double-helical DNA, *J. Am. Chem. Soc.* 116, 7983–7988 (1994).
12. X. Chen, B. Ramakrishnan, S. T. Rao, and M. Sundaralingam, Binding of two distamycin A molecules in the minor groove of an alternating B-DNA duplex, *Struct. Biol.* 1, 169–175 (1994).
13. V. A. Nikolaev, S. L. Grokhovsky, A. N. Surovaya, T. A. Leinsoo, N. Yu. Sidorov, A. S. Zasedatelev, A. L. Zhuze, G. A. Strachan, R. H. Shafer, and G. V. Gursky, Design of sequence-specific DNA binding ligands that use a two-stranded peptide motif for DNA sequence recognition, *J. Biomol. Struct. Dyn.* 14(1), 31–47 (1996).
14. B. H. Geierstanger, M. Mrksich, P. B. Dervan, and D. E. Wemmer, Design of a G7C-specific DNA minor groove-binding peptide, *Science* 266, 646–650 (1994).
15. M. L. Kopka, D. S. Goodsell, G. W. Han, T. K. Chiu, J. W. Lown, and R. E. Dickerson, Defining GC-specificity in the minor groove: side-by-side binding of diimidazole lexitropsin to CATGGCCATG, *Structure* 5, 1033–1044 (1997).
16. A. N. Surovaya, G. Burckhardt, S. L. Grokhovsky, E. Birch-Hirschfeld, G. V. Gursky, and C. Zimmer, Hairpin polyamides that use parallel and antiparallel side-by-side peptide motifs in binding to DNA, *J. Biomol. Struct. Dyn.* 14(5), 595–606 (1997).
17. S. L. Grokhovsky, A. N. Surovaya, G. Burckhardt, V. F. Pismensky, B. K. Chernov, C. Zimmer, and G. V. Gursky, DNA sequence recognition by bis-linked netropsin and distamycin derivatives, *FEBS Lett.* 439(3), 346–350 (1998).
18. A. N. Surovaya, G. Burckhardt, S. L. Grokhovsky, E. Birch-Hirschfeld, A. M. Nikitin, H. Fritzsche, C. Zimmer, and G. V. Gursky, Binding of bis-linked netropsin derivatives in the parallel-stranded hairpin form to DNA. *J. Biomol. Struct. Dyn.* 18(5), 689–701, (2001).
19. T. A. Beerman, J. M. Woynarowski, R. D. Sigmund, L. S. Gawron, K. E. Rao, and J. W. Lown, Netropsin and bis-netropsin analogs as inhibitors of the catalytic activity of mammalian DNA topoisomerase II and topoisomerase cleavable complexes, *Biochim. Biophys. Acta.* 1090(1), 52–60 (1991).
20. G. Burkhardt, H. Simon, K. Storl, H. Triebel, A. Walter, J. W. Lown, and C. Zimmer, DNA binding studies and influence on the activity of DNA topoisomerases of bis-netropsins: different effects of analogs containing cis and trans ethylene linkers, *J. Biomol. Struct. Dyn.* 15(1), 81–95 (1997).
21. M. E. Filipowsky, M. L. Kopka, M. Brazil-Zison, J. W. Lown, and R. E. Dickerson, Linked lexitropsins and the in vitro inhibition of HIV-1 reverse transcriptase RNA-directed DNA polymerization: a novel induced-fit of 3, 5 m-pyridyl bisdistamycin to enzyme-associated template-primer, *Biochemistry* 35(48), 15397–15410 (1996).
22. N. Neamati, A. Mazumder, S. Sunder, J. M. Owen, M. Tandon, J. W. Lown, and Y. Pommier, Highly potent synthetic polyamides, bis-distamycins, and lexitropsins as inhibitors of human immunodeficiency virus type 1 integrase, *Mol. Pharmacol.* 54(2), 280–290 (1998).
23. S. White, J. W. Szewczyk, J. M. Turner, E. E. Baird, and P. B. Dervan, Recognition of the four Watson-Crick base pairs in the DNA minor groove by synthetic ligands, *Nature* 391(6666), 468–471 (1998).
24. A. R. Urbach, J. W. Szewczyk, S. White, J. M. Turner, E. E. Baird, and P. B. Dervan, Sequence selectivity of 3-hydroxypyrrole/pyrrole ring pairings in the DNA minor groove, *J. Am. Chem. Soc.* 121(50), 11621–11629 (1999).
25. L. A. Dickinson, R. J. Gulizia, J. W. Trauger, E. E. Baird, D. E. Mosier, J. M. Gottesfeld, and P. B. Dervan, Inhibition of RNA polymerase II transcription in human cells by synthetic DNA-binding ligands, *Proc. Natl. Acad. Sci. USA.* 95(22), 12890–12895 (1998).

26. S. L. Belikov, S. L. Grokhovsky, M. G. Isaguliants, A. N. Surovaya, and G. V. Gursky, Sequence-specific minor groove binding ligands as potential regulators of gene expression in Xenopus Laevis oocytes, *J. Biomol. Struct. Dyn*. 23(2), 193–202 (2005).
27. A. S. Zasedatelev, Geometrical correlations useful for design of sequence-specific DNA narrow groove binding ligands, *FEBS Lett*. 281(1–2), 209–211 (1991).
28. D. Goodsell and R. E. Dickerson, Isohelical analysis of DNA groove-binding drugs, *J. Med. Chem*. 29(5), 727–733 (1986).
29. A. M. Nikitin and G. V. Gursky, New structural motifs isohelical to DNA, *Doklady Biochem. Biophys*. 390(1–6), 139–142 (2003).
30. M. S. Molchanova, W. Shcherbukhin, and N. S. Zefirov, Computer generation of molecular structures by SMOG program, *J. Chem. Inform. Comp. Sci*. 36(4), 888–899 (1996).
31. T. A. Halgren, Merck molecular force field: I. Basis, form, scope, parameterization and performance of MMFF94, *J. Comput. Chem*. 17(5–6), 490–519 (1996).
32. J. P. Michael and G. Pattenden, Marin metabolites and metal ion chelation: the facts and the fantasies, *Angew. Chem., Int. Ed*. 32(1), 1–23 (1993).
33. P. Yorgey, J. Lee, J. Kördel, E. Vivas, P. Warner, D. Jebarathan, and R. Kolter, Posttranslational modifications in microcin B17 define an additional class of DNA gyrase inhibitors. *Proc. Natl. Acad. Sci. USA*. 91, 4517–4523 (1994).
34. C. L. Kielkopf, R. E. Bremer, S. White, J. W. Szewczyk, J. M. Turner, E. E. Baird, P. B. Dervan, and D. C. Rees, Structural effects of DNA sequence on T7A recognition by hydroxypyrrole/pyrrole pairs in the minor groove, *J. Mol. Biol.,* 295(3), 557–567 (2000).
35. A. M. Nikitin, S. A. Rodin, V. F. Pismensky, A. N. Surovaya, and G. V. Gursky, A new pseudopeptide motif for designing specific DNA-binding compounds capable of recognizing long DNA sequences, *Doklady Biochem. Biophys*. 384(1–6), 167–171 (2002).
36. C. K. Chiang, C. R. Fincher Jr., Y. W. Park, A. G. Heeger, H. Shirakawa, E. J. Louis, S. C. Gau, and A. G. MacDiarmid, Electrical conductivity in doped polyacetylene, *Phys. Rev. Lett*. 39(17), 1098–1101 (1977).
37. T. Hasegawa, S. Haraguchi, M. Numata, C. Li, A.-H. Bae, T. Fujisawa, K. Kaneko, K. Sakurai, and S. Shinkai, Poly(diacetylene)-nanofibers can be fabricated through photo-irradiation using natural polysaccharide schizophyllan as a one-dimensional mold, *Org. Biomol. Chem*. 3(24), 4321–4328 (2005).
38. M. Shimomura, R. Mitamura, J. Matsumoto, and K. Ijiro, DNA-mimetics: towards novel molecular devices having molecular information, *Synthetic Metals* 133–134, 473–479 (2003).
39. N. C. Seeman, Structural DNA nanotechnology: an overview, *Methods Mol. Biol*. 303, 143–166 (2005).
40. E. Braun, Y. Eichen, U. Sivan, and G. Ben-Yoseph, DNA-templated assembly and electrode attachment of a conducting silver wire, *Nature*. 391(6669), 775–778 (1998).
41. V. L. Andronova, S. L. Grokhovsky, S. L. Surovaya, and Gursky, G. A. Galegov, Antiherpetic activity of dimeric derivatives of netropsin, *Doklady Biochem. Biophys*. 380(1–6), 345–348 (2001).
42. A. N. Surovaya, S. L. Grokhovsky, V. L. Andronova, G. A. Galegov, and G. V. Gursky, DNA binding properties and antiviral activity of two bis-netropsins containing cis-diammineplatinum(II) group in the linker between two netropsin moeties, Book of the abstract: Albany 2007, Conservation 15, June 19–23 2007.
43. A. N. Surovaya, V. L. Andronova, S. L. Grokhovsky, G. A. Galegov, and G. V. Gursky, DNA-binding and antiviral activity of bis-netropsins, *Biophysics* 50(6), 884–893 (2005).
44. A. Aslani, M. Olsson, and P. Ellias, ATP-dependent unwinding of a minimal origin of DNA replication by the origin-binding protein and single-stranded DNA binding protein ICP8 from herpes simplex virus type I, *J. Biol. Chem*. 227, 41204–41212 (2002).

DNA Self-Assembling Nanostructures Induced by Trivalent Ions and Polycations

Nina Kasyanenko[1,*] **and Daria Afanasieva**[1]

Abstract The purpose of this work is to compare DNA condensation induced by small multivalent ions and polycations. DNA complexes with trivalent ions Fe^{3+}, La^{3+}, $[Co(NH_3)_6]^{3+}$, spermidine and cationic polymers in a solution were investigated. The influence of cations on the volume, persistent length, and secondary structure of DNA was studied. A comparison of DNA packaging induced by trivalent ions and polycations was made. DNA complexes with trivalent metal ions and polycations were characterized by means of low gradient viscometry, dynamic light scattering, circular dichroism, UV spectrometry, flow birefringence, and atomic force microscopy.

Keywords DNA condensation, DNA-polymer complexes, cobalt hexamine, trivalent metal ions

1 Introduction

The development of nanotechnology requires the creation of new materials and devices. Nanodimension is a typical scale for biological systems. The formation of self-assembling complexes for nucleic acids and proteins with different ligands in a solution can give us the possibility of new applications for biological macromolecules as components in nanostructures.

DNA is a promising construction material in nanotechnology owing to its properties, including a huge charge density, high rigidity (persistence length around 50 nm), the affinity of complementary sequences, a well-stacked antiparallel double-helical backbone that is largely regular regardless of sequence, and the possibility to easily divide it into single-stranded chains. DNA can be used for the selective binding with macromolecular components and small ligands. The interaction of DNA with different compounds can be diverse and highly specific. Not only

---

[1] Dept. of Molecular Biophysics, Faculty of Physics, St. Petersburg State University, Uluanovskaya St. 1, 198504, St. Petersburg, Russia

[*] To whom correspondence should be addressed. e-mail: kasyan@paloma.spbu.ru

M. Giersig and G. B. Khomutov (eds.),
Nanomaterials for Application in Medicine and Biology

the high-specific binding plays an important role in this regard. The collection of low-specific, non-covalent contacts between distinct ligands and atomic groups of DNA through hydrogen bonding, electrostatic, and hydrophobic interactions makes the organization of high-ordered reversible structures possible. DNA packaging in a solution induced by different agents can be accompanied by the formation of small discrete particles including toroids and rods.[1–4] Investigators have assumed that DNA in toroids is in B-form and its double helix is packed up with mutually oriented segments.[5,6] The toroid is a morphology used by nature for the high-density packing of genomes in sperm cells and in bacteriophages.[7]

Recently, polypeptides and synthetic polymers have been applied to condense DNA into nanoparticles and thus provide efficient non-viral vectors for gene transfer to eukaryotic cells *in vitro* and *in vivo*.[8–11] The transfection efficiency generally paralleled the ability of these cations to condense DNA. Thus, *in vitro* methods for producing and studying condensed DNA have potential technological applications. The investigation of DNA condensation in a solution enables us to clearly explain the molecular mechanism of DNA reorganization in a cell.

DNA condensation is a collapse of swollen molecular coils into small dense particles. Since DNA is a highly-charged polyion, the key question is how the electrostatic interaction between charged monomers changes from repulsive to attractive. This phenomenon is not yet completely understood.

The main purpose of this work is to compare DNA condensation induced by small multivalent ions and polycations. The influence of cations on the volume, the persistent length, and the secondary structure of DNA was investigated. A comparison of DNA packaging induced by trivalent ions and polycations was made.

2 Materials and Experimental Methods

In our experiments, we used calf thymus DNA (Sigma) with the molecular mass MM = $9 \cdot 10^6$, poly-L-lysine hydrobromide (PLL) (Sigma), MM = 57,000, spermidine (Sigma), hexamminecobalt (III) $[Co(NH_3)_6]Cl_3$. Polyallylamine (PAA), MM = 20,000 and Polytrimethylammonioethyl methacrylate chloride (PTMAEM) MM = 200,000 were synthesized by Dr. Olga Nazarova at the Institute of Macromolecular Compounds, RAS (St. Petersburg).[11] Systems were prepared by mixing together equal volumes of the initial DNA and condensing agent solutions in 0.005 M NaCl. Experiments were carried out after the storage of the systems for 12 h at 4 °C.

2.1 Low Gradient Viscometry

The relative viscosity η_r of the respective solution at various flow rate gradients g was measured in a Zimm-Crothers type rotation viscometer. The intrinsic viscosity $[\eta]$ was determined by the extrapolation of specific viscosity $\eta_{sp} = (\eta_r - 1)/C$ to zero concentration C:

$$[\eta]=\lim_{\substack{C\to 0\\ g\to 0}}\frac{\eta_r-1}{C}$$

The $[\eta]$ value is proportional to the volume of the DNA molecular coil in a solution.

2.2 Flow Birefringence

The dependence of the birefringence value Δn on the flow rate gradient for DNA solutions of different concentrations can yield the dynamooptical constant:

$$[n]=\lim_{\substack{g\to 0\\ C\to 0}}\frac{\Delta n}{gC\eta_0}$$

where η_o is the solvent viscosity. The ratio $[n]/[\eta]$ is proportional to the optical anisotropy of the molecular coil ($\gamma_1-\gamma_2$). For DNA solutions the value $\frac{(\Delta n/g)_{g\to 0}}{(\eta_r-1)\eta_0}$ is equal to the ratio $[n]/[\eta]$. For DNA, the value ($\gamma_1-\gamma_2$) is determined by the optical anisotropy of a statistical segment ($\alpha 1-\alpha 2$) = SΔβ, where Δβ is the difference between the polarizabilities of a nucleotide pair along the DNA helix axis and perpendicular to it, and S is the number of nucleotide pairs in a statistical segment. S determines the rigidity of DNA.

2.3 Dynamic Light Scattering

The measurements were performed using a PhotoCor-SP, (PhotoCor, Russia). The optical source employed for the scattering measurements was a He-Ne-Laser (Russia), tuned at 632.8 nm with a typical power of 25 mW. The time autocorrelation functions of the scattered intensity, $g^{(2)}(q, t)$, were accumulated by a correlator with 288 canals and analyzed using CONTIN. Seven scattering angles from, typically, 30° to 110° were used. Measurements were made at a temperature of 25°C.

2.4 Spectral Methods

The DNA concentration was determined from the difference in optical absorption of hydrolysed DNA solutions at wavelengths $\lambda = 270$ nm and $\lambda = 290$ nm. The DNA native state was controlled by the value of the hyperchromic effect. UV absorption spectra of the solutions were recorded with a Specord UV-Vis spectrophotometer. Circular dichroism (CD) spectra were recorded using a Jobin-Yvon Mark IV dichrograph.

2.5 Atomic Force Microscopy

A drop of DNA solution C(DNA) = 5×10^{-6} M with different compounds was deposited on a freshly cleaved mica surface for 1–2 min. It was then washed with distilled water and dried. Samples were imaged in a Nanoscope IIIa atomic force microscope operating in tapping mode in air (for DNA complexes with polycations), and in a fluid cell under ethanol (for DNA complexes with La^{3+}).

3 DNA Interaction with Trivalent Metal Ions and Polycations in a Solution

It was shown that trivalent metal ions form stable complexes with DNA which are not dissociated by dilution.[12,13] It is known that the polymeric molecule will reach the conformation of an isolated statistical coil in a dilute solution. The size of the coil is determined by the polymer – solvent interaction. The main reason for the polyelectrolyte swelling of DNA in a solution is the electrostatic repulsion between charged phosphates. The presence of trivalent metal ions in a solution causes the shrinkage of the DNA coil at low NaCl concentration. The same decrease in DNA-intrinsic viscosity is observed at high ionic strength, at full suppression of DNA polyelectrolyte swelling (Fig. 1, left). The shrinkage is typical for DNA in a solution of high and low ionic strength, irrespective of the type of trivalent metal ion. It is significant that the dissociation of the compound $[Co(NO_2)_6]Na_3$ in a water solution produces a negative complex ion, $[Co(NO_2)_6]^{3-}$. Nevertheless, it interacts with DNA as a trivalent cation due to the transformation into the form of $[Co(H_2O)_6]^{3+}$. DNA shrinkage is accompanied by an increase in molecular optical anisotropy ($\gamma_1 - \gamma_2$) (Fig. 1b). The optical anisotropy ($\gamma_1 - \gamma_2$) has the maximal value for B-DNA. Any change in DNA secondary structure causes the falling of the ($\gamma_1 - \gamma_2$) value.

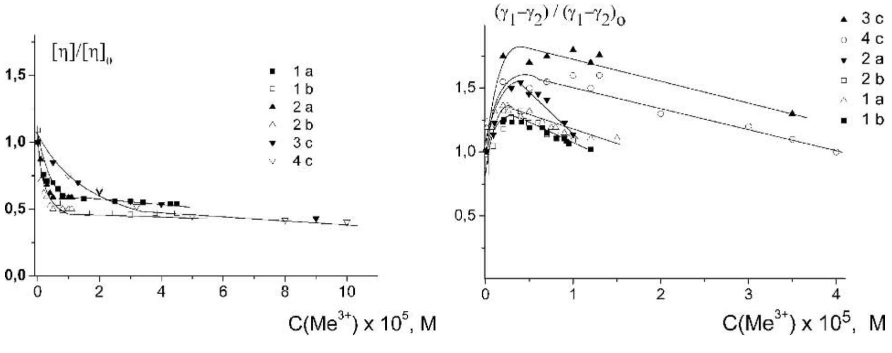

Fig. 1 Dependence of the relative change in DNA-intrinsic viscosity (left) and in DNA optical anistropy (right) on the concentration of $FeCl_3$ (1), $LaCl_3$ (2), $[Co(NH_3)_6]Cl_3$ (3), $[Co(NO_2)_6]Na_3$ (4), in 0.005 M NaCl. (a), 1 M NaCl. (b), and 0.003 M NaCl (c)

The increase of ($\gamma_1 - \gamma_2$) can only be explained as a result of intramolecular reorganization of the DNA coil.[12,13]

DNA packaging induced by trivalent metal ions at low and high NaCl concentration is observed due to the appearance of mutually oriented segments, held side-by-side by means of trivalent ions. From the AFM images we can make out the tendency of parallel segments to appear due to DNA interaction with La^{3+} (Fig. 2). DNA fixation on the mica surface was accomplished by La^{3+} without other additions.

Other changes in DNA structure in complexes with polycations were observed. Our experiments have shown that the optical anisotropy of DNA and the specific viscosity of solutions with the same DNA and different polycation contents do not vary essentially until N/P = 1 (Fig. 3), where N is the concentration of polycation-positive

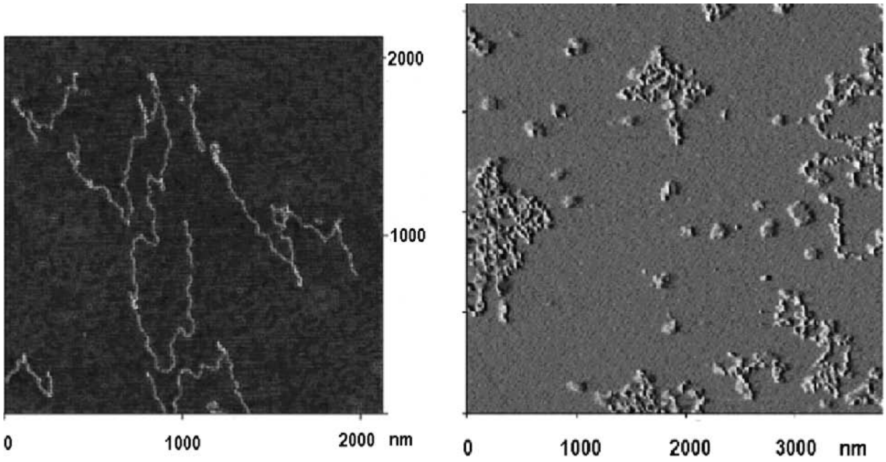

Fig. 2 Tapping AFM images of free DNA (left) and DNA in complexes with La+ (right), $C(LaCl_3) = 7 \times 10^{-6}$ M

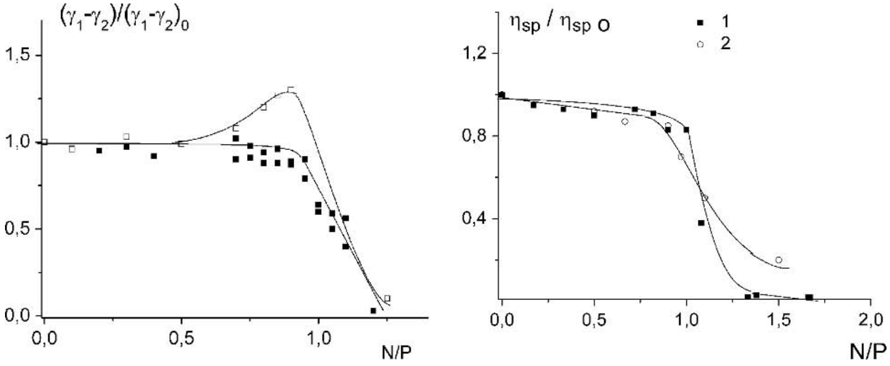

Fig. 3 Dependence of the relative change in DNA optical anisotropy (left) and in the specific viscosity of DNA solution with PLL (right) on N/P in 0.0005 M NaCL (1) and 1 M NaCl (2)

groups and P is the concentration of DNA-negative phosphates. At N/P ≈ 1, a significant decrease in solution viscosity and DNA optical anisotropy is observed. This decrease is observed for DNA-polymeric solutions irrespective of the type of polycations.[11,14]

The DNA optical anisotropy ($\gamma_1 - \gamma_2$) is very sensitive to any change in persistent length or in the secondary structure of macromolecules. The value of ($\gamma_1 - \gamma_2$) in the solutions under consideration does not decrease to the point of N/P = 1.

We can conclude that the secondary structure and the persistent length of DNA do not change at N/P < 1. It is possible to assume that the size of the DNA coil also does not change significantly with an increase of polycation concentration under these conditions.

The CD spectra of the DNA reflect the distinction between the influence of trivalent metal ions and polycations on DNA conformation (Fig. 4). One can see the shift of the positive maximum in the CD spectra to short waves and its increase in

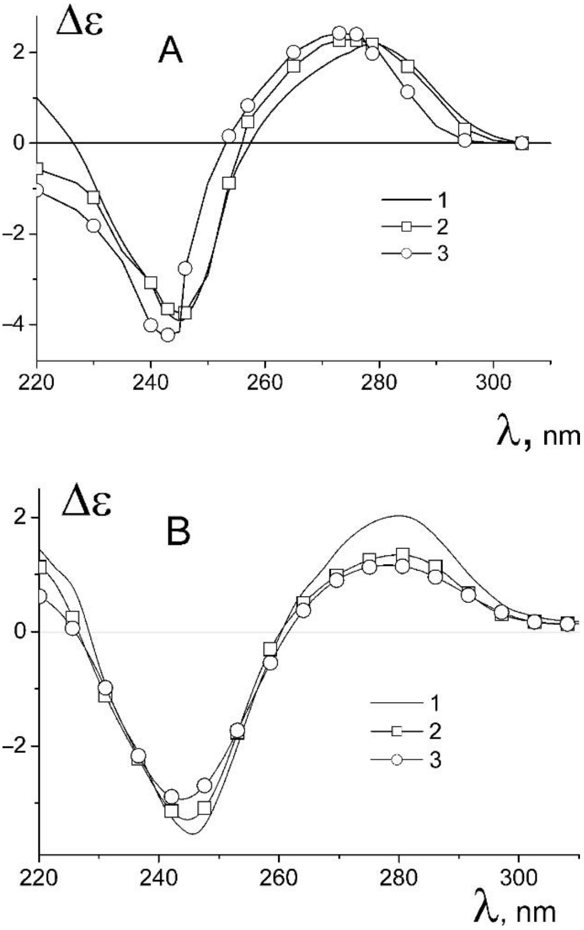

Fig. 4 (continued)

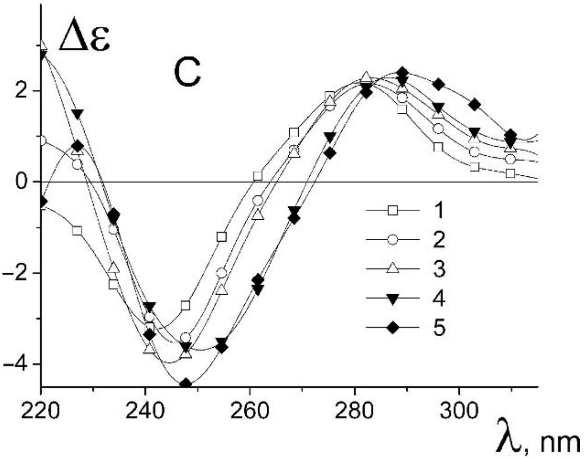

Fig. 4 (continued) A: CD spectra of DNA in complexes with $[Co(NH_3)_6]^{3+}$ in 0.005 M NaCl. $C(Co^{3+}) = 0$ (1), 9.5×10^{-6} (2), and 7.5×10^{-6} (3). B. DNA complexes with La^{3+}. $C(La^{3+}) = 0$ (1), 7.3×10^{-6} M (2), 9.0×10^{-6} M (3). C: DNA complexes with PLL. N/P = 0 (1), 0.5 (2), 0.75 (3), 1.25 (4), 1.5 (5). C(DNA) = 0.001%

amplitude for DNA complexes with $[Co(NH_3)_6]^{3+}$ in comparison with results for free DNA. The increase in positive CD maximum amplitude corresponds to the growth of DNA optical anisotropy (Fig. 1). The binding of La^{3+} to DNA causes the decrease of the positive band in CD spectra without the shift. The shift of the positive maximum to long waves without its appreciable growth is typical for the DNA solution with PLL.

4 Comparison of DNA Condensation Induced by Trivalent Ions and Polycations

Linear DNA in a water solution is a rigid, double-helical polymer with a high density of negative charges. DNA condensation (or, the collapse of the molecular coil into a dense, compact form without aggregation) can be observed in strongly diluted solutions of low ionic strength in the presence of multivalent cations. The destruction or strong perturbation of the DNA double-helical structure can cause aggregation instead of condensation. Single-stranded DNA differs significantly from a double-helical molecule due to its great loss in rigidity. Water is a better solvent for the double-stranded DNA than for the single-stranded nucleic acids due to the easy approach of water molecules to the hydrophobic bases (hydrophobic hydratation on nanometer scale). The binding of cations with negative phosphates with the displacement of water molecules from the DNA hydration shell involves the deterioration of the hydrophilic property of the macromolecule. The change of the DNA conformation concurrent with the destruction of hydrogen bonds between nitrogen bases from the different strands prevents the formation of a reversible compact structure. Usually, the main problem in the experiment is to separate the reversible packaging of DNA in B-form the DNA collapse caused by the perturbation in its secondary structure. The destabilizing effect of ligands on DNA secondary structure can prevent the formation of biologically active complexes.

It was shown that at identical salt concentration, the increase in valency of counterions leads to a greater reduction of DNA volume. The comparison of the DNA packaging in complexes with polycations and the DNA condensation induced by trivalent ions has shown that the concentration of the condensing agents producing the DNA collapse increases from small trivalent ions $[Co(NH_3)_6]^{3+}$ to polycationic PLL (Fig. 5). For PLL, we used the molar concentration of monomers.

Achieving DNA condensation depends on C_{ag} in a solution for small condensing agents $[Co(NH_3)_6]^{3+}$ and Spd irrespective of C(DNA). The development of DNA condensation induced by polycations depends on the relation of polyion concentrations C(DNA)/C(pol).[11] C(DNA) is the molar concentration of phosphates. Fig. 5 demonstrates that $Co(NH_3)_6{}^{3+}$ causes DNA shrinkage at C(Co)/C(DNA) concentration ratio ≈ 0.01. Spermidine has three positive charges divided by CH_2 groups. It causes the DNA packaging at C(Spd)/ C(DNA) ≈ 0.1. PLL induces DNA condensation at N/P ≈ 1. The dependence of the DNA hydrodynamic radius R_H on the concentration of condensing agents in a solution is also presented in Fig. 5. The R_H value was calculated from DLS data with Stokes-Einstein relation $R_H = \dfrac{kT}{6\pi\eta_0 D_t}$, where D_t is the coefficient of translation diffusion, η_0 is the solvent viscosity, k is the Boltzmann's constant, and T is an absolute temperature.

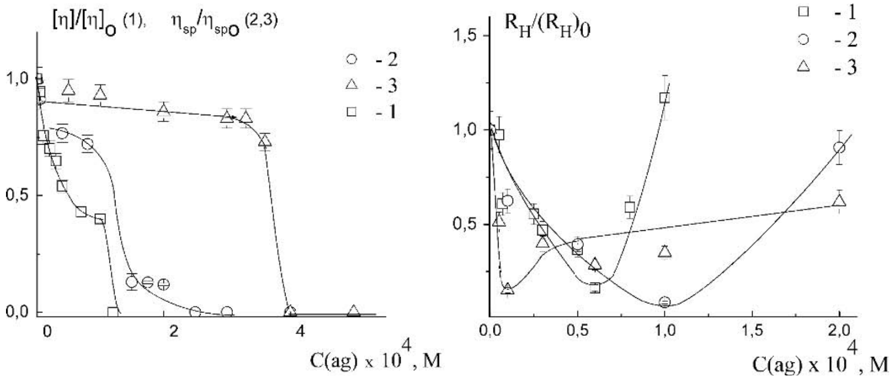

Fig. 5 Dependence of the relative change in intrinsic viscosity of DNA in complexes with CoHex(1), the relative change in specific viscosity of DNA solution ($C_{DNA} = 3 \times 10^{-4}$ M) with Spd (2) and PLL (3) on concentration of condensed agents C_{ag}, (left). Dependence of the relative change in hydrodynamic radius of DNA nanoparticles on C_{ag} (right): for PLL (1), Spd (2), and CoHex (3)

It was shown that DNA packaging caused by interaction with small multivalent ions is accompanied by an increase in DNA optical anisotropy, whereas polycations do not cause the growth of ($\gamma_1 - \gamma_2$). The increase in optical anisotropy of DNA in complexes with trivalent ions can be related to the formation of ordered structures with mutually oriented DNA segments. We should stress that polycations cause DNA shrinkage in a different way. Indeed, small multivalent ions can contact with DNA more effectively. In a dilute solution, the presence of counterions around the polycations and polyanions prevents the electrostatic attraction of polymeric coils. The increase in polymer concentration leads to the penetration of polycations into DNA-excluded volume. In that case, condensation can be observed. For semidilute DNA solutions, the aggregation and DNA precipitation were realized at $N/P < 1$.

AFM images (Fig. 6) show the formation of small particles after DNA condensation induced by polycations at $N/P > 1$. One can see free DNA in the presence of polycations at $N/P < 1$. We have selected the effective condensing polymer PAA and the polymer PTMAEM with high MM[12] for AFM examination. PAA causes the sharp DNA collapse at $N/P = 1$. PTMAEM induces the gradual falling of the specific viscosity of DNA solution with the increase of N/P. It is obvious that PAA causes the DNA packaging into discrete particles at $N/P > 1$ (Fig. 6). Contrary to this, free DNA molecules are observed at $N/P < 1$ in the presence of PTMAEM.

It is possible to conclude that DNA condensation induced by polycations is realized in a different way than the collapse of DNA caused by trivalent ions. Polycations do not provoke DNA shrinkage in a solution at $N/P < 1$. DNA condensation is observed at $N/P > 1$ as a result of intermolecular linkage by means of the multiple electrostatic bonds.

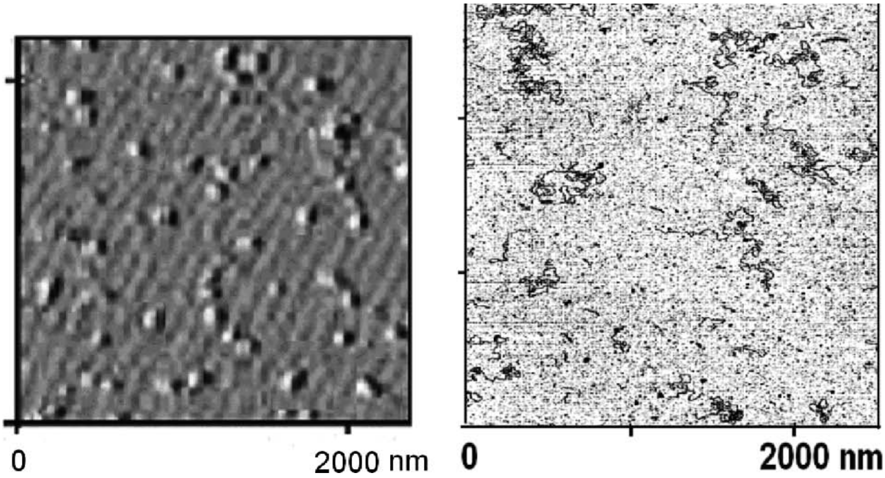

Fig. 6 Tapping AFM images of DNA complexes with PAA at N/P = 2 (left) and DNA complexes with PTMAEM at N/P = 0.5 (right)

Acknowledgements The authors would like to express their gratitude to Professor Alexei R. Khokhlov and Dr. Sergei Abramchuk for the opportunity to obtain several AFM images and for valuable discussions. We also would like to thank Dr. Alexei Bogdanov for the participation in a number of experiments. And we acknowledge Dr. Olga Nazarova for the synthetic polymers PAA and PTMAEM.

References

1. L. S. Lerman, A transition to a compact form of DNA in polymer solutions, *Proc. Natl. Acad. Sci. USA,* 68(8), 1886–1890 (1971).
2. L. C. Gosule and J. A. Schellman, Compact form of DNA induced by spermidine, *Nature* 259, 333–335 (1976).
3. J. Widom and R. L. Baldwin, Cation-induced toroidal condensation of DNA: studies with Co3+(NH3)6, *J. Mol. Biol.* 144(4), 431–453 (1980).
4. R. W. Wilson and V. A. Bloomfield, Counterion-induced condensation of deoxyribonucleic acid. A light-scattering study, *Biochemistry* 18(11), 2192–2196 (1979).
5. J. A. Schellman and N. Parthasarathy, X-ray diffraction studies on cation-collapsed DNA. *J. Mol. Biol.* 175, 313–329, (1984).
6. K. A. Marx and G. C. Ruben, Evidence for hydrated spermidine-calf thymus DNA toruses organized by circumferential DNA wrapping, *Nucleic Acids Res.* 11(6), 1839–1854 (1983).
7. S. M. Klimenko, T. I. Tikkchonenko, and V. M. Andreeva, Packing of DNA in the head of bacteriophage T2, *J. Mol. Biol.* 23(3), 523–533. (1967).
8. P. R. Dash, V. Toncheva, E. H. Schacht, and L. W. Seymour, Synthetic polymers for vectorial delivery of DNA: characterisation of polymer/DNA complexes by photon correlation spectroscopy and stability to nuclease degradation and disruption by polyanions in vitro, *J. Controlled Release* 48(2), 269–276 (1997).
9. S. C. De Smedt, J. Demeester, and W. E. Hennink, Cationic polymer based gene delivery systems, *Pharm. Res.*, 17(2), 113–126 (2000).
10. P. Dubruel, B. Christiaens, B. Vanloo, K. Bracke, M. Rosseneu, J. Vanderckhove, and E. Schacht, Physicochemical and biological evaluation of cationic polymethacrylates as vectors for gene delivery, *Eur. J. Pharm. Sci.* 18(3–4), 211–220 (2003).
11. A. V. Slita, N. A. Kasyanenko, O. V. Nazarova, I. I. Gavrilova, E. M. Eropkina, A. K. Sirotkin, T. D. Smirnova, O. I. Kiselev, and E. F. Panarin, DNA-polycation complexes, Effect of polycation structure on physico-chemical and biological properties, *J. Biotechnol.* 127(4), 679–693, (2007).
12. N. A. Kasyanenko, N. Arikainen, and E. Frisman, Investigation of DNA complexes with Iron ions in solution, *Biophys. Chem.* 70(2), 93–100 (1998).
13. N. Kasyanenko, A. Zanina, O. Nazarova, and E. Panarin, DNA interaction with complex ions in solution, *Langmuir* 5(23), 7912–7917 (1999).
14. N. A. Kasyanenko, D. A. Afanasieva, B. A. Dribinsky, D. V. Mukhin, O. V. Nazarova, and E. F. Panarin, DNA interaction with synthetic polymers in solution, *Struct. Chem.* 18(4), 519–525, (2007).

DNA-Based Synthesis and Assembly of Organized Iron Oxide Nanostructures

Gennady B. Khomutov*

Abstract Organized bio-inorganic and hybrid bio-organic-inorganic nanostructures consisting of iron oxide nanoparticles and DNA complexes have been formed using methods based on biomineralization, interfacial and bulk phase assembly, ligand exchange and substitution, Langmuir-Blodgett technique, DNA templating and scaffolding. Interfacially formed planar DNA complexes with water-insoluble amphiphilic polycation or intercalator Langmuir monolayers were prepared and deposited on solid substrates to form immobilized DNA complexes. Those complexes were then used for the synthesis of organized DNA-based iron oxide nanostructures. Planar net-like and circular nanostructures of magnetic Fe_3O_4 nanoparticles were obtained via interaction of cationic colloid magnetite nanoparticles with preformed immobilized DNA/amphiphilic polycation complexes of net-like and toroidal morphologies. The processes of the generation of iron oxide nanoparticles in immobilized DNA complexes via redox synthesis with various iron sources of biological (ferritin) and artificial ($FeCl_3$) nature have been studied. Bulk-phase complexes of magnetite nanoparticles with biomolecular ligands (DNA, spermine) were formed and studied. Novel nano-scale organized bio-inorganic nanostructures – free-floating sheet-like spermine/magnetite nanoparticle complexes and DNA/spermine/magnetite nanoparticle complexes were synthesized in bulk aqueous phase and the effect of DNA molecules on the structure of complexes was discovered.

Keywords DNA, polyamine, spermine, complex, ferritin, iron oxide, synthesis, nanoparticles, magnetite, organized nanostructures, self-assembly, interface

1 Introduction

The integration and the combining of nanocomponents of a different nature into novel hybrid systems opens wide possibilities for the design and creation of new nanosystems and nanomaterials with advanced or even novel properties and functional advantages

---

Faculty of Physics, Moscow State University, Leninskie Gory 1, 119992 Moscow, Russia

* To whom correspondence should be addressed. E-mail: gbk@phys.msu.ru

M. Giersig and G. B. Khomutov (eds.),
Nanomaterials for Application in Medicine and Biology

important for real-world applications. The fabrication and study of organized nanostructures with integrated biological and synthetic components can be important for nanotechnological, medical, biotechnological, and many other applications. It can result in the development of new advanced materials, films and biocompatible coatings with high reproducibility, functional specificity, and effectiveness characteristic for biological systems along with functionality, multifunctionality, enhanced processability and applicability due to the synthetic polymeric and/or inorganic components. Many biomolecules and biomolecular structures are fairly nonrobust. The engineered integrated systems with immobilized and stabilized bio-components can allow them to be used in real practical applications. From a basic point of view, the studies of interactions of biomolecules, supramolecular, and membrane systems with synthetic organic and inorganic structures contribute to a better understanding of their specific properties, functionalities, and such factors as mechanisms of structure formation and composition stability giving important information necessary to find optimal ways for the integration of biological structures into devices and for the design and preparation of functional integrated hybrid systems.

Biologically related aspects of nanotechnology are first and foremost concerned with the development of effective approaches to control the processes of nano-scale structural organization and functioning in biological, bio-organic, and bio-inorganic systems, which is of principal importance for advancements in a wide number of practical fields related to living systems as medicine and health care, cosmetics, agriculture, bioengineering, sensors and diagnostic systems, such as biochips, separation technologies, drug carriers and delivery systems including gene delivery vectors, nano-bionics, lab-on-a-chip and micro- and nanofluidic devices, *in vivo* usable drugs and cell tagging agents, tissue engineering, biocompatible and bio-active nanostructured surfaces, nanostructured biomaterials and coatings for implants and prostheses, etc.

The other important points are biomimetic and bioinspired approaches in research and development of efficient technological processes, synthetic functional nanostructures, nanostructured materials and nanodevices. The application of biomolecular assembly processes and principles for the formation of synthetic or bio-hybrid functional nanostructures and bioinspired nanomaterials can be useful for the development of cost-effective nanofabrication methods in nanotechnology. The important advantage of those methods is related to the possibility of carrying out synthetic procedures and the building up of nanostructures at ambient and ecologically-friendly conditions with high reproducibility of structure and properties of the resulting nanomaterials characteristic of natural biological systems.

1.1 Bio-Inorganic Nanostructures

Various natural bio-inorganic structures varying in size from bones to molecular nanoclusters in metalloproteins play important structural and functional roles in biological systems. Many highly organized inorganic (including magnetic) and hybrid organic-inorganic nanostructures are synthesized in biological and model molecular structures via biomineralization and biomimetic synthetic processes in which a key role is played by the nature, composition, and organization of the molecular matrix interacting with inorganic nanophase.[1–3]

Engineered organized bio-inorganic structures are interesting for basic studies as model systems and can also be useful for technological applications. Historically, photographic films based on gelatin comprised of Ag particles are one example of a successful practical application of the integrated bio-inorganic system. For many years, colloidal nanoparticles were used for labeling in microscopy studies of biological samples. Recently, a number of integrated bio-inorganic nanosystems based on inorganic nanoparticles[4–6] and 1-D nanostructures (nanowires and nanotubes)[7–13] have been formed and have proven to be promising for diagnostics, sensing, labeling, and other applications. 2-D structures as layers of metalloproteins on conducting inorganic substrates were obtained and used for nanobioelectrochemical investigations.[14,15] Complex electronic materials can be produced using biomolecular scaffolds, targeted deposition, and growth of metal nanoparticles.[16]

An important point of nanobiotechnological developments is the problem of biocompatibility and even toxicity of synthetic nanostructures and nanomaterials. Of particular interest in this connection are functional nanostructures containing natural biogenic inorganic nanomaterials (as, for example, iron oxide nanoparticles, see section 1.3).

1.2 DNA-Based Bio-Inorganic Nanostructures

DNA molecules are attractive candidates for building up precisely-controlled and reproducible nanostructures due to their unique DNA recognition capabilities and highly selective binding, predictability of interactions, physicochemical and mechanical stability, and synthetic availability of practically any desired nucleotide sequences and lengths.[6,17] Examples of DNA-based bio-inorganic nanostructures include, in particular, nanowires and networks formed via DNA metallization,[18–20] DNA-noble metal nanoparticle conjugates applicable for diagnostics and analytics using optical or electrical detection techniques,[5,21] DNA labeling by semiconductor quantum dots,[22] DNA complexes with inorganic nanoparticles as non-viral transfection agents,[23–28] DNA-assisted assembly of desired functional structures as, for example, nanoelectronic devices – carbon nanotube field-effect transistor,[29] organized metallic aggregates prepared using DNA specific Watson-Crick base-paring interactions,[30–33] semiconductor and iron oxide nanoparticle arrays and nanostructures formed via DNA templating and scaffolding.[34–38]

1.3 Iron Oxide Nanostructures in Biology and Medicine

Biogenic iron-containing magnetic nanoparticles were found in many organisms including magnetotactic bacteria, algae, honeybee, migratory ant, termites, salmon, trout, a number of amphibians, bobolink, pigeon, dolphin, and human;

they constituted iron-containing compounds, mainly oxides.[1,39] The formation of iron oxide nano-phases accompanies many neurodegenerative diseases and the disruption of iron homeostasis in the brain.[39] Self-organized 1-D nanostructures (chains) of iron oxide (magnetite, Fe_3O_4, with admixture of γ-Fe_2O_3) and greigite (Fe_3S_4) magnetic nanoparticles are present in magnetotactic bacteria and play an important physiological role in their space orientation via their interaction with the geomagnetic field.[1,40]

Magnetic nanoparticles, nanocomposite materials, and organized magnetic nanoparticle assemblies and superstructures are currently the subject of wide basic and applied research due to their interesting and practically useful properties (see, for example, Refs. 41–49). Synthetic magnetic nanoparticles and, in particular, iron oxide nanoparticles, can be prepared and functionalized by a number of chemical techniques.[49–54]

Biogenic and synthetic magnetic iron oxide nanoparticles (usually superparamagnetic due to their small size) with appropriate surface modification and functionalization have been used in a number of bio-medical applications.[55,56] Among current applications are magnetic resonance imaging contrast enhancement,[57–59] the magnetic detection of biomolecular interactions and bioassays,[60] the preparation of magnetic gels,[61] biocompatible films,[62] anti-cancer agents and targeting hyperthermia,[63,64] targetable drug delivery[65–68] and gene delivery (magnetic transfection)[69–71] with carrier localization in a specific area, magnetic separation,[72,73] DNA analyses,[74] and cell labeling.[75] The redox processes in biological systems in which iron oxide nanoparticles are involved are still not well understood, although antioxidant properties of magnetite nanoparticles have been reported.[76]

Due to their biocompatibility and their good magnetic properties, iron oxide nanoparticles also have the potential for being used in the development of new integrated functional nanosystems and nanostructured materials. The resulting properties of integrated and hybrid nanosystems are substantially dependent on the nano-scale organization of structural and functional nano-components and their collective behavior. This opens up possibilities for fine tuning and controlling the properties of integrated nanosystems, which is important for applications. To realize those possibilities, the insights into basic mechanisms which govern the nanoscale processes of inorganic phase growth and morphological evolution, interparticle interactions and structural organization of nanoparticulate systems and nanostructures are necessary. The investigation of those mechanisms and the development of novel organized functional nanomaterials have been the focus of research in our group.[77–79] In this paper, we focus on synthetic and assembling nanofabrication methods related to nanobiotechnology which were introduced and developed in our group, and on recent progress in the preparation of organized low-dimensional bio-inorganic nanostructures based on DNA and iron oxide nanoparticle complexes.

2 DNA-based Iron Oxide Nanostructures

2.1 *Experimental Details*

2.1.1 Materials and Chemicals

Salmon thymus native DNA (Na salt), $FeCl_3$, and NaCl were obtained from Sigma/Aldrich, water-insoluble amphiphilic dye N,N -Dioctadecyloxacarbocyanine-4-toluenesulfonate was obtained from Serva. Spermine and ferritin were obtained from Fluka. All chemicals were purchased and used as supplied. Water-insoluble amphiphilic polycation derivatives of poly-4-vinilpyridine (PVP) with 16% and 20% of cationic cetylpyridinium groups (PVP-16 and PVP-20, correspondingly) were synthesized and supplied by Dr. A. A. Rakhnyanskaya (MSU).[80] A stable aqueous acidic suspension of cationic magnetite nanoparticles (mean diameter 10 nm) was prepared using conventional methods[49,50] including reaction of solutions of $FeSO_4$ and $FeCl_3$ salts with ammonium hydroxide, extraction of magnetic fraction of the product with following purification, resuspension in water and pH adjustment. A Milli-Q water purification system was used to produce water with an average resistivity of 18 MΩ-cm for all experiments.

2.1.2 Procedures

Formation of Langmuir monolayers, surface pressure-monolayer area isotherm measurements and monolayer transfer to solid substrates were carried out using a fully automatic conventional Teflon trough at 21°C as described elsewhere.[81] DNA/PVP-16 and DNA/PVP-20 complex monolayers were formed via binding of the bulk phase DNA molecules with cationic Langmuir monolayers of water-insoluble amphiphilic polycations.[82] Immobilized DNA complexes with amphiphilic polycations were prepared using the conventional Langmuir-Blodgett (LB) deposition technique. The immobilization of DNA molecules on the solid substrates was also carried out via the binding of DNA with Langmuir monolayers of amphiphilic water-insoluble intercalating dye N,N′-Dioctadecyloxacarbocyanine-4-toluenesulfonate and the subsequent deposition of the complex monolayer onto the solid substrates. Immobilized DNA/spermine complexes were prepared via incubation of immobilized DNA bound with amphiphilic dye monolayer LB film in aqueous spermine solution (5×10^{-4} M, pH = 5.6). Iron-containing nanoparticles in DNA complexes were synthesized by incubation of Fe^{3+}-containing precursor film (DNA/Fe^{3+}/PVP-16 complex film obtained via incubation of preformed DNA/PVP-16 LB film in the $FeCl_3$ solution 2×10^{-4} M, pH = 2.7) in the sodium borohydride (5×10^{-4} M) or ascorbic acid (1×10^{-3} M) aqueous solutions followed by the incubation of the film in the high pH aqueous media (pH = 10) at ambient conditions for 2 h. Also, nanoparticles were formed using ferritin as an iron source via incubation of immobilized DNA/amphiphilic dye or DNA/amphiphilic dye/spermine complex films in aqueous ferritin solution (1 mg/ml, pH = 7.5) with subsequent washing in pure water and incubation of the films in ascorbic acid solution (1×10^{-3} M, pH=7.5). The preliminary analyses of the generated iron-containing nanoparticles using electron diffraction technique pointed to the iron oxide nature (dominating magnetite and possible minor maghemite phases) of the obtained nanoparticles.

Monolayer samples for TEM measurements were prepared by nanoparticulate monolayer deposition from aqueous solution onto the ultrathin amorphous carbon or Formvar film supported by the copper grid (diameter = 3 mm). Samples with bulk phase nanoparticulate nanostructures were prepared by deposition and drying of a droplet of the corresponding suspension on a carbon film supported by the copper grid.

Spermine/magnetite nanoparticle complexes were synthesized in bulk aqueous phase by the addition of colloidal Fe_3O_4 nanoparticles into aqueous spermine solution (10^{-2} M). A DNA/spermine/magnetite nanoparticle complex was formed by addition of spermine/magnetite nanoparticle complex aggregates to DNA solution (2×10^{-4} M per monomer).

TEM images were obtained using Jeol JEM-100B, Jeol JEM-1010 and LEO 912 AB IOMEGA (Carl Zeiss) microscopes.

2.2 Iron Oxide Nanostructures Formed in Immobilized DNA Complexes

DNA complexes immobilized on the solid substrate surfaces were used as templates and iron-containing precursor material in the synthesis of iron oxide nanoparticulate structures. First, interfacial planar DNA complexes with Langmuir monolayers of an amphiphilic polycation were formed via binding of bulk-aqueous-phase DNA molecules with a floating monolayer and then deposited onto the solid substrates (mica, silicon wafers with natural oxide layer, TEM grids with carbon layer).[83] The ultrastructure of the deposited LB films of amphiphilic polycations PVP-16 and PVP-20 was dependent on the corresponding Langmuir monolayer surface pressure and the incubation time on the aqueous phase surface.[82] The effective surface concentration of amphiphilic polycation molecules in Langmuir monolayer interacting with bulk phase DNA molecules can be easily and controllably changed and adjusted by variation of the monolayer area. Figure 1 shows characteristic morphologies of interfacially formed DNA-amphiphilic polycation complexes deposited onto the mica substrate surface. Planar net-like or lattice structures were obtained when DNA molecules interacted with uncompressed PVP-16 Langmuir monolayer (Fig. 1a). The height value of the complex shown in Fig. 1a derived from the cross-section profile (Fig. 1c) is close to that measured by AFM in DNA-multistranded aggregated structures (~2.1 nm).[84] Single stretched DNA molecules

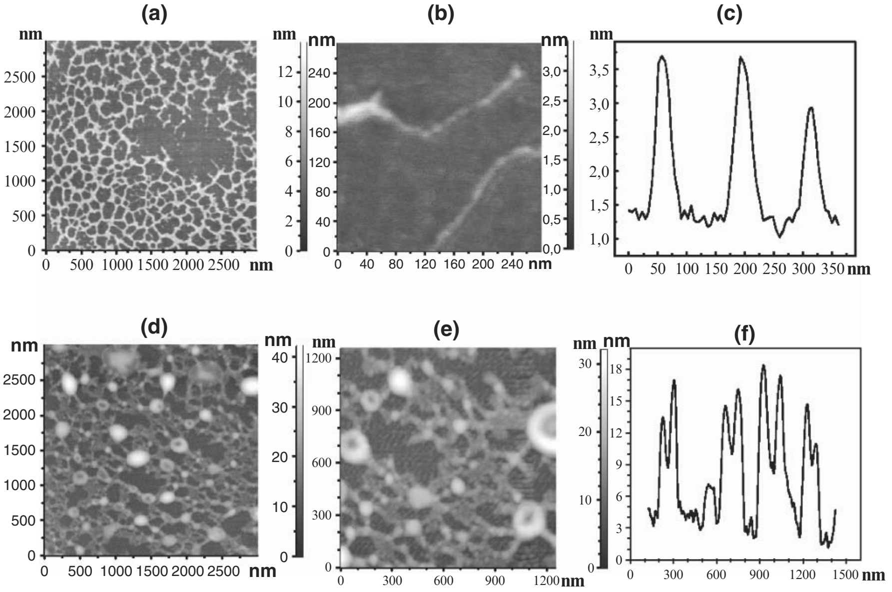

Fig. 1 AFM topographic images of DNA/PVP-16 complex bilayer LB film formed on mica substrate. The complex was formed under monolayer surface pressure value 0 (Images (a), (b)) and surface pressure $\pi = 20\,\mathrm{mN/m}$ (Images (d), (e)). Pictures (c) and (f): typical height cross-section profiles of the images (a) and (e), correspondingly. Experimental details are presented in Antipina et al.[82] and Khomutov et al.[83]

bound with PVP-16 monolayer were also observed (Fig. 1b). Figure 1d–f show the structure of DNA/PVP-16 complexes formed in those cases when a compressed PVP-16 Langmuir monolayer with quasi-homogeneous positively charged surface interacted with DNA molecules from the aqueous phase. Quasi-circular toroidal structures bound by fibers can clearly be identified from Fig. 1d and e (topographical images) and from the corresponding height cross-section profile (Fig. 1f). Such a toroidal morphology is known for compacted DNA structures and represents the most common morphology in DNA condensates from aqueous solution.[85,86] The diameter of the toroids can be estimated from the characteristic cross-section profile shown in Fig. 1f – approximately 200 nm. These results demonstrate the possibilities for controlling the structure of interfacially formed amphiphilic polyelectrolyte complexes with bulk phase polymeric ligands via controlling the conditions of the interfacial complex formation.

Figure 2 demonstrates the iron oxide nanoparticulate structures synthesized in immobilized planar DNA/Fe^{3+}/PVP-16 complex LB films. The use of DNA/Fe^{3+}/PVP-16 complex films as precursors resulted in the generation of quasi-linear arrays (Fig. 2a) and circular aggregates (Fig. 2b) of iron oxide nanoparticles. It was found that the spatial structure of the synthesized arrays of iron oxide nanoparticles correlated with the morphology of DNA/PVP-16 complex LB film used as a template

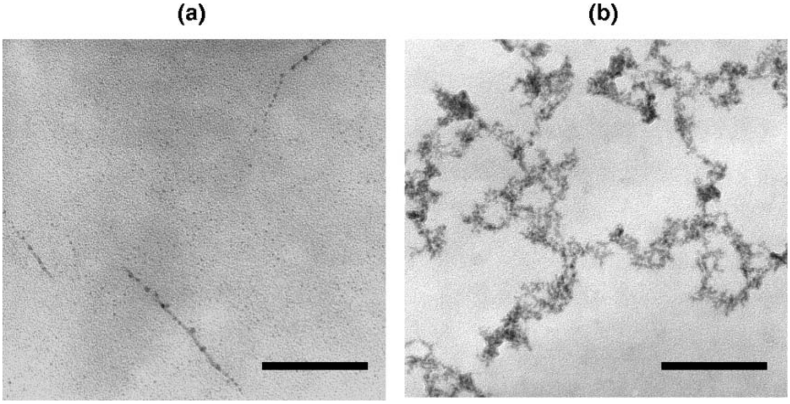

Fig. 2 Transmission electron micrographs showing iron oxide nanoparticulate structures synthesized in immobilized planar DNA/Fe^{3+}/PVP-16 complex LB films. Image (a): DNA/PVP-16 complex LB film with morphology shown in Fig. 1a was used as a template. Image (b): DNA/PVP-16 complex LB film shown in Fig. 1d and e was used as a template. $NaBH_4$ (5×10^{-4} M) was used as a reductant. Bar size: (a) 100 nm; (b) 170 nm

(linear nanoparticulate aggregates in Fig. 2a corresponded to the net-like DNA/PVP-16 complex shown in Fig. 1a, circular nanoparticulate structures corresponded to DNA/PVP-16 complex LB film with toroidal morphology shown in Fig. 1d and e). The planar structure of the nanoparticulate DNA/amphiphilic polycation nanocomposite films was not destroyed by the synthesis of iron oxide nanoparticles.[77] A similar effect of formation of quasi-linear nanoparticulate structures was observed when semiconductor CdS nanoparticles were generated in DNA/Cd^{2+}/PVP-16 complex LB film.[83]

The presented results demonstrate that the dimensions and the structural organization of iron oxide nanostructures synthesized in immobilized DNA complexes are dependent on the complex composition and morphology.

2.2.1 Iron Oxide Nanoparticulate Structures Synthesized Using Ferritin as an Iron Source

We were interested in the modeling and study of the biomineralization processes connected with the formation of magnetic iron oxide nanoparticles in DNA complexes in the presence of reagents of biological nature only – ferritin as an iron source, ascorbic acid as a reductant, at physiological pH value (7.5) and ambient conditions. Ferritin is known as a spherical protein bio-inorganic complex composed of protein shell and inorganic iron-containing core in the form of hydrous ferric oxide. The inner inorganic core of the protein complex is usually 5–8 nm in diameter and is able to incorporate roughly 4,500 iron atoms in the form of paracrystalline iron oxyhydroxide.[87–89]

TEM images of ferritin molecules used in our experiments are shown in Fig. 3a and b. From Fig. 3 it follows that ferritin inorganic cores are monodisperse with a mean diameter of about 6 nm. The absence of marked reflections on the corresponding electron diffractogram (the insert in Fig. 3a and b) points to the low crystallinity of ferritin samples in accordance with the literature data.[87–89] The native double-stranded DNA molecules were immobilized via amphiphilic intercalating dye followed by monolayer complex deposition onto the substrate. Also, immobilized DNA/spermine complexes were formed by incubation of the substrate

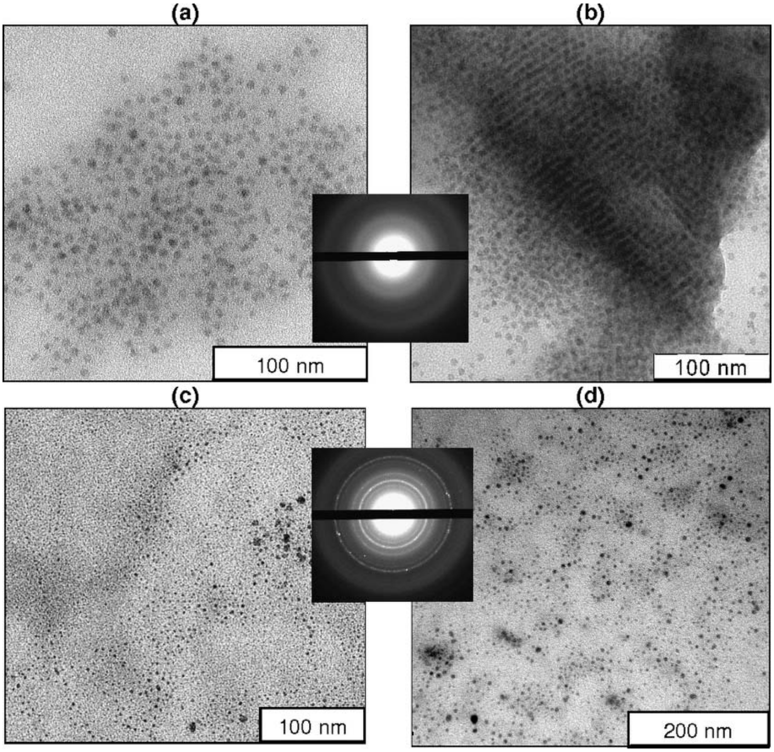

Fig. 3 Images (a) and (b): Transmission electron micrographs of ferritin. Samples were prepared by drying a droplet of ferritin solution onto a TEM substrate (copper grid with carbon film). The inserts in images (a) and (b) show typical selected area electron diffraction pictures obtained in ferritin samples. Images (c) and (d): Iron oxide nanoparticles synthesized in immobilized DNA complexes. DNA was immobilized via binding of amphiphilic intercalating dye N,N'-Dioctadecyloxacarbocyanine-4-toluenesulfonate followed by monolayer deposition onto a TEM substrate. Image (c): Iron oxide nanoparticles synthesized via incubation of the deposited amphiphilic dye monolayer with bound DNA molecules in ferritin suspension for 1 h followed by incubation in ascorbic acid solution (1 h). Image (d): Iron oxide nanoparticles synthesized via incubation of the deposited amphiphilic dye monolayer with bound DNA molecules in spermine solution (1 h) followed by incubation in ferritin suspension for 1 h and then in ascorbic acid solution (1 h), pH = 7.5. The insert in images (c) and (d) shows a typical selected area electron diffraction picture obtained in those samples containing synthesized iron oxide nanoparticles

with immobilized DNA/amphiphilic dye layer in the aqueous spermine solution. The obtained immobilized DNA complex samples were first incubated for various time intervals in the aqueous ferritin suspension and, after washing in pure water, were placed in the reductant ascorbic acid solution at ambient glove box conditions. TEM investigation of the samples before their placement in ascorbic acid solution did not reveal any considerable quantities of bound unwashed ferritin molecules or any inorganic nanoparticles. It follows from Fig. 3c and d that the described synthetic procedures result in the generation of inorganic polydisperse nanoparticles with a size distribution from 1 to 15 nm, a mean diameter of about 3 nm, and an apparently developed crystalline structure. The typical corresponding electron diffraction picture obtained with those samples is shown in the insert in Fig. 3c and d. The character of diffraction is typical for polycrystalline systems of iron oxide (particularly, magnetite) nanoparticles and points to the pronounced crystalline structure of the generated nanoparticles in contrast to the ferritin. In Fig. 3c one can see organized quasi-linear chain arrays of small (~ 2 nm) nanoparticles which could be a result of the attachment of nanoparticles to the linear DNA molecules. Nanoparticles in the DNA/spermine complex sample (Fig. 3d) form rather dense aggregates, which may be a result of the more compact structure of condensed DNA/spermine complexes. Substantial differences in size and structure between ferritin and the generated nanoparticles along with their linear arrangement in the DNA complex sample (Fig. 3c) could be a result of the formation of the observed iron oxide nanoparticles from iron ions transferred from ferritin to linear DNA molecules during incubation of immobilized DNA complexes in ferritin solution. The surface density of synthesized nanoparticles in the DNA/spermine complex (Fig. 3d) is substantially higher than that in the DNA sample (Fig. 3c). This result points to the higher Fe cations-binding capacity of DNA/spermine complexes in comparison with DNA molecules alone due to the presence of polyamine in the sample. The data obtained give evidence for the possibility of forming magnetic iron oxide nanoparticles in DNA and DNA/polyamine complexes in biological systems under appropriate conditions, i.e. providing a source of Fe ions and redox processes. This finding can be related to possible natural biogenic processes involving iron metabolism in living systems.

2.2.2 Immobilized DNA Complexes with Magnetite Nanoparticles

Figure 4 shows the structure of assemblies of colloidal cationic Fe_3O_4 nanoparticles bound with immobilized DNA/amphiphilic polycation complex. One can see that the structure of magnetite nanoparticulate assemblies is dependent on the morphology of the DNA/PVP-20 complex used as a binding substrate. Planar extended net-like nanostructures (Fig. 4a) and massive circular aggregates (Fig. 4b) of magnetic Fe_3O_4 nanoparticles were obtained via interaction of colloidal magnetite nanoparticles with preformed net-like (Fig. 1a) and toroidal (Fig. 1d and e) immobilized DNA/amphiphilic polycation complexes. The size of the circular aggregates in Fig. 4b is

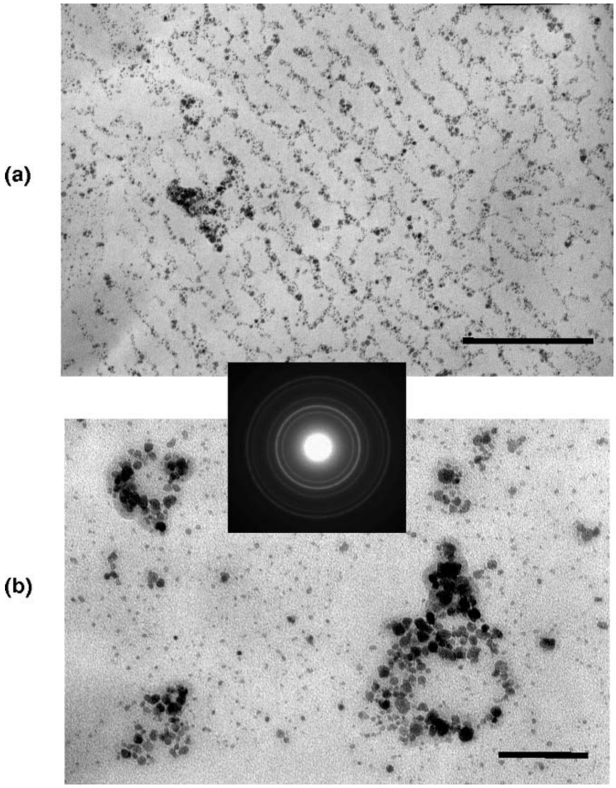

Fig. 4 Transmission electron micrographs of magnetite nanoparticulate structures formed via incubation of DNA/PVP-20 complex LB film in suspension of colloidal cationic magnetite nanoparticles. Image (a) corresponds to DNA/PVP-20 LB film shown in Fig. 1a. Image (b) corresponds to DNA/PVP-20 LB film shown in Fig. 1d and e. Bar size: (a) 400 nm; (b) 100 nm. The insert shows a typical selected area electron diffraction picture obtained in those samples containing magnetite nanoparticles

of the order of 100 nm and corresponds to the order of magnitude of the mean diameter of toroidal structures in Fig. 1d–f.

A similar procedure of incubation of such deposited DNA/amphiphilic polycation complexes in aqueous suspension of cationic colloidal CdSe nanorods resulted in the formation of highly organized anisotropic collinear monorod strings and bunch structures of about micrometer length and tens of nanometers in diameter.[77] The data presented give new insights into features of nanoscale structure formation in immobilized DNA complexes and demonstrate possibilities for the formation of composite bio-inorganic complex films with integrated DNA and nano-size inorganic components characterized by nano-scale structural ordering.

2.3 Bulk Phase DNA and Spermine Complexes with Magnetite Nanoparticles

Figure 5a shows typical linear necklace-like aggregates of positively charged colloidal magnetite nanoparticles formed in a bulk aqueous phase in presence of DNA molecules at pH = 4. For comparison, typical disordered aggregates of magnetite nanoparticles formed by drying a droplet of magnetite nanoparticle colloid suspension on the TEM substrate are shown in Fig. 5b.

Novel hybrid biomolecular nanostructures – complexes of natural polyamine (spermine) and magnetite nanoparticles – are presented in Fig. 6. That figure shows characteristic TEM images of aggregate structures composed of spermine complexes with colloidal cationic magnetite nanoparticles formed under various experimental conditions in the bulk aqueous phase. When the suspension of magnetite nanoparticles was mixed with spermine solution under low ionic strength and pH values (pH = 5), the formation of disordered nanoparticulate aggregates of various sizes and shapes with loose and porous structure was observed (Fig. 6a and b). The addition of spermine to the suspension of magnetite nanoparticles at higher pH values resulted in the formation of organized free-floating planar sheet-like spermine/magnetite nanoparticle complexes with a dense compact ultrastructure (Fig. 6c and e). These complexes belong to a novel class of highly organized nanofilm nanostructured materials representing the free-floating self-assembled planar colloidal nanostructures (nano-sheets) composed of nano-components chemically bonded in the plane of the film. The general approach to the formation of such materials is based on controlled processes of self-assembly and self-organization of colloidal nano-components during the formation of their complexes with polyfunctional ligands in a bulk liquid phase in the absence of any surfaces and interfaces.[90] The preliminary

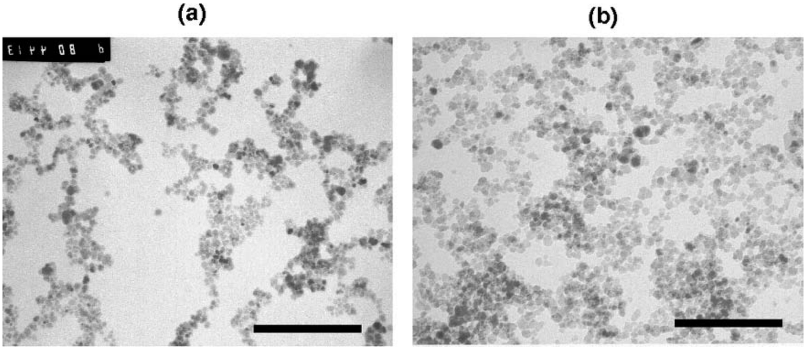

Fig. 5 Transmission electron micrographs of magnetite nanoparticles. (a) Quasi-linear structures of magnetite nanoparticles formed in the presence of DNA (10^{-5} M per monomer) in colloidal magnetite nanoparticle suspension, pH = 4. (b) Typical aggregates of magnetite nanoparticles formed by drying a droplet of magnetite nanoparticle suspension on the TEM substrate. Bar size: (a) 150 nm; (b) 130 nm

AFM analyses of the obtained nanocomposite spermine/magnetite nanoparticulate sheet-like material points to the thickness of the nanofilm material corresponding to about 2–4 magnetite nanoparticle diameters (20–40 nm) with the thickness/length or width ratio of about 1:1,000 or less. The planar character of the discovered structures and their quasi-straight boundaries are a result of the minimization of free energy of the system, competition and balancing of interparticle attracting

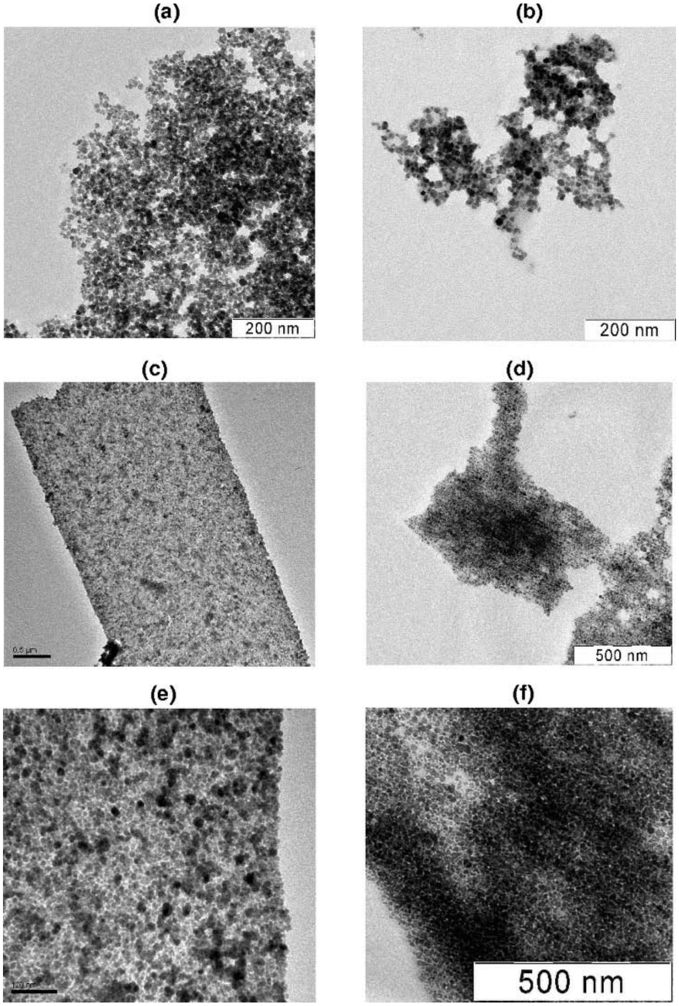

Fig. 6 Transmission electron micrographs of spermine and DNA complexes with colloidal cationic magnetite nanoparticles. Complexes were formed in a bulk aqueous phase. Images (a), (b), (c), and (e): spermine/magnetite nanoparticle complexes formed under various solution conditions. Images (d) and (f): bio-inorganic nanostructures formed via the incubation of spermine/magnetite nanoparticle complexes in DNA solution (2×10^{-4} M per monomer, pH = 5.6) for 24 h. Image (c): bar size 500 nm; image (e): bar size 100 nm

interactions (van-der-Waals forces and chemical binding via polyfunctional ligands) and repulsive electrostatic interactions of cationic nanoparticles with bound polyamine molecules. An interesting effect of self-organization was observed when DNA was added to the suspension of free-floating spermine/magnetite nanoparticle complex nano-sheets. After a 24-h incubation time with DNA, the structure of the spermine/Fe_3O_4 nanoparticle complexes was transformed to that shown in Fig. 6d and f. One can see the formation of an organized nanoparticulate ultrastructure in the DNA/spermine/Fe_3O_4 nanoparticle complex aggregates as quasi-parallel chains of magnetite nanoparticles shown in Fig. 6d and f. Such a transformation could be a result of the incorporation of DNA molecules into the spermine/magnetite nanoparticle complexes causing the structural reorganization of the complex governed by the processes of the minimization of free energy of the system. The organic ligand nature along with electrostatic and/or magnetic interactions are important factors of morphological control of inorganic nanostructures,[78] and the data obtained illustrate this fact for the case of iron oxide nanoparticles and biogenic ligands, such as DNA and spermine. The presence of magnetic iron oxide nanoparticles in these sheet-like complexes implies the possibility for the remote control of the behavior and the spatial localization of such complexes by magnetic field and via magnetic interactions, which makes them promising for practical applications. Biocompatible nanocomposite magnetic free-floating nano-sheets can be useful for systems of controlled binding, separation, coating, covering, transport and delivery in liquid media (in particular, for manipulations with drugs, bioactive compounds, and biocolloids).

3 Conclusion

We demonstrate the formation of new nano-scale-organized nanostructures consisting of iron oxide nanoparticles and biogenic ligands including polyamine spermine and various DNA complexes. The nanostructures were formed using synthetic methods based on interfacial synthesis and assembly, ligand exchange and substitution, self-organization principles, LB technique, DNA templating and scaffolding.

Planar DNA complexes immobilized on solid substrates were formed using the LB technique via DNA binding with water-insoluble amphiphilic polycation or intercalator Langmuir monolayers. Those complexes have been proven to be an efficient tool in studies of the generating of organized iron oxide nano-phases using various precursors and reaction procedures. It was shown that the structure of assemblies of colloidal cationic Fe_3O_4 nanoparticles bound with immobilized DNA/amphiphilic polycation complex was dependent on the morphology of the complex. Planar net-like and circular nanostructures of magnetic Fe_3O_4 nanoparticles were obtained via interactions of colloidal magnetite nanoparticles with preformed net-like and toroidal immobilized DNA complexes.

The processes of generating iron oxide nanoparticles in immobilized DNA complexes via redox synthesis with various iron sources of biological (ferritin) and artificial ($FeCl_3$) nature were studied. The formation of iron oxide nanoparticles was demonstrated at normal conditions in a system consisting of biogenic components only, such as DNA, ferritin, spermine, and ascorbic acid. This finding can be related to natural biogenic processes involving iron metabolism in organic systems.

Bulk-phase complexes of cationic colloidal magnetite nanoparticles with biomolecular ligands (DNA, spermine) were formed and studied. Necklace-like nanostructures were obtained via DNA binding with cationic colloidal magnetite nanoparticles in a bulk aqueous phase. Novel nano-scale organized bio-inorganic nanostructures – a bulk-phase free-floating planar sheet-like spermine/magnetite nanoparticles complex was obtained for the first time. The effect of DNA on the structure of those spermine/magnetite nanoparticle complexes was discovered indicating the important role of DNA molecules in the formation of organized DNA-based nano-constructions.

The synthetic strategies and methods described can be useful for the investigation of fundamental mechanisms of nano-scale structure formation, organization, and transformations in complex nanosystems. The methods are relatively simple, rapid, inexpensive, and allow large-scale preparation of organized nanostructures at ambient and ecologically-friendly conditions. It makes them promising practical instruments for molecular nanotechnology with the potential for nanobiotechnological and biomedical applications.

Acknowledgements This work was supported in part by the Russian Foundation for Basic Research (Grant 05–03–32756) and the Federal Agency of Science and Innovations RF (Contract # 02.513.11.3019). AFM images were gratefully obtained by Dr. R. V. Gainutdinov and Dr. A. L. Tolstikhina, Institute of Crystallography RAS (Moscow). I would like to thank Prof. S. P. Gubin, Dr. Yu. A. Koksharov, Dr. M. N. Antipina, Dr. A.N. Sergeev-Cherenkov, Dr. A. A. Rakhnyanskaya, Dr. A. V. Volkov, and D. I. Chernichko for their collaboration in the experimental work and valuable discussions.

References

1. R. B. Frankel and R. P. Blakemore (eds.), *Iron biominerals,* (Plenum, New York, 1991).
2. S. Mann, *Biomineralization: principles and concepts in bioinorganic materials chemistry* (Oxford University Press, New York, 2001).
3. E. Bauerlein (ed.), *The biomineralization of nano- and micro-structures* (Wiley-VCH, Weinheim, 2000).
4. W. J. Parak, D. Gerion, T. Pellegrino, D. Zanchet, C. Micheel, S. C. Williams, R. Boudreau, M. A. Le Gros, C. A. Larabell, and A. P. Alivisatos, Biological applications of colloidal nanocrystals, *Nanotechnology* 14, R15–R27 (2003).
5. N. L. Rosi and C. A. Mirkin, Nanostructures in biodiagnostics, *Chem. Rev*. 105(4), 1547–1562 (2005).
6. C. M. Niemeyer, and C. A. Mirkin (eds.), *Nanobiotechnology: concepts, applications and perspectives* (Wiley-VCH, Weinheim, 2004).
7. L. A. Bauer, N. S. Birenbaum, and G. J. Meyer, Biological applications of high aspect ratio nanoparticles, *J. Mater. Chem.* 14, 517–526 (2004).
8. J. Hahm and C. M. Lieber, Direct ultrasensitive electrical detection of DNA and DNA sequence variations using nanowire nanosensors, *Nano Lett*. 4(1), 51–54 (2004).

9. J. Gamby, J.-P. Abid, M. Abid, J.-P. Ansermet, and H. H. Girault, Nanowires network for biomolecular detection using contactless impedance tomoscopy technique, *Anal. Chem.* 78(15), 5289–5295 (2006).
10. Z. Li, Y. Chen, X. Li, T. I. Kamins, K. Nauka, and R. S. Williams, Sequence-specific label-free DNA sensors based on silicon nanowires, *Nano Lett.* 4(2), 245–247 (2004).
11. B. Munge, G. Liu, G. Collins, and J. Wang, Multiple enzyme layers on carbon nanotubes for electrochemical detection down to 80 DNA copies, *Anal. Chem.* 77(14), 4662–4666 (2005).
12. J. Wang, G. Liu, and M. R. Jan, Ultrasensitive electrical biosensing of proteins and DNA: carbon-nanotube derived amplification of the recognition and transduction events, *J. Am. Chem. Soc.* 126(10), 3010–3011 (2004).
13. H.-M. So, K. Won, Y. Hwan Kim, B.-K. Kim, B. H. Ryu, P. S. Na, H. Kim, and J.-O. Lee, Single-walled carbon nanotube biosensors using aptamers as molecular recognition elements, *J. Am. Chem. Soc.* 127(34), 11906–11907 (2005).
14. G. B. Khomutov, L. V. Belovolova, S. P. Gubin, V. V. Khanin, A. Yu. Obydenov, A. N. Sergeev-Cherenkov, E. S. Soldatov, and A. S. Trifonov, STM study of morphology and electron transport features in cytochrome c and nanocluster molecule monolayers, *Bioelectrochemistry* 55(1–2), 177–181 (2002).
15. L. Andolfi and S. Cannistraro, Conductive atomic force microscopy study of plastocyanin molecules adsorbed on gold electrode, *Surf. Sci.* 598(1–3), 68–77 (2005).
16. R. T. Hill, J. L. Lyon, R. A. Keith J. Stevenson, and J. B. Shear, Microfabrication of three-dimensional bioelectronic architectures, *J. Am. Chem. Soc.* 127(30), 10707 –10711 (2005).
17. N. C. Seeman, DNA in a material world, *Nature* 421, 427–431 (2003).
18. J. Richter, Metallization of DNA, *Physica. E* 16(2), 157–173 (2003).
19. L. Berti, A. Alessandrini, and P. Facci, DNA-templated photoinduced silver deposition, *J. Am. Chem. Soc.* 127(32), 11216–11217 (2005).
20. G. Wei, H. Zhou, Z. Liu, Y. Song, L. Wang, L. Sun, and Z. Li, One-step synthesis of silver nanoparticles, nanorods, and nanowires on the surface of DNA network, *J. Phys. Chem. B.* 109(18), 8738–8743 (2005).
21. R. Möller, R. D. Powell, J. F. Hainfeld, and W. Fritzsche, Enzymatic control of metal deposition as key step for a low-background electrical detection for DNA chips, *Nano Lett.* 5(7), 1475–1482 (2005).
22. W. J. Parak, D. Gerion, T. Pellegrino, D. Zanchet, C. Micheel, S. C. Williams, R. Boudreau, M. A. Le Gros, C. A. Larabell, and A. P. Alivisatos, Biological applications of colloidal nanocrystals, *Nanotechnology* 14, R15–R27 (2003).
23. P. Frayssinet, N. Rouquet, and D. Mathon, Bone cell transfection in tissue culture using hydroxyapatite microparticles, *J. Biomed. Mater. Res. A* 79(2) 225–228 (2006).
24. A. Maitra, Calcium phosphate nanoparticles: second-generation nonviral vectors in gene therapy, *Expert Rev. Mol. Diagnostics* 5(6), 893–905 (2005).
25. A. K. Salem, P. C. Searson, and K. W. Leong, Multifunctional nanorods for gene delivery, *Nat. Mater.* 2(10) 668–671 (2003).
26. K. K. Sandhu, C. M. McIntosh, J. M. Simard, S. W. Smith, and V. M. Rotello, Gold nanoparticle-mediated transfection of mammalian cells, *Bioconjug. Chem.* 13(1), 3–6 (2002).
27. V. I. Kulkarni, V. S. Shenoy, S. S. Dodiya, T. H. Rajyaguru, and R. R. Murthy, Role of calcium in gene delivery, *Expert Opin. on Drug Delivery* 3(2), 235–245 (2006).
28. E. H. Chowdhury, and T. Akaike, Bio-functional inorganic materials: an attractive branch of gene-based nano-medicine delivery for 21st century, *Curr. Gene Ther.* 5(6), 669–676 (2005).
29. K. Keren, R. S. Berman, E. Buchstab, U. Sivan, and E. Braun, DNA-templated carbon nanotube field-effect transistor, *Science* 302, 1380–1382 (2003).
30. C. A. Mirkin, R. L. Letsinger, R. C. Mucic, and J. J. Storhoff, A DNA-based method for rationally assembling nanoparticles into macroscopic materials, *Nature* 382, 607–609 (1996).
31. A. P. Alivisatos, K. P. Johnsson, X. Peng, T. E. Wilson, C. J. Loweth, M. P. Bruchez Jr., and P. G. Schultz, Organization of nanocrystal molecules using DNA, *Nature* 382, 609–611 (1996).

32. J. K. N. Mbindyo, B. D. Reiss, B. R. Martin, C. D. Keating, M. J. Natan, and T. E. Mallouk, DNA-directed assembly of gold nanowires on complementary surfaces, *Adv. Mater*. 14(4), 249–254 (2001).
33. M. Li, and S. Mann, DNA-directed assembly of multifunctional nanoparticle networks using metallic and bioinorganic building blocks, *J. Mater. Chem*. 14(14), 2260–2263 (2004).
34. J. L. Coffer, S. R. Bigham, X. Li, R. F. Pinizzotto, Y. G. Rho, R. M. Pirtle, and I. L. Pirtle, Dictation of the shape of mesoscale semiconductor nanoparticle assemblies by plasmid DNA, *Appl. Phys. Lett*. 69(25), 3851–3853 (1996).
35. W. U. Dittmer, and F. C. Simmel, Chains of semiconductor nanoparticles templated on DNA, *Appl. Phys. Lett*. 85(4), 633–635 (2004).
36. S. Rath, G. B. N. Chainy, S. Nozaki, S. N. Sahu, DNA template-driven synthesis of HgTe nanoparticles, *Physica. E* 30(1–2), 182–185 (2005).
37. G. B. Khomutov, M. N. Antipina, A. N. Sergeev-Cherenkov, A. A. Rakhnyanskaya, M. Artemyev, D. Kisiel, R. V. Gainutdinov, A. L. Tolstikhina, and V. V. Kislov, Organized planar nanostructures via interfacial self-assembly and DNA templating, *Int. J. Nanosci*. 3(1/2) 65–74 (2004).
38. D. Nyamjav, and A. Ivanisevic, Templates for DNA-templated Fe_3O_4 nanoparticles, *Biomaterials* 26(15), 2749–2757 (2005).
39. I. Safarik, and M. Safarikova, Magnetic nanoparticles and biosciences, *Chemical Mon*. 133, 737–759 (2002).
40. R. B. Frankel, R.P. Blakemore, and R.S. Wolfe magnetite in freshwater magnetotactic bacteria, *Science* 203(4387), 1355–135 (1979).
41. M. P. Pileni, (ed.) *Nanocrystals forming mesoscopic structures* (Wiley-VCH, Weinheim, 2005).
42. S. F. Dumestre, S. Martinez, D. Zitoun, M.-C. Fromen, M.-J. Casanove, P.Lecante, M. Respaud, A. Serres, R. E. Benfield, C. Amiens, and B. Chaudret, Magnetic nanoparticles through organometallic synthesis: evolution of the magnetic properties from isolated nanoparticles to organised nanostructures, *Faraday Discuss*. 125, 265–278, (2004).
43. Y.-W. Jun, J.-S Choi, and J. Cheon, Heterostructured magnetic nanoparticles: their versatility and high performance capabilities, *Chem. Commun*. 1203–1214 (2007).
44. G. Schmid (ed.) *Nanoparticles – from theory to applications* (Wiley VCH, Weinheim, 2004).
45. D. L. Leslie-Pelecky and R. D. Rieke, Magnetic properties of nanostructured materials, *Chem. Mater*. 8(8), 1770–1783 (1996).
46. X. Batlle and A. Labarta. Finite-size effects in fine particles: magnetic and transport properties, *J. Phys. D* 35, R15 (2002).
47. J. L. Dormann and D. Fiorani (eds.), *Magnetic properties of fine particles* (Elsevier, Amsterdam, 1992).
48. R. H. Kodama, Magnetic nanoparticles, *J. Magnetism Magn. Mater*. 200(1–3), 359–372 (1999).
49. S. P. Gubin, Yu. A. Koksharov, G. B. Khomutov, and G. Yu. Yurkov, Magnetic nanoparticles: preparation methods, structure and properties, *Russ. Chem. Rev*. 74 (6), 539–574 (2005).
50. U. Schwertmann and R.M. Cornell, *Iron oxides in the laboratory: preparation and characterization* (VCH, Weinheim, Cambridge, 1991).
51. A. K. Gupta and M. Gupta, Synthesis and surface engineering of iron oxide nanoparticles for biomedical applications, *Biomaterials* 26(18), 3995–4021 (2005).
52. D. K. Kim, Y. Zhang, W. Voit, K. V. Rao, J. Kehr, B. Bjelke, and M. Muhammed, Superparamagnetic iron oxide nanoparticles for bio-medical applications, *Scr. Materialia* 44 (8–9), 1713–1717 (2001).
53. Y. Zhang, N. Kohler, and M. Zhang, Surface modification of superparamagnetic magnetite nanoparticles and their intracellular uptake, *Biomaterials* 23(7), 1553–1561 (2002).
54. C. C. Berry and A. S. G. Curtis, Functionalisation of magnetic nanoparticles for applications in biomedicine, *J. Phys. D* 36(13), R198-R206 (2003).
55. Q. A. Pankhurst, J. Connolly, S. K. Jones, and J. Dobson, Applications of magnetic nanoparticles in biomedicine, *J. Phys. D* 36(13), R167–R181 (2003).

56. D. Schuler and R. B. Frankel, Bacterial magnetosomes: microbiology, biomineralization and biotechnological applications, *Appl. Microbiol. Biotechnol.* 52(4), 464–473 (1999).
57. Y.-X. J. Wang, S. M. Hussain, and G. P. Krestin, Superparamagnetic iron oxide contrast agents: physicochemical characteristics and applications in MR imaging, *Eur. Radiol.* 11(11), 2319–2331 (2001).
58. D. Portet, B. Denizot, E. Rump, J.-J. Lejeune, and P. Jallet, Nonpolymeric coatings of iron oxide colloids for biological use as magnetic resonance imaging contrast agents, *J. Colloid Interface Sci.* 238(1), 37–42 (2001).
59. E. X. Wu, and H. Tang, Applications of ultrasmall superparamagnetic iron oxide contrast agents in the MR study of animal models, *NMR in Biomed.* 17(7), 478–483 (2004).
60. T. Osaka, T. Matsunaga, T. Nakanishi, A. Arakaki, D. Niwa, and H. Iida, Synthesis of magnetic nanoparticles and their application to bioassays, *Anal. and Bioanal. Chem.* 384(3), 593–600 (2006).
61. M. Zrínyi, L. Barsi, and A. Büki, Ferrogel: a new magneto-controlled elastic medium, *Polym. Gels and Networks* 5(5), 415–427 (1997).
62. C. Albornoz, and S. E. Jacobo, Preparation of a biocompatible magnetic film from an aqueous ferrofluid, *J. Magn. Magn. Mater.* 305(1), 12–15 (2006).
63. D. C. F. Chan, D. B. Kirpotin, and P. A. Bunn, Jr., Synthesis and evaluation of colloidal magnetic iron oxides for the site-specific radiofrequency-induced hyperthermia of cancer, *J. Magn. Magn. Mater.* 122(1–3), 374–378 (1993).
64. A. Jordan, R. Scholz, P. Wust, H. Schirra, S. Thomas, H. Schmidt, and R. Felix, Endocytosis of dextran and silan-coated magnetite nanoparticles and the effect of intracellular hyperthermia on human mammary carcinoma cells in vitro, *J. Magn. Magn. Mater.* 194(1), 185–196 (1999).
65. A. Senyei, K. Widder, and G. Czerlinski, Magnetic guidance of drug-carrying microspheres, *J. Appl. Phys.* 49(6), 3578–3583 (1978).
66. T. Kubo, T. Sugita, S. Shimose, Y. Nitta, Y. Ikuta, and T. Murakami, Targeted systemic chemotherapy using magnetic liposomes with incorporated adriamycin for osteosarcoma in hamsters, *Int. J. of Oncol.* 18(1), 121–125 (2001).
67. Ch. Alexiou, A. Schmidt, R. Klein, P. Hulin, Ch. Bergemann, and W. Arnold, Magnetic drug targeting: biodistribution and dependency on magnetic field strength, *J. Magn. Magn. Mater.* 252(1–3), 363–366 (2002).
68. A. S. Lubbe, C. Bergemann, J. Brock, and D. G. McClure, Physiological aspects in magnetic drug-targeting, *J. Magn. Magn. Mater.* 194(1), 149–155 (1999).
69. F. Scherer, M. Anton, U. Schillinger, J. Henke, C. Bergemann, A. Kruger, B. Gansbacher, and C. Plank, Magnetofection: enhancing and targeting gene delivery by magnetic force in vitro and in vivo, *Gene Ther.* 9(2), 102–109 (2002).
70. C. Plank, U. Schillinger, F. Scherer, C. Bergemann, J.-S. Rémy, F. Krötz, M. Anton, J. Lausier, and J. Rosenecker, The magnetofection method: using magnetic force to enhance gene delivery, *Biological Chem.* 384(5), 737–747 (2003).
71. Z. P. Xu, Z. Q. Hua, G. Q. Lu, and A. B. Yu, Inorganic nanoparticles as carriers for efficient cellular delivery, *Chem. Eng. Sci.* 61(3), 1027–1040 (2006).
72. O. Olsvik, T. Popovic, E. Skjerve, K. S. Cudjoe, E. Hornes, J. Ugelstad, and M. Uhlen, Magnetic separation techniques in diagnostic microbiology, *Clinical Microbiol. Rev.* 7(1), 43–54 (1994).
73. W. Kemmner, G. Moldenhauer, P. Schlag, and R. Brossmer, Separation of tumor cells from a suspension of dissociated human colorectal carcinoma tissue by means of monoclonal antibody-coated magnetic beads, *J. Immunol. Methods* 147(2), 197–200 (1992).
74. L. Josephson, J. Manuel Perez, and R. Weissleder, Magnetic nanosensors for the detection of oligonucleotide sequences, *Angew. Chem. Int. Ed.* 40(17), 3204–3206 (2001).
75. A. K. Gupta, and A. S. G. Curtis, Lactoferrin and ceruloplasmin derivatized superparamagnetic iron oxide nanoparticles for targeting cell surface receptors, *Biomaterials*, 25(15), 3029–3040 (2004).

76. D. G. Shchukin, T. Shutava, E. Shchukina, G. B. Sukhorukov, and Y. M. Lvov, Modified polyelectrolyte microcapsules as smart defense systems, *Chem. Mater.* 16(18), 3446–3451 (2004).
77. G. B. Khomutov, Interfacially formed organized planar inorganic, polymeric and composite nanostructures, *Adv. Colloid Interface Sci.* 111(1–2), 79–116(2004).
78. G. B. Khomutov, and Yu. A. Koksharov, Effects of organic ligands, electrostatic and magnetic interactions in formation of colloidal and interfacial inorganic nanostructures, *Adv. Colloid Interface Sci.* 122(1–3), 119–147 (2006).
79. G. B. Khomutov, Organized planar bio-molecular and hybrid bio-organic-inorganic nanostructures, in: *Biocatalytic Technology and Nanotechnology*, G. E. Zaikov (ed.), (Nova Science, Hauppauge, NY, 2004), pp. 1–28.
80. A. A. Yaroslavov, E. G. Yaroslavova, A. A. Rakhnyanskaya, F. M. Menger, V. A. and Kabanov, Modulation of interaction of polycations with the negative unilamellar vesicles, *Colloids Surf. B* 16(1), 29–43 (1999).
81. G. B. Khomutov, T. V. Yurova, S. A. Yakovenko, V. V. Khanin, and E. S. Soldatov, Effect of stearic acid monolayer compression extent on the interface copper ions binding and clusters formation, *Supramol. Sci.* 4(3–4), 349–355 (1997).
82. M. N. Antipina, R. V. Gainutdinov, A. A. Rachnyanskaya, A.L. Tolstikhina, T. V. Yurova, and G. B. Khomutov, Studies of nanoscale structural ordering in planar DNA complexes with amphiphilic mono- and polycations, *Surf. Sci.* 532–535, 1025–1033 (2003).
83. G. B. Khomutov, M. N. Antipina, A. N. Sergeev-Cherenkov, T. V. Yurova, A. A. Rakhnyanskaya, V. V. Kislov, R. V. Gainutdinov, A. L. Tolstikhina, Interfacially-organized DNA/polycation complexes: a route to new planar polymeric and composite nanostructures, *Mat. Sci. Eng. C.* 23(6–8) 903–908 (2003).
84. M. A. Batalia, E. Protozanova, R. B. Macgregor Jr., and D. A. Erie, Self-assembly of frayed wires and frayed-wire networks: nanoconstruction with multistranded DNA, *Nano Lett.* 2(4), 269–274 (2002).
85. L. C. Gosule and J. A. Schellmann, Compact form of DNA induced by spermidine, *Nature* 259, 333–334 (1976).
86. T. H. Eickbush and E. N. Moudrianakis, The compaction of DNA helices into either continuous supercoils or folded-fiber rods and toroids, *Cell* 13(2), 295–306 (1978).
87. D. M. Lawson, P. J. Artymiuk, S. J. Yewdall, J. M. A. Smith, J. C. Livingstone, A. Treffry, A. Luzzago, S. Levi, P. Arosio, G. Cesareni, C. D. Thomas, W. V. Shaw, and P. M. Harrison, Solving the structure of human H ferritin by genetically engineering intermolecular crystal contacts, *Nature* 349, 541–544 (1991).
88. N. D. Chasteen, Mineralization in ferritin: an efficient means of iron storage *J. Struct. Biol.* 126(3), 182–194 (1999).
89. E. C. Theil, M. Matzapetakis, and X. Liu, Ferritins: iron/oxygen biominerals in protein nanocages, *J. Biol. Inorg. Chem.* 11(7), 803–810 (2006).
90. G. B. Khomutov and Yu. A. Koksharov, Nanofilm materials and the method for production of nanofilm materials, *Patent pending* RU2006147123 (2006).

This page intentionally blank

DNA-Based Nanostructures: Changes of Mechanical Properties of DNA upon Ligand Binding

Yury Nechipurenko[1,*], Sergey Grokhovsky[1], Georgy Gursky[1], Dmitry Nechipurenko[2], and Robert Polozov[3]

Abstract The formation of DNA-based nanostructures involves the binding of different kinds of ligands to DNA as well as the interaction of DNA molecules with each other. Complex formation between ligand and DNA can alter physicochemical properties of the DNA molecule. In the present work, the accessibility of DNA-ligand complexes to cleavage by DNase I are considered, and the exact algorithms for analysis of diagrams of DNase I footprinting for ligand-DNA complexes are obtained. Changes of mechanical properties of the DNA upon ligand binding are also demonstrated by the cleavage patterns generated upon ultrasound irradiation of cis-platin-DNA complexes. Propagation of the mechanical perturbations along DNA in the presence of bound ligands is considered in terms of a string model with a heterogeneity corresponding to the position of a bound ligand on DNA. This model can reproduce qualitatively the cleavage patterns obtained upon ultrasound irradiation of cis-platin-DNA complexes.

Keywords DNA-ligand binding, DNA-based nanostructures, quantitative analysis of footprinting diagram, ultrasound DNA cleavage, string model, DNA tensegrity

1 Introduction

Two approaches are developed for the formation of DNA-based nanostructures. In the context of the first approach complicated interactions in the living cell are modeled by more simple interactions between DNA and synthetic ligands. For

---

[1] V.A. Engelhardt Institute of Molecular Biology, Russian Academy of Sciences, Vavilov Str. 32, Moscow, 119991, Russia

[2] Department of Physics, Moscow State University, Leninskie Gory, Moscow, 119992, Russia

[3] Institute for Theoretical and Experimental Biophysics, Moscow Region, Instituskaya Str. 3, Puschino, 142290, Russia

* To whom correspondence should be addressed. E-mail: nech@eimb.ru

M. Giersig and G. B. Khomutov (eds.),
Nanomaterials for Application in Medicine and Biology

example, studies on the binding of various antibiotics and drugs to DNA and the synthesis of new sequence-specific DNA-binding-ligands may help to understand more complicated interactions underlying the recognition of specific target DNA sites by the transcription factors.[1] The second approach implies the formation of new artificial structures stabilized by interaction between single-stranded DNA segments and complementary oligonucleotides or structures formed when DNA molecules form associates upon ligand binding.[2,3]

Models for a quantitative description of DNA-ligand binding have been developed in several works.[4–9] A number of natural and artificial compounds bind to DNA and change its properties. In the first part of this communication we demonstrate that binding of the dimeric analogue of the antibiotic netropsin changes the accessibility of DNA for cleavage by DNase I. In the second part, we describe a model which allows us to interpret the observed cleavage patterns generated upon ultrasound irradiation of cis-platin – DNA complexes.

2 Quantitative Analysis of Footprinting Diagrams

Modern experimental techniques developed in the past years such as different variants of footprinting allow to determine the sites of predominant location of a ligand bound on a DNA fragment with a known sequence of base pairs. The method of footprinting is based on the fact that DNA regions occupied by a ligand are inaccessible for cleavage by DNase I or another reagent capable of hydrolyzing the sugar-phosphate backbone of DNA. However, analysis methods for footprinting diagrams, which enable one to evaluate the probabilities of ligand binding to different DNA regions, have so far only been developed insufficiently.

Here, we briefly describe the algorithm that allows to calculate the probabilities of binding a ligand with the binding sites on a DNA fragment with a known sequence of base pairs.[6,9] A statistical mechanics approach allows the most complete characterization of the system and a clear representation of the effects related to its statistical properties. This algorithm can be used for the quantitative analysis of diagrams of DNase footprinting for the complexes of the dimeric analogue of the antitumor antibiotic netropsin, which exhibits a high binding selectivity.[9] This antibiotic binds in the minor DNA groove to runs of four and five AT base pairs.[10,11] An obvious way to increase the selectivity of binding of these compounds is to synthesize dimeric (oligomeric) analogues, in which two or more netropsin fragments are bound covalently.[1,12] This group of compounds includes Pt-bis-netropsin, in which two netropsin fragments are covalently linked via the cis-diaminoplatinum group.[13] It was shown earlier that Pt-bis-netropsin forms three types of complexes with DNA,[13–16] but only one of them dominates under the experimental conditions used.

2.1 The Thermodynamical Model of Adsorption

Consider a solution at constant temperature and pressure which contains DNA molecules with adsorbed ligands and free ligand molecules. The DNA molecule represents a linear polymer consisting of *N* units (nucleotide pairs). Upon binding, the ligand occupies *L* units of the polymer, which become inaccessible for binding with other ligand molecules. Henceforth we refer to these *L* units as "the binding site". Assume that the ligand cannot protrude beyond DNA ends. Let us number the units of the polymer from 1 to *N*, thus the first binding site is the site including *L* first units; the second binding site begins with the second unit and ends with the unit $L + 1$, etc. By $K(i)$ we designate the constant of ligand binding with *i*-th binding site, which begins with the unit *i* and ends with the unit $i + L - 1$.

All thermodynamical characteristics of the system can be calculated if the expression for the great partition function Ξ_N is known. The latter can be calculated using the method of recurrent equations. Recurrent equations for describing noncooperative binding of extended ligands on a homo- and heteropolymer were obtained previously.[6,8] In the case of noncooperative binding, the recurrent equation will be as follows:

$$\Xi_N = \Xi_{N-1} + K(N-L+1)\cdot m\cdot \Xi_{N-\mathrm{L}} \tag{1}$$

with boundary condition:

$$\Xi_N = 1 \; if \; i < L, \Xi_L = K(1)\cdot m + 1 \tag{2}$$

where $K(i)$ is the constant of binding of the ligand with the *i*-th binding site and *m* is the free ligand concentration in solution. In case of specific binding on the heteropolymer, $K(i)$ depends on the nucleotide sequence in the DNA site occupied by the ligand. The probability, $P(i)$, that the *i*-th site of DNA is occupied by the ligand can be calculated using the standard equation (see Nechipurenko and Gursky[8]):

$$P(i) = \frac{\partial \ln \Xi_N}{\partial \ln[K(i)\cdot m]}. \tag{3}$$

2.2 PT-Bis-Netropsin Binding with DNA

The curves of titration of poly(dA)~poly(dT) with Pt-bis-netropsin show that the size, *L*, of the binding site for Pt-bis-netropsin is equal to eight base pairs.[14,15] The probability $P(i)$ can be calculated using recurrent Eqs. (1) and (3), if the set of constants $K(i)$ $(1 \le i \le N - L + 1)$ is known. The binding constant $K(i)$ depends on the contribution to the binding energy of both specific and nonspecific (i.e., independent of the nucleotide sequence) interactions between the ligand and DNA. To calculate the

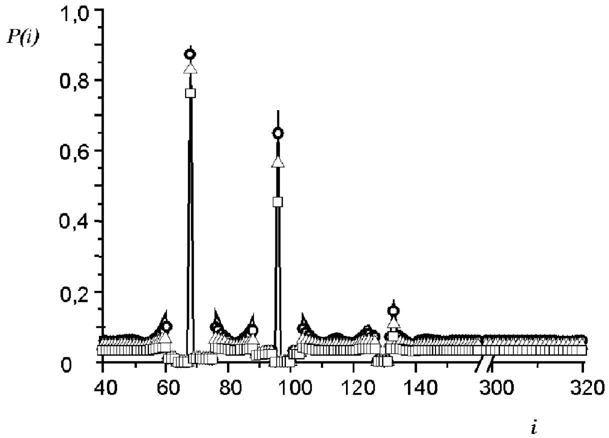

Fig. 1 Dependence of the probability of ligand binding to the i-th binding site of DNA, *P*(*i*), on the base pair number, *i*. Curves were calculated for the following concentrations of free ligand in solution: 0.125 μM (□), 0.25 μM (△), 0.5 μM (O), and 1 μM (solid line)

profiles of distribution of the ligand bound on a DNA fragment *N* base pairs long, it is necessary to determine the constants of binding of the ligand with $N - L + 1$ overlapping binding sites on the DNA fragment with the specified nucleotide sequence. The constants *K*(*i*) can be estimated based on the isotherms of adsorption of the ligand on DNA oligomers. The interaction of the ligand with weaker binding sites can be characterized using a certain binding constant K_{AV}, which is averaged with respect to all "weak" binding sites. In our calculations, we used the value $K_{AV} = 5 \cdot 10^5\ M^{-1}$. The use of a smaller K_{AV} value only slightly affects the relative positions of the maxima and minima on the profiles of distribution of the ligand bound on the DNA fragment.

Figure 1 shows calculated profiles of distribution of Pt-bis-netropsin bound on a DNA fragment with known sequence15 for different ligand concentrations.

In our calculations we used the experimental values of constants of binding of Pt-bis-netropsin with DNA regions with three strongest sites ($4 \cdot 10^7\ M^{-1}$, $1 \cdot 10^7\ M^{-1}$ and $1 \cdot 10^6\ M^{-1}$). The *P*(*i*) values directly correlated with information obtained using the footprinting technique (see Yu et al.[9] for details).

3 The Propagation of Mechanical Perturbations along the DNA Molecule

Protein-DNA interactions can induce DNA bending and twisting and might be responsible for a local change in electric and mechanical properties of a DNA molecule. In the last decade new approaches have been developed for studies of mechanical properties of a single DNA molecule.[17,18] Studies on the effect of mechanical perturbations induced in DNA upon ultrasonic irradiation in solution may also provide information on the mechanical properties of DNA and its complexes with regulatory proteins and anticancer drugs. Recent observations show that the efficiency of DNA breakage upon ultrasound irradiation depends on the nucleotide sequence near the cutting site.[19] DNA breaks occur most frequently at 5′-CG-3′ steps. The interaction of DNA with cis-platin greatly increases the probability of DNA cutting by ultrasound in the close proximity of a bound cis-platin molecule on DNA.

Here, we propose a simple model for the description of the propagation of mechanical disturbances along the DNA molecule. The model can be used to describe some of the recent experimental observations on effects of ultrasound irradiation upon DNA.

3.1 Ultrasonic Irradiation of DNA–Ligand Complexes

The effects of ultrasonic irradiation are based on the cavitation phenomenon: tiny bubbles are produced in solution and their collapses initiate microjets with a speed of about 100 m/sec.[20] It is assumed that those jets are capable of breaking the sugar-phosphate backbone of a DNA molecule. The sizes of the bubbles and the jet diameters have recently been estimated experimentally.[21] The typical jet size is approximately 300 nm, a value which greatly exceeds the diameter of a DNA molecule (2 nm). That is why DNA fragments containing at least several hundreds of nucleotide pairs might be considered to be one-dimensional structures.

3.2 String Model of a DNA Molecule

The dynamical features of a DNA fragment are determined by both electrical and mechanical properties of the molecule. Repulsion between phosphate groups creates a tension within a single DNA molecule which might be compensated by the strain of valence and non-valence bonds, creating a total tension of the molecule. Thus, the DNA molecule might be considered a self-stressed mechanical construction (a tensegrity system).[22] Tensegrity plays a fundamental role in many biological processes.[23] Both tensegrity and one-dimensionality make it reasonable to model the DNA fragment as a string in order to study the propagation of mechanical perturbations along the DNA.

The propagation of perturbation along the string is determined by the wave equation with the initial and boundary conditions which will be formulated as follows:

$$\frac{\partial^2 U}{\partial t^2} = \frac{F}{\rho(x)} \frac{\partial^2 U}{\partial x^2} + g(x,t) \tag{4}$$

where $U(x,t)$ is the transverse displacement of a string's element with the coordinate x at time interval t; F is the overall tension of the string (the appropriate estimate of F for a DNA molecule is about 10 pN);[22] $\rho(x)$ is the linear density of the string (approximately $3 \cdot 10^{-15}$ kg/m for DNA); $g(x,t)$ – is the external force (which acts on the string at position x and time t) divided by the linear density $\rho(x)$.

$C = \sqrt{[F/\rho(x)]}$ gives the speed of propagation of transverse perturbations along the string. The estimated value of this parameter is about 100 m/sec.

We considered the problem of propagation of the mechanical impulse along the string provided the linear density of the string involves a step-like heterogeneity. The external force has been chosen to be of exponential form:

$g(x,t) = [A/\rho(x)] \exp[-a \cdot (t^2 + 2 \cdot (x - x_o)/b)]$, here x_o is the centre of the application of external force; A, a, b are parameters.

The numerical values have been chosen to make the time span of the force action shorter than the time needed for the propagation of a disturbance along the string. This mode of force action might correspond to the interaction of DNA with cavitational microjets in the regions of high velocity gradients.

The numerical values of parameters used in calculations are as follows: the string's length $l = 100$, so that x varies in the interval: $0 \le x \le 100$; $A = 600$; $a = 1$; $b = 30$; $C^2 = F/\rho(x) = 10$. The linear density of the string is assumed to be a step function: in a small region of the string the value of density is twofold greater than in other string parts:

$$\rho(x) = 1 \text{ if } 0 \le x \le 70 \text{ and } 80 \le x \le 100;\ \rho(x) = 2 \text{ if } 70 < x < 80.$$

A step-wise change of linear density may model complexes of DNA with proteins and anticancer drugs. A typical example is the binding of cis-platin, which forms a crosslink between adjacent guanine residues on the same DNA strand and increases the mass of the corresponding DNA segment.

Equation (4) with zero displacements and zero velocities as initial conditions and free-ends of string as boundary conditions has been solved numerically. We have analyzed the time-dependence of deformation energy density. To solve the equation, the standard "cross" difference scheme has been used. The analytical grid has been chosen to have coordinate step $\Delta x = 1$ and time step $\Delta t = 0.001$ These values make the difference scheme stable.[24]

The calculation shows that when perturbation reaches the region of heterogeneity on a string, there is a considerable increase in the deformation energy density at the boundaries between string segments with different linear densities. This effect is attributed to the string's heavy region's dynamics: since this region has a greater inertia ($\rho(x) = 2$), it can not respond to the perturbation as rapidly as the adjacent segment which is characterized by a lower linear density value ($\rho(x) = 1$). This is why the amplitude of string deformation increases.

Figure 2 shows the deformation energy profiles for two points in time shortly after the initial perturbation of the string occurs.

Figure 3 illustrates the string's deformation energy profile at the time t_3, when the wave reaches the density's heterogeneity. One can see that an increase of the deformation energy takes place on the boundary between "light" and "heavy" string segments ($x = 70$). It is significant that the effect still takes place when the initial impulse is applied directly to the region where string heterogeneity is located.

The string model clearly demonstrates that deformation energy increases at the boundary between "light" and "heavy" string segments. Such an increase might be considered as a basis for the explanation of recent observations showing that the probability of DNA breakage by ultrasound is increased at the preferred ligand binding site on DNA.[19]

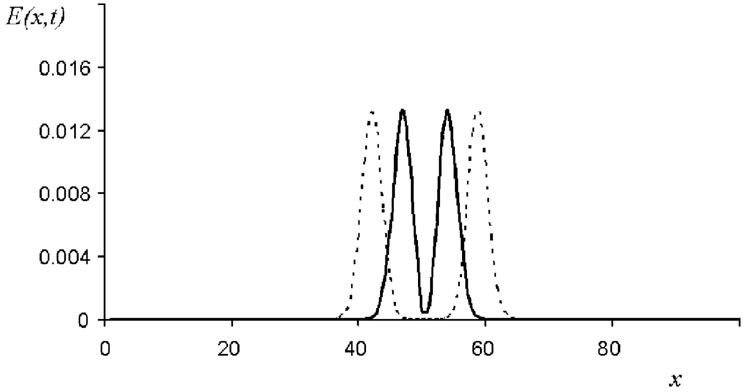

Fig. 2 The string's deformation energy profiles for two points in time shortly after the initial perturbation. x – distance from the left end of the string; $E(x,t)$ – string's deformation energy density

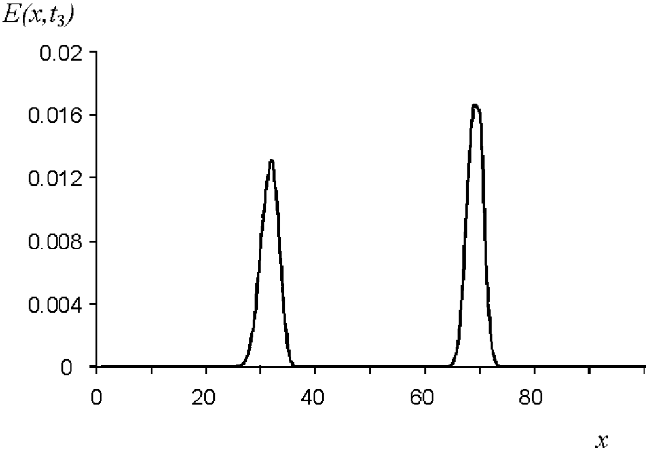

Fig. 3 The string's deformation energy profile at the moment when the perturbation wave reaches the boundary of linear density's heterogeneity. x – distance from the left end of the string; $E(x,t_3)$ – string's deformation energy density. The deformation energy increases at the boundary of heterogeneity ($x = 70$)

Acknowledgements We would like to thank V. F. Ryabokon, B. Jovanovic, E. A. Vorobiev, and M. V. Golovkin for helpful discussions and technical assistance. This research was supported by State Grant "Construction of new drugs for therapy and prophylaxis of antiviral diseases by methods of organic chemistry", Grant of Presidium RAN for Molecular and Cell Biology and RFBR grant 04-04-49364.

References

1. G. V. Gursky, A. S. Zasedatelev, A.L. Zhuze, A. A. Khorli., S. L. Grokhovsky, S. A. Streltsov, A. N. Surovaya, A. M. Nikitin, A. S. Krylov, V. O. Retchinsky, R. S. Beabealashvili, and B. P. Gottikh, Synthetic sequence-specific ligands, *Cold Spring Harbor Symp. Quant. Biol.* 47, 367–378 (1983).
2. N. C. Seeman, Structural DNA nanotechnology: an overview, *Methods Mol. Biol.* 303, 143–166 (2005).
3. M. A. Zakharov, Yu. M. Yevdokimov, S. G. Skuridin, and Yu. D. Nechipurenko, Nanotechnology based on spatially fixed ds DNA (RNA) molecules, *Nanotech. Technical Proceedings of the 2005 NSTI Nanotechnology Conference and Trade Show* 1, 288–291 (2005).
4. A. S. Zasedatelev, G. V. Gursky, and M. V. Vol'kenshtein, Theory of one-dimensional adsorption. I. Adsorption of small molecules on a homopolymer, *Mol. Biol. (Moscow)* 5, 194–198 (1971).
5. J. D. McGhee and P. H. von Hippel, Theoretical aspects of DNA-protein interactions: co-operative and non-co-operative binding of large ligands to a one-dimensional homogeneous lattice. *J. Mol. Biol.* 86, 469–489 (1974).
6. G. V. Gursky and A. S. Zasedatelev, Thermodynamical and stereochemical aspects of binding interactions between sequence-specific ligands and DNA, *Sov. Sci. Rev. D. Physicochem. Biol.* 5, 53–139 (1984).
7. Yu. D. Nechipurenko and G. V. Gursky, Cooperative effects on binding of proteins to DNA, *Biophys. Chem.* 24, 195–209 (1986).
8. Yu. D. Nechipurenko and G. V. Gursky, Thermodynamical models of binding ligands to nucleic acids, *Biofizika*. 48, 773–796 (2003).
9. Yu. D. Nechipurenko, B. Jovanovic, V. F. Riabokon, and G. V. Gursky, Quantitative methods of analysis of footprinting diagrams for the complexes formed by a ligand with a DNA fragment of known sequence, *Ann. N. Y. Acad. Sci.* 1048, 206–214 (2005).
10. M. L. Kopka, C. Yoon, D. Goodsell, P. Pjura, and R. E. Dickerson, The molecular origin of DNA-drug specificity in netropsin and distamycin, *Proc. Natl. Acad. Sci. USA*. 82, 1376–1380 (1985).
11. L. Tabernero, N. Verdaguer, M. Coll, I. Fita, G. A. van der Marel, J. H. van Boom, A. Rich, and J. Aymami, Molecular structure of the A-tract DNA dodecamer d(CGCAAATTTGCG) complexed with the minor groove binding drug netropsin, *Biochemistry*. 32, 8403–8410 (1993).
12. C. Bailly and J. B. Chaires, Sequence-specific DNA minor groove binders, Design and synthesis of netropsin and distamycin analogues, *Bioconjug. Chem.* 9, 513–538 (1998).
13. S. L. Grokhovsky and V. E. Zubarev, Sequence-specific cleavage of double-stranded DNA caused by x-ray ionization of the platinum atom in the Pt-bis-netropsin – DNA complex, *Nucl. Acids Res.* 19, 257–264 (1990).
14. A. N. Surovaya, G. Burckhardt, S. L. Grokhovsky, E. Birch-Hirschfeld, G. V. Gursky, and C. Zimmer, Hairpin polyamides that use parallel and antiparallel side-by-side peptide motifs in binding to DNA, *J. Biomol. Struct. Dyn.* 14, 595–606 (1997).
15. S. L. Grokhovsky, A. N. Surovaya, G. Burckhardt, V. F. Pismensky, B. K. Chernov, C. Zimmer, and G. V. Gursky, DNA sequence recognition by bis-linked netropsin and distamycin derivatives, *FEBS Lett.* 439, 346–350 (1998).

16. A. N. Surovaya, S. L. Grokhovsky, G. Burckhardt, H. Fritzsche, C. Zimmer, and G. V. Gursky, Effect of DNA local conformation on the affinity and binding specificity of bis-netropsins to DNA, *Mol. Biol. (Moscow)* 36, 901–911 (2002).
17. C. Bustamante, Z. Bryant, and S. B. Smith, Ten years of tension: single-molecule DNA mechanics, *Nature* 421, 423–427 (2003).
18. C. Bustamante, Y. R. Chemla, N. R. Forde, and D. Izhaky, Mechanical processes in biochemistry, *Ann. Rev. Biochem*. 73, 705–748 (2004).
19. S. L. Grokhovsky, The specific cleavage of DNA with ultrasound, *Mol. Biol. (Moscow)* 40, 317–325 (2006).
20. Yu. A. Grivnin and S. P. Zubrilov, Influence of the physical properties of fluids on pulsation and destruction of non-spherical cavitational bubbles, *Zh. Fiz. Khim. (Moscow)* 54, 56–59 (1980).
21. J. Lee, M. Ashokkumar, S. Kentish, F. Grieser, Determination of the size distribution of sonoluminescence bubbles in a pulsed acoustic field, *JACS*. 127, 16810–16811 (2005).
22. D. Yu. Nechipurenko, R. V. Polozov, Yu. D. Nechipurenko, DNA as self-stressed mechanical construction, *Biofizika (in press)*.
23. D. E. Ingber, Tensegrity I. Cell structure and hierarchical systems biology, *J. Cell Sci*. 116, 1157–1173 (2003).
24. I. S. Berezin, N. P. Zhidkov, *Metodi Vichislenii, V. 2,* (Moscow, Fizmatgiz, 1960) [in Russian].

This page intentionally blank

Nanoconstructions Based on Spatially Ordered Nucleic Acid Molecules

Yu. M. Yevdokimov*

Abstract Different strategies for the design of nanoconstructions whose building blocks are both linear molecules of double-stranded nucleic acids and nucleic acid molecules fixed in the spatial structure of particles of liquid-crystalline dispersions are described.

Keywords Nanostructure, nucleic acids, liquid-crystalline dispersions, chelate complexes, nanobridges, circular dichroism

1 Introduction – Nucleic Acid Molecules as a Basis for the Creation of Nanoconstructions

Nanodesign based on double-stranded (ds) nucleic acids (NAs), i.e. the directed creation of three-dimensional, spatial constructions with tailored properties, the "building blocks" of which are ds NA molecules or their complexes with biologically active compounds, is a topic of current theoretical and experimental interest.[1–7] The very possibility of using ds NA for formation of nanoconstructions (NaCs) with controlled parameters is based on a small number of properties characteristic of NA molecules only:

- Samples of NA molecules of preset sequence of nitrogen bases ranging in length from just a few nucleotides to chains several tens of micrometers long can be obtained in production quantities using routine biotechnological procedures. (This is not the case for any other polymer.)
- Short helical molecules of ds NA with lengths of the order of 100–1,000 Å have a high local rigidity under standard solvent conditions that allows such

---

V.A. Engelhardt Institute of Molecular Biology of the Russian Academy of Sciences,
Vavilov Str. 32, 119991, Moscow, Russia

* To whom correspondence should be addressed. E-mail: yevdokim@eimb.ru

M. Giersig and G. B. Khomutov (eds.),
Nanomaterials for Application in Medicine and Biology

molecules to be used as "building blocks" without disturbing their physical properties.
- The predicted spatial families of rigid ds NA molecules and the nature of intermolecular interaction under various conditions as well as the intrinsic susceptibility of the NA secondary structure to external stimuli mediated by small molecules or ions, open up a gate for the directed regulation of the characteristics of designed spatial constructions to fabricate nanomechanical devices.
- The nitrogen bases in the spatial NA constructions retain their capacity to interact with diverse chemical compounds and biologically active substances, as well as to orient these compounds along the NA molecular axis, which imparts an additional chemical reactivity to the whole structure.
- The flexible single-stranded NA "recognizes" its complementary strand and, owing to H-bonds, forms a stable complex with the latter, thus providing an opportunity to prepare a rigid ds of preset composition.
- The formation of branching points in the ds NA molecules combined with complementary (recognizing, "sticky") ends allows one to design plane lattices and sophisticated spatial structures.

There are two nanodesign strategies, which utilize different NA properties, however, irrespective of the strategy, the structure of nanomaterials based on the ds NA may be controlled up to a molecular-level precision.

2 Nanoconstruction Design Strategies

2.1 "Step-by-Step" Design

To date, the NaC design strategy approach based on the consecutive modification of a starting ds NA molecule (or synthetic polynucleotide), that is, what may conventionally be referred to as the consecutive, or step-by-step, design has been described in detail.[1,2,4] This approach was pioneered by N. Seeman[8] in 1982. Using the NA fragments containing "sticky" ends and cruciform structures, he created an initial nanostructure – a plane NA lattice.

There are other approaches, which one might call "supplementary" to Seeman's approach.[9–10] Various aspects of this strategy have been reviewed and different plane lattices as well as a cube-shaped nanostructures, octahedrons, dodecahedrons, and so on, in which ds DNA molecules served as the stiffening ribs, have been discussed.[11]

The creation of 3-D structures (Fig. 1) does not influence the physical and chemical characteristics of NA molecules. This opens a principal way for the immobilization of molecules of various compounds ("guest" molecules) in the structure of NaCs. However, one can stress two aspects related to the problem of these guest molecules. First, it is well-documented that ds NA molecules can easily "absorb"

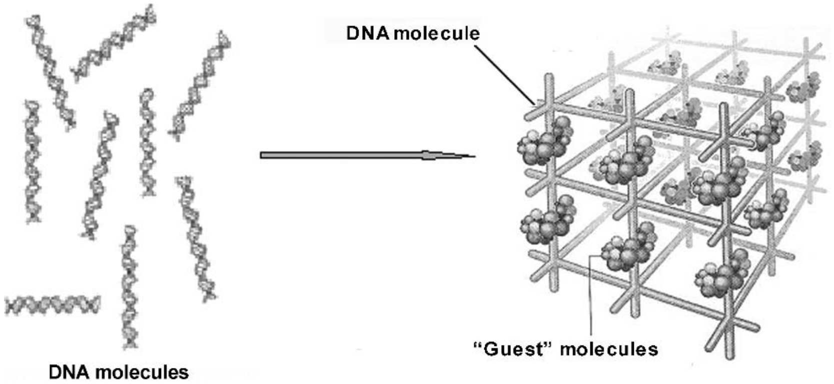

Fig. 1 Hypothetical nanostructure containing "guest" molecules (From N. Seeman. With permission)

such molecules as intercalators or groove-binders. In this case, there is no difference in the concentrations of guest molecules absorbed by initial ds NA or ds NA molecules in the content of the 3-D structure. Second, there is a another aspect to this problem,[12] namely the immobilisation of guest molecules in a free space between neighboring NA molecules in the 3-D structure. From this point of view, the creation of NaC following a "step-by-step" strategy and containing a high concentration of guest molecules is difficult.[13–14]

To design spatial NaCs containing built-in guest molecules, a number of researchers almost simultaneously began to use synthetic single-stranded NA fragments linked to metallic nanoparticles. In their approach to nanodesign, Mirkin et al.[15] and Alivisatos et al.[16] have used single-stranded NA linked to colloidal gold nanoparticles as building blocks. If an alien NA, in which the sequence of nitrogen bases is complementary to the starting NA, is added to the above-mentioned system, the hybridization leads to the formation of a rigid ds NA. In this case, the gold nanoparticles are equally spaced, and this distance may be controlled within 3.4 Å. Attaching a larger number of single-stranded NA fragments to the gold nanoparticles makes its possible to design three-dimensional nanostructures, in which gold atoms alternate at regular intervals with ds NA molecules. Various aspects of the creation and possible application of this kind of nanoparticles have been reviewed recently.[5,17]

It should be noted that the issue of the practical application of NaCs created from a single ds NA molecule via a step-by-step technology seems to depend on the tasks to be solved by researchers. For instance, guest molecules may be "targets" for other biologically active compounds. With view to this property, it is feasible to develop biosensors for identifying substances that recognize guest molecules. In addition, according to a concept of E. Di Mauro and C. Hollenberg,[18] DNA might be used in chip construction in order to realize sizes below 100 nm.

2.2 "All-At-Once" Design

The strategy we proposed[19] for designing NaCs that contain ds NA molecules differs fundamentally from any variant of the step-by-step approach. The fact is that, in contrast to the latter, which is based on the use of unit NA molecules, our strategy is based on particles of cholesteric liquid-crystalline dispersions (LCDs) that emerge with the phase exclusion of these molecules from water-salt polymer-containing solutions.[20–22]

As a result of phase exclusion, initial, "pure", rigid ds molecules of NA (or polynucleotides) form particles composed of about 10^4 molecules; each particle is about 500 nm in size (Fig. 2), which was evaluated by several experimental techniques (low speed sedimentation, UV-light scattering, laser correlation spectroscopy, etc.) and confirmed by theoretical calculations. According to x-ray studies,[21–23] NA molecules are ordered in the particle at distances of 2.5–5.0 nm, i.e., they acquire the properties of a crystal, but the molecules in the neighboring layers are mobile, i.e. they retain the properties of a liquid. Such a combination of properties allows this structure to be called "liquid-crystalline" (see review 23 and early references cited therein). The most important features of dsNA LCDs are well established by now. First, LCDs exist under certain boundary conditions, which are determined by solution ionic strength, by the value of osmotic pressure of water-salt-polymeric solution, etc. The osmotic pressure, which depends on the polymer concentration in solution, determines the distance between the NA molecules in a particle. Second, spontaneous constraint of diffusional degrees of freedom of neighboring

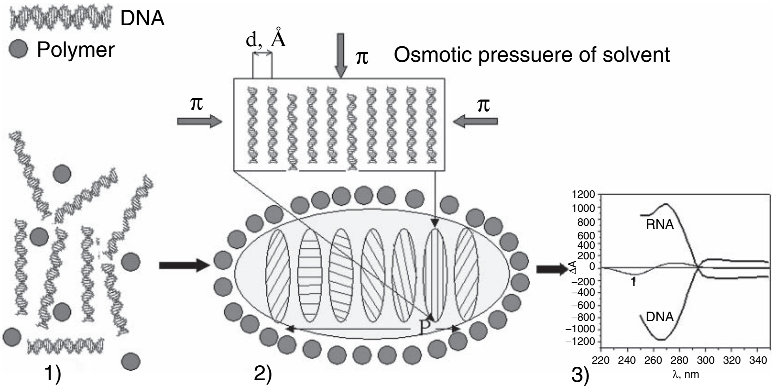

Fig. 2 The formation of particles of the double-stranded nucleic acid cholesteric liquid-crystalline dispersion. Polymer molecules are indicated by filled circles (**1**) and the DNA CLCD particle is encircled by an oval (**2**). π is the osmotic pressure of the solvent; the ordering of DNA molecules in one layer is shown. Note that the polymer molecules do not enter the composition of nucleic acid LCD particles. The formation of CLCD particles characterized by the spatially twisted packing of neighboring DNA (or RNA) molecules is accompanied by the appearance of an abnormal negative band in the CD spectrum (**3**) in the case of DNA and a positive band in the case of RNA in the absorption region of nitrogen bases

NA molecules takes place upon phase exclusion. (However, and this is important to stress, the distance between NA molecules and the "liquid-like" way of packing these molecules provide the conditions for a quick diffusion of many compounds (i.e. guest molecules) between the NA molecules in one layer as well as between the neighboring NA layers in the spatial structure of the LCD). Third, the combination of geometrical and optical anisotropy of NA molecules causes each subsequent layer formed by NA molecules in the structure of the liquid-crystalline particles (a so-called "quasinematic" layer) to be twisted in a certain angle with respect to the previous one, i.e. the twisted or a so-called "cholesteric structure" of the particle arises. Fourth, because NA molecules contain chromophores (nitrogen bases absorbing in the UV-region of the spectrum), the resulting cholesteric may be termed "colored cholesteric". Since the bases are virtually perpendicular to the long axis of NA molecules forming adjacent layers in the structure of the cholesteric, theory[24] predicts the appearance of an intense (abnormal) band in the circular dichroism (CD) spectrum in the base absorption region, which is, indeed, observed experimentally (Fig. 2). Finally, the chemical reactivity of the NA components (nitrogen bases, etc.) in the particles of NA LCD with respect to chemical or biological compounds (guest molecules) is retained. This provides not only a convenient point for tethering high concentrations of guest molecules inside the LCD particles, but opens up a way for a specific alteration of the properties of these molecules. It should be noted that theory[24] imposes no limitations on the number of chromophores that could be introduced into the NA structure in the same manner, so one could expect the appearance of the abnormal CD bands for compounds intercalating between the NA base pairs. This means that there would be an analytical "instrument" capable of monitoring the finest variations in the properties of NA molecules and cholesterics made from them.

Thus, there is a fundamental possibility to use NA molecules spatially fixed within the particles of LCD as precursors with adjustable properties for NaC formation, i.e. it is possible to create NaC, whose properties can be specified in advance by controlling both the properties of NA molecules and the solvent used.

With cholesteric LCD particles (that is, a structure in which adjacent NA molecules are ordered and slow moving) at hand, we then formed cross-links from guest molecules with known properties between adjacent NA molecules. In doing so, we had to retain the spatial arrangement of the particle (its abnormal optical activity). Thus, at the initial stage of research, we attempted to design a NaC with properties preset by both NA molecular characteristics and those of compounds bound with the NA or located in the external environment. Hence, the problem is reduced to the formation of cross-links with adjustable properties between neighboring NA molecules fixed at a distance of 2.5–5.0 nm in the structure of LCD particles. Taking these distances into account, one can call these cross-links "nanobridges" between NA molecules.

To form such nanobridges, it is necessary to have the "beginning" and "end" loci on the surface of a NA molecule. Theoretically, such loci may be metal ions capable both of forming chelates with pairs of NA bases and of specific fixation in a groove (grooves) on the NA surface and attaching other ligands. Molecules of planar compounds (ligands) also tend to form an external complex with NA molecules. In addition, they facilitate the insertion of reactivity of hydroxyl, keto-oxygen, and amino or sulfhydryl groups within these compounds. Consequently, the locus for the beginning or end of the prospective nanobridge between NA molecules may be either a metal ion bound with nitrogen bases or a molecule of some additional ligand.

Hence, our nanoconstruction technology is based on results of theoretical and experimental research concerning the spatial ordering of adjacent, closely spaced NA molecules in cholesteric LCD particles and the relative limitation of their diffusive mobility; the formation of chelate complexes from alternating metal ions and anthracycline molecules under conditions of the phase exclusion of NA molecules; and on the use of copper ions or anthracycline molecules as the loci for the beginning or end of nanobridges.

The prerequisites for the formation of nanobridges (i.e. the structure of anthracycline compounds, the "phasing" and distance between ds NA molecules, etc.) clearly show that the creation of these bridges is a very delicate stereochemical process, which can be realized only under rather strict conditions.[6] The number of Cu^{2+} ions contained in the nanobridges under the conditions we used could be estimated directly,[25] because the Cu^{2+} ion forms a chelate complex with four reactive oxygen atoms; this complex is in a d^{9} state, which exhibits nonzero magnetic moment.

The emergence of nanobridges that are of the type [Cu^{2+}–DAU-Cu^{2+}–DAU-Cu^{2+}–…–Cu^{2+} –DAU-Cu^{2+} –DAU–Cu^{2+}] (here - DAU is the abbreviation for an anthracycline antibiotic – daunomycin) between adjacent NA molecules leads, first, to the amplification of the amplitude of the abnormal bands located both in the NA absorption region ($\lambda \sim 270$ nm) and in the [Cu^{2+}–DAU-Cu^{2-}] absorption region ($\lambda \sim 500$ nm). Second, the thermal stability of the formed structure is determined by the number and the properties of the nanobridges themselves. This implies that there are conditions under which this structure maintains itself, even in a water-salt solution and, therefore, it can be visualized. Indeed, immobilization of the DNA LCD particles treated by DAU and then by $CuCl_2$ on a nuclear membrane filter shows that every particle is a 3-D construction. The sizes varied from 0.3 μm to 0.8 μm with 0.5 μm as the average, which agrees quite well with results obtained by other techniques.[6,7]

Thus, we were the first both to visualize NaCs based on cholesteric DNA LCD (as well as other synthetic polydeoxyribonucleotides and polyribonucleotides) particles and to measure morphological characteristics of these particles. The existence of sufficiently stable structures, whose properties to a considerable extent are independent of the properties of water-salt-polymeric solution, allowed us to suggest a hypothetical structure of the particles of NaCs on the basis of cholesteric NA LCD (Fig. 3).

Since all NA molecules in the structure of the cholesteric NA LCD particles are identical in their physicochemical properties, and, hence, in their ability to form DAU–Cu^{2+} nanobridges, the hypothetical structure takes into account two modes of arranging of these nanobridges. According to the scheme, the DAU–Cu^{2+} should be located within NA quasinematic layers as well as between these layers.

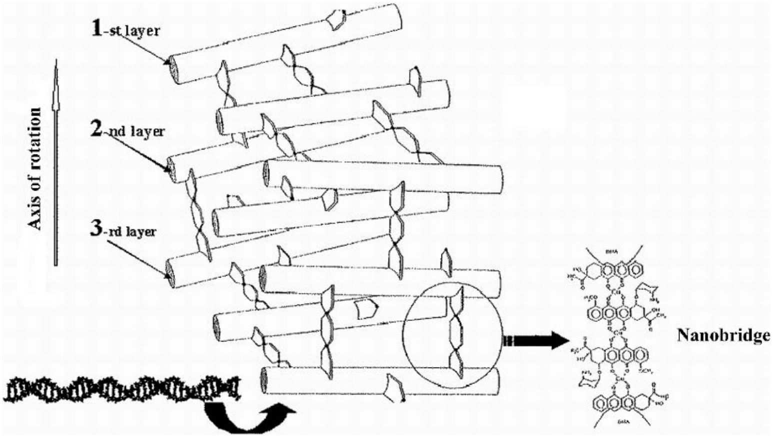

Fig. 3 A hypothetical spatial structure of NaC based on cholesteric LCD particles, in which adjacent ds DNA molecules are connected by nanobridges (a version of this bridge structure is shown on the right)

The resulting NaC is a spatially ordered structure where the diffusion mobility of neighboring NA molecules is sharply decreased; therefore, the structure lacks many properties characteristic of the LCDs of NAs. Indeed, x-ray diffraction analysis indicates a higher degree of crystallinity of the DNA NaCs as compared with the particles of DNA LCD.[20–23] There are a few principal differences between initial particles of the NA LCDs and NA NaCs. First, in contrast to the NA LCD, the structure of NaC is not "liquid-crystalline" any more; rather it is a rigid, crystal-like, three-dimensional structure. Second, in contrast to the NA LCD, NaC has an extraordinary high optical activity both in the UV- and visible regions of the CD spectrum. Third, NaC (probably) consists of two cholesterics. Along with a cholesteric composed of initial NA molecules, there is a possibility for the formation of a cholesteric from the nanobridges located between neighboring NA layers. This means that, in the process of the formation of the NaC, the abnormal optical activity in the absorption band of the antibiotic ($\lambda \sim 500\,\mathrm{nm}$) rises dramatically, enabling us to observe minor changes in the properties of the NaC designed. Theoretical analysis of the properties of such structures was begun recently;[26] preliminary results show that the properties of cholesterics formed by nanobridges may not "follow" the properties of cholesterics formed by NA molecules.

We would like to emphasize the uniqueness of our NaC. Despite the "solid" (rigid) structure of NaC, many compounds (from ascorbic acid to poly(aminoacids) and peptides with molecular masses up to 60 kDa) diffuse very easily inside the spatial structure of NaC.[27] Besides, this structure accommodates a high concentration not only of NA molecules alone (up to 400 mg/ml) but antibiotic molecules (about 200 mg/ml) and copper ions. As a result, when using cholesteric NA LCD particles for nanodesigning, we attain the ordering of both adjacent NA molecules and guest molecules. Hence, the use of LCD particles for nanodesign automatically solves the problem of spatial ordering both neighboring NA and guest molecules, which is not solved yet in the case of a step-by-step strategy.

We would like to note that this approach itself may be further improved. In particular, other chemicals or biologically active compounds, as well as their complexes, may be used for nanobridges, or the surface of NA molecules may be chemically modified to diversify the reactivity and afford new types of NaCs. Below, we will describe the first attempt to form a NaC using the procedure based on a different mechanism of condensation of ds nucleic acid molecules, i.e. their "enthalpy condensation" based on the interaction of NA molecules with polycations.

The important features of the dispersions of (NA–polycation) complexes are shown in Fig. 4.

First, the exclusion of the ds NA acid occurs when a critical concentration of polycations in the solution is reached (note that in this case, polycation molecules are always part of the composition of the dispersion particles formed). Second, the distance between the molecules of the (NA–polycation) complex in the particles formed is fixed and generally close to 2.5 nm. Third, in some cases, depending on the nature of polycation molecules, an LCD can be formed from (NA–polycation) complexes, which is characterized not only by the larger (but, as previously, fixed) distance between molecules of (NA–polycation) complexes, but also a strong CD band; i.e., it becomes possible to form a cholesteric LCD. Finally, during formation of particles of an LCD of (NA–polycation) complexes, the reactivity of NA molecules can be significantly limited as a result of the steric location of polycation

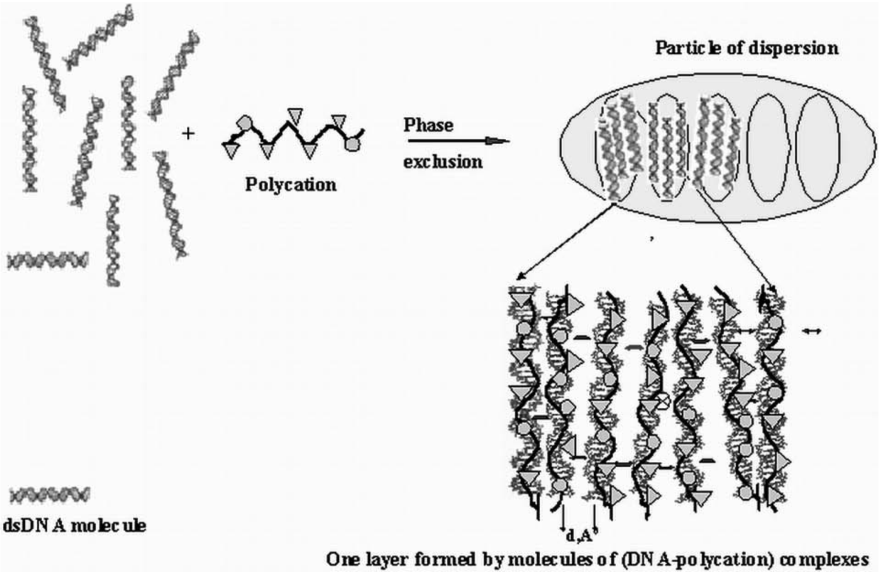

Fig. 4 The "enthalpy" condensation of ds DNA molecules

molecules on the surface of a NA molecule. However, reactivity caused by chemical groups of polycation molecules arises instead. This circumstance opens up the fundamental possibility of using such groups as new reactive centers having a high diffusion availability.

Therefore, despite the significant differences from the first mechanism of condensation, a high local concentration of polycation molecules in cholesteric NA LCD particles and the reactivity of chemical polycation groups in combination with an ordered arrangement of polycation molecules can provide the possibility of cross-linking neighboring, closely spaced molecules of (NA–polycation) complexes in LCD particles and designing NaCs.

From this point of view, the natural biodegradable biocompatible polyaminosaccharide – Chitosan (poly-[β-(1– 4)-2-amino-2-deoxy-*D*-glucopyranose], Chi) seems to be promising. In view of the specific features of the spatial structure of Chi molecules,[28] positively charged Chi amino groups can alternately interact with negatively charged DNA phosphate groups.

Indeed, experiments showed[28] that when the critical Chi concentration is reached, an abnormal positive band in the DNA absorption region (λ ~ 270 nm) arises in the CD spectrum. This band is indicative of cholesteric packing of (DNA–Chi) complexes in particles of dispersion. The data obtained[28] show that, depending on the combination of two parameters, specifically, the ionic strength and the percentage of amino groups, cholesteric LCDs of the (DNA–Chi) complex can be formed, which exhibit either negative or positive abnormal bands in the CD spectra.

The x-ray scattering curves for the phase formed of particles of a cholesteric LCD of the (DNA–Chi) complex demonstrate a single Bragg reflection ($\mathbf{d}_{\mathbf{Bragg}}$ ~ 2.6 nm) which is much smaller than the value of $\mathbf{d}_{\mathbf{Bragg}}$ for particles of the LCD of pure DNA, and corresponds to the transition region between the cholesteric and hexagonal LC phases.

Chi molecules interact with DNA in such a way as to allow amino groups of Chi sugar residues not only to neutralize the negative charges of DNA phosphate groups but also to form a specific distribution of positively charged free amino groups near the DNA surface.[29] Since neighboring free amino and hydroxy groups in Chi molecules intensively form chelate complexes with copper ions,[29] to perform cross-linking of neighboring Chi molecules fixed in the structure of DNA–Chi CLCD particles, the same approach that had been used above to form nanobridges between pure DNA molecules was applied. Amplification of the band in the absorption region of the [DAU-Cu^{2+}] chromophore (λ ~500 nm) again indicates that this chromophore becomes spatially fixed with respect to Chi molecules in any cholesteric LCDs formed by different (DNA–Chi) complexes.

The amplification of the abnormal band in the CD spectrum of (DNA–Chi) cholesteric LCDs depends also, as in the case of pure DNA, on the concentration of DAU molecules and copper ions.

Hence we believe that the amplification of the band at (λ ~ 500 nm) in the CD spectrum of LCDs of different (DNA–Chi) complexes is related to the formation of nanobridges of the [- Cu^{2+}-DAU - Cu^{2+} -] type between neighboring Chi molecules that are bound into complexes with DNA molecules in LCD particles. Allowing for the fact that, as in the case of pure DNA, nanobridges can be formed both between neighboring Chi molecules within the same layer and between neighboring Chi molecules belonging to neighboring layers, the amplification of the band at λ ~ 500 nm reflects the formation of a spatial NaC.

The fact that the physical size of nanobridges can be small in the case of (DNA–Chi) cholesteric LCDs, in combination with the ability of copper ions to form very strong chelate complexes with neighboring amino and hydroxyl groups of Chi sugar residues, suggests[29] that the structure and properties of NaCs obtained may significantly differ from the NaCs based on the pure DNA.

Thus, comparison of the results obtained in this section with the data on the nanodesign based on pure DNA suggest that nanobridges can be formed between neighboring Chi molecules in (DNA–Chi) complexes that are fixed in the spatial structure of cholesteric LCD particles; i.e., NaC of a new type can be designed.

3 Conclusion

Our data show that ds NA molecules spatially ordered in the structure of particles of cholesteric LCDs represent a polyfunctional object of nanobiotechnology. A targeted, controlled variation of NA properties affords extensive opportunities for creating nanobiostructures that can be applied in various areas of science and technology.

Combination of various molecular properties of the nucleic acid and the antibiotic that participates in the formation of a nanobridge provides many opportunities for the practical application of nanoconstructions:

- Nanoconstructions, in which the NA concentration is higher than 200 mg/ml, may be used as "carriers" for genetic material or as a "reservoir" for high concentrations of the diverse biologically active compounds easily embedded in these constructions, and could be applied in medicine and biotechnology.
- Nanoconstructions based on cholesteric LCD particles of dsDNA (RNA) represent sensing elements of optical biosensors that allow one to detect the presence of biologically active compounds, in particular, genotoxicants, in physiological fluids. These can be used in medicine, ecology, and biotechnology.
- Nanoconstructions with controlled physicochemical properties immobilized in synthetic polymeric films (hydrogels) can be used as optical filters in optics and electronics.
- Finally, the nanoconstructions described here could be used as molecular sieves and macromolecular scaffolds for the assembly of molecular electronic materials.

Acknowledgements This research was supported in part by a grant from the Russian Foundation for Basic Research (project no. 06-04-08073-ofi).

References

1. N. C. Seeman, DNA nanotechnology: novel DNA constructions, *Ann. Rev. Biophys. Biomol. Struct*. 27, 225–228 (1998).
2. C. N. Niemeyer, Progress in "engineering up" nanotechnology devices utilizing DNA as construction material, *Appl. Phys. A* 68, 119–124 (1999).
3. C. R. Lowe, Nanobiotechnology: the fabrication and application of chemical and biological nanostructures, *Curr. Opin. Struct. Biol*. 10, 426–434 (2000).
4. A. Csáki, G. Maubach, D. Born, J. Reichert, and W. Fritzsche, DNA-based molecular nanotechnology, *Single Mol*. 3, 275–280 (2002).
5. E. Kats and I. Willner, Intergrated nanoparticles-biomolecule hybrid systems: synthesis, properties and applications, *Angew. Chem. Int. Ed*. 43, 6062–6108 (2004).
6. Yu. M. Yevdokimov, S. G. Skuridin, Yu. D. Nechipurenko, M. A. Zakharov, V. I. Salyanov, A. A. Kurnosov, V. D. Kuznetsov, and V. N. Nikiforov., Nanoconstructions based on double-stranded nucleic acids, *Int. J. Biol. Macromol.,* 36(1–2), 103–115 (2005).
7. Yu. M. Yevdokimov, M. A. Zakharov, and S. G. Skuridin, Nanotechnology based on nucleic acids, *Herald Rus. Acad.Sci*.76, 5–11 (2006).
8. N. C. Seeman, Nucleic acid junctions and lattices, *J. Theor. Biol*. 22, 237–247 (1982).
9. C. N. Niemeyer, T. Sano, C. L. Smith, and C. R. Cantor, Oligonucleotide-directed self-assembly of proteins: synthetic DNA-streptavidin hybrid molecules as connectors for the generation of macroscopic arrays and the construction of supramolecular bioconjugates, *Nucl. Acids Res*. 22(25), 5530–5539 (1994).
10. J. Shi and D. E. Bergstrom, Assembly of novel DNA circles with rigid tetrahedral linkers, *Angew. Chem. Int. Ed*. 36, 111–113 (1997).
11. U. Feldkamp and C. N. Niemeyer, Rational design of DNA nanoarchitectures, *Angew. Chem. Int. Ed*. 45, 1856–1876 (2006).
12. Yu. M. Yevdokimov, V. I. Salynov, L. V. Buligin, A. T. Dembo, E. Gedig, F. Spener, and M. Palumbo, Liquid-crystalline structure of nucleic acids: effect of anthracycline drugs and copper ions, *J. Biomol. Struct. Dynamics* 15, 97–105 (1997).
13. M. Sarikaya, C. Tamerler, A. K-J. Jen, K. Schulten, and F. Baneyx, Molecular biomimetics: nanotechnology through biology, *Nat. Mater*. 2, 577–585 (2003).
14. P. J. Paukstelis, J. Nowakowski, J. J. Birktoft, and N. Seeman, Crystal structure of a continuous three-dimensional DNA lattice, *Chem. Biol*. 11(8), 1119–1126 (2004).
15. C. A. Mirkin, R. L. Letsinger, R. C. Mucic, and J. J. Storhoff., A DNA-based method for rationally assembling nanoparticles into macroscopic materials, *Nature* 382, 607–609 (1996).
16. A. P. Alivisatos, K. P. Johnsson, X. Peng, T. E. Wilson, C. J. Loweth, M. P. Bruchez, and P. G. Schultz., Organization of "nanocrystal molecules" using DNA, *Nature* 382, 609–611 (1996).
17. R. J. Mumper, Z. Cui, and M. O. Oyewumi, Nanotemplate engineering of cell specific nanoparticles, *J. Dispersion Sci. Technol*. 24, 569–588 (2003).
18. E. Di Mauro and C. P. Hollenberg, DNA technology in chip constructions, *Adv. Mater*. 5, 384–386 (1993).
19. Yu. M. Yevdokimov, V. I. Salyanov, E. Gedig, and F. Spener, Formation of polymeric chelate bridges between double-stranded DNA molecules fixed in spatial structure of liquid-crystalline dispersions, *FEBS Lett*. 392(3), 269–273 (1996).
20. Yu. M. Yevdokimov, V. I. Salyanov, E. Gedig, and F. Spener, Formation of polymeric chelate bridges between double-stranded DNA molecules fixed in spatial structure of liquid-crystalline dispersions, *FEBS Lett*. 392(3), 269–273 (1996).
21. F. Livolant, Ordered phases of DNA in vivo and in vitro, *Physica A* 176, 117–137 (1991).
22. F. Livolant and A. Leforestier, Condensed phases of DNA: structure and phase transitions, *Prog. Polym. Sci,* 21, 1115–1164 (1966).

23. Yu. M. Yevdokimov, Liquid crystalline forms of DNA and their biological role, *Liq. Cryst, Prac. Appl.* 3, 10–47 (2003) [in Russian].
24. V. A. Belyakov, V. P. Orlov, S. V. Semenov, S. G. Skuridin, and Y. M. Yevdokimov, Comparison of calculated and observed CD spectra of liquid crystalline dispersions formed from double-stranded DNA and from DNA complexes with coloured compounds, *Liq. Cryst.* 20(6), 777–784 (1996).
25. V. A. Nikiforov, V. D. Kuznetsov, Yu. D. Nechipurenko, V. I. Salyanov, and Yu. M. Yevdokimov, Magnetic properties of copper as a constituent of nanobridges formed between spatially fixed deoxyribonucleic acid molecules, *JETP Lett.* 81(6), 264–266 (2005).
26. V. L. Golo, E. I. Kats, Yu. S. Volkov, V. I. Salyvanov, and Yu. M. Yevdokimov, Novel cholesteric phase in dispersions of nucleic acids due to polymeric chelate bridges, *J. Biol. Phys.* 27(1), 81–93 (2001).
27. Yu. M. Yevdokimov, V. I. Salyanov, G. B. Lortkipanidze, E. Gedig, F. Spener, and M. Palumbo, Sensing biological effectors through the response of bridged nucleic acids and polynucleotides fixed in liquid-crystalline dispersions, *Biosens. Bioelectron.* 13(3–4), 279–291 (1998).
28. Yu. M. Yevdokimov and V. I. Salyanov, Liquid crystalline dispersions of complexes formed by chitosan with double-stranded nucleic acids, *Liq. Cryst.* 30, 1057–1074 (2003).
29. Yu. M. Yevdokimov, M. A. Zakharov, and V. I. Salyanov, Liquid crystalline dispersions of double-stranded nucleic acids and their complexes as a background for nanodesign, *Kristallografiy* 51, 1082–1097 (2006) [in Russian].

Nanospearing – Biomolecule Delivery and Its Biocompatibility

Dong Cai[1,3,*], Krzysztof Kempa[2], Zhifeng Ren[2], David Carnahan[3], and Thomas C. Chiles[1]

Abstract Introduction of exogenous DNA into mammalian cells represents a powerful approach for manipulating signal transduction. However, the currently available techniques have serious limits in terms of either low transduction efficiency or low cell viability. It is found that carbon nanotubes (CNTs) can mediate molecule transportations via various mechanisms. We have reported a highly efficient molecular delivery technique, called nanotube spearing, based on the penetration of Ni-particle-embedded nanotubes into cell membranes by magnetic field driving. DNA was immobilized onto the nanotubes and subsequently speared into targeted cells. We have achieved a high transduction efficiency in Bal17 B-lymphoma cell line, *ex vivo* B cells, and primary neurons with high viability. This technique may provide a powerful tool for highly efficient gene transfer in a variety of cells, especially, in the hard-to-transfect cells. However, CNTs have been associated with environmental and public health concerns which arose in the course of research on possible biomedical applications. The disturbances CNTs cause in the immune system have been met with particular interest because any ideal in vivo application of CNTs should not trigger any undesirable bodily responses. It is imperative to unravel the effects of CNTs on B cells, which represent the humoral component of acquired immunity, so that the potential risk of CNTs to public health can be thoroughly understood and advanced strategies can be employed to develop safe applications. We investigated the compatibility of the PECVD nanotubes and the nanospearing procedure in terms of cell viability, growth, and intracellular signal pathways by means of flow cytometry and biochemical analysis. No additional cell death was observed after the spearing treatment, nor had B cell activation been indicated by changes in cell size, growth, CD69 expression, and kinase phosphorylation. The post-spearing cells preserve the ability to respond to stimulation in as robust a manner as cells left untreated. Our study suggests the biocompatibility of

---

[1] Department of Biology, [2] Department of Physics, Boston College, 140 Commonwealth Avenue, Chestnut Hill, MA 02467, USA

[3] NanoLab, Inc., Newton, MA 02458, USA

* To whom correspondence should be addressed. E-mail: caid@bc.edu

M. Giersig and G. B. Khomutov (eds.),
Nanomaterials for Application in Medicine and Biology

the nanospearing procedure and PECVD nanotubes under the proposed spearing conditions with regard to the humoral component of the immune system, therefore, reducing concerns that surround in vivo applications of CNTs.

Keywords Carbon nanotubes, transfection, delivery, lymphocyte, compatibility, toxicity

1 Introduction

Nanomaterials are inspiring people to explore a new line of molecule delivery techniques, as can be seen from a number of recent studies. Nanotubes,[1,2,3] nanorods,[4] and nanoparticles[5] have been employed to transport molecules into cells, and they have demonstrated good potential. Particularly, the distinctive electric and magnetic properties of carbon nanotubes have inspired research interest in the development of novel avenues for molecule delivery.[6,7]

In our efforts to explore nanomaterials for biomedical application, CNTs synthesized by plasma enhanced chemical vapor deposition (PECVD)[8] were used to conduct efficient molecule delivery to mammalian cells through a unique technique termed "nanospearing."[9] In order to understand the biocompatibility of nanospearing so as to be able to develop an efficient and safe technique for in vivo applications, we studied our nanospeared cells with regard to viability, cell cycle, protein expression, and phosphorylation. In this study, the humoral component of the immune system was selected for conducting the evaluation.

1.1 Basic Phenomenon

CNTs grown by PECVD for this particular application are multi-walled and vertically aligned on substrates (see Fig. 1). Due to the nature of the PECVD process, nanoparticles of a ferromagnetic catalyst metal (Ni) are embedded in the nanotube tips.[10] These particles render the nanotubes responsive to magnetic stimuli. When CNTs are removed from the substrate and suspended in a solution, they can easily be pulled to the side wall of the vessel by a permanent magnet (see Fig. 1, inset). This magnetic response can also be demonstrated by placing a carbon nanotube suspension on a magnetic stirrer plate, without a magnetic stirring bar in the container. Magnetically susceptible nanotubes show an optical "flashing" effect, synchronized with the rotating magnetic field. Observations using electron microscopy show that the magnetically susceptible nanotubes are short ($<2\,\mu m$) and contain a needle-like magnetic particle with an aspect ratio (length to width) greater than three. The nanotubes used for this project were, on average, $1\,\mu m$ in length and $80\,nm$ in diameter.

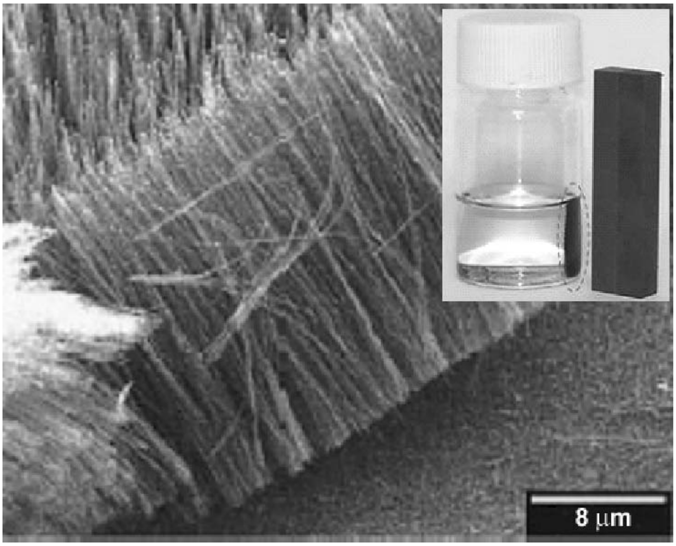

Fig. 1 Magnetically responsive carbon nanotubes

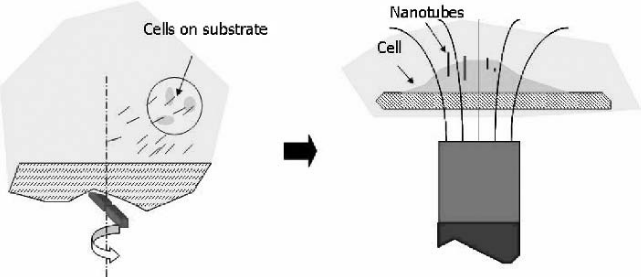

Fig. 2 Scheme of the nanospearing procedures (Cai[9])

1.2 The Principle of Nanospearing

This type of nanotubes can be used to penetrate the cell membranes and thereby deliver macromolecules immobilized on them into cells. A testing setup and procedure is illustrated in Fig. 2. The rotating magnetic field drives the nanotubes suspended in medium towards and into cells cultured on a substrate (step 1). Subsequently, the speared cells (still on the substrate) are transferred to culture dishes containing a nanotube-free medium, and are exposed to a persistent magnetic field from a permanent magnet (step 2). In this step, the nanotubes are driven further into the cells by the field gradient.

Figure 3 shows the SEM and confocal characterization of membrane penetration by carbon nanotubes. The MCF-7 cell is the human breast adenocarcinoma cell line, and Bal17 cell is the mouse lymphoma cell line.

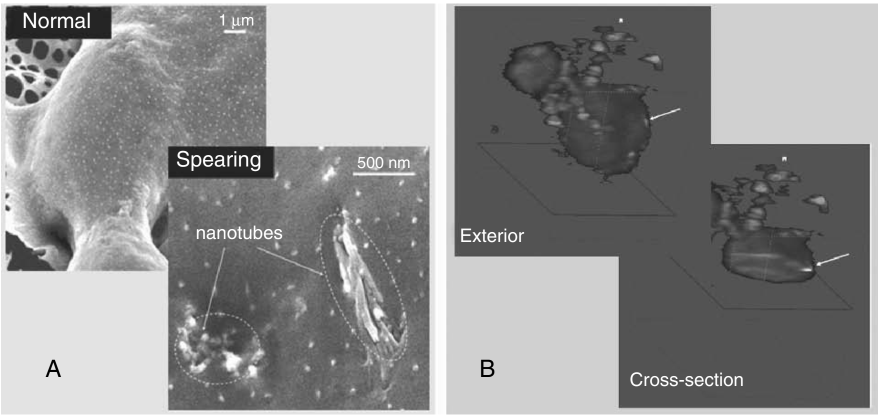

Fig. 3 Membrane penetration by carbon nanotubes in MCF-7 (**A**, Cai[9]) and Bal17 (**B**) cells

2 Nanospearing for Biomolecule Delivery

2.1 Biomolecule Immobilization

2.1.1 CNT Functionalization

To prepare CNTs for nanospearing, carboxyl group functionalization is carried out by a well-recognized process.[11,12] Of special concern is how to maintain the integrity of the nanotube structures, especially the Ni particle, during the chemical process. The normal acidic treatment can break the carbon sheet on the tip and completely remove the Ni particle. We employed a milder treatment with 0.5 M HNO_3 for 48 h, followed by sonication of the chip in ethyl alcohol to bring the nanotubes into suspension. The volume of the functionalized CNT suspension was adjusted to get the CNT concentration to 2 pM based on O.D.296. (~1.23). According to the SEM image, the CNT site density on the chip is around 5×10^9. Equivalently, a 2 pM CNT suspension can be made by dispersing a 0.3 cm^2 CNT chip in 1 ml ethyl alcohol.

2.1.2 Biomolecule Immobilization and Characterization

We integrated the idea of a layer-by-layer technique into our non-covalent immobilization strategy. Biocompatible polyelectrolytes, such as polylysine (PLL), are covalently linked to CNTs by amide linkages first. The reaction takes overnight and the product is purified and rinsed through in at least four sonication and centrifugation cycles. The thus-yielded CNT–PLL complex will exert positive charges. By electrostatic attraction, nucleic acids can be absorbed onto the PLL–CNTs and then condensed into compact structures based on the same mechanisms as described elsewhere.[13]

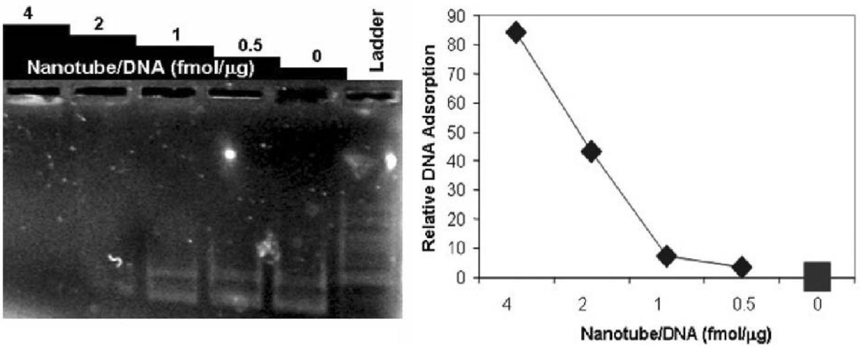

Fig. 4 Agar gel electrophoresis and UV-VIS spectrometry for characterizing the immobilization

A semi-quantitative assay of nucleic acid immobilization can be carried out by the combination of agarose gel electrophoresis and UV-VIS spectrometry of the reaction supernatant. As shown in Fig. 4, both methods revealed a consistent relationship between DNA adsorption and the ratio of PLL-CNTs to DNA. The 4 fmol PLL-CNTs are able to absorb more than 90% of 1 µg, or equivalently, 1 pmol, pBluescript (pBT) plasmid. Each nanotube can condense 250 plasmids and is equivalent to 30,000 double-stranded 25-mer oligo nucleotides. This provides a practical approach to efficiently immobilize molecules, especially large plasmids, to facilitate transfection with CNTs. Since the condensed plasmid DNA can resist disruptive sonication and DNase I catalyzed hydrolysis,[14,15] we assume that siRNA immobilized by this technique will remain stable during the transfection procedure and yield a better genetic knock down.

Due to the non-covalent facet of the immobilization, there is no chemical reaction that the biomolecule will be exposed to during the process. At large, this will allow for the preservation of the activity of the molecules. Also, once delivered into the cell, the DNA–PLL–CNT complex will dissociate upon a change in chemical environment such as in pH-value, therefore the DNA molecules can be released to perform their biological functions.

2.2 *Nanospearing-Mediated Transfection*

As mentioned above, we modified the spearing protocol to a one-step process some time ago. The cells, about 1×10^6, were dispersed on PLL-coated cover slips of 18 mm in diameter. After letting them settle for 1 h, the cells were transferred for spearing by putting the coverslips into Petri dishes with the serum-free media. The DNA–PLL–CNT complex was added to the culture dishes at a certain dilution level. The cells were speared by positioning the culture dishes on Nd-Fe-B permanent

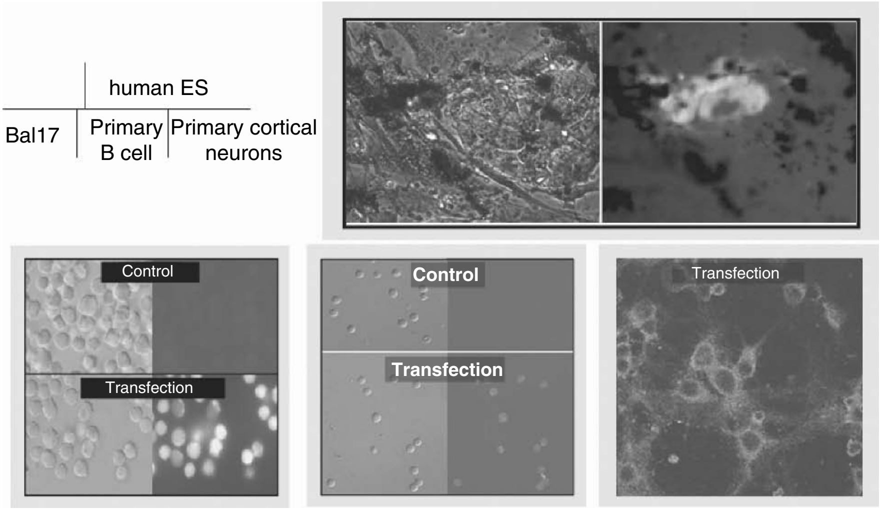

Fig. 5 Nanospearing transfection in difficult-to-transfect cells. Bal17 cell, primary B cell, and primary cortical neurons (Data are from Cai[9])

magnets for 15 min. Our data show that Oligo-FITC can dissociate from the complex and be released to cytoplasm after brief incubation, usually 20 min to 1 h, at 37 °C.

Difficult-to-transfect cells, including Bal17, mouse splenic *ex vivo* B cells, and primary cortical neurons, were transfected by nanospearing as shown in Fig. 5. Primary B cells were purified from Balb/c mice and cultured as reported.[16] The cortical neurons were separated from embryonic C57/BL6 mice. Current methods for the introduction of macromolecules into primary B cells, such as transfection and retroviral-mediated transduction, require prior stimulation of B cells with lipopolysaccharide (LPS). In both methods, the transduction efficiency is low (~less than 15% of cells) and requires B cells to be engaged in the cell cycle prior transfection/transduction.[17]

Our results indicate that nanospearing serves as a non-viral transfection technique that can match the transfection efficiency of viral infection.

3 Biocompatibility of Nanospearing to Humoral Immunity in vitro

The influence of CNTs on human and animal health has been studied in various experimental models with respect to nanotube physical structure characters, chemical modifications, and catalytic impurities, etc. Pulmonary toxicity was demonstrated by intratracheal or intrapharyngeal administration.[18,19] Oxidative stress was revealed to be underlying their toxicity in vivo[20,21] and in vitro.[22,23] It has also been found that the cytotoxicity of SWNTs and MWNTs can be reverted by surface chemical modifications.[24–26]

The disturbance of the immune system by CNTs is an important issue with regard to any of its in vivo applications. Previously, MWCNTs were found to be capable of releasing the proinflammatory cytokine interleukin 8 in epithelial keratinocytes.[27] Macrophages contacted with CNTs showed characteristic features of necrosis and degeneration.[28] In human T lymphocytes and the Jurkat cell line, oxidized nanotubes did not induce noticeable toxicity in terms of cell viability, nor did they (at a certain concentration) induce T-cell antigen receptor activation according to anti-phosphotyrosine immunoblotting.[29] This study represents initial points of interest investigated so far to clarify the compatibility of the chemically treated CNTs to the acquired immunity.

We used primary splenic B lymphocytes as a model to study the humoral component of the acquired immunity, to investigate the compatibility of the PECVD nanotubes under nanospearing conditions. We studied the influence on cell viability, cell growth, and intracellular signal pathways by means of flow cytometry and biochemical assay.

3.1 Cell Viability

Bal17 cells (the B lymphocyte cell line) and primary B lymphocytes were stained with propidium iodide after nanospearing and monitored by flow cytometry. Bal17 cell viability was maintained at 90% over the whole time span in both speared and unspeared cells without obvious differences (data not shown). Primary B lymphocytes usually only remain viable in culture for 72 h. Any unfavorable treatment can lead to a dramatic increase in apoptosis and necrosis. According to Fig. 6, the spearing did not introduce any obvious disturbances in the viability time course of

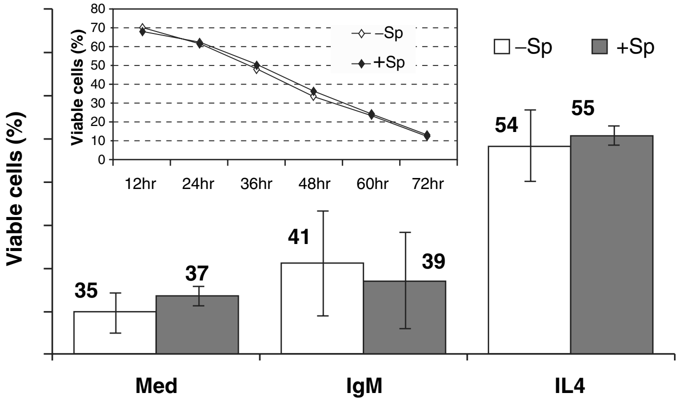

Fig. 6 Cell viability corresponding to the nanospearing

resting B cells cultured in medium (Med) over 72 h, nor did it exert influence on cells treated with $F(ab')_2$ fragments of anti-IgM (IgM) or cytokine interleukin 4 (IL4) treatment at 48 h. This suggests that the spearing process as well as the nanotube itself used for the spearing are not destructive or toxic to the resting B lymphocytes. The chemical modification of the nanotubes could be one of the reasons. Also, the nanoscale dimension of the nanotubes may be beneficial in our efforts to make the spearing treatment non-fatal to cells even though mechanical penetration is, of course, cell-invasive. According to previous studies, PLL and Ni^{2+} demonstrate toxic effects in cells.[13,30] However, the carbon encapsulation of Ni particles may prevent the dissolving of Ni in cells. The PLLs attached to CNTs may not be as toxic to cells as their freely dispersed form.

3.2 *Cell Cycle*

Bal17 was used to investigate the cell cycle upon nanospearing. As shown in Fig. 7, the nanotube spearing did not change the distribution of cells in G_0/G_1, S, G_2 + M phases of the cell cycle based on the comparison to control Bal17 cells as determined by propidium iodide staining of nuclei.[31] The percentages of cells in G0/G1, S, G2/M for control cells were 44.8, 47.5, and 7.7, respectively, whereas the percentages of speared cells in G0/G1, S, G2/M were 42.6, 49.7, and 7.7, respectively.

3.3 *Cell Growth and Activation*

The lymphocytes in the immune system are intrinsically responsive to antigen stimulations. The B cell activation is hallmarked by the cling growth and the expression of activation marker proteins, such as CD69. We wonder if the carbon

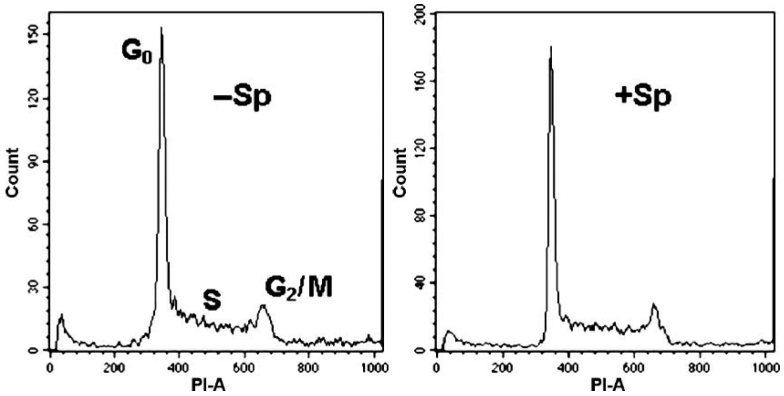

Fig. 7 Cell cycle corresponding to the nanospearing (Cai[9])

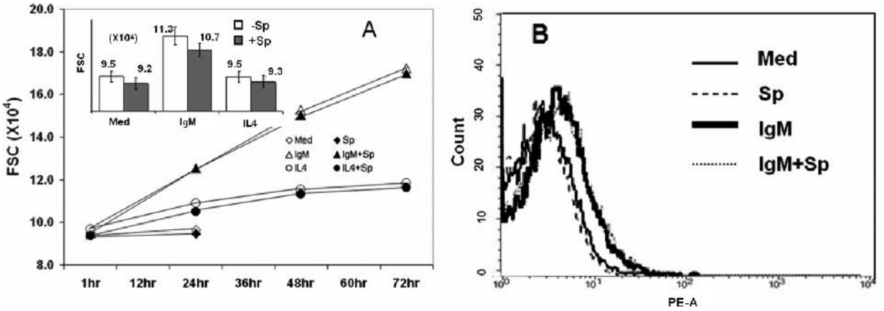

Fig. 8 Cell growth and activation corresponding to the nanospearing

nanotubes – as a non-protein antigen – can trigger or interfere with the activation cascade in B cells. As shown in Fig. 8A, no considerable differences were observed between FSC of primary B lymphocytes with and without spearing in 72 h. Immunofluorescence staining of CD69, the early activation marker, followed by flow cytometry assay did not reveal remarkable changes by the spearing either (see Fig. 8B). This suggests that the B cells are not activated upon contact or invasion of carbon nanotubes, judging from cell growth and surface marker expression. When anti-IgM was used to engage BCR, we did not observe a different responsiveness of B cells with and without the spearing treatment, respectively, in terms of FSC and CD69 signals.

3.4 *Intracellular Signal*

The early events of BCR signaling include the recruitment of kinases and an increased phosphorylation of many key signaling proteins.

MEK1/2 and Akt are protein kinases that are known to participate in intracellular signal transduction downstream of BCR engagement. By comparing both resting and stimulated cells that had been subjected to nanospearing, we could assess the nanospearing interference with these signaling pathways. As shown in Fig. 9, nanospearing did not trigger additional kinase phosphorylation in resting cells or alter the levels in artificially activated cells. In cells stimulated after nanospearing there was the same level of phospho-Akt and phospho-MEK1/2 as in the stimulated cells that had not undergone nanospearing. Thereby, the western blots did not show that nanospears may induce or impair cell signaling through resting or IgM-stimulated cells respectively.

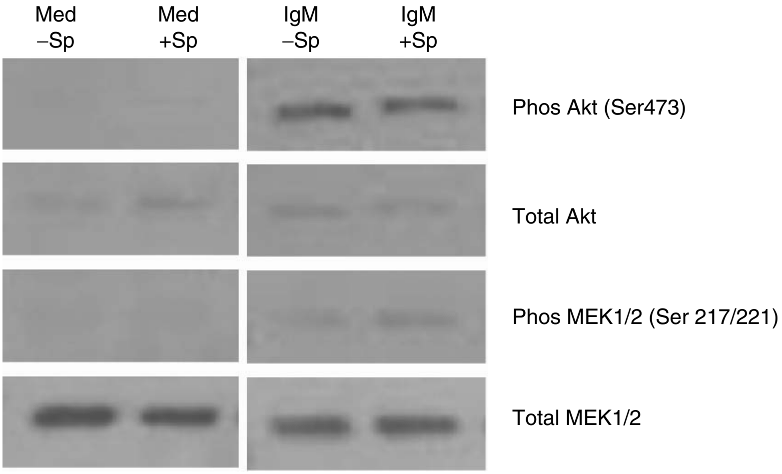

Fig. 9 Protein kinases corresponding to the nanospearing

4 Conclusion

The nanotube spearing technique exhibits an unprecedented transfection efficiency through its unique delivery mechanism. The success of the implementation relies on the incorporation of magnetically responsive CNTs into the transfection complex. It demonstrates the impressive benefits of nanomaterials for biomedical applications. Our data demonstrate that the process of nanospearing as well as the nanospears themselves do not affect resting or activated B cells in terms of viability, cell growth, protein expression, and kinase phosphorylation. Therefore, it is demonstrated that biocompatibility of nanomaterials can be accomplished by proper chemical modification and careful handling of the interaction between nanomaterials and biological samples.

References

1. D. Pantarotto, J. P. Briand, M. Prato, and A. Bianco, Translocation of bioactive peptides across cell membranes by carbon nanotubes, *Chem. Comm.* 1, 16–17 (2004).
2. N. W. S. Kam, T. C. Jessop, P. A. Wender, and H. Dai, Nanotube molecular transporters: internalization of carbon nanotube-protein conjugates into mammalian cells, *J. Am.Chem. Soc.* 126, 6850–6851 (2004).
3. H. Hu, Y. Ni, V. Montana, R. C. Haddon, and V. Parpura, Chemically functionalized carbon nanotubes as substrates for neuronal growth, *Nano Lett.* 4, 507–511 (2004).
4. T. E. McKnight, A.V. Melechko, G. D. Griffin, M. A. Guillorn, V. I. Merkulov, F. Serna, D. K. Hensley, M.J. Doktycz, D. H. Lowndes, and M. L. Simpson, Intracellular integration of synthetic nanostructures with viable cells for controlled biochemical manipulation, *Nanotechnology* 14 (5), 551–556 (2003).

5. T. M. Klein, R. Arentzen, P. A. Lewis, and S. Fitzpatrick-McElligott, Transformation of microbes, plants and animals by particle bombardment, *Biotechnology* 10, 286–291 (1992).
6. J. D. Yantzi and J. T. W. Yeow. Carbon nanotubes enhanced pulsed electric field electroporation for biomedical applications, *Proceedings of the IEEE International Conference of Mechatronic & Automation*, Niagara Falls, Canada, July (2005).
7. J. A. Rojas-Chapana, J. Troszczynska, I. Firkowska, C. Morsczeck, and M. Giersig, Multi-walled carbon nanotubes for plasmid delivery into *Escherichia coli* cells, *Lab on a Chip* 5, 536–539 (2005).
8. Z. F. Ren, Z. P. Huang, J. W. Xu, J. H. Wang, P. Bush, M. P. Siegal, and P. N. Provencio, Synthesis of large arrays of well-aligned carbon nanotubes on glass, *Science* 282, 1105–1107 (1998).
9. D. Cai, J. Mataraza, Z.-H. Qin, Z. Huang, J. Huang, T. C. Chiles, D. Carnahan, K. Kempa, and Z. Ren, Highly efficient molecular delivery into mammalian cells using carbon nanotube spearing, *Nat. Methods* 6, 449–454 (2005).
10. J. G. Wen, Z. P. Huang, D. Z. Wang, J. H. Chen, S. X. Yang, Z. F. Ren, J. H. Wang, L. E. Calvet, J. Chen, J. F. Klemic, and M. A. Reed, Growth and characterization of aligned carbon nanotubes from patterned nickel nanodots and uniform thin films, *J. Mater. Res.* 16, 3246–3253 (2001).
11. K. A. Williams, P. T. M. Veenhuizen, B. G. de la Torre, R. Eritjia, and C. Dekker, Nanotechnology: Carbon nanotubes with DNA Recognition, *Nature* 420, 761 (2002).
12. M. Hazani, R. Naaman, F. Hennrich, and M. M. Kappes, Confocal fluorescence imaging of DNA-functionalized carbon nanotubes, *Nano Lett.* 3, 153–155 (2003).
13. W. Zauner, M. Ogris, and E. Wagner, Polylysine-based transfection systems utilizing receptor-mediated delivery, *Adv. Drug Delivery Rev.* 30, 97–113 (1998).
14. K. Kogure, R. Moriguchi, K. Sasaki, M. Ueno, S. Futaki, and H. Harashima, Development of a non-viral multifunctional envelope-type nano device by a novel lipid film hydration method, *J. Controlled Release* 98, 317–323 (2004).
15. H. G. Abdelhady, S. Allen, M. C. Davies, C. J. Roberts, S. J. B. Tendle, and P. M. Williams, Direct real-time molecular scale visualisation of the degradation of condensed DNA complexes exposed to DNase I, *Nucleic Acids Res.* 31, 4001–4005 (2003).
16. S. F. Amato, K. Nakajima, T. Hirano, and T. C. Chiles, Transcriptional regulation of the junB promoter in mature B lymphocytes. Activation through a cyclic adenosine 3′,5′-monophosphate-like binding site, *J. Immunol.* 157, 146–155 (1996).
17. H. M. Wilcox and L. J. Berg, Itk phosphorylation sites are required for functional activity in primary T cells, *J. Biol. Chem.* 278(39), 37112–37121 (2003).
18. C. W. Lam, J. T. James, R. McCluskey, S. Arepalli, and R. L. Hunter, A review of carbon nanotube toxicity and assessment of potential occupational and environmental health risks, *Crit Rev. Toxicol.* 36(3), 189–217 (2006).
19. J. Muller, F. Huaux, N. Moreau, P. Misson, J. F. Heilier, M. Delos, M. Arras, A. Fonseca, J. B. Nagy, and D. Lison, Respiratory toxicity of multi-wall carbon nanotubes, *Toxicol. Appl. Pharmacol.* 207(3), 221–231 (2005).
20. K. Donaldson, R. Aitken, L. Tran, V. Stone, R. Duffin, G. Forrest, and A. Alexander, Carbon nanotubes: A review of their properties in relation to pulmonary toxicology and workplace safety, *Toxicol. Sci* 92(1), 5–22 (2006).
21. M. Bottini, S. Bruckner, K. Nika, N. Bottini, S. Bellucci, A. Magrini, A. Bergamaschi, and T. Mustelin, Multi-walled carbon nanotubes induce T lymphocyte apoptosis, *Toxicol. Lett.* 160(2), 121–126 (2006).
22. A. A. Shvedova, E. R. Kisin, R. Mercer, A. R. Murray, V. J. Johnson, A. I. Potapovich, Y. Y. Tyurina, O. Gorelik, S. Arepalli, D. Schwegler-Berry, A. F. Hubbs, J. Antonini, D. E. Evans, B. K. Ku, D. Ramsey, A. Maynard, V.E. Kagan, V. Castranova, and P. Baron, Unusual inflammatory and fibrogenic pulmonary responses to single-walled carbon nanotubes in mice, *Am. J. Physiol. Lung Cell Mol. Physiol.* 289(5), L698–L708 (2005).
23. S. K. Manna, S. Sarkar, J. Barr, K. Wise, E. V. Barrera, O. Jejelowo, A. C. Rice-Ficht, and G. T. Ramesh, Single-walled carbon nanotube induces oxidative stress and activates nuclear transcription factor-kappaB in human keratinocytes, *Nano Lett.* 5(9), 1676–1684 (2005).

24. C. M. Sayes, F. Liang, J. L. Hudson, J. Mendez, W. Guo, J. M. Beach, V. C. Moore, C. D. Doyle, J. L. West, W. E. Billups, K. D. Ausman, and V. L. Colvin, Functionalization density dependence of single-walled carbon nanotubes cytotoxicity in vitro, *Toxicol. Lett.* 161(2), 135–142 (2006).
25. D. Pantarotto, R. Singh, D. McCarthy, M. Erhardt, J. P. Briand, M. Prato, K. Kostarelos, and A. Bianco, Functionalized carbon nanotubes for plasmid DNA gene delivery, *Angew. Chem. Int. Ed. Engl.* 43(39), 5242–5246 (2004).
26. D. Pantarotto, J. P. Briand, M. Prato, and A. Bianco, Translocation of bioactive peptides across cell membranes by carbon nanotubes, *Chem. Commun. (Camb.)* 1, 16–17 (2004).
27. R. Singh, D. Pantarotto, L. Lacerda, G. Pastorin, C. Klumpp, M. Prato, A. Bianco, and K. Kostarelos, Tissue biodistribution and blood clearance rates of intravenously administered carbon nanotube radiotracers, *Proc. Natl. Acad. Sci. U.S.A* 103(9), 3357–3362 (2006).
28. N. A. Monteiro-Riviere, R. J. Nemanich, A. O. Inman, Y. Y. Wang, and J. E. Riviere, Multi-walled carbon nanotube interactions with human epidermal keratinocytes, *Toxicol. Lett.* 155(3), 377–384 (2005).
29. G. Jia, H. Wang, L. Yan, X. Wang, R. Pei, T. Yan, Y. Zhao, and X. Guo, Cytotoxicity of carbon nanomaterials: Single-wall nanotube, multi-wall nanotube, and fullerene, *Environ. Sci. Technol. 39* (5), 1378–1383 (2005).
30. R. Y. Cheng, A. Zhao, W. G. Alvord, D. A. Powell, R. M. Bare, A. Masuda, T. Takahashi, L. M. Anderson, and K. S. Kasprzak, Gene expression dose-response changes in microarrays after exposure of human peripheral lung epithelial cells to nickel (II), *Toxic Appl. Phar.* 191, 22–39 (2003).
31. S. F. Amato, K. Nakajima, T. Hirano, and T. C. Chiles, Transcriptional regulation of the junB promoter in mature B lymphocytes, Activation through a cyclic adenosine 3′,5′-monophosphate-like binding site, *J. Immunol.* 157, 146–155 (1996).

Multifunctional Glyconanoparticles: Applications in Biology and Biomedicine

Soledad Penadés[1,*], Jesus M. de la Fuente[1], África G. Barrientos[1], Caroline Clavel[1], Olga Martínez-Ávila[1], and David Alcántara[1]

Abstract The design and preparation of complex bio-functional glyconanoparticles (GNPs) and their application as polyvalent tools to study and intervene in carbohydrate mediated biological interactions are highlighted. As examples, the preparation and study of GNPs as anti-adhesion agents in inhibition of metastasis, as potential microbicides for blocking HIV-1 infection, or as anti-cancer vaccines are also discussed. In addition, magnetic glyconanoparticles for application in cellular labelling and magnetic resonance imaging (MRI) are also reviewed.

Keywords Glyconanotechnology, multifunctional glyconanoparticles, quantum dots, magnetic glyconanoparticles, carbohydrate interactions, multivalence, glycobiology

1 Introduction

The application of nanomaterials to medicine is emerging as one of the most important areas in nanotechnology. The term nanomedicine identifies nanotools for imaging, diagnostics, therapeutics, and drug delivery among others.[1,2] Metallic nanoparticles are very promising candidates for electronic, optical, magnetic, and biomedical applications. Bio-compatibility and bio-functionality of nanoparticles are, however, essential for medical application. At present, it is straightforward to control and modify the properties of nanostructures to better suit their integration with biological systems; for example, controlling their size, modifying their surface layer for enhanced aqueous solubility, biocompatibility, or biorecognition.[3–5]

The use of gold nanoparticles in biological applications was first highlighted in the 1970s with the immunogold staining procedures.[6] Since then, the labeling of target molecules with gold nanoparticles has revolutionized the visualization of

---

[1] Laboratory of Glyconanotechnology, CIC biomaGUNE and CIBER-BBN Networking Centre on Bioengineering, Biomaterials and Nanomedicine, Paseo Miramón 182, Parque Tecnológico de San Sebastián, 20009 San Sebastián, Spain

[*] To whom correspondence should be addressed. E-mail: spenades@cicbiomagune.es

M. Giersig and G. B. Khomutov (eds.),
Nanomaterials for Application in Medicine and Biology

cellular and/or tissue components by means of electron microscopy. During the last 10 years several groups have prepared gold nanoparticles functionalized with proteins and DNA.[3,7–13] Nanoparticles covered with carbohydrates, however, have not been reported until 2001.[14] This article reviews progresses in the development of nanoparticles functionalized with biologically relevant oligosaccharides and their application in biotechnology and biomedicine.

Carbohydrates, together with nucleic acids and proteins, are very important constituent parts of living organisms. Much is already known about the structure, interactions, and function of nucleic acids and proteins. However, the role of carbohydrates in the cell is less clear. The surface of mammalian cells is covered by a dense coating of carbohydrates named glycocalyx.[15] In the glycocalyx, carbohydrates appear mainly conjugated to proteins and lipids (glycoproteins, glycolipids and proteoglycans) and it is as glycoconjugates that they develop their biological function. It is known that these complex oligosaccharides are involved in the control of many normal and pathological processes.[16–17] The extreme low affinity of carbohydrates to biological objects has to be compensated by multivalent ligands.

For this reason, we developed a new integrated approach that we have named "Glyconanotechnology strategy"[4] to study and intervene in carbohydrate-carbohydrate and carbohydrate-protein-mediated interactions. Glyconanotechnology is a strategy for tailoring sugar bio-functional gold nanoclusters (*glyconanoparticles*) in a simple and versatile way.[14,18] Glyconanoparticles (GNPs) provide a glycocalix-like surface with multivalent carbohydrate presentation and globular shape. The GNPs present a number of advantages over other previously prepared colloids, such as: (1) easy preparation and purification; (2) exceptional small core size and narrow distribution sizes; (3) control over ligand number and nanoparticle size; (4) water solubility; (5) high storage stability without flocculation; (6) singular physical properties; and (7) absence of cytotoxicity.

The manipulation of the metallic cluster to obtain luminescent *glyco*-quantum dots (semiconductors)[19] and magnetic nanoparticles for application in cellular labeling and imaging by magnetic resonance (MRI), is comprised within the potential of this novel technology. Furthermore, the introduction of additional ligands can be used to guide the assembly of the nanoclusters creating a wealth of different nanostructures.[20]

2 Preparation of Gold Glyconanoparticles

Our approach to biofunctional nanoparticles began in 1999 with the preparation of gold nanoclusters functionalized with sugars. For the preparation of these nanoclusters, we developed a single step reaction, inspired by a procedure of Brust and colleagues[21] where a gold salt is reduced in the presence of an excess of thiol-functionalized neoglycoconjugate to give the corresponding glyconanocluster.[18] This methodology provides nanoclusters of so small dimensions that they adopt the properties of the organic molecules connected to them. The thus-prepared glyconanoparticles are stable,

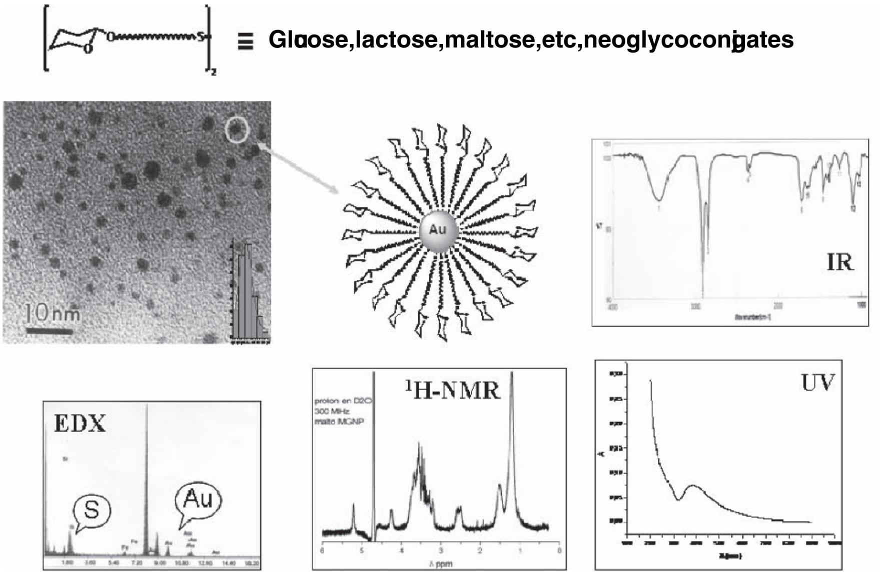

Fig. 1 Neoglycoconjugates, glyconanoparticles, and their characterization

water soluble and can be manipulated as a water-soluble biological macromolecule. The glyconanoparticles are purified by dialysis or centrifugal filtering and they are fully characterized by transmission electron microscopy (TEM), energy dispersion x-ray (EDX), and ^{1}H-NMR, UV, IR, induced coupling plasma (ICP) spectroscopies. Elemental analysis and mass spectrometry are also used to characterize the nanoparticles (Fig. 1). The GNPs are monodispersed and the corresponding core size distribution histograms indicate a mean diameter of 1.8 nm for the gold core in most GNPs prepared in this way.

3 From Glyconanoparticles to “Artificial Nanocells”

Glyconanotechnology has put a methodology in our hands to prepare – in a simple way – a great variety of water-soluble biofunctional nanoclusters of globular shape and a chemically well-defined composition to intervene in in vivo cell-cell adhesion and recognition processes.

The glyconanoparticles offer a platform to introduce a broad variety of ligands in a controlled way to obtain multifunctional nanoparticles with more than one type of ligand on the surface (Fig. 2).

Glyconanoparticles (GNPs) with biologically significant carbohydrates (antigens) and with differing carbohydrate density have also been prepared to study biological processes[14,22–23] and to intervene in cell adhesion events.[24] The methodology

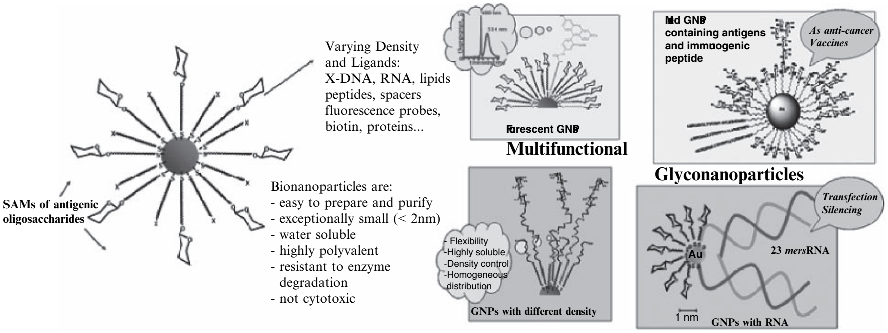

Fig. 2 The glyconanoparticle platform and some prepared multifunctional glyconanoparticles

includes the preparation of *hybrid* GNPs incorporating carbohydrates and other molecules such as fluorescent probes, biotin as well as biological molecules such as peptides, DNA and RNA, etc. For example, hybrid glyconanoparticles incorporating fluorescein have been prepared for cellular labeling.[18] Multifunctional glyconanoparticles incorporating an immunogenic peptide and different carbohydrate antigens have been prepared as potential anticancer vaccines.[25] Furthermore, GNPs functionalized with small interfering RNAs and glucose have already been prepared for transfection and silencing assays (Fig. 2).

4 Glyconanoparticles in Medicine

Glyconanoparticles constitute a good bio-mimetic model of carbohydrate presentation at the cell surface, opening new avenues in the fields of chemistry, glycobiology, and biomedicine. In spite of the short history of these new glyconanomaterials, some applications have already been reported, focused mainly on the study and evaluation of carbohydrate interactions.[26] Furthermore, the glyconanoparticle concept allows the manipulation of the metallic core to produce biofunctional nanoparticles with magnetic properties.

Three examples can illustrate the potentiality of GNPs in biotechnology and biomedicine: glyconanoparticles as anti-adhesion agents in metastasis, glyconanoparticles as microbicides against HIV infection, and magnetic glyconanoparticles as contrast agents for magnetic resonance imaging.

4.1 Glyconanoparticles as Anti-Adhesion Agents in Metastasis

One of the critical steps in metastasis is the adhesion of tumor cells to the vascular endothelium. After adhesion, tumoral cells transmigrate and create new tumor foci.

Interactions between tumor-associated antigens and epithelial cell selectins promote tumoral cell metastasis. Glycosphingolipids expressed on the tumoral and endothelial cell surfaces seem to be involved in the critical adhesion step. An interaction between the glycosphingolipids GM3, expressed in a murine melanoma cell line (B16), and Gg3 or lactosylceramide of endothelium cells has been proposed to be involved in the first adhesion step of tumoral cells to endothelium before transmigration.[27]

Therefore, inhibition of this step by glyconanoparticles that present carbohydrate antigens expressed either in the tumor or the endothelium cells might provide effective anti-adhesion therapy. Lactose glyconanoparticles were tested as a potential inhibitor of the binding of melanoma cells to the endothelium. An *ex vivo* experiment was designed for the evaluation of the anti-metastasis potential of the glyconanoparticles. Mice were injected with melanoma cells pre-incubated with lactose gold glyconanoparticles and, after three weeks, the animals were sacrificed and both lungs examined under the microscope for analysis of tumor foci. A 70% tumor inhibition was reported as compared with the group inoculated only with melanoma cells.[24]

4.2 Glyconanoparticles as Microbicides Against HIV Infection

Within the framework of a European Integrated Project[28] we are presently investigating the potential of gold glyconanoparticles to modulate the binding and dissemination of HIV by dendritic cells. A major mechanism of HIV infection implies the interaction of the virus envelop glycoprotein gp120 with DC-SIGN (dendritic cell-specific ICAM3 grabbing non-integrin) receptor expressed in dendritic cells.[29] DC-SIGN is a type II trans-membrane protein with a COOH terminal Carbohydrate Recognition Domain (CRD) that belongs to the C-type Ca^{2+} dependent lectin family. DC-SIGN selectively recognizes endogenous high-mannose-type oligosaccharide structures of the HIV envelop glycoprotein gp120. The majority of oligosaccharides on gp120 are high-mannose structures (Fig. 3). Furthermore, interaction of DC-SIGN with HIV can be inhibited by Ca^{2+} chelators or mannan (a natural mannose polysaccharide).[30]

We reasoned that GNPs presenting the mannose structures recognized by DC-SIGN receptor could interact with the latter and therefore inhibit the virus adhesion to dendritic cells (Fig. 4).

We have designed and prepared a series of gold nanoparticles bearing mannose mono-, di- and trisaccharides based on the hybrid type or high-mannose-type oligosaccharides (Fig. 4). The activity of these GNPs was investigated by means of SPR and cell-based model experiments. We evaluated the effect on the inhibition of HIV binding to DC-SIGN expressing cells and HIV dissemination from these cells to T cell populations.

Biosensor experiments allowed us to perform inhibition studies of DC-SIGN interaction with gp120. The activity of GNPs compared to the corresponding monovalent oligosaccharide structures has been evaluated. A highly significant improvement in inhibiting DC-SIGN/gp120 interaction was detected for nanoparticles bearing the Manα1-2Man disaccharide. Inhibition was 10,000-fold more effective

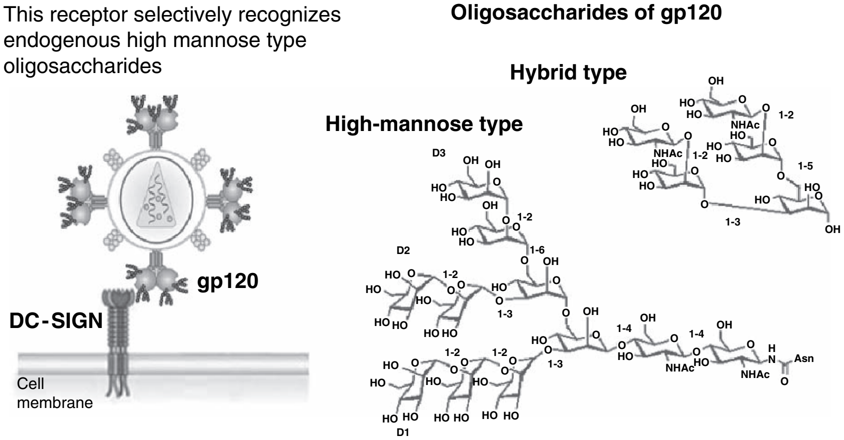

Fig. 3 The interaction between the HIV envelop glycoprotein gp120 and the DC-SIGN receptor and the oligosaccharidic structures recognized by DC-SIGN

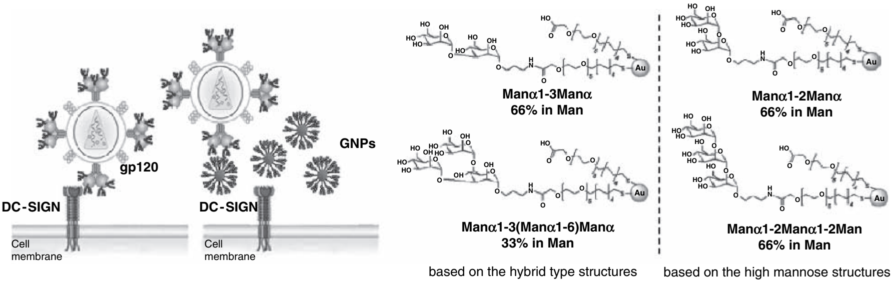

Fig. 4 A strategy to block gp120/DC-SIGN interaction by GNPs and some prepared glyconanoparticles presenting mannose oligosaccharides

(100% inhibition at 10 nm) than with the corresponding monovalent disaccharide Manα1-2Man (100% inhibition at 500 μM), showing clearly the multivalence effect of the GNPs.

This result was confirmed in the cellular assays. First of all, inhibition of gp120-DC-SIGN binding was evaluated in a model using DC-SIGN-transfected Raji B cells. GNPs efficient at blocking the binding of R5 HIV-1 BaL to the Raji DC-SIGN + cells compared to the untreated control cells would result in reducing the risk of infection being disseminated by dendritic cells. The result indicates that GNPs bearing the Manα1-2Man disaccharide inhibited binding of HIV-1 to DC-SIGN by 85%, while free mannan inhibited binding only by 60%. Inhibition of DC-SIGN receptor binding due to GNP pre-exposure was further investigated to evaluate whether it would also inhibit DC-SIGN mediated *trans*-infection of PM-1 T cells. Manα1-2Man-GNPs were able to inhibit *trans*-infection of PM-1 T cells by HIV-1 by 80%, compared to free mannan, which inhibited binding by 50%. A similar trend was demonstrated using immature dendritic cells instead of Raji B cells (as a model closer to the in vivo state). The same GNPs inhibit infection by 66%, slightly better that the free mannan which inhibited infection by 40%. These results are very encouraging and we are further investigating the GNPs' effect on uptake and *trans*-infection by dendritic cells.

4.3 Magnetic Glyconanoparticles as Contrast Agents for Magnetic Resonance Imaging

Magnetic nanoparticles offer exciting new opportunities including the improvement of the quality of magnetic resonance imaging (MRI), hyperthermia treatment for malignant cells, site-specific drug delivery, and also the manipulation of cell membranes, which has been of particular interest to researchers of late.[13,31–32] The biological applications of these nanomaterials require the nanoparticles to have high magnetization values, a size smaller than 20nm, narrow particle size distribution, and a special surface coating for both avoiding toxicity and allowing the coupling of biomolecules.[33] Bio-conjugated magnetic nanoparticles to peptides, proteins and antibodies have been developed and tested as biological markers or in hyperthermia treatments. However, so far there has not been one example of magnetic glyconanoparticles.

Following the same procedure as for the gold glyconanoparticles, we prepared gold-iron nanoparticles functionalized with glucose, maltose, and lactose by adding an iron salt to the aqueous $HAuCl_4$ solution.[34] The nanoparticles produced in this way are water soluble, stable, and exceptionally small. The properties of these nanoparticles are particularly interesting because of their quantum size. They show a complex magnetic behaviour with both paramagnetic and ferromagnetic components. This anomalous behaviour may be attributed to the gold atoms that predominate in the metallic cluster with an atomic Au/Fe ratio from 50:1 to 5:1.[35]

Our main interest is focussed on the development of magnetic nanoparticles as contrast agents in MRI. For this application, biocompatibility is an important issue. We have studied the cytotoxicity of these nanoparticles on human dermal fibroblasts in vitro. Glucose and lactose GNPs are not cytotoxic while maltose-GNPs presented an 80% cytotoxicity.

Glucose-Au/Fe GNPs show relaxation times T1 and T2 in buffer significantly smaller than those of Resovist. However, the difference in T2 decreases significantly in plasma. This result encourages us to test the glucose GNPs in vivo to image an experimental C6 glioma in mice.

The preliminary T2 weight images obtained with the help of glucose GNPs clearly indicate an accumulation of GNPs in the tumoral area as well as in the cerebrospinal fluid.

5 Conclusion

The development of this glyconanotechnology has opened new avenues in the field of glycobiology as well as in biotechnology and biomedicine. Glyconanoparticles have proved to be excellent tools to mimic carbohydrate presentation at the cell surfaces. The results described here confirm glyconanoparticles as a versatile platform for many applications in nanomedicine.

Acknowledgements This work was supported by the Ministry of Education and Science (grants CTQ2005-07993 and NAN2004-09125) and the European Union (IP-EMPRO and Marie Curie project GLYCOGOLD). We thank Dr. S. Cerdán (IIB-CSIC) for his help with the MRI experiments and Dr. C. Kelly (King's College, London) and Dr. R. Shattock (St. George's Hospital Medical School, London) for the biosensor and cellular experiments. Without their help it would not have been possible to develop this project.

References

1. US NIH Nanomedicine road map.
2. European Science Foundation (ESF) nanomedicina report www.esf.org/publication/214/Nanomedicine.pdf.
3. E. Katz and I. Willner, Integrated nanoparticle-biomolecule hybrid systems: Synthesis, properties, and applications, *Angew. Chem. Int. Ed.* 33, 6042–6108 (2004).
4. J. M. de la Fuente and S. Penadés, Understanding carbohydrate-carbohydrate interactions by means of glyconanotechnology, *Glycoconj. J.* 21(3/4), 149–163 (2004).
5. J. M. Perez, L. Josephson, and R. Weissleder, Use of magnetic nanoparticles as nanosensors to probe for molecular interactions, *ChemBioChem* 5(3), 261–264 (2004).
6. J. M. Polak and I. M. Varndell, *Immunolabeling for electron microscopy* (Elsevier Science Publishers, Amsterdam, 1984).
7. C. M. Niemeyer, Nanoparticles, proteins, and nucleic acids: biotechnology meets materials science, *Angew. Chem. Int. Ed.* 40(22), 4128–4158 (2001).
8. C. B. Murray, C. R. Kagan, and M. G. Bawendi, Synthesis and characterization of monodisperse nanocrystals and close-packed nanocrystal assemblies, *Annu. Rev. Mater. Sci.* 30, 545–610 (2000).
9. M.-C. Daniel and D. Astruc, Gold nanoparticles: Assembly, supramolecular chemistry, quantum-size-related properties, and applications towards biology, catalysis and nanotechnology, *Chem. Rev.* 104(1), 293–346 (2004).
10. U. Drechsler, B. Erdogan, and V. M. Rotello, Nanoparticles: Scaffolds for molecular recognition, *Chem.-Eur. J.* 10(22), 5570–5579 (2004).
11. A. Verma and V. M. Rotello, Surface recognition of biomacromolecules using nanoparticle receptors, *Chem. Comm.* 3, 303–312 (2005).
12. J. Wang, Nanomaterial-based amplified transduction of biomolecular interactions, *Small* 1(11), 1036–1043 (2005).
13. D. L. Huber, Synthesis, properties, and applications of iron nanoparticles, *Small* 1(5), 482–501 (2005).
14. J. M. de la Fuente, A. G. Barrientos, T. C. Rojas, J. Rojo, J. Cañada, A. Fernández, and S. Penadés, Gold glyconanoparticles as water-soluble polyvalent models to study carbohydrate interactions, *Angew. Chem. Int. Ed.* 40(12), 2257–2261 (2001).
15. A. Frey, K. T. Giannasca, R. Weltzin, P. J. Giannasca, H. Reggio, W. I. Lencer, and M. R. Neutra, Role of glycocalyx in regulating access of microparticles to apical plasma membranes

of intestine epithelial cells: Implications for microbial attachment and oral vaccine targeting, *J. Exp. Med*. 184(3), 1045–1059 (1996).

16. A. Varki, Biological roles of oligosaccharides: All of the theories are correct, *Glycobiology* 3(2), 97–130 (1993).
17. R. A. Dwek, Glycobiology: Toward understanding the function of sugars, *Chem. Rev*. 96(2), 683–720 (1996).
18. A. G. Barrientos, J. M de la Fuente, T. C. Rojas, A. Fernández, and S. Penadés, Gold glyconanoparticles: synthetic polyvalent ligands mimicking glycocalyx-like surfaces as tools for glycobiological studies, *Chem.-Eur. J*. 9(9), 1909–1921 (2003).
19. J. M. de la Fuente and S. Penadés, Glyco-quantum dots: a new luminescent system with multivalent carbohydrate display, *Tetrahedron: Asymmetry* 16(2), 387–391 (2005).
20. T. C. Rojas, J. M. de la Fuente, A. G. Barrientos, S. Penadés, L. Ponsonnet, and A. Fernandez, Gold glyconanoparticles as building blocks for nanomaterials design, *Adv. Mater*. 14(8), 585–588 (2002).
21. M. Brust, J. Fink, D. Bethell, D. J. Schiffrin, and C. J. Kiely, Synthesis and reactions of functionalised gold nanoparticles, *J. Chem. Soc. Chem. Commun*. (1995) 1655–1656.
22. M. J. Hernáiz, J. M. de la Fuente, A. G. Barrientos, and S. Penadés, A model system mimicking glycosphingolipid clusters to quantify carbohydrate self-interactions by surface plasmon resonance, *Angew. Chem. Int. Ed*. 41(9), 1554–1557 (2002).
23. J. M. de la Fuente, P. Eaton, A.G. Barrientos, M. Menedez, and S. Penadés, Thermodynamic evidence for Ca^{2+} -mediated self-aggregation of Lewis X gold glyconanoparticles. A model for cell adhesion via carbohydrate-carbohydrate interaction, *J. Am. Chem. Soc*. 127(17), 6192–6197 (2005).
24. J. Rojo, V. Diaz, J. M. de la Fuente, I. Segura, A. G. Barrientos, H. H. Riese, A. Bernad, and S. Penadés, Gold glyconanoparticles as new tools in antiadhesive therapy, *ChemBioChem* 5(3), 291–297 (2004).
25. R. Ojeda, J. L. de Paz, A. G. Barrientos, M. Martín-Lomas, and S. Penadés, Preparation of multifunctional glyconanoparticles as a platform for potential carbohydrate-based anticancer vaccines, *Carbohyd. Res*. 342, 448–459 (2007).
26. For a recent review see: J. M. de la Fuente and S. Penadés, Glyconanoparticles: types, synthesis and application in glycoscience, biomedicine and material science, *Biochim. Biophys. Acta*, 1760(4), 636–651 (2006).
27. S. Hakomori, Aberrant glycosylation in tumors and tumor-associated carbohydrate antigens, *Adv. Cancer Res*. 52, 257–331 (1989).
28. European Microbicides Project (EMPRO); http://www.empro.org.uk/home.php4
29. T. B. H. Geijtenbeek, D. S. Kwon, R. Torensma, S. J. van Vliet, G. C. F. van Duijnhoven, J. Middel, I. L. Cornelissen, H. S. Nottet, V. N. Kewal-Ramani, D. R. Littman, C. G. Figdor, and Y. van Kooyk, DC-SIGN, a dendritic cell-specific HIV-1-binding protein that enhances trans-infection of T cells, *Cell* 100, 587–597 (2000).
30. Y. Guo, H. Feinberg, E. Conroy, D. A. Mitchell, R. Alvarez, O. Blixt, M. E. Taylor, W. I. Weis, and K. Drickamer, Structural basis for distinct ligand-binding and targeting properties of the receptors DC-SIGN and DC-SIGNR, *Nat. Struct. Mol. Biol*. 11(7), 591–598 (2004).
31. C. C. Berry and A. S. G. Curtis, Functionalisation of magnetic nanoparticles for applications in biomedicine, *J. Phys. D: Appl. Phys*. 36, R198–206 (2003).
32. Q. A. Pankhurst, J. Connolly, S. K. Jones, and J. Dobson, Applications of magnetic nanoparticles in biomedicine, *J. Phys. D: Appl. Phys*. 36, R167–181 (2003).
33. P. Tartaj, M. P. Morales, S. Veintemillas-Verdaguer, T. Gonzalez-Carreño, and C. J. Serna, The preparation of magnetic nanoparticles for applications in biomedicine, *J. Phys, D: Appl. Phys*. 36, R182–R197 (2003).
34. J. M. de la Fuente, D. Alcántara, P. Eaton, P. Crespo, T. C. Rojas, A. Fernández, A. Hernando, and S. Penadés, Gold and gold-iron oxide magnetic glyconanoparticles: Synthesis, characterization and magnetic properties, *J. Phys. Chem. B*, 110(26), 13021–13028 (2006).
35. P. Crespo, M. A. García, E. Fernández, M. Multigner, D. Alcántara, J. M. de la Fuente, S. Penadés, and A. Hernando, Fe impurities weaken the ferromagnetic behavior in Au glyconanoparticles, *Phys. Rev. Lett*. 97, 177203 (2006).

This page intentionally blank

Plasmonics of Gold Nanorods. Considerations for Biosensing

Luis M. Liz-Marzán[1,*], Jorge Pérez-Juste[1], and Isabel Pastoriza-Santos[1]

Abstract In this chapter, we explore the sensitivity of gold nanorods toward changes in the dielectric constant of the surrounding medium. Experimental data for pure and silica-coated nanorods with varying shell thickness are compared to calculations based on the boundary element method (BEM). They indicate that anisotropy and sharp tips make nanoparticles more environmentally sensitive. We also find that sensitivity decreases as silica shell thickness increases, as expected from a dielectric screening effect. Even when coated with thin shells, gold nanorods are found to be excellent candidates for biosensing applications.

Keywords Metal nanoparticles, gold, biosensing, optical properties, modeling

1 Introduction

The optical properties of metal nanoparticles are dominated by surface plasmon resonances, i.e. collective oscillations of conduction electrons in phase with an external electromagnetic wave.[1] The resonance frequency can be modulated through the composition, size, shape, and electromagnetic environment of the metal particles.[2,3] Because of the enormous interest from both the scientific and technological points of view, research on such metallic nanostructures has been tremendously intense during the past couple of decades. Although initially only spherical nanoparticles were investigated, it was soon realized that anisotropy effects were much more dramatic than those derived from size and even composition. Therefore, research on metal nanorods,[4] nanowires,[5] nanocubes,[6] nanoprisms,[7,8] or even nanostars[9] has demonstrated that small variations in the morphology of the particles could strongly influence the optical response. In the case of small gold nanorods, two

---

[1] Departamento de Química Física, and Unidad Asociada CSIC- Universidade de Vigo, 36310 Vigo, Spain

[*] To whom correspondence should be addressed. E-mail: lmarzan@uvigo.es

M. Giersig and G. B. Khomutov (eds.),
Nanomaterials for Application in Medicine and Biology

plasmon resonances are possible, which are related to parallel (longitudinal plasmon band, LPB) and perpendicular (transverse plasmon band, TPB) electron oscillations, the LPB being much more sensitive to the nanorod aspect ratio (length/width) than the TPB.[10] Although the study of the optical properties of metal nanoparticles has a relatively long tradition,[11] it has recently attracted renewed interest because of their potential applications in medical diagnostics and therapy. While therapeutical uses are largely related to the release of thermal energy upon surface plasmon absorption, mainly in the NIR spectral region,[12] opportunities for biosensing-related diagnostics arise from the high sensitivity of the (localized) surface plasmon resonance condition upon small changes in the dielectric properties of the surrounding medium, so that the adsorption of (bio)molecules results in an observable shift of the plasmon resonance frequency.[13] In this case, the preferred wavelength range is the visible, so that detection devices can be simplified. Several examples of localized surface plasmon-based biorecognition have been demonstrated,[14–16] but there is a need to identify optimized shapes and sizes to provide better sensitivity.[13,17,18]

In this paper we present a preliminary study showing the potential use of gold nanorods for biosensing applications, which is based on experimental data and theoretical modeling based on the boundary element method (BEM),[19,20] which has recently been demonstrated to show very good agreement with experimental results for Au nanodecahedra.[21] In the BEM the induced electric and magnetic fields are viewed as originating from equivalent boundary sources (i.e., equivalent surface electric charges and currents), which are used to fulfill the customary boundary conditions of the electromagnetic field at the interfaces between different media. The surface integrals are then discretized by means of boundary elements, thus yielding a linear system of equations that are solved numerically. This is a rigorous approach to solve Maxwell's equations with extremely good convergence with respect to the number of boundary elements. The latter increases quadratically with the size of the particle, since only surface boundaries between different media need to be parametrized. This results in a relatively modest computational demand that allows us to directly solve the entire linear algebra problem. In the present study, the axial symmetry of the particles is utilized to reduce the computational size of the problem to one dimension (the radial contour of the particle with respect to the axis of rotation). Our calculated results for geometrical models devised on the basis of the nanoparticle morphologies observed in the TEM images show good agreement with measured optical spectra and allow us estimating the environmental sensitivity of nanorods and silica-coated nanorods, on the basis of full extinction spectra and near-field enhancement maps associated to the particle surface plasmons observed through absorption bands.

2 Experimental

The gold nanorods were prepared by the seeding growth method in aqueous CTAB solution, following the method devised by Nikoobakht and El-Sayed.[22] Several parameters can be manipulated in this method to tune the geometry of the particles (size and aspect ratio), through which the optical response can be easily manipulated. Deposition of uniform silica shells on gold nanorods was realized by a recently reported method,[23] based on a combination of the polyelectrolyte layer-by-layer technique and the hydrolysis of tetraethoxysilane in an isopropanol-water mixture. The rods were initially coated with the polyelectrolyte pair formed by polystyrene sulphonate (PSS, Mw 13,400) and polyallylamine hydrochloride (PAH, Mw 15,000) and wrapped with poly(vinylpyrrolidone) (PVP, Mw 10,000), prior to ammonia-catalyzed TEOS hydrolysis and condensation in isopropanol. The shell thickness was mainly determined through the nanorod and TEOS concentrations.

For the study of refractive index effects, the particles were immobilized on glass slides and subsequently dipped in a cuvette filled with different solvents. Optical characterization was carried out by UV-visible-NIR spectroscopy on a Cary 5000 UV-Vis-NIR spectrophotometer. Transmission electron microscopy (TEM) images were obtained with a JEOL JEM 1010 transmission electron microscope operating at an acceleration voltage of 100 kV. Scanning electron microscopy (SEM) images were obtained using a JEOL JSM-6700F FEG-SEM operating at an acceleration voltage of 15 kV for secondary-electron imaging (SEI).

3 Results and Discussion

3.1 Environmental Sensitivity of Non-Coated Nanorods

Before addressing the sensitivity toward local refractive index changes, we describe the effect of solvent refractive index on the surface plasmon resonance frequency of gold nanorods. The chemical nature of the nanorod surface (a bilayer of CTAB) makes it very complicated to exchange the solvent without compromising the stability of the colloid. For this reason, an alternative method was used, involving the deposition of well-separated nanoparticles on a glass substrate, which actually is also required for the fabrication of biosensing devices, so that the biorecognition events can be monitored. The separation between particles is necessary to ensure that interparticle interactions are negligible and the optical response from individual particles is obtained. We achieved uniform deposition by first priming the glass surface with polyelectrolytes as extensively described in the literature.[24,25] The uniform and high surface charge achieved in this way promotes a fast and uniform deposition of the gold nanorods on the surface, as can be seen in the SEM image shown in Fig. 1. The experimental UV-vis-NIR spectra for nanorods with an average aspect ratio of 3.08, deposited on glass slides an immersed in air and solvents with varying refractive indices, are also shown in Fig. 1, showing a progressive red-shift of the LPB as the solvent refractive index increases (almost 200 nm shift for a refractive index change from 1.0 up to 1.62), which agrees with previous reports.[4]

In the same figure, calculated spectra (averaged for all incident angles) are shown for rods with a similar aspect ratio, revealing a similar trend with a large LPB shift with increasing medium refractive index. It is interesting to note that for

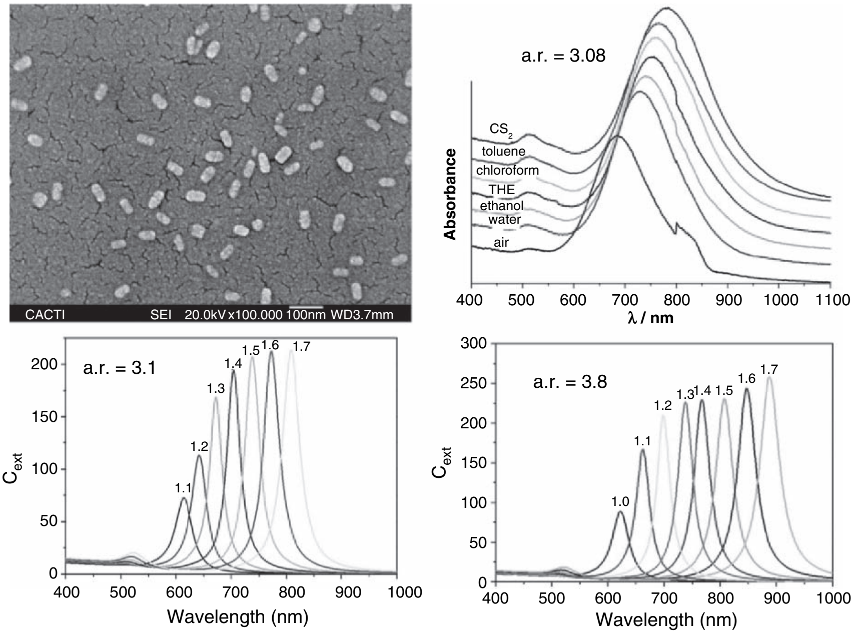

Fig. 1 Top: SEM image of gold nanorods (a.r. 3.08) on a glass slide, and the corresponding UV-vis-NIR spectra in different solvents. Bottom: BEM simulations of the spectra for rods with two different aspect ratios, immersed in dielectric media with varying refractive index

longer rods (larger aspect ratio), a much larger shift (ca. 300 nm) is observed for the same refractive index difference, demonstrating that metal nanoparticles become more sensitive toward environmental changes as their geometry deviates further from the spherical shape. Unfortunately, this is accompanied by spectral features in the near IR, rather than in the visible, making the development of biosensors more impractical.

3.2 Sensing with Silica-Coated Gold Nanorods

The use of metal nanoparticles as biological sensors is determined by the possibility to functionalize them with various kinds of biomolecules, such as antibodies, proteins, enzymes or oligonucleotides.[26–28] The linkage of biological receptors onto nanoparticles (biofunctionalization) is usually carried out through binding of terminal thiol groups with the surface of the metal nanoparticles. Despite of the validity of this approach, this type of surface functionalization is often complicated because of the different degree of affinity of the thiol toward the metallic surface and the stabilizer used during the synthesis of the nanoparticles, while in other cases where the functionalization is carried out through a non-covalent linkage, this may not be stable enough, leading to aggregation/destabilization of the particles mainly due to ligand desorption or dynamic surface exchange. An alternative approach is the growth of thin silica shells on the nanoparticles, since they provide a greater stability, and the surface chemistry of silica is very versatile, allowing covalent bioconjugation reactions through other functional groups,[29,30] such as aldehydes or carboxylic acids. For this reason, it is important to assess medium sensitivity of gold nanorods upon growth of uniform shells of SiO_2 with various thicknesses.

We have recently demonstrated the growth of silica shells on gold nanorods through a standard sol-gel process based on the base-catalyzed hydrolysis and condensation of tetraethoxysilane (TEOS), upon surfactant removal and wrapping with polyelectrolytes.[23] This procedure permits a tight control over shell thickness, as shown in the TEM images of Fig. 2. A gradual red-shift of the LPB was observed (Fig. 2d) when increasing silica shell thickness, with saturation (and even a slight blue shift) for shells thicker than about 25 nm, which suggests that sensitivity toward the outer environment is lost at that point. However, for thin shells, the rods still "feel" an effective medium composed of silica and the solvent, so that solvent changes should affect the LPB position. This was investigated through numerical calculations based on the boundary element method (BEM),[19,20] for a geometry consisting of a cylinder capped with hemispheres, for both the gold core and the silica shell. Dielectric data for gold and silica were obtained from Johnson and Christy[31] and Palik[32], respectively. The results are summarized in Fig. 3, where we have plotted the wavelength of maximum extinction in the LPB versus solvent refractive index, for gold nanorods with aspect ratio 3 (10 × 30 nm), coated with concentric silica shells of various thicknesses. As expected, a pseudo-linear trend is observed in all cases, though with decreasing slopes as the silica shell thickness increases, confirming the experimental observation that thicker shells significantly hamper the nanorod sensitivity toward dielectric changes in the environment.

A final demonstration of the screening effect of the silica shells is provided by the maps of near-field enhancement at the corresponding LPB wavelengths for the nanorods coated with shells of varying thickness (Fig. 4). Thin shells below 5 nm slightly perturb the enhancement profile, but large enhancement is still observed in the close proximity of the outer (silica) surface. However, when increasing the shell

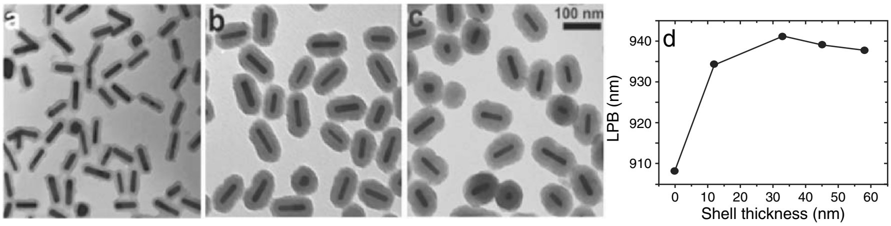

Fig. 2 (a–c) Transmission electron micrographs (TEM) of silica-coated gold nanorods with silica shell thickness increasing from a to d. The scale is the same for all images. (d) Dependence of LPB on silica shell thickness for rods 52 nm long and 13 nm thick

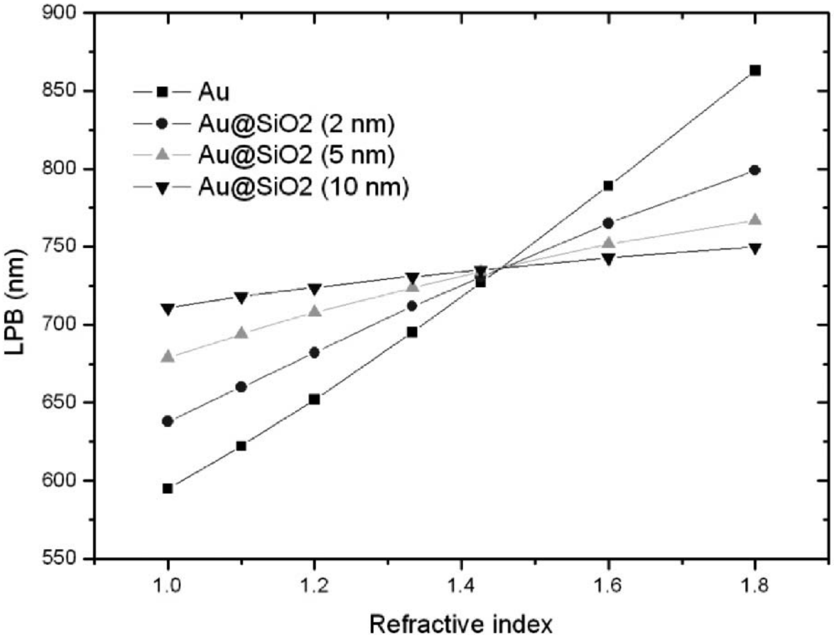

Fig. 3 Calculated (BEM) maximum wavelength of the longitudinal plasmon band for silica-coated gold nanorods (10×30, shell thickness indicated) as a function of medium refractive index

thickness further, the enhancement outside the shell becomes lower and lower, until it is hardly noticeable for shells thicker than 20 nm.

4 Conclusion

Gold nanorods have a great potential to be used as sensing elements within biosensors, on the basis of changes in the position of the localized longitudinal plasmon band, derived from variations in the refractive index of the surrounding medium. Growth of silica shells can be used to anchor biomolecular receptors, at the expense, however, of partly losing dielectric sensitivity, and therefore only thin shells should be considered. Further experiments and calculations where the refractive index only changes in the area closer to the surface are still required for a complete description of this system.

Acknowledgements This work has been supported by the Spanish Ministerio de Educación y Ciencia, through Grants No. MAT2004-02991 and PCI2005-A7-0075. The authors are grateful to Dr. F. Javier García de Abajo for providing the BEM code.

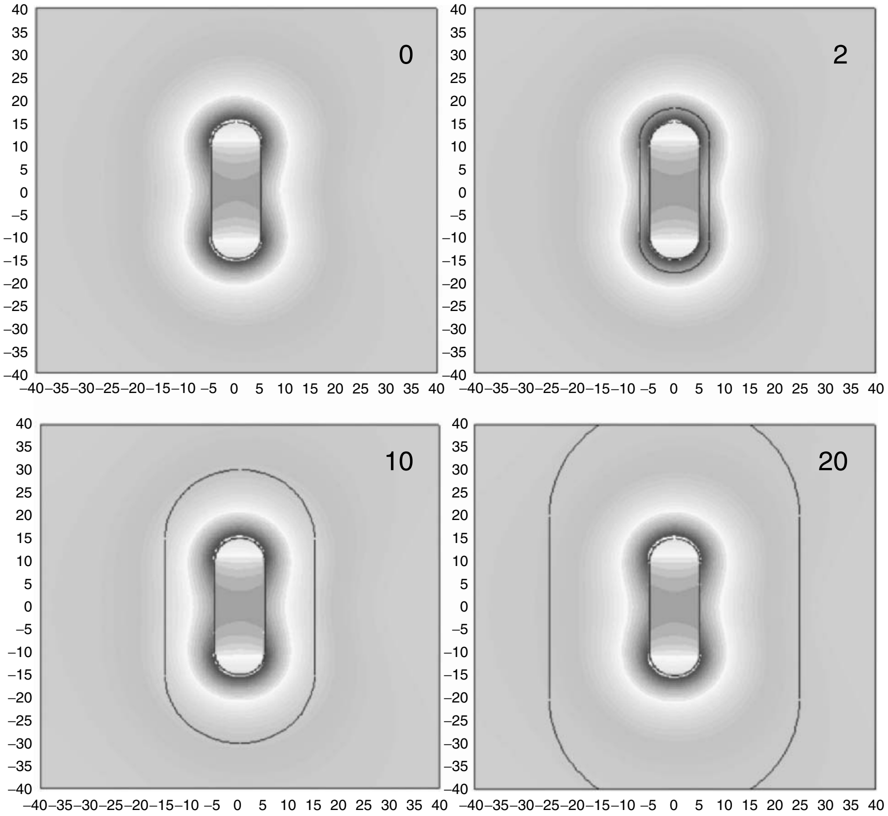

Fig. 4 Near field $|\mathbf{E}|^2$ maps for longitudinal modes of gold nanorods in water and the same rods coated with silica shells of varying thickness (solid lines), as indicated in the labels

References

1. U. Kreibig and M. Vollmer, Optical Properties of Metal Clusters (Springer, Berlin, 1996).
2. Special issue on Synthesis and Plasmonic Properties of Nanostructures, *MRS Bull.* 30(5) (2005).
3. L. M. Liz-Marzán, Tailoring surface plasmon resonance through the morphology and assembly of metal nanoparticles, *Langmuir* 22(1), 32–41 (2006).
4. J. Pérez-Juste, I. Pastoriza-Santos, L. M. Liz-Marzán, and P. Mulvaney, Gold nanorods: synthesis, characterization and applications, *Coord. Chem. Rev.* 249(17–18), 1870–1901 (2005).
5. Y. Xia, P. D. Yang, Y. Sun, Y. Wu, B. Mayers, B. Gates, Y. Yin, F. Kim, and H. Yan, One-dimensional nanostructures: synthesis, characterization, and applications, *Adv. Mater.* 15(5), 353–389 (2003).
6. S. H. Im, T. T. Lee, B. Wiley, and Y. Xia, Large-scale synthesis of silver nanocubes: the role of HCl in promoting cube perfection and monodispersity, *Angew. Chem., Int. Ed.* 44(14), 2154–2157 (2005).
7. J. E. Millstone, S. Park, K. L. Shuford, L. Qin, G. C. Schatz, and C. A. Mirkin, Observation of a quadrupole plasmon mode for a colloidal solution of gold nanoprims, *J. Am. Chem. Soc.* 127(15), 5312–5313 (2005).

8. I. Pastoriza-Santos and L. M. Liz-Marzán, Synthesis of silver nanoprisms in DMF, *Nano Lett.* 2(8), 903–905 (2002).
9. C. L. Nehl, H. Liao, and J. H. Hafner, Optical properties of star-shaped gold nanoparticles, *Nano Lett.* 6(4), 683–688 (2006).
10. S. Link and M. A. El-Sayed, Spectral properties and relaxation dynamics of surface plasmon electronic oscillations in gold and silver nano-dots and nano-rods, *J. Phys. Chem. B* 103(40), 8410–8426 (1999).
11. M. Faraday, *Philos. Trans. Royal Soc. London* 147, 145 (1857); A. Henglein, Small-particle research: physicochemical properties of extremely small colloidal metal and semiconductor particles, *Chem. Rev*. 89(8), 1861–1873 (1989); U. Kreibig, Systems of small metal particles: optical properties and their structure dependences. *Z. Phys. D* 3(2–3), 239–249 (1986); C. F. Bohren, D. F. Huffman, *Absorption and scattering of light by small particles* (Wiley, New York, 1983); P. Mulvaney, Surface plasmon spectroscopy of nanosized metal particles, *Langmuir* 12(3), 788–800 (1996).
12. L. R. Hirsch, R. J. Stafford, J. A. Bankson, S. R. Sershen, B. Rivera, R. E. Price, J. D. Hazle, and N. J. Halas, Nanoshell-mediated near-infrared thermal therapy of tumors under magnetic resonance guidance, *Proc. Natl. Acad. Sci., USA* 100(23), 13549–13554 (2003).
13. D. A. Stuart, A. J. Haes, C. R. Yonzon, E. M. Hicks, and R. P. van Duyne, Biological applications of localised surface plasmonic phenomenae, *IEEE Proc. Nanobiotechnol.* 152(1), 13–32 (2005).
14. A. J. Haes and R. P. van Duyne, A nanoscale optical biosensor: sensitivity and selectivity of an approach based on the localized surface plasmon resonance spectroscopy of triangular silver nanoparticles, *J. Am. Chem. Soc.* 124(35), 10596–10604 (2002).
15. L. R. Hirsch, J. B. Jackson, A. Lee, N. J. Halas, and J. L. West, A whole blood immunoassay using gold nanoshells, *Anal. Chem.* 75(10), 2377–2381 (2003).
16. G. Raschke, S. Kowarik, T. Franzl, C. Sönnichsen, T. A. Klar, J. Feldmann, A. Nichtl, and K. Kürzinger, Biomolecular recognition based on single gold nanoparticle light scattering, *Nano Lett.* 3(7), 935–938 (2003).
17. H. Wang, D. W. Brandl, F. Le, P. Nordlander, and N. J. Halas, Nanorice: a hybrid plasmonic nanostructure, *Nano Lett.* 6(4), 827–832 (2006).
18. P. K. Jain, K. S. Lee, I. H. El-Sayed, and M. A. El-Sayed, Calculated absorption and scattering properties of gold nanoparticles of different size, shape, and composition: application in biological imaging and biomedicine, *J. Phys. Chem. B* 110(14), 7238–7248 (2006).
19. F. J. García de Abajo and A. Howie, Relativistic electron energy loss and electron-induced photon emission in inhomogeneous dielectrics, *Phys. Rev. Lett.* 80, 5180–5183 (1998).
20. F. J. García de Abajo and A. Howie, Retarded field calculation of electron energy loss in inhomogeneous dielectrics, *Phys. Rev. B* 65(11), 115418-1-17 (2002).
21. A. Sánchez-Iglesias, I. Pastoriza-Santos, J. Pérez-Juste, B. Rodríguez-González, F. J. García de Abajo, and L. M. Liz-Marzán, Synthesis and optical properties of gold nanodecahedra with size control, *Adv. Mater.* 18(19), 2529–2534 (2006).
22. B. Nikoobakht and M. A. El-Sayed, Preparation and growth mechanism of gold nanorods (NRs) using seed-mediated growth method, *Chem. Mater.* 15(10), 1957–1962 (2003).
23. I. Pastoriza-Santos, J. Pérez-Juste, and L. M. Liz-Marzán, Silica-coating and hydrophobation of CTAB-stabilized gold nanorods, *Chem. Mater.* 18(10), 2465–2467 (2006).
24. N. A. Kotov, I. Dekany, and J. H. Fendler, Layer-by-layer self-assembly of polyelectrolyte-semiconductor nanoparticle composite films, *J. Phys. Chem.* 99, 13065–13069 (1995).
25. I. Pastoriza-Santos, D. S. Koktysh, A. A. Mamedov, M. Giersig, N A. Kotov, and L. M. Liz-Marzán, One-Pot synthesis of Ag@TiO_2 core-shell nanoparticles and their layer-by-layer assembly, *Langmuir* 16(6), 2731–2735 (2000).
26. A. P. Alivisatos, K. P. Jonson, X. G. Peng, T. E. Wilson, C. J. Loweth, M. P. Bruchez, and G. P. Schultz, Organization of 'Nanocrystal Molecules' using DNA, *Nature* 382, 609–611 (1996).
27. R. Jin, G. Wu, Z. Li, C. A. Mirkin, and G. C. Schatz, What controls the melting properties of DNA-linked gold nanoparticles assemblies?, *J. Am. Chem. Soc.* 125(6), 1643–1654 (2003).

28. L. A. Lyon, M. D. Musick, and M. J. Natan, Colloidal Au-enhanced surface plasmon resonance immunosensing, *Anal. Chem*. 70(24), 5177–5183 (1998).
29. S. Liu and M. Han, Synthesis, functionalization, and bioconjugation of monodisperse, silica-coated gold nanoparticles: robust bioprobes, *Adv. Funct. Mater*. 15(6), 961–967 (2005).
30. J. E. Smith, L. Wang, and W. Tan, Bioconjugated silica-coated nanoparticles for bioseparation and bioanalysis, *Trends Anal. Chem*. 25(9), 848–855 (2006).
31. P. B. Johnson and R. W. Christy, Optical constants of the noble metals, *Phys. Rev. B* 6(12), 4370–4379 (1972).
32. E. D. Palik, *Handbook of optical constants of solids* (Academic, New York, 1985).

Influence of the S-Au Bond Strength on the Magnetic Behavior of S-Capped Au Nanoparticles

María J. Rodríguez Vázquez[1], José Rivas[1], M. Arturo López-Quintela[1],*
Antonio Mouriño Mosquera[2], and Mercedes Torneiro[2]

Abstract Recently, large permanent atomic magnetic moments have been found in Au nanoparticles capped with thiols. It is assumed that the formation of localized Au-S bonds at the particle surface induces the damping of the surface plasmon resonance and the appearance of a ferromagnetic-like behavior. In this work we will show for the first time that thioethers can also induce both phenomena, i.e., the damping of the plasmon band and the appearance of permanent magnetic moments. Furthermore, we have studied the influence of the Au-S bond strength on both phenomena using two different synthesized thioether ligands. It will be shown that, although both ligands can induce a complete damping of the plasmon band, only with one of the ligands (the one corresponding to the stronger S-Au bond) the appearance of a ferromagnetic-like order is observed. This is an indication of the extreme sensitivity of the magnetism on the strength of the charge transfer at the S-Au bond.

Keywords S-capped Au nanoparticles, ferromagnetic-like Au nanoparticles

1 Introduction

The synthesis of nanomaterials has received a lot of attention in recent years because of its scientific and technological implications.[1] The main interest of these materials lies basically in the unusual dependences of the properties, such as electronic, optical, and magnetic, on the size and shape of the nanoparticles,

---

[1] Laboratory of Magnetism and Nanotechnology, Institute of Technological Research, Departments of Physical Chemistry and Applied Physics, University of Santiago de Compostela, Edificio da Imprenta, 15782 Santiago de Compostela, Spain

[2] Department of Organic Chemistry, CSIC Associated Unit, University of Santiago de Compostela, Spain

* To whom correspondence should be addressed. E-mail: qfarturo@usc.es

M. Giersig and G. B. Khomutov (eds.),
Nanomaterials for Application in Medicine and Biology

since the above-mentioned properties differ from the bulk materials. Among these properties, the magnetic behavior observed in nanoparticles and capped thin films with metals (like Pd,[2] Au,[3] etc.) still constitutes an open question to be resolved.[4,5,6,7] Among the possible explanations for the observed giant magnetic anisotropies at the nanoscale, the strong spin-orbit coupling at the nanoparticle surface and the existence of an ordered arrangement are thought to be the origin of the observed giant orbital momenta.[8] Mostly, thiol groups have been used for cappings because of the assumed charge transfer from the gold atoms to the organic cappings. An electron transfer of only 0.1 e per atom has been observed in these systems,[9] which seems to be enough to induce the observed large magnetic anisotropies.[3] The strong S-Au interaction traps the electrons, which can be spin polarized in localised bonds, inducing a drastic decrease of the electron mobility and a damping of the surface plasmon resonance.[10] Because of this, usually both effects (disappearance of the plasmon band and presence of orbital ferromagnetism) seem to be associated.[3] In order to get a deeper insight into this novel phenomenon, we have studied the influence of the S-Au bond strength on the plasmon and magnetic behavior of Au nanoparticles in this work. To this purpose, two S-terminated ligands with different chemical surroundings have been synthesized and used for capping Au nanoparticles. Although in both cases it is observed, as we will show here, that the strong S-Au bond is enough to totally damp the plasmon band, the small differences in chemical properties of the S atom (due to the different chemical surroundings) induce a completely different magnetic behavior of the Au nanoparticles.

2 Experimental Section

2.1 Synthesis of Ligand Methyl 4–(Dec–9–Enyloxy)Benzoic (1)

To a solution of methyl 4–hydroxybenzoate and triphenylphosphine in dry THF in flask under argon atmosphere, 9 – decen–1–ol was added. DEAD was added under cooling with a water/ ice bath. DEAD is an orange oil that loses its color as it dissolves in the reaction solution. The solution was then stirred for 6 h and concentrated under reduced pressure to eliminate THF. A white solid precipitate was obtained. The precipitate dissolves in ethoxyethane. This solution was washed three times with HCl 5%, $NaCl_{sat}$ and water, dried over Na_2SO_4 and concentrated under reduced pressure. The product was finally purified by column chromatography (silica gel, hexane) to give **1,** which is a white solid, with a yield of 70%. ^1H NMR (250 MHZ, $CDCl_3$, δ): 1.33 (m, 10 H, 5 CH_2), 1.79 (m, 2H, CH_2), 2.05 (m, 2H, CH_2), 3.87 (s, CH_3), 3.99 (trip, 2H, CH_2O), 4.93 (m, 1H, $=CH_2$trans), 5.02 (s, 1H, $=CH_2$cis), 5.80 (m, 1H, =CH gem), 6.88 (d, 2H, CHAr), 7.96 (d, 2H, CHAr).^{13}C NMR (75.46 MHZ, $CDCl_3$, δ): 26.0 (CH_2), 28.9 (CH_2), 29.0 (CH_2), 29.1 (CH_2), 29.3 (CH_2), 29.4 (CH_2), 33.8 (CH_2), 51.8 (CH_3), 68.1 (CH_2O), 113.9 (CHAr), 114.0 (CH_2=), 122.2 (CAr), 131.4 (CHAr), 138.9 (CH=), 162.7 (CAr), 166.6 (CO).

2.2 Synthesis of Ligand 4–(Dec–9–Enyloxy)Benzoic Acid (2)

To a solution of methyl 4–(dec–9–enyloxy)benzoate in dry THF in flask under argon atmosphere, a solution of LiOH 2 N in water was added, with a molar proportion of **1** with LiOH 1:8. The mixture was heated to reflux and stirred overnight. The solution was concentrated under reduced pressure to eliminate THF, and a white solid appeared. This precipitate dissolves in ethyl acetate. The solution was washed with HCl 5%, dried over Na$_2$SO$_4$ and concentrated under reduced pressure to give **2**. A white solid was obtained, with a yield of 99%. ^{1}H NMR (250 MHz, CDCl$_3$, δ): 1.35 (m, 10 H, 5 CH$_2$), 1.82 (m, 2H, CH$_2$), 2.05 (m, 2H, CH$_2$), 4.03 (trip, 2H, CH$_2$O), 4.95 (m, 1H, =CH$_2$trans), 5.03 (s, 1H, =CH$_2$cis), 5.82 (m, 1H, =CH gem), 6.93 (d, 2H, CHAr), 8.05 (d, 2H, CHAr). ^{13}C NMR (75.46 MHz, CDCl$_3$, δ): 26.0 (CH$_2$), 29.0 (CH$_2$), 29.1 (CH$_2$), 29.1 (CH$_2$), 29.1 (CH$_2$), 29.4 (CH$_2$), 29.5 (CH$_2$), 33.8 (CH$_2$), 68.3 (CH$_2$O), 114.1 (CHAr), 114.1 (CH$_2$=), 121.3 (CAr), 132.22 (CHAr), 139.11 (CH=), 163.5 (CAr), 171.9 (CO).

2.3 Synthesis of Ligand Methylthiomethyl 4–(Dec–9–Enyloxy) Benzoate (3)

Different methods were tried for obtaining compound **3**. It was observed that the method giving good results and, at the same time, being the fastest, was the method described in Blankemeyer-Menge (see scheme 1).[11] The material used in this synthesis has to be completely dry. To a solution of 4–(dec–9–enyloxy)benzoic acid (3 eq) in dry dichloromethane in flask under argon atmosphere MeIm (2.25 eq) was added. The solution was stirred for 10 min. Then MSNT (4 eq) was added. The solution was stirred again for 10 min. Then 2-methylthioethanol was added. The solution was stirred for 1 h under argon atmosphere and the mixture concentrated

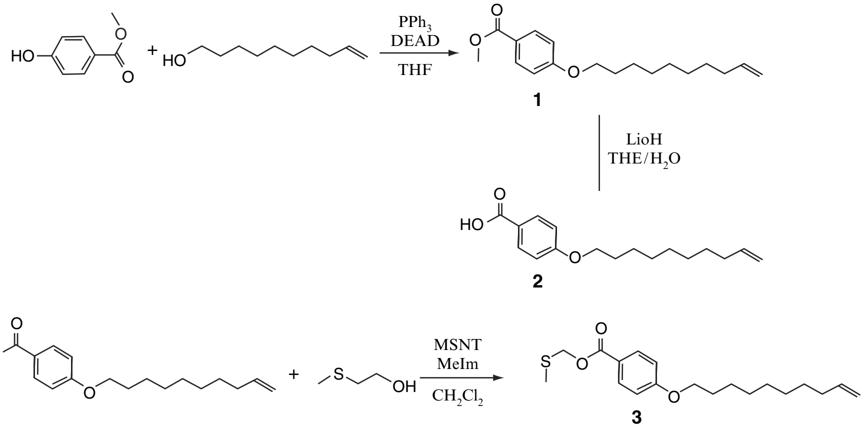

Scheme 1 Synthetic procedure for the preparation of ligand **3**

under reduced pressure. The product was purified by column chromatography (silica gel, hexane) to give **3** as colorless solid with a yield of 99%. ^1H NMR (250 MHZ, $CDCl_3$, δ): 1.33 (m, 10 H, CH_2), 1.71 (m, 2H, CH_2), 2.00 (m, 2H, CH_2), 2.09 (s, CH_3), 2.81 (trip, 2H, CH_2-S), 3.94 (trip, 2H, CH_2-O), 4.42 (trip, 2H, CH_2-COO), 4.97 (m, 1H, =CH_2trans), 5.00 (m, 1H, =CH_2cis), 5.78 (m, 1H, =CH gem), 6.85 (d, 2H, CHAr), 7.86 (d, 2H, CHAr). ^{13}C NMR (75.46 MHZ, $CDCl_3$, δ): 17.1 (CH_3), 26.0 (CH_2), 29.7 (5 CH_2), 33.1 (CH_2-S), 33.9 CH_2), 63.4 ($\underline{C}H_2$-COO), 68.9 (CH_2-O), 114.0 (CHAr), 114.1 (CH_2=), 121.8 (CAr), 131.0 (CHAr), 138.1 (CH=), 181.8 (CAr), 166.2 (COO).

2.4 *Synthesis of Ligand (4–(Dec–9–Enyloxy)Phenyl) (Methyl)Sulfane (4)*

To a solution of methyl 4–(methylthio)phenol and triphenylphosphine in dry THF in flask under argon atmosphere was added 9–decen–1–ol. DEAD was added under cooling with a water/ ice bath. DEAD is an orange oil that loses its color as it dissolves in the reaction solution. Then, the solution was stirred for 6 h and concentrated under reduced pressure to eliminate THF. A white solid precipitate was obtained. The precipitate dissolves in ethoxyethane. This solution was washed three times with HCl 5%, $NaCl_{sat}$ and water, dried over Na_2SO_4 and concentrated under reduced pressure. The product was finally purified by column chromatography (silica gel, hexane) to give **4** (see scheme 2) which is a white solid, with a yield of 75%. ^1H NMR (250 MHZ, $CDCl_3$, δ): 1.33 (m, 10 H, CH_2), 1.71 (m, 2H, CH_2), 1.96 (m, 2H, CH_2), 2.50 (s, CH_3), 3.94 (trip, 2H, CH_2-O), 4.97 (m, 1H, =CH_2trans), 5.01 (m, 1H, =CH_2cis), 5.72 (m, 1H, =CH gem), 6.70 (d, 2H, CHAr), 7.10 (d, 2H, CHAr). ^{13}C NMR (75.46 MHZ, $CDCl_3$, δ): 15.0 (CH_3), 26.0 (CH_2), 29.7 (5 CH_2), 33.1 (CH_2-S), 33.7 CH_2), 68.9 (CH_2-O), 114.0 (CHAr), 114.5 (CH_2=), 127.1 (CHAr), 128.0 (CAr), 138.0 (CH=), 154.2 (CAr).

2.5 *Preparation of Au Nanoparticles without Ligand*

In a typical preparation,[12] 100 ml of 50 mM toluene solution of NR_4Br (R = octyl) was added to 38 ml of 30 mM aqueous solution of $HAuCl_4.3H_2O$. The mixture was stirred for 30 min. Then 33 ml of 0.4 M aqueous solution of $NaBH_4$ was slowly added under vigorous stirring and the solution was continuously stirred for 20 min. The organic phase was washed with 100 ml of 0.1 M aqueous solution of H_2SO_4, and five times with 100 ml of water. Finally the organic phase was dried over Na_2SO_4.

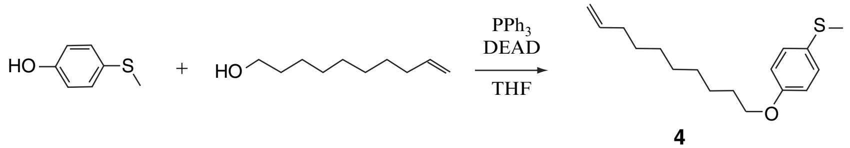

4

Scheme 2 Synthetic procedure for the preparation of ligand **4**

2.6 Preparation of Au Nanoparticles with Thioether–Ligands (3 and 4)

To 22.2 ml of 30 mM aqueous solution of $HAuCl_4.3H_2O$ was added 40.4 ml of 50 mM toluene solution of NR_4Br (R = octyl). The mixture was stirred for 30 min. The aqueous phase changes the color: yellow to colorless. The organic phase changes too: colorless to dark orange. The ligand **3** or **4** was then added (3.5 eq for each eq of $HAuCl_4.3H_2O$). The mixture was heated to reflux at 100°C. The organic phase changes the color: dark orange to light yellow. The solution was cooled at room temperature. 18 ml of 0.4 M aqueous solution of $NaBH_4$ were slowly added under vigorous stirring and the solution was continuously stirred for 20 min. The organic phase was first washed with 50 ml of 0.1 M aqueous solution of H_2SO_4, then five times with 50 ml of water, and finally dried over Na_2SO_4. The solvent was evaporated to 5 ml under reduced pressure. 200 ml of ethanol was added and the mixture was cooled to −18°C for 4 h. The mixture was centrifuged to give a crude precipitate of Au nanoparticles. The solid was washed with ethanol, centrifuged, and finally dried under reduced pressure. For analysis purposes, Au nanoparticles were dispersed in distilled chloroform. It is possible to verify the capping of the nanoparticles by NMR ^1H observing the displacement of some ^1H signals (see Supporting Information). The most important displacements correspond to the protons of the CH_2 groups linked with both the MeS group and the carboxylic group. These facts clearly indicate that Au nanoparticles are linked with ligand **3** across the sulphur, so that not only the MeS protons are affected, but also the protons of the closest CH_2 groups.

Materials. All chemicals were purchased from Sigma-Aldrich and Fluka and used without further purification.

Equipment. UV-Vis spectra were taken with a HP 8,452A UV-Vis spectral photometer. ^1H and ^{13}C NMR spectra were made with a Bruker 250 NMR spectral photometer. Transmission electron microscopy (TEM) was performed with a 120 kV Philips CM-12 TEM microscope. Electron paramagnetic resonance (EPR) measurements were carried out with a Bruker EMX and the magnetization measurements were made on a SQUID from Quantum Design. Particle size distributions were measured by counting 100 nanoparticles deposited on a copper grid.

3 Results

Figure 1 shows a TEM picture of Au nanoparticles synthesised without thioether-ligands, together with a histogram of the particle size distribution. These particles, with a size of 5.8 ± 0.9 nm and a small ordering, display a characteristic surface plasmon resonance band, with a maximum centred at 524 nm, as it can be seen in the UV–Vis spectrum shown in Fig. 2. It is observed that these Au nanoparticles, capped with NR_4Br (R=octyl), i.e. without thioether ligands, exhibit a diamagnetic behavior, similar to that of bulk gold (see Fig. 3).

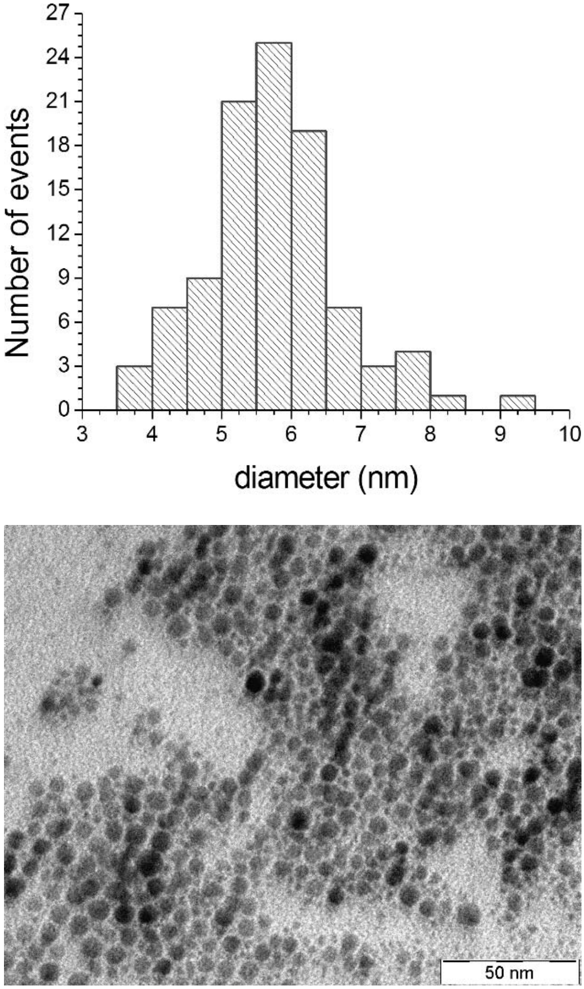

Fig. 1 TEM image of NR_4Br-capped Au nanoparticles

Au nanoparticles stabilized with ligand **3** observed by TEM show a remarkable degree of self-assembly into regular arrays, as can be seen in the TEM picture in Fig. 4. A pseudo-hexagonal close-packed arrangement is observed for these nanoparticles with a size of 4.8 ± 0.7 nm, whose histogram is included in the right part of Fig. 4. The UV–Vis spectrum of these particles (Fig. 5) clearly shows the complete absence of the surface plasmon resonance band, and only a band with a maximum centred at 256 nm is observed. Figure 6 shows a hysteresis loop at 300 K similar to a system formed by ultrafine ferromagnetic particles with a blocking temperature above room temperature. The observed coercive force is of the same order of that previously reported for thiol-capped Au nanoparticles.[3]

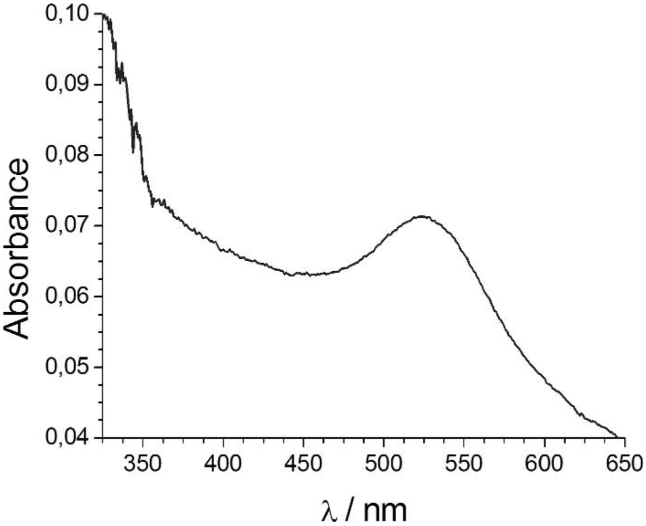

Fig. 2 UV-Vis spectrum of NR_4Br-capped Au nanoparticles

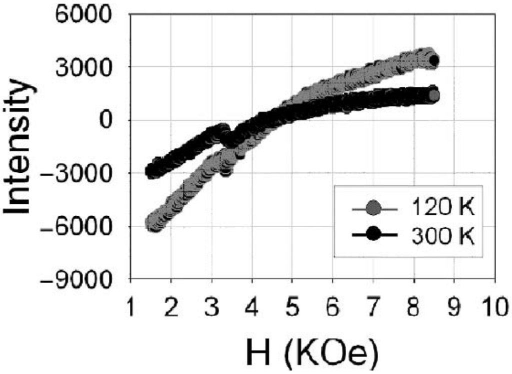

Fig. 3 EPR curves of NR_4Br-capped Au nanoparticles

A TEM picture of Au nanoparticles stabilized with ligand **4** is shown in Fig. 7 together with the corresponding size histogram. Two points can be emphasized. First, smaller particles (2.0 ± 0.4 nm) are now formed with this ligand. Second, particle ordering is not observed, and only different arrangements of groups of nanoparticles were observed. The UV–Vis spectrum (see Fig. 8) in this case also shows the complete absence of the surface plasmon resonance band and only the presence of a band located at 290 nm. Figure 9 shows that the Au nanoparticles stabilized with ligand **4** are diamagnetic, similar to the S-uncapped Au nanoparticles.

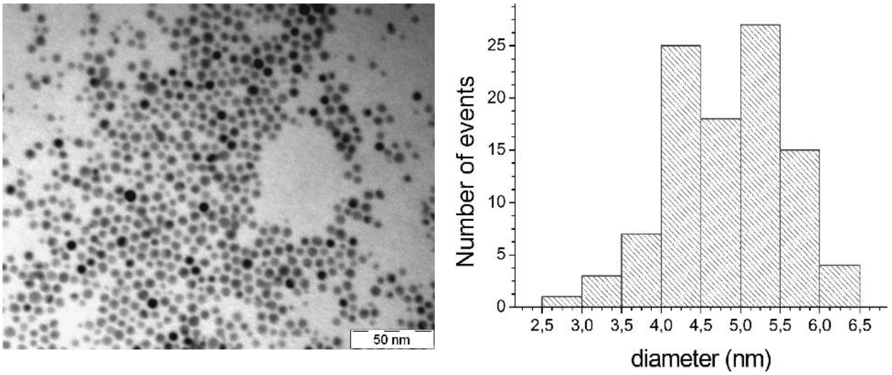

Fig. 4 TEM image of thioether-capped Au nanoparticles (ligand **3**)

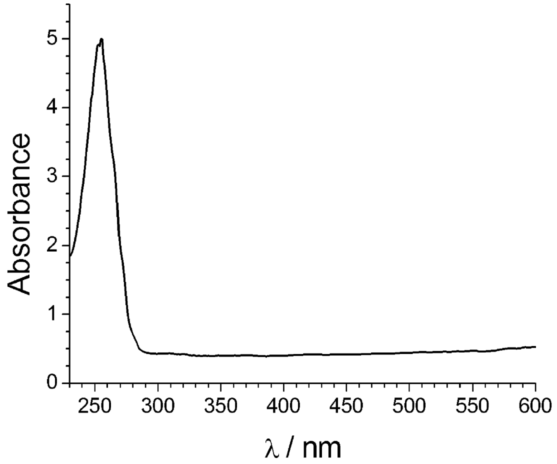

Fig. 5 UV-Vis spectrum of thioether-capped Au nanoparticles (ligand **3**)

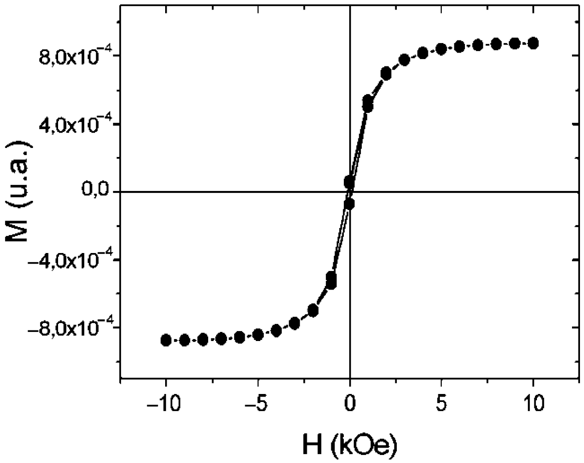

Fig. 6 Magnetization curve of thiother-capped Au nanoparticles (ligand **3**)

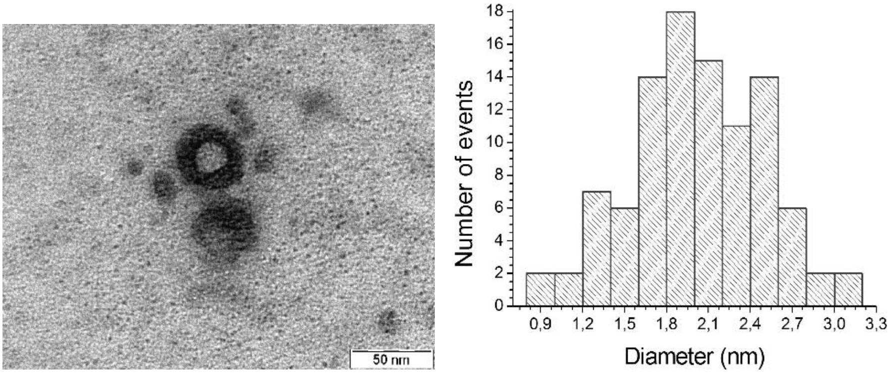

Fig. 7 TEM image of thioether-capped Au nanoparticles (ligand **4**)

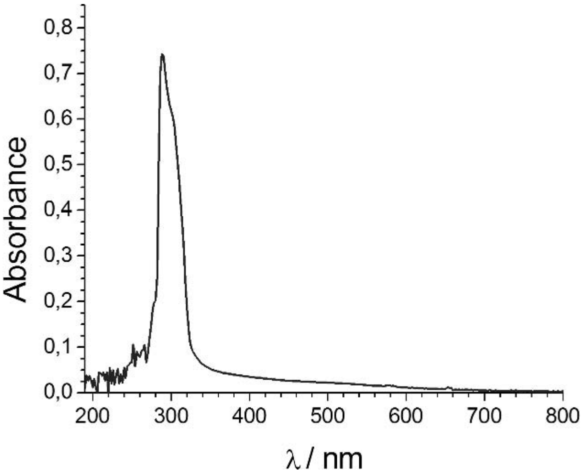

Fig. 8 UV-Vis spectrum of thioether-capped Au nanoparticles ligand **4**)

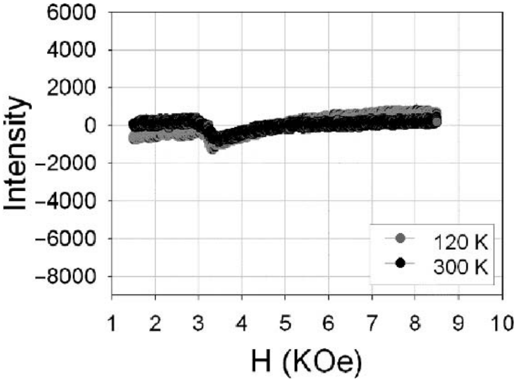

Fig. 9 EPR curves of thioether-capped Au nanoparticles (ligand **4**)

4 Discussion

Au nanoparticles capped with ligand **3** show magnetization values similar to those obtained by Crespo et al.[3] for thiol-capped Au nanoparticles.[1] We can then say that these Au nanoparticles have a localized permanent magnetism - a behavior which is in contrast to the metallic diamagnetism characteristic of Au nanoparticles without thioether ligands or bulk Au. Again, similar to Crespo's results, the magnetic Au nanoparticles do not display the characteristic surface plasmon resonance, showing only an absorption band centred at 256 nm. The presence of this ferromagnetic-like behavior has been attributed to the formation of strong sulphur–gold localized bonds. It has been claimed that this S-Au bond can induce a hole localization in the Au nanoparticles, losing its metallic character and giving rise to the disappearance of the surface plasmon resonance. The permanent magnetic moments associated with the spin of extra *d* holes localized near the S-Au bonds are then assumed to be responsible for this strong magnetic behavior. From this point of view, the Au nanoparticles capped with ligand 4 have the same "ingredients" as those capped with ligand **3**, i.e., a S-Au link and the absence of the plasmon band. However, Au nanoparticles with ligand **4** are diamagnetic, like Au nanoparticles without thioether ligands. Therefore, there should be other factors which also have to play an important role in developing the observed unusual magnetism in Au nanoparticles. The main "external" differences between the Au nanoparticles capped with ligands **3** and **4** are the size and the self-assembly of the nanoparticles (being bigger and much more ordered for the ligand-3 capped Au nanoparticles). Because a smaller size should favor the appearance of permanent magnetic moments, this explanation can be disregarded. Alternatively, one could think that the self-assembly of Au nanoparticles is the key factor in developing the observed magnetic behavior, but this is in contrast with the results obtained by Crespo et al.,[3] whose pictures clearly show the absence of self-assembly in their magnetic thiol-capped Au nanoparticles. Therefore, there should be other "internal" factors which are important for developing this strong magnetism in these kinds of systems. One of these factors can be related to the percentage of charge transfer from the Au to the S atom. It can be stated that, in fact, there is an "internal" difference between the particles capped with ligands **3** and **4** related to the strength of the S-Au bond. The S atom in ligand **3** should exert a less negative charge than in ligand **4**, because of the different chemical character of the groups linked to the S atom (larger electron-withdrawing of the neighboring CH_2COO group in ligand **3** than the benzene ring in ligand **4**). This would imply a larger electron-withdrawing from the Au atom in the S-Au bond with ligand **3** than with ligand **4**. In other words, the S-Au bond

---

[1] All samples with different cappings were prepared with the same batch of reactants; therefore ferromagnetic behavior cannot be attributed to the presence of impurities. Furthermore, X ray fluorescence analysis shows that the impurities of magnetic elements are so small that they cannot explain the magnetic properties observed in the samples capped with ligand **3**.

should be stronger with ligand **3** than with ligand **4**. Because the presence of permanent magnetic moments is only found with ligand **3**, this result suggests that the extra *d* hole localization strongly depends on the strength of the S-Au bond. It is observed that, although in both cases the electron localization is strong enough to prevent the formation of the plasmon band, the appearance of ferromagnetism is more sensitive to this charge transfer. The results further indicate that there should be a critical bond strength, i.e., a critical number of generated holes (or transferred charge) for inducing the permanent atomic magnetic moments observed in these nanomaterials. However, more investigations using a wider systematic variation of the S-Au bond strength are needed to be able to arrive at a definitive conclusion. Investigations in this direction are under way.

5 Conclusions

We have synthesized Au nanoparticles by a modification of Brust's method including two different thioether capping agents in the synthesis procedure. It is observed that, contrary to particles capped with the NR_4Br salt, particles covered with thioethers do not show the plasmon band, which seems to be a first indication of electron localization by the strong S-Au bond created at the particle interface. However, differing magnetic behavior is observed for both thioether cappings, which seems to be associated with the different bond strengths, which depend on the surrounding chemical groups around the S atom. A larger inductive effect, which is expected when the ligand carries a CH_2COO group compared to the benzene ring, gives rise to a more polarized S-Au bond in the Au nanoparticles capped with the ligand carrying a CH_2COO group and, in turn, to the appearance of a permanent magnetic moment in this compound. These results show that a fine tuning of the S-Au bond strength is needed to drive the induction of a ferromagnetic-like order.

Acknowledgements We thank the MEC, Spain, for its financial support (Grants No. MAT2005-07554-C02-01, NAN2004-09133-C03-02, NAN2004-09195-C04-01, and NanoBioMed CONSOLIDER-INGENIO 2010), as well as the Xunta de Galicia, Spain (Grant No. PGDIT03PXIC20907PN). Likewise we thank the European Union for its continuous contribution to support our research (Contract No. 037465-FLUOROMAG, EU-FP6 Framework Programme LIFESCIHEALTH-6).

References

1. For a recent review, see, e.g., International Conference on Nanoscience and Nanotechnology (ICN+T 2006), Basel/ Switzerland, July 30–August 4, 2006.
2. A. Hernando, B. Sampedro, R. Litrán, T. C. Rojas, J. C. Sánchez-López, and A. Fernández, Room temperature permanent magnetism in thiol-capped Pd-rich nanoparticles, *Nanotechnology* 17(5), 1449–1453 (2006).

3. P. Crespo, R. Litrán, T. C. Rojas, M. Multigner, J. M. de la Fuente, J. C. Sánchez-López, M. A. García, A. Hernando, S. Penadés, and A. Fernández, Permanent magnetism, magnetic anisotropy, and hysteresis of Thiol-capped gold nanoparticles, *Phys. Rev. Lett.* 93, 087204 (2004).
4. Z. Vager, I. Carmeli, G. Leitus, S. Reich, and R. Naaman, Surprising electronic-magnetic properties of closed packed organized organic layers, *J.Phys. Chem. of Solids* 65(4), 713–717 (2004).
5. I. Carmeli, G. Leitus, R. Naaman, S. Reich, and Z. Vager, Magnetism induced by the organization of self-assembled monolayers, *J. Chem. Phys.* 118(23), 10372–10375 (2003).
6. Y. Yamamoto, T. Miura, M. Suzuki, N. Kawamura, H. Miyagawa, T. Nakamura, K. Kobayashi, T. Teranishi, and H. Hori, Direct observation of ferromagnetic spin polarization in gold nanoparticles, *Phys. Rev. Lett.* 93(11), 116801–1 (2004).
7. T. Shinohara, T. Sato, and T. Taniyama, Surface ferromagnetism of Pd fine particles, *Phys. Rev. Lett.* 91, 197201 (2003).
8. A. Hernando, P. Crespo, and M. A. García, Origin of orbital ferromagnetism and giant magnetic anisotropy at the nanoscale, *Phys. Rev. Lett.* 96, 057206 (2006).
9. P. Zhang and T. K. Sham, X-ray studies of the structure and electronic behavior of Alkanethiolate-capped gold nanoparticles: the interplay of size and surface effects, *Phys. Rev. Lett.* 90, 245502 (2003).
10. M. A. García, J. de la Venta, P. Crespo, J. Llopis, S. Penadés, A. Fernández, and A. Hernando, Surface plasmon resonance of capped Au nanoparticles, *Phys. Rev. B* 72, 241403(R) (2005).
11. B. Blankemeyer-Menge, M. Nimtz, and R. Frank, An efficient method for anchoring FMOC-amino acids to hydroxyl-functionalised solid supports, *Tetrahedron Lett.* 31(12), 1701–1704 (1990).
12. J. Fink, C. J. Kiely, D. Bethell, and D. J. Schiffrin, Self-organization of nanosized gold particles, *Chem. Mater.* 10(3), 922–926 (1998).

Supporting Information

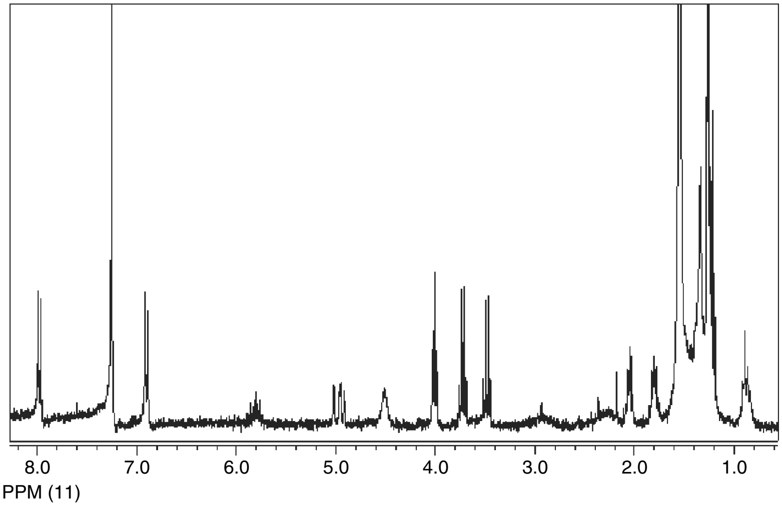

Fig. SI-1 RMN^{1}H of Au nanoparticles stabilized with ligand **3**

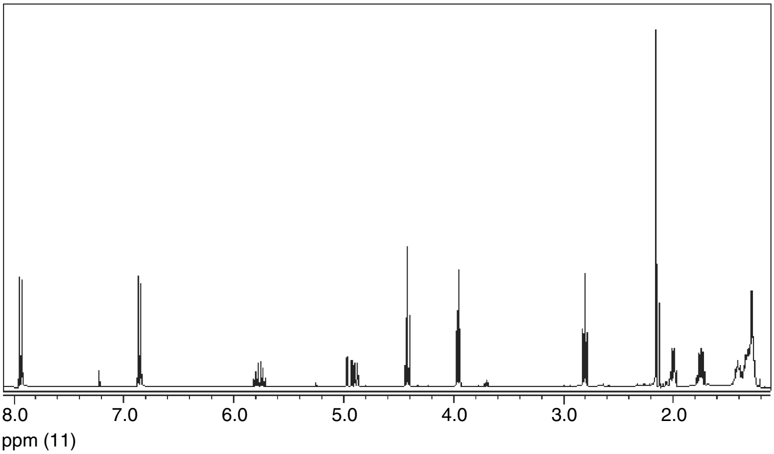

Fig. SI-2 RMN^{1}H of ligand **3**

This page intentionally blank

Long-Term Retention of Fluorescent Quantum Dots In Vivo

Byron Ballou,[1,2,*] Lauren A. Ernst,[1] Susan Andreko,[1] Marcel P. Bruchez,[1,3] B. Christoffer Lagerholm,[1,4] and Alan S. Waggoner[1,2]

Abstract Quantum dots that emit in the near-infrared can be used in vivo to follow circulation, to target the reticuloendothelial system, and to map lymphatic drainage from normal tissues and tumors. We have explored the role of surface charge and passivation by polyethylene glycol in determining circulating lifetimes and sites of deposition. Use of long polyethylene glycol polymers increases circulating lifetime. Changing surface charge can partially direct quantum dots to the liver and spleen, or the lymph nodes. Quantum dots are cleared in the order liver > spleen > bone marrow > lymph nodes. Quantum dots retained by lymph nodes maintained fluorescence for two years, suggesting either that the coating is extremely stable or that some endosomes preserve quantum dot function. We also explored migration from tumors to sentinel lymph nodes using tumor models in mice; surface charge and size make little difference to transport from tumors. Antibody and Fab·conjugates of polymer-coated quantum dots failed to target tumors in vivo, probably because of size.

Keywords In vivo, circulating lifetime, quantum dot, sentinel lymph node

1 Overview

Our group has synthesized several surface coats for quantum dots that serve to render them soluble in water, reasonably nontoxic, and useful for conjugation to biomolecules. In this paper, we discuss results obtained by using a primary polymer

---

[1] Molecular Biosensor and Imaging Center

[2] Department of Biological Sciences

[3] Department of Chemistry

Mellon Institute, Carnegie Mellon Unversity, 4400 Fifth Avenue, Pittsburgh, PA 15213, USA

[4] Present address: Memphys, Physics Department, University of Southern Denmark, Campusvej 55, 5230 Odense, Denmark

[*] To whom correspondence should be addressed. E-mail: bbal@andrew.cmu.edu

M. Giersig and G. B. Khomutov (eds.),
Nanomaterials for Application in Medicine and Biology

coat that has proved remarkably stable and adaptable. This primary polymer coat ("amp" for amphiphilic) was a polyacrylic acid substituted to approximately 50% using octylamine.[1] This amp coat made it possible to solubilize quantum dots in water with excellent retention of their fluorescence efficiency (quantum yields in excess of 80% are usual). The carboxyl surface made it easy to react many other chemical groups to create a wide range of secondary coats and conjugates of biological materials. We found that polymer-coated quantum dots, even without being conjugated to biological materials, could be used for many purposes in vivo, for example, as long-circulating vascular markers, for mapping the reticuloendothelial system (=RES, =MPS, mononuclear phagocytic system), or for lymph node mapping, each use depending on their secondary surfaces and sites of injection.

1.1 Size

Figure 1 shows quantum dots, primary amp coat, and secondary coats of methoxy-terminated polyethylene glycol (mPEG) drawn to scale, with the PEG polymer assumed to be in the fully extended configuration. If this were so, then the size of the 5,000 kDa PEG-substituted quantum dot should dwarf the size of the original amp-quantum dot. However, this is not so; the hydrodynamic diameter of the amp-coated quantum dots is ~15 nm, in agreement with Larson et al.,[2] while that of the methoxy-terminated PEG-5,000-substituted amp-coated quantum dot is ~22 nm, both as assessed by fluorescence correlation spectroscopy in our laboratory, and in agreement

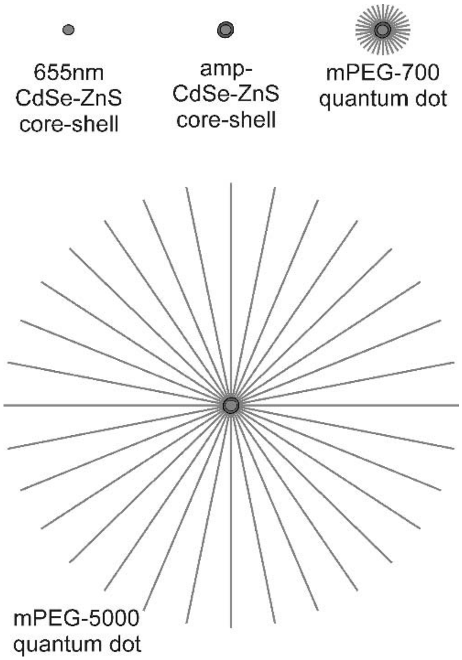

Fig. 1 Relative sizes of quantum dots and coats. A 7-nm diameter core-shell quantum dot, with amp-coating, and two PEG-secondary coats are drawn to approximate scale

with electron microscopy of negatively stained quantum dots (data not shown). Thus the surface PEG polymer must be folded into a compact conformation.

1.2 Labeling Vasculature

Our initial efforts were to create a secondary surface that would allow long-term circulation in vivo; without this, there would be little chance of targeting quantum dots to sites of interest, for they would not remain in circulation long enough to penetrate and bind to non-vascular tissues. On intravenous injection, amp-coated quantum dots had half-lives measured in minutes; we found that substitution with polyethylene glycol allowed circulating half-lives of several hours to days, but circulation time was critically dependent on polymer size and density.[3] Considerable effort was required to minimize variation from batch to batch of coated quantum dots. Methoxy-terminated PEG-5000 substituted amp-quantum dots proved most generally useful. With this material, we were able to visualize surface vasculature with high sensitivity and good resolution.[3] As noted in reference 3, quantum dots coated with smaller polymers had shorter half-lives. In subsequent experiments, we found that adding charged termini to PEG also decreased half-lives. Similar experiments by other workers[4] have shown that a triblock copolymer terminated with PEG can give acceptable circulating half-lives. We found it easy to visualize the subsurface vasculature of mice, even using 605-nm-emitting quantum dots; moving to the near-infrared and using 800-nm and 850-nm-emitting quantum dots permitted visualization of deeper blood vessels, though with decreasing resolution. We note that Larson et al. showed that two-photon excitation of quantum dots permits visualization of small capillaries through skin and at tissue depths up to 250 µ.[2] Our direct imaging by macro camera cannot compare in resolution, but does give penetration to depths of several millimeters.

1.3 Excretion

It was of interest to determine where quantum dots were ultimately disposed. Quantum dots are found in the feces, with the bulk excreted one to two days after injection. We believe that this is the principal route of excretion. We have not, however, confirmed this quantitatively, nor have we demonstrated that presence of quantum dots in the feces is a result of the classical route of excretion via the bile duct.

1.4 Sites of Deposition

Necropsy at different time intervals after intravenous injection of quantum dots allowed us to visualize the sites where quantum dots accumulated. Digital imaging

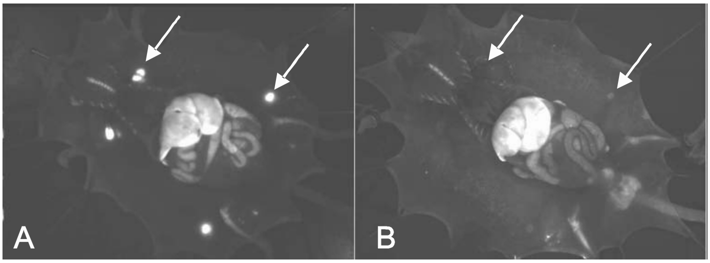

Fig. 2 Mice dissected 24 h post injection of mPEG-coated 655-nm-emitting amp-coated quantum dots. A, mPEG-750; B, mPEG-5,000. Liver, spleen, and bone marrow are labeled by both mPEG-coated quantum dots, but note the much decreased labeling of lymph nodes (arrows) by mPEG-5000 coated quantum dots in B

was performed using either broadband halogen lamps equipped with fiber optic cables and suitable filters, or by 1 or 5 watt power LEDs, typically 450 nm or 630 nm nominal emission wavelength. Quantum dots were found in the expected RES sites (liver, spleen, bone marrow, lymph nodes). What was unexpected was the very strong effect of seemingly minor changes in the secondary surface. Figure 2 shows that substitution of PEG-5000 for PEG-750 nearly abolishes lymph node deposition, while allowing uptake at other RES sites.

We tested the effects of using carboxy- or amino-terminated PEG substituents, typically at molar ratios of amino- or carboxy-PEG to mPEG (1:3). Some rules that emerged from this work were that charged surfaces result in rapid trapping in the RES; placing the charge on the tip of a PEG polymer mitigates the effect of charge, but the degree is dependent on the exact polymer used.[5] Hairpinning of the charged polymers (typically diamino or dicarboxyl), charge masking by methoxy PEG, and adsorption of non-covalently bound polymer all complicate a clear understanding of these effects. In further work, we assessed the effect of surface charge on migration from tumors to sentinel lymph nodes (see below).

1.5 Stability In Vivo

mPEG-5000-coated quantum dots were injected into Balb/c mice and nude mice (Balb/c background); subsequently, mice were euthanatized, then necropsied at intervals from 15 min to two years post injection. Organs were cleared in the order liver, spleen, followed by bone marrow; the quantum dots remained visible longest in lymph nodes (Fig. 3). Lymph nodes remained fluorescent for two years after injection, as assessed by both gross fluorescence and light microscopy of tissue sections (Fig. 4). This very long term signal is unprecedented; if similar stability can be engineered into quantum dot reagents for cell labeling, long-term tracer studies of (for example) stem cell deposition over months and years would be possible.

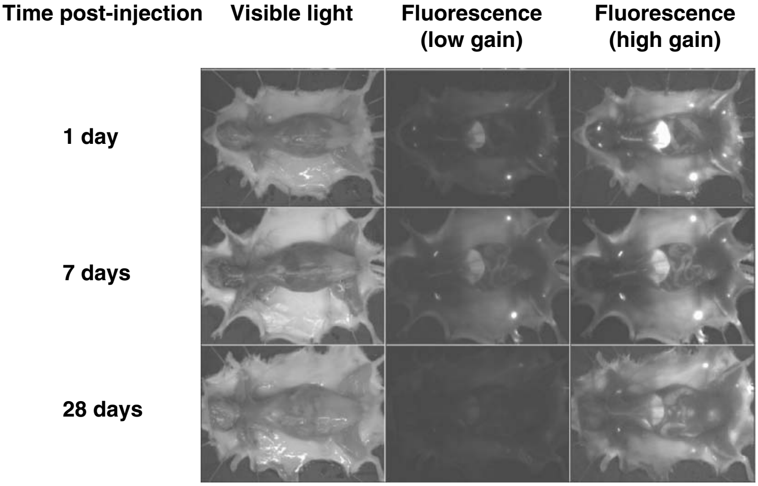

Fig. 3 Clearance of quantum dots after intravenous injection. Three mice, dissected at indicated times after injection; camera set to low sensitivity (low gain) or high sensitivity (high gain.) Organs cleared in the order liver, spleen, bone marrow, then lymph nodes

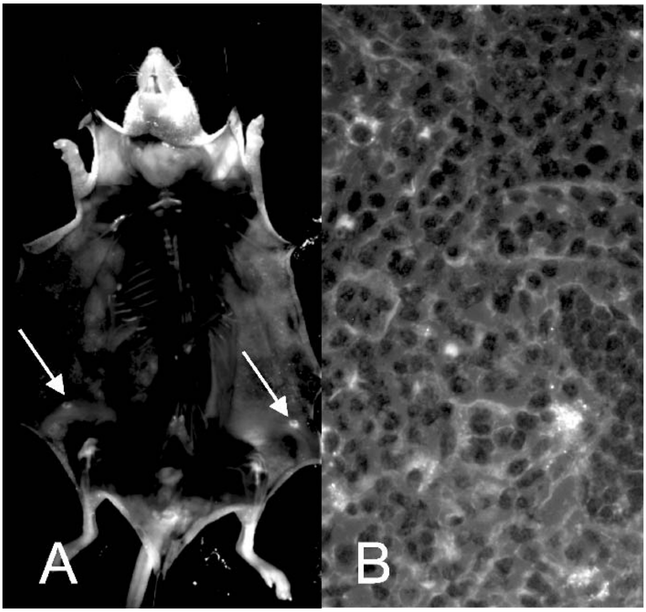

Fig. 4 Lymph nodes remain fluorescent two years after injection of 655-nm-emitting quantum dots. A. Whole mouse, showing fluorescence in inguinal nodes (arrows.) B. Paraffin section of left inguinal lymph node, showing quantum dots in scattered mononuclear cells. 10 µ section, hematoxylin stain, 400X

Examination of animals and tissue sections by an experienced veterinary pathologist in single-blind experiments showed neither local nor systemic effects from injections of as much as 400 picomoles of amp-PEG coated CdSe-ZnS quantum dots per animal.

It is worth asking whether the coating of the quantum dots or their segregation in a protected site is responsible for the long-term stability of these quantum dots in vivo. Hanaki et al. showed that mercaptoacetic acid-capped, albumin-coated quantum dots were stably fluorescent for several days after cellular uptake.[6] This coating would not be expected to be especially stable; thus it is at least possible that some endosomes provide a stabilizing site for quantum dots. It is unlikely that the quantum dots are retained by the same cells that originally mediated uptake; rather, several cycles of mononuclear phagocyte death and re-uptake of the quantum dots by scavenging phagocytes would be expected. However, we have not proved this; a small minority of long-lived phagocytes could account for our results.

1.6 Labeling the Lymphatic System

Quantum dots injected into almost any tissue will accumulate in draining lymph nodes, a very effective method of mapping lymphatic flow.[7–12] We have used quantum dot injection into the tail flesh of mice to map flow from the tissue into draining lymph nodes. By using 800 and 850 nm quantum dots, we were able to follow lymphatic flow non-invasively using time-lapse photography. Figure 5 shows six frames from one such labeling, displaying the pulsatile nature of the flow and the labeling of successive lymph nodes along the path.

While labeling multiple lymph nodes and the connecting lymphatics in a chain is a welcome development, this is probably not due to the passage of quantum dots through the filtration machinery of the lymph nodes. Mouse lymph nodes possess a pathway that allows circulation via the periphery of the node, by-passing the central regions; thus particles are not necessarily halted at the first node in a succession.[13] Upon dissection of the mouse shown in Fig. 5, the flow pathway could be seen more clearly (Fig. 6).

1.7 Sentinel Lymph Nodes

We used three tumor models to investigate whether varying the surface charges on our polymer-coated quantum dots would affect migration from the tumor to sentinel nodes, as we found that quantum dots having charged surfaces are more rapidly taken up in the RES. We injected paired quantum dots having neutral or charged (amino- or carboxy-) surfaces directly into tumors, then imaged adjacent lymph nodes both noninvasively and after necropsy. We found no effect of surface charge, a somewhat surprising result, given the effect of surface charge on lymph node

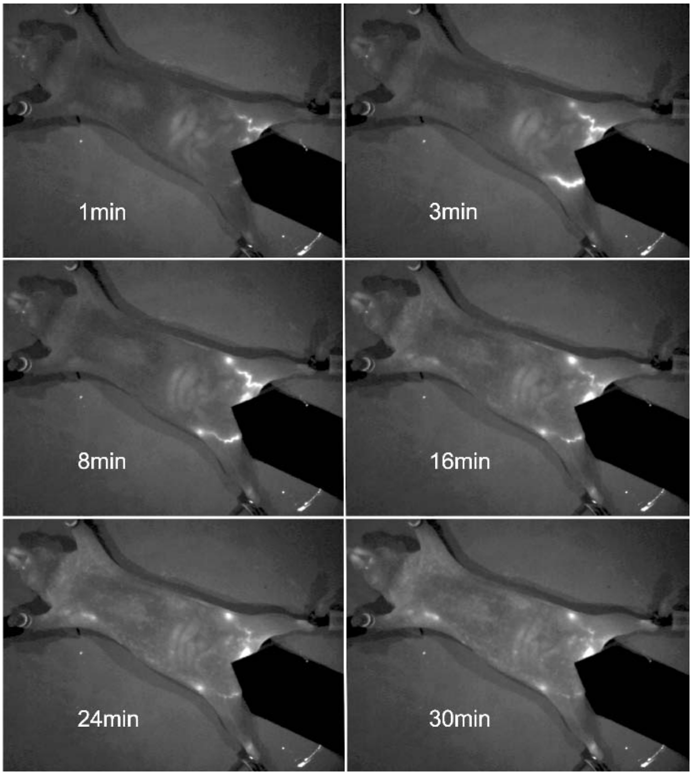

Fig. 5 Following quantum dots into lymph nodes. Mouse injected using 800-nm-emitting quantum dots in the tail interstitium. Note the rapid accumulation in lymph nodes, pulsatile flow in lymphatics, and absence of fluorescence in the general circulation

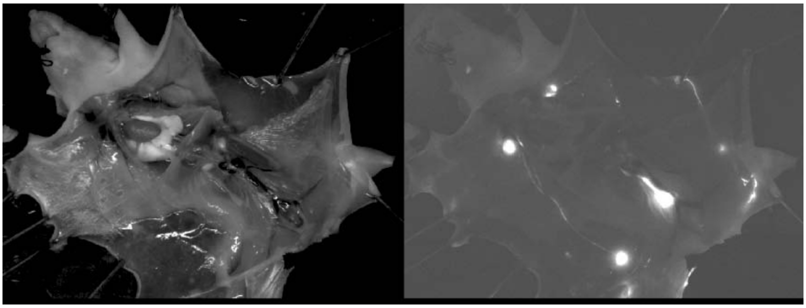

Fig. 6 Necropsy of mouse in Fig. 4. (Left) white light; (right) fluorescence. Note very bright lumbar nodes, bright inguinal and axillary nodes, and connecting lymphatics

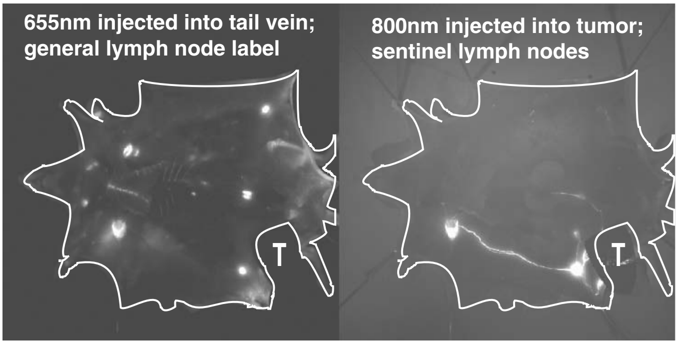

Fig. 7 Sentinel lymph node mapping. Nude mouse bearing M21 melanoma (right thigh); 655-nm-emitting carboxyl-quantum dots were injected intravenously into the tail vein, and 1 h later, 800-nm-emitting mPEG-5000 quantum dots were injected into the tumor. 30 min later, the mouse was necropsied and imaged. Note labeling of all lymph nodes by intravenous 655 nm quantum dots, while only sentinel nodes are labeled by intratumoral injection of 800 nm quantum dots. T, site of tumor; tumor is masked to allow visualization of sentinel lymph nodes

trapping of intravenously injected quantum dots. To demonstrate the different labeling of lymph nodes by intratumoral injection, and also to probe for unlabeled lymph nodes in the vicinity of tumors, we labeled lymph nodes generally by tail-vein injection of carboxyl-surfaced quantum dots, then injected quantum dots having a different emission wavelength into tumors; thus we could compare the two labels and map adjacent lymph nodes that did not drain the tumor. Figure 7 shows one result, where quantum dots injected intravenously labeled all the lymph nodes, while intratumoral injection labeled only lymph nodes in the vicinity of the tumor.

1.8 Labeling Tumors In Vivo

We have used two tumor-monoclonal antibody targeting models, the mouse MH-15 teratocarcinoma and the human M21 melanoma.[14,15] Both are well understood systems, which have a long history of targeting by antibody and fragments in mouse models. Both are easily targeted, with good antibody uptake and high tumor-to-normal tissue ratios when labeled using radioactive antibodies (ibid.). We prepared whole antibody and fragment conjugates to amp- and PEG-surfaced quantum dots, using tumor-targeting and isotype-matched control immunoglobulins; we also made antibody conjugates to Cy5 and Cy7 cyanine fluorochromes. Conjugates were tested for binding and specificity. We then mixed and co-injected the specific and non-specific antibody conjugates (for example, tumor-targeting antibody-800 nm quantum dots, non-specific antibody-655 nm quantum dots, and the reciprocal combination). We also co-injected combinations of the cyanine dye conjugates and quantum dot conjugates. In no case was there any specific tumor targeting by the quantum dot conjugates, while in all cases the cyanine dye conjugates targeted as expected. At no point did we see any evidence for passive uptake of the particles by either of the tumor models. In further experiments, we attempted to target quantum dots by first injecting biotinylated antibody, then injecting streptavidin-conjugated quantum dots; this approach also failed to give significant tumor targeting, possibly due to the extremely short circulating lifetimes of the streptavidin conjugates (minutes). Figure 8 shows a typical result of comparing cyanine-dye antibody conjugates to quantum dot conjugates. Cy5- and Cy7-conjugated antibodies were paired with 800 nm and 655 nm quantum dots, respectively. In both cases, the cyanine dye conjugates labeled the tumor, while neither of the quantum dot conjugates targeted.

The image displays another important point: Quantum dot conjugates do lodge in the RES, are retained there for at least days, and thus give a high nonspecific background. Of course, one may reduce the background by using quantum dots that emit in the visible; but the signal will be reduced correspondingly.

Given the level of effort expended by ourselves and others, it is surprising that there is only one report of successful tumor targeting by quantum dots in the literature.[4] What are the difficulties? One part is surely the relatively short serum lifetime of the conjugates, a problem that has dogged antibody conjugates from the beginning. It was to solve this problem that we prepared PEG–quantum dot conjugates. Part is the large size of the conjugates, which probably blocks extravasation; however, we note that whole IgM targets MH-15 well (one reason for choosing this tumor model); Fab2-quantum dot conjugates are about twice as large as whole IgM

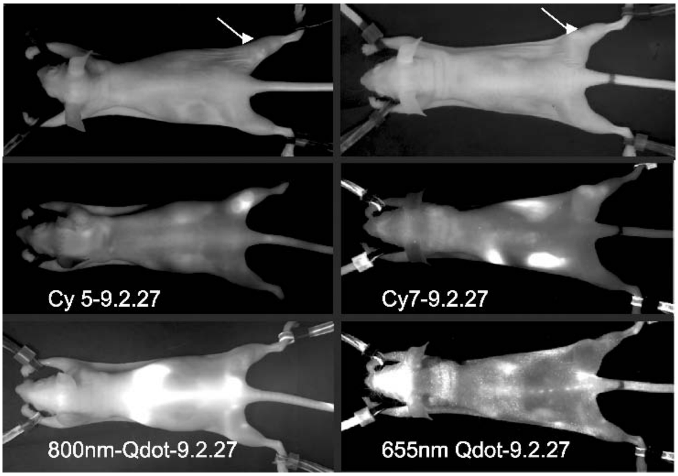

Fig. 8 Targeting of M21 human melanoma by Cy dye and quantum conjugates. Monoclonal antibody 9.2.27 was conjugated to quantum dots or to Cy5 and Cy7 as indicated. Cy5 and 800 nm Qdot conjugates were coinjected into one tumor-bearing mouse (left), while Cy7 and 655 nm Qdot conjugates were injected into another (right). (Top) visible light images; (middle) Cy dye windows; bottom, Qdot windows. Tumor (arrows) was targeted by Cy dye conjugates, but not by Qdot conjugates

(22 nm vs 12 nm). We believe that the size problem will be solved[16–19] and hope that smaller quantum dot conjugates that can extravasate will target tumors. Targeting quantum dots is certainly worth doing; organic dyes do provide an acceptable alternative,[20,21] but they are unlikely to afford sensitivity and stability comparable to that allowed by quantum dots.

2 Outlook

The studies by our group were directed toward an assessment of the practicality of amp-coated quantum dots for in vivo use. These reagents are stable in vivo and effective for vascular labeling, RES labeling, and sentinel lymph node identification at present. Toxicity was minimal or nonexistent, at least over the lifetime of the animals. However, these quantum dots have significant limitations, probably due to their size. We expect that these limitations will be overcome by synthesis of new quantum dots having smaller size and thinner coats. It remains to be seen whether such small quantum dots will have the high absorptivity and quantum yields that have made the current generation of quantum dots so useful.

Acknowledgements Monoclonal antibody 9.2.27 and M21 melanoma were kind gifts from R.A. Reisfeld. The authors are grateful for assistance with quantum dot manufacture by Joseph Treadway (present address: Invitrogen, 29851 Willow Creek Road, Eugene OR 97402). We also thank Lisa McGaw (Department of Biological Sciences, Carnegie Mellon University) for assistance with animal handling. This work was supported by NIH grant number R01 EB 000364. The work at Quantum Dot Corporation was partly funded by NIST-ATP 70NANB0H3000.

References

1. X. Wu, H. Liu, J. Liu, K. N. Haley, J. A. Treadway, J. P. Larson, N. Ge, F. Peale, and M. P. Bruchez, Immunofluorescent labeling of cancer marker her2 and other cellular targets with semiconductor quantum dots, *Nat. Biotechnol.* 21(1), 41–46 (2003).
2. D. R. Larson, W. R. Zipfel, R. M. Williams, S. W. Clark, M. P. Bruchez, F. W. Wise, and W. W. Webb, Water-soluble quantum dots for multiphoton fluorescence imaging in vivo, *Science* 300(5624), 1434–1436 (2003).
3. B. Ballou, B. C. Lagerholm, L. A. Ernst, M. P. Bruchez, and A. S. Waggoner, Noninvasive imaging of quantum dots in mice, *Bioconjug. Chem.* 15(1), 79–86 (2004).
4. X. Gao, Y. Cui, R. M. Levenson, L. W. Chung, and S. Nie, In vivo cancer targeting and imaging with semiconductor quantum dots, *Nat. Biotechnol.* 22(8), 969–976 (2004).
5. B. Ballou, Quantum dot surfaces for use in vivo and in vitro, *Curr. Top. Dev. Biol.* 70, 103–120 (2005).
6. K. Hanaki, A. Momo, T. Oku, A. Komoto, S. Maenosono, Y. Yamaguchi, and K. Yamamoto, Semiconductor quantum dot/albumin complex is a long-life and highly photostable endosome marker, *Biochem. Biophys. Res. Commun.* 302(3), 496–501 (2003).
7. S. Kim, Y. T. Lim, E. G. Soltesz, A. M. De Grand, J. Lee, A. Nakayama, J. A. Parker, T. Mihaljevic, R. G. Laurence, D. M. Dor, L. H. Cohn, M. G. Bawendi, and J. V. Frangioni, Near-infrared fluorescent type ii quantum dots for sentinel lymph node mapping, *Nat. Biotechnol.* 22(1), 93–97 (2004).

8. C. P. Parungo, Y. L. Colson, S. W. Kim, S. Kim, L. H. Cohn, M. G. Bawendi, and J. V. Frangioni, Sentinel lymph node mapping of the pleural space, *Chest* 127(5), 1799–1804 (2005).
9. C. P. Parungo, S. Ohnishi, A. M. De Grand, R. G. Laurence, E. G. Soltesz, Y. L. Colson, P. M. Kang, T. Mihaljevic, L. H. Cohn, and J. V. Frangioni, In vivo optical imaging of pleural space drainage to lymph nodes of prognostic significance, *Ann. Surg. Oncol.* 11(12), 1085–1092 (2004).
10. C. P. Parungo, S. Ohnishi, S. W. Kim, S. Kim, R. G. Laurence, E. G. Soltesz, F. Y. Chen, Y. L. Colson, L. H. Cohn, M. G. Bawendi, and J. V. Frangioni, Intraoperative identification of esophageal sentinel lymph nodes with near-infrared fluorescence imaging, *J. Thorac. Cardiovasc. Surg*. 129(4), 844–850 (2005).
11. E. G. Soltesz, S. Kim, S. W. Kim, R. G. Laurence, A. M. De Grand, C. P. Parungo, L. H. Cohn, M. G. Bawendi and J. V. Frangioni, Sentinel lymph node mapping of the gastrointestinal tract by using invisible light, *Ann. Surg. Oncol*. 13(3), 386–396 (2006).
12. E. G. Soltesz, S. Kim, R. G. Laurence, A. M. DeGrand, C. P. Parungo, D. M. Dor, L. H. Cohn, M. G. Bawendi, J. V. Frangioni, and T. Mihaljevic, Intraoperative sentinel lymph node mapping of the lung using near-infrared fluorescent quantum dots, *Ann. Thorac. Surg*. 79(1), 269–277 (2005).
13. M. C. Kowala and G. I. Schoefl, The popliteal lymph node of the mouse: Internal architecture, vascular distribution and lymphatic supply, *J. Anat*. 148, 25–46 (1986).
14. T. F. Bumol and R. A. Reisfeld, Unique glycoprotein-proteoglycan complex defined by monoclonal antibody on human melanoma cells, *Proc. Natl. Acad. Sci. U.S.A* 79(4), 1245–1249 (1982).
15. R. A. Reisfeld, Monoclonal antibodies to human malignant melanoma, *Nature* 298(5872), 325–326 (1982).
16. S. W. Kim, J. P. Zimmer, S. Ohnishi, J. B. Tracy, J. V. Frangioni, and M. G. Bawendi, Engineering inas(x)p(1-x)/inp/znse iii-v alloyed core/shell quantum dots for the near-infrared, *J. Am. Chem. Soc*. 127(30), 10526–10532 (2005).
17. J. H. Warner, A. Hoshino, A. Shiohara, K. Yamamoto, and R. D. Tilley, The synthesis of silicon and germanium quantum dots for biomedical applications, *Proceedings of SPIE-The International Society for Optical Engineering* 6096 (Colloidal Quantum Dots for Biomedical Applications), 13–20 (2006).
18. J. H. Warner, A. Hoshino, K. Yamamoto, and R. D. Tilley, Water-soluble photoluminescent silicon quantum dots, *Angew. Chem. Int. Ed. Engl*. 44 (29), 4550–4554 (2005).
19. J. P. Zimmer, S. W. Kim, S. Ohnishi, E. Tanaka, J. V. Frangioni, and M. G. Bawendi, Size series of small indium arsenide-zinc selenide core-shell nanocrystals and their application to in vivo imaging, *J. Am. Chem. Soc*. 128(8), 2526–2527 (2006).
20. B. Ballou, G. W. Fisher, T. R. Hakala, and D. L. Farkas, Tumor detection and visualization using cyanine fluorochrome-labeled antibodies, *Biotechnol. Prog*. 13(5), 649–658 (1997).
21. S. Ohnishi, S. J. Lomnes, R. G. Laurence, A. Gogbashian, G. Mariani, and J. V. Frangioni, Organic alternatives to quantum dots for intraoperative near-infrared fluorescent sentinel lymph node mapping, *Mol. Imaging* 4(3), 172–181 (2005).

This page intentionally blank

Towards Polymer-Based Capsules with Drastically Reduced Controlled Permeability

Daria V. Andreeva[1,*] **and Gleb B. Sukhorukov**[2]

Abstract Small molecules (dyes, therapeutics, etc.) could be easily handled, stored, delivered, and released by polyelectrolyte capsules. To make the polyelectrolyte capsule more efficient for small molecule encapsulation, capsule permeability should be significantly decreased. Here, we demonstrate the possibility to entrap water-soluble molecular species into polyelectrolyte capsules modified by a low permeable dense polymer (polypyrrole). Possible future areas in PE capsule application as carriers for gases and volatiles in the pharmaceutical, food, and gases industry, agriculture and cosmetology are discussed.

Keywords Coatings, microencapsulation, polyelectrolytes, polypyrrole, gases, volatiles

1 Introduction

Encapsulation of small molecules (gases), volatiles (fragrances, spice components, anesthetic drugs) and water-soluble compounds has been researched intensively over the past years. The chemical, biomedical, and food industries widely use oxygen (O_2), carbon dioxide (CO_2), nitrogen (N_2), ammonium oxide (NH_3), chlorine (Cl_2), and ethylene (C_2H_4). CO_2 and nitrous oxide (N_2O) are major greenhouse gases and huge amounts of CO_2 are released into the air upon the burning of fuels such as oil, coal, wood, and natural gas.[1,2] The anesthetic gases and vapors of concern are nitrous oxide and halogenated agents (vapors) such as halothane, enflurane, methoxyflurane, trichloroethylene, and chloroform.[3] They leak into the surrounding room

---

[1] Max Planck Institute of Colloids and Interfaces, Am Muehlenberg 1, 14476, Golm/Potsdam, Germany

[2] Department of Materials, Queen Mary, University of London, Mile End Road, E1 4NS, London, United Kingdom

[*] To whom correspondence should be addressed. E-mail: daria.andreeva@mpikg.mpg.de

M. Giersig and G. B. Khomutov (eds.),
Nanomaterials for Application in Medicine and Biology

during medical procedures and can cause nausea, dizziness, headache, fatigue, and irritability, as well as sterility, miscarriages, birth defects, cancer, and liver and kidney diseases among operating room staff.[4–10]

Controlling the retention of chemicals during product manufacture and their release during consumption are of major interest to pharmaceutical, cosmetics, and food manufacturers. The use of encapsulation to ensure chemical retention is well-established. Over the past decades, a very convenient method of layer-by-layer (LBL) adsorption of oppositely charged PE on the surface of colloidal template particles of 0.1–20 µm diameter was developed.[11] This technique permits the step-wise adsorption of various components as the layer growth is governed by their electrostatic attraction, and allows the formation of multilayer shells with nanometer (thickness) precision. The modification of the capsule shells by tailoring different functionalities and impregnating inorganic nanoparticles (fluorescent, magnetic, metal) provides multifunctional capsule applications.[12]

The capsule properties strongly depend on the core of a capsule and its shell materials. Core materials can be used as a template only and in this case should be dissolved to yield hollow containers.[13–15] Template cores for the fabrication of hollow capsules are desired to be monodisperse and completely dissoluble. Weakly cross-linked melamine formaldehyde lattices[13,16] and polystyrene lattices,[17] silica particles,[14] red blood cells,[18] and inorganic carbonate crystals ($CaCO_3$, $MnCO_3$, and $CdCO_3$)[19] seem very promising for carrier formation. Shell polymers are classified in accordance with the type of external condition that causes their structural change (pH and ionic strength,[20,21] temperature,[15] irradiation of light,[22] etc.).

To entrap small molecules (e.g., gases, volatiles, fragrances) in PE capsules, the encapsulation technique and novel shell and core materials should be researched and developed. We propose the following ways of small molecule encapsulation into defined hollow volume cages: 1) bubble stabilization (PE layers are supposed to be formed on the surfaces of surfactant-stabilized bubbles filled with a particular gas); 2) solidified volatiles can be used as cores for LBL (vanillin, naphthalene); 3) gases and volatiles might be trapped with molecular sorbents (cyclodextrin, cucurbit[7]uril, amylose) and then covered with polyelectrolytes.

2 Novel Polymer Materials for Low Permeable Capsule Walls

At present, the most important and interesting trend in encapsulation technology is the control of capsule permeability. Bruening et al.[23,24] managed to obtain high-selective gas separation planar membranes using the technique of alternating polyelectrolyte deposition. This method involves the alternating immersion of charged substrates in solutions containing oppositely charged polyelectrolytes. The thickness and permeability of the membranes was shown to be very easy to control by the number of the layers and deposition variables as pH, supporting salt concentration and solvents. Thus, polyelectrolyte multilayers could be used for capturing and storing gas and other volatile compounds.

The PE capsules are hydrophilic. Capsule usage, especially as drug carriers, occurs mostly in aqueous media which causes swelling of the PE shells and even increases capsule permeability. Several attempts were made to encapsulate low molecular weight compounds manipulating the shell polymer structure. Koehler et al.[25] developed the method of PE capsule sealing by temperature treatment. The PE capsules are saturated with the encapsulate and subsequently temperature treated which causes polymer conformation changes and capsule shrinkage. However, the permeability for encapsulated macromolecules was only slowed down due to increased thickness.

We suggested an alternative way to control capsule permeability. According to this method, the capsule surface should be coated by a low permeable polymer.[26] The inspiration for this kind of coating came from gas separation membrane formation principles.[27] Highly selective polymers are usually characterized by very low permeability. To increase membrane efficiency, a nanometer gas-selective working layer is formed on the surface of a high permeable polymer support providing proper mechanical properties. This type of membrane structure is known as a composite membrane. That means that the coating material should not be hydrophobic so as not to exhibit water-resistant properties or low permeability. To obtain a homogeneous and nonporous cover on PE capsules, two main features are important: a coating polymer should have affinity to one of the shell components and form dense and low permeable films.

Over the past years, conductive polymer coatings have been intensively developed and studied.[27] One of the conducting polymers, polypyrrole (PPy), was found to exhibit outstanding gas selectivity and low permeability.[28]

PPy has been widely studied during the last decades mostly due to its electrochemical properties, easy synthesis, and stability in air.[28] Furthermore, PPy films are characterized by outstanding density due to π electron delocalization along the polymer chains and their high stiffness.[29] At the same time, PPy is known to be a very brittle material and not able to form films.[30] To overcome these disadvantages *in situ* pyrrole polymerization on a supporting polymer was developed. This method results in a composite membrane structure formed by two layers: a selective skin PPy layer and a polymer support. Andreeva et al.[31] developed and characterized gas separation composite membranes based on PPy and poly (phenylene) oxide as a polymer support. The PPy layer was shown to be homogeneous and defectless and exhibited very high selectivity for gases. Furthermore a PPy skin layer formed on the capsule surface might supply the desired properties to PE shells. Apart from its low permeability, the transport properties of PPy coating can be changed by a redox process.[29] That means that the polymer changes reversibly from a neutral (reduced) to an oxidized (charged) state. As a result, important structural changes take place in the polymer, which passes from a compact (neutral) state to a gel (oxidized) state because the polymer matrix swells during oxidation as water and counterions penetrate into the polymer matrix.[32] Due to this selective, membrane-like behavior of PPy, the controlled permeability through capsule shells can occur.

In a previous article,[26] we described a novel method of PPy coating formation on PE microcapsules. We proposed a way of encapsulating water-soluble compounds that is based on the formation of dense PPy coating on the capsule surface. PPy

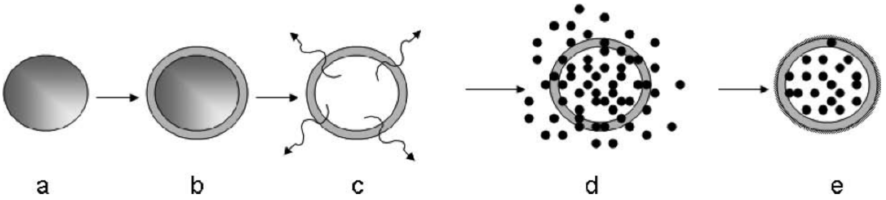

Fig. 1 Sketch of capsule preparation and PPy modification

deposition from 10 wt% aqueous polymer solution was found the most effective method of capsule modification. In this case, homogeneous and defectless PPy coatings can be formed. The magnetic microcapsules containing consequent layers of iron oxide and poly(allylamine hydrochloride) (PAH) with external poly(sodium 4-styrenesulfonate) (PSS) layers were used for the encapsulation of water-soluble species. As a model compound, the water-soluble dye tetramethylrhodamine isothiocyanate (TRITC) was used. To encapsulate water-soluble compounds by shell modification method, both encapsulation and capsule sealing processes should be carried out simultaneously (Fig. 1).

The capsules were saturated with TRITC solution first, then the PPy layer was formed to trap the encapsulated compounds inside the capsule cages. The magnetic properties of the capsule shell allowed to apply gentle capsule sedimentation with a constant magnet instead of using a centrifugation process. In this way, we managed to avoid mechanical impact on the brittle PPy shell which might cause shell rupture. As a result, the low permeable capsules with the maximum concentration of magnetite nanoparticles were prepared.

3 Perspectives

Our results showed the principle possibility of PPy usage for water-resistant capsule formation. PPy is able to form homogeneous and defectless coatings on PE capsule surfaces not causing capsule deformation or aggregation. This approach to capsule modification significantly expands capsule handling and application. PPy coatings provide control over capsule permeability by a PPy redox process. Furthermore, PPy is approved for medical application and can be safely used in pharmacology and cosmetology. The high surface energy of PPy films offers the possibility of direct sorption of some active molecules on the capsule surfaces.

Potential applications of low capsule permeability include a wide range of fields in pharmaceutics, cosmetology, the food and agricultural industries (Fig. 2). First of all, PPy-covered capsules can be used for gas encapsulation. The controlled storage, release, and transportation of gases is desirable in a huge range of sectors. Oxygen (O_2) is of great importance in such diverse areas as medicine and steel making,

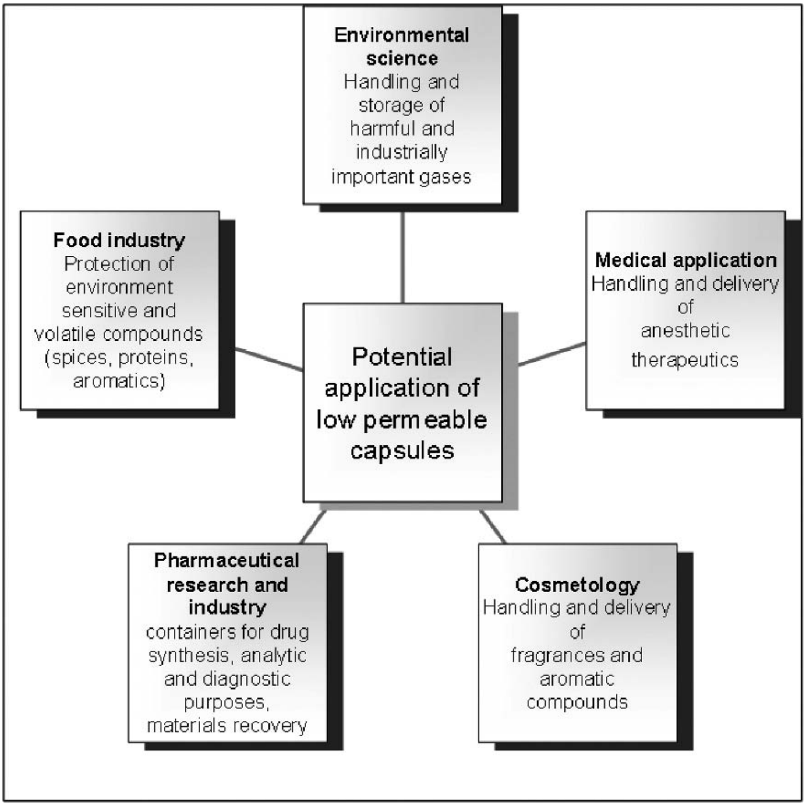

Fig. 2 Potential applications of the low permeable capsules

while nitrogen (N_2) is utilized in space technology and in the production of ammonia (NH_3). The safe storage and transportation of hydrogen (H_2) is important for its utilization as fuel in car engines or aircraft turbines.[33,34]

The encapsulation of gases is based on the usage of nanoscale sorbents for gas trapping. Recently, Leontiev and Rudkevich[35,36] demonstrated that a simple molecular container, a hemicarcerand, reversibly traps, stores, and exchanges gases in the solid state at normal temperatures and pressures. The molecular complexes, gas – molecular trapper, can be used as a core for PE shells with barrier properties.

Another way of gas encapsulation is the stabilization of hollow gas-filled microbubbles. The polymeric shells can be formed around microbubbles and, therefore, stabilize them. Cavalieri et al.[37] entrapped air in a polymer shell obtained by chemically cross-linking modified poly(vinyl alcohol) at the air-water interface. These bubbles exhibited unusual chemical and colloidal stability and could be used as potential drug delivery devices. Furthermore, as dense a polymer as PPy might form a barrier coating for gases on surfaces of microbubbles filled with a particular gas. The bubbles can be generated by ultrasound method or by membrane emulsification and stabilized by *in situ* pyrrole polymerization.

One of the most challenging demands with regard to volatile and gas encapsulation concerns pharmaceutical compounds. Several drugs, including some cancer therapeutics and volatile anesthetics, are highly fluorinated. Many of these fluorinated drugs cannot be safely delivered orally or intravenously.[38] We propose to use an encapsulation process to create nano/microcapsules of volatile drugs, allowing their intravenous delivery. The development of the encapsulation technology provides the following benefits:

- It allows intravenous delivery of gaseous anesthetics and other fluorinated compounds.
- It provides a way to induce anesthesia in patients who cannot be intubated.
- Intravenous injection of encapsulated anesthetics could be used to quickly boost anesthesia if needed.
- Encapsulation can prolong the anesthetic effect.
- Capsule shell modification might significantly reduce possible side effects due to targeted delivery and controlled release.
- Capsules may also be useful for drug synthesis, for analytic and diagnostic purposes, for the sequestering of molecules for materials recovery, and for pollution abatement.

Similar methods to the ones described above for possible gas encapsulation could be applied to anesthetic gases. The enhancement of drug-delivery performance using formulations based on cyclodextrin – drug inclusion complexes, such as improved drug stability, solubility, dissolution rate and, in some instances, reduction of adverse side effects, is well known.[39] These complexes could also be used as cores for PE shells and then sealed by PPy or another low permeable polymer.

The process of encapsulation is widely employed in the flavor industry to protect volatile and/or labile flavoring materials during storage (Fig. 3).[40]

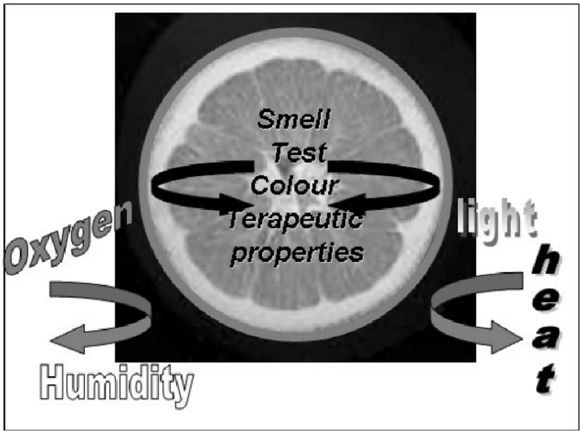

Fig. 3 Protection of volatiles by using low permeable coatings

Encapsulation of interest to the food industry involves the incorporation of food ingredients, enzymes, cells, or other components into coating materials. One of the largest fields within flavor encapsulation are food and cosmetic oils. Encapsulation can significantly prolong their aromatic properties. The spice flavors, for example, are incorporated into processed foods, mainly by essential oil or by active components of solvent-extracted spices (oleoresin).[41] Oleoresin is known to undergo oxidative degradation. Volatile encapsulation techniques are well known in the food and cosmetics industry. They include spray drying, spray chilling, or spray cooling, extrusion coating, fluidized bed coating, liposome entrapment, coacervation, inclusion complexation, centrifugal extrusion, and rotational suspension separation.[42] Applications for this technique have increased in the food industry since the encapsulated materials can be protected from moisture, heat, or other extreme conditions, thus enhancing their stability and maintaining their viability. A disadvantage is that the properties of the capsules are difficult to control. All the encapsulation techniques listed above result in the simple coating of the encapsulates by the shell material. In such a case, the coatings can hardly be modified and functionalized. Therefore, the capsules cannot be delivered to the particular place and opened at the moment that is crucial for successful application. Volatiles and fragrances can be entrapped into a PE shell either in the form of the above-described complexes or in solidified forms. Vanillin, for example, could be one of the model compounds to study the encapsulation of volatiles (Fig. 4).

Thus, PPy coating presents a new approach in the control over capsule permeability. The dense packing of PPy chains could easily seal off the low-molecular-weight

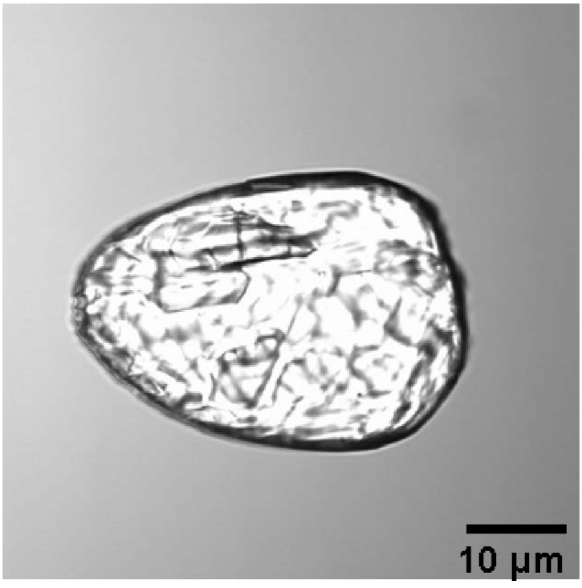

Fig. 4 Optical microscopy image of vanillin crystals covered by one layer of PPy

encapsulates in nanometer-size capsule cages. PPy as well as a wide range of other polymer materials with similar properties (hydrophobic (paraffin, wax), water resistant (polyurethanes), etc.) open up an alternative area in PE capsule application. Therefore, aromatic compounds, fragrances, and gases can be successfully encapsulated, targeted, delivered, and released.

Acknowledgements This work was supported by EU-project STREP N001428 "Nanocapsules for targeted delivery of chemicals". Prof. Dr. Helmuth Möhwald is greatly acknowledged for reading the manuscript and giving valuable comments.

References

1. N. W. Frank, Introduction and historical review of electron beam processing for environmental pollution control, *Radiat. Phys. Chem.* 45(6), 989–1002 (1995).
2. Y. H. Wang and D. J. Jacob, Anthropogenic forcing on tropospheric ozone and OH since preindustrial times, *J. Geophys. Res.* 103(D23), 31,123–31,136 (1998).
3. J. Stachnik, Inhaled anesthetic agents, *Am. J. of Health-Syst. Pharm.* 63, 623–634 (2006).
4. A. A. Malekirad, A. Ranjbar, K. Rahzani, M. Kadkhodaee, A. Rezaie, B. Taghavi, and M. Abdollahi, Oxidative stress in operating room personnel: Occupational exposure to anesthetic gases, *Hum. Exp. Toxicol.* 24(11), 597–601 (2005).
5. American Society of Anesthesiologists, Occupational disease among operating room personnel: A national study. Report of an ad hoc committee on the effect of trace anesthetics on the health of operating room personnel, *Anesthesiology* 41, 321–340 (1970).
6. National Institute for Occupational Safety and Health (NIOSH) Criteria for a Recommended Standard: Occupational Exposure to Waste Anesthetic Gases and Vapors U.S. Department of Health and Human Services, Public Health Service, Centers for Disease Control and Prevention: Cincinnati, Ohio (1977) DHEW Pub. No. 77B140.
7. G. Smith and A. W. Shirley, A review of the effects of trace concentrations of anaesthetics on performance, *Br. J. Anaesth.* 50(7), 701–712 (1978).
8. E. N. Cohen, C. H. Gift, W. B. Brown, W. Greenfield, M. L. Wu, T. W. Jones, C. E. Whitcher, E. J. Driscoll, and J. B. Brodsky, Occupational disease in dentistry and chronic exposure to trace anesthetic gases, *J. Am. Dent. Assoc.* 101, 21–31 (1980).
9. S. S. Guirguis, L. P. Pelmear, L. M. Roy, and L. Wong, Health effects associated with exposure to anaesthetic gases in Ontario hospital personnel, *Brit. J. Ind. Med.* 47(7) 490–7 (1990).
10. K. Hoerauf, M. Lierz, G. Wiesner, K. Schroegendorfer, P. Lierz, A. Spacek, L. Brunnberg, and M. Nüsse, Genetic damage in operating room personnel exposed to isoflurane and nitrous oxide, *Occup. Environ. Med.* 56(7), 433–437 (1999).
11. G. Decher, Fuzzy Nanoassemblies: Toward Layered Polymeric Multicomposites, *Science* 277(5330), 1232–1237 (1997).
12. (a) G. B. Sukhorukov, H. Möhwald, G. Decher, and Y. M. Lvov, Assembly of polyelectrolyte multilayer films by consecutively alternating adsorption of polynucleotides and polycations, *Thin Solid Films* 286, 220–223 (1996); (b) Y. Lvov, K. Ariga, and T. Kunitake, Assembly of multicomponent protein films by means of electrostatic layer-by-layer adsorption, *J. Am. Chem. Soc.* 117, 6117–6123 (1995); (c) S. W. Keller, S. A. Johnson, E. S. Brigham, E. H. Yonemoto, and T. E. Mallouk, Photo induced charge separation in multilayer thin films growth by sequential adsorption of polyelectrolytes, *J. Am. Chem. Soc.* 117, 12879–12880 (1995); (d) G. Decher, B. Lehr, K. Lowack, Y. Lvov, and J. Schmitt, New nanocomposite films for biosensors: Layer-by-layer adsorbed films of polyelectrolytes, proteins or DNA, *Biosens. Bioelectron.* 9, 677–684 (1994); (e) G. B. Sukhorukov, M. M. Montrel, A. I. Petrov, L. I. Shabarchina, and B. I. Sukhorukov, Multilayer films containing immobilized nucleic

acids. Their structure and possibilities in biosensor applications, *Biosens. Bioelectron.* 11(9), 913–922 (1996); (f) G. B. Sukhorukov, J. Schmitt, and G. Decher, Reversible swelling of polyanion/polycation multilayers films in solutions of different ionic strength, *Ber. Bunsen-Ges. Phys. Chem.* 100, 948–953 (1996).

13. Y. S. Gu, A. E. Decker, and D. J. McClements, Production and characterization of oil-in-water emulsions containing droplets stabilized by multilayer membranes consisting of β-lactoglobulin, ι-carrageenan and gelatin, *Langmuir* 21(13), 5752–5760 (2005).
14. A. A. Antipov and G. B. Sukhorukov, Polyelectrolyte multilayer capsules as vehicles with tunable permeability, *Adv. Colloid Interface Sci.*, 111(1–2), 49–61 (2004).
15. X. Qiu, S. Leporatti, E. Donath, and H. Möhwald, Studies on the drug release properties of polysaccharide multilayers encapsulated Ibuprofen microparticles, *Langmuir* 17(17), 5375–5380 (2001).
16. G. Ibarz, L. Dähne, E. Donath, and H. Möhwald, Smart micro- and nanocontainers for storage, transport, and release, *Adv. Mater.* 13, 1324–1327 (2001).
17. C. Déjugnat and G. B. Sukhorukov, Ph-responsive properties of hollow polyelectrolyte microcapsules templated on various cores, *Langmuir* 20, 7265–7269 (2004).
18. B. Neu, A. Voigt, R. Mitlohner, S. Leporatti, C. Y. Gao, E. Donath, H. Kiesewetter, H. Möhwald, H. J. Meiselman, and H. Bäumler, Biological cells as templates for hollow microcapsules, *J. Microencapsulation* 18(3), 385–395 (2001).
19. G. B. Sukhorukov, D. V. Volodkin, A. M. Günther, A. I. Petrov, D. B. Shenoy, and H. Möhwald, Porous calcium carbonate microparticles as templates for encapsulation of bioactive compounds, *J. Mater. Chem.* 14, 2073–2081 (2004).
20. D. Yoo, S. S. Shiratori, and M. F. Rubner, Controlling bilayer composition and surface wettability of sequentially adsorbed multilayers of wear polyelectrolytes, *Macromolecules* 31, 4309–4318 (1998).
21. S. A. Sukhishvili and S. Granick, Layered, erasable, ultrathin polymer films, *J. Am. Chem Soc.*, 122, 9550–9551 (2000).
22. K. G. Yager and C. J. Barrett, All-optical patterning of azo polymer films, *Curr. Opin. Solid State Mater. Sci.* 5(6), 487–494 (2001).
23. K. P. Xiao, J. J. Harris, A. Park, C. M. Martin, V. Pradeep, and M. L. Bruening, Formation of ultrathin, defect-free membranes by grafting of poly(acrylic acid) onto layered polyelectrolyte films, *Langmuir* 17, 8236–8241 (2001).
24. D. M. Sullivan and M. L. Bruening, Ultrathin, Gas-selective polyimide membranes prepared from multilayer polyelectrolyte films, *Chem. Mater.* 15, 281–287 (2003).
25. K. Köhler, D. Shchukin, H. Möhwald, G. B. Sukhorukov, Thermal behavior of polyelectrolyte multilayer microcapsules. The effect of odd and even layer number, *J. Phys. Chem. B* 109, 18250–18259 (2005).
26. D. V. Andreeva, D. A. Gorin, D. G. Shchukin, and G. B. Sukhorukov, Magnetic microcapsules with low permeable polypyrrole skin layer, *Macromol. Rapid Commun.* 27(12), 931–936 (2006).
27. R. E. Kesting and A. K. Fritzsche, *Polymeric gas separation membranes* (Wiley, New York, 1993).
28. R. V. Parthasarathy, V. P. Menon, and C. R. Martin, Unusual gas-transport selectivity in a partially doped form of the conductive polymer polypyrrole, *Chem. Mater.* 9, 560–566 (1997).
29. J. A. Conklin, T. M. Su, S. C. Huang, and R. B. Kaner, Gas and liquid separation applications of polyaniline membrane, in: *Handbook of conductive polymers*, T. A. Skotheim (ed.) (Marcel Dekker, New York, 1986), pp. 945–962.
30. M. C. De Jesus, R. A. Weiss, and Y. Chen, The development of conductive composite surfaces by a diffusion-limited in situ polymerization of pyrrole in sulfonated polystyrene ionomers, *Polym. Sci.: part B: Polym. Phys.*, 1997, 35(2), 347–357.
31. D. V. Andreeva, Z. Pientka, L. Brozová, M. Bleha, G. A. Polotskaya, and G. K. Elyashevich, Effect of polymerization conditions of pyrrole on formation, structure and properties of high gas separation thin polypyrrole films, *Thin Solid Film* 406(1), 54–63(10) (2002).

32. J. J. Lopez Cascales, A. J. Fernandez, and T. F. Otero, Characterization of the reduced and oxidized polypyrrole/water interface: A molecular dynamics simulation study, *J. Phys. Chem. B* 107 (35), 9339–9343, (2003).
33. G. Brunner, *Gas extraction: An introduction to fundamentals of supercritical fluids and the application to separation processes* (Steinkopff, Darmstadt, 1994).
34. W. Peschka, Operating characteristics of a LH_2-fuelled automotive vehicle and of a semi-automatic LH_2-refuelling station, *Int. J. Hydrogen Energy* 7(8), 661–669 (1982).
35. A. V. Leontiev and D. M. Rudkevich, Encapsulation of gases in the solid state, *Chem. Commun*. 2004, 1468–1469.
36. D. M. Rudkevich, Emerging supramolecular chemistry of gases, *Angew. Chem. Int. Ed. 43*, 558–571 (2004).
37. Y. F. Cavalieri, A. E. Hamassi, E. Chiessi, and G. Paradossi, Tethering functional ligands onto shell of ultrasound active polymeric microbubbles, *Biomacromolecules* 7, 604–611 (2006).
38. A. El-Aneed. An overview of current delivery systems in cancer gene therapy, *J.Controlled Release* 94(1), 1–14 (2004).
39. J. Szejtli, Introduction and general overview of cyclodextrin, *Chem. Rev*. 98(5), 1743–1754 (1998).
40. K. G. H. Desai and H. J. Park, Recent developments in microencapsulation of food ingredients, *Drying Technol*. 23, 1361–1394 (2005).
41. J. Shaikh, R. Bhosale, and R. Singhal, Microencapsulation of black pepper oleoresin, *Food Chem*. 94(1), 105–110 (2006).
42. T. A. Reineccius, G. A. Reineccius, and T. L. Peppard, The effect of solvent interactions on α-, β-, and γ-Cyclodextrin/Flavor molecular inclusion complexes, *J. Agric.Food Chem.,* 53(2), 388–392 (2005).

Polyelectrolyte-Mediated Transport of Doxorubicin Through the Bilayer Lipid Membrane

Alexander A. Yaroslavov[1,*], Marina V. Kitaeva[1], Nikolay S. Melik-Nubarov[1], and Frederic M. Menger[2]

Abstract A model is developed for the effect of ionic polymers on the transport of doxorubicin, an antitumor drug, through a bilayer membrane. Accordingly, a protonated (cationic) form of doxorubicin binds to an anionic polymer, poly(acrylic acid), the resulting complex being several hundred nanometers in size. Nevertheless, large complex species associate with neutral egg lecithin liposomes by means of hydrophobic attraction between the doxorubicin and the liposome bilayer. Then, the doxorubicin enters the liposome interior which has been imparted with an acidic buffer to protonate the doxorubicin. The rate of transmembrane Dox permeation decreases when elevating the polyacid-to-doxorubicin ratio. A cationic polymer, polylysine, being coupled with liposomes containing the negative lipid cardiolipin, accelerates membrane transport of doxorubicin with the maximum rate at a complete neutralization of the membrane charge by an interacting polycation. The effect of a polycation on doxorubicin transport becomes more pronounced as small negative liposomes (60–80 nm in diameter) are changed to larger ones (approx. 600 nm in diameter). An opportunity thus opens up for the manipulation of the kinetics of drug uptake by cells and, ultimately, the control of the pharmaceutical action of drugs.

Keywords Polyelectrolytes, doxorubicin, liposomes, membrane transport

1 Introduction

A controllable delivery of bioactive compounds into affected cells is a key problem in modern pharmacology. A great variety of compounds with high therapeutic potentials has been developed up to now; however, in practice, their use is often

---

[1] School of Chemistry, M.V. Lomonosov Moscow State University,
Leninskie Gory, Moscow 119899, Russia

[2] Department of Chemistry, Emory University, Atlanta, GA 30322, USA

[*] To whom correspondence should be addressed. E-mail: yaroslav@genebee.msu.ru

M. Giersig and G. B. Khomutov (eds.),
Nanomaterials for Application in Medicine and Biology

restricted by side-effects which they cause when being administered systemically.[1,2] An addressed delivery can decrease undesirable effects of drugs and increase their therapeutic activities.[3]

Over the last thirty years, a promising drug targeting approach has been designed based on the use of synthetic and native ionic polymers (polyelectrolytes). In particular, it has been shown that complexation of bioactive compounds with polyelectrolytes results in an increase in the former's circulation time in the body[4,5] and decrease in their toxicity[6] and it also ensures the protection of drugs from the surrounding environment[7] and their delivery to target cells and organs.[5,8]

However, in spite of impressive achievements, a number of principal questions still require to be addressed in more detail. This, e.g., concerns the kinetics and the mechanism of polyelectrolyte-mediated drug transport through the biological membrane. To examine this problem, a suspension of bilayer lipid vesicles (liposomes) can be applied. Liposomes of different compositions and sizes have served as cell-mimetic systems in studies of the effects produced by interacting polymers in biological membranes: clusterization of lipids,[9–11] polymer-mediated lipid flip-flop,[11,12] increase in membrane permeability,[13–15] fusion of membranes,[16,17] and others.

In the present paper, we describe the composition, structure, and stability of complexes formed by polyelectrolytes with liposomes and an antitumor drug, doxorubicin (Dox), and how the complexation influences the membrane transport of Dox. The following points were investigated:

- Complexation of an anionic polymer, poly(acrylic acid) (PAA) with Dox
- Interaction of PAA–Dox complexes with neutral and negative liposomes
- Binding of a cationic polypeptide poly-L-lysine (PL) on the membrane of negative liposomes
- Kinetics and mechanism of polyelectrolyte-mediated Dox membrane transport

2 Experimental

Dox from the *Russian Institute of Antibiotics* (Russia), egg yolk lecithin (EL) and cardiolipin (CL^{-2}) from *Bioleck* (Ukraine), 1,2-dipalmitoylphosphoethanolamine-N-[methoxy(polyethylene glycol)-1,000] (DPPA-POE) from *Avanti* (USA) as well as PAA with M_w = 5,000, PL with M_w = 15,700, and the buffer components: tris(hydroxymethyl) aminomethane (Tris) and N-2-hydroxyethylpiperazine-N′-ethanesulfonate free acid (HEPES) from *Sigma-Aldrich* (USA) were used as received. Concentrations of polyelectrolytes are given in moles of monomer units per liter.

Fluorescence measurements were performed using an F-4000 fluorescence spectrophotometer (*Hitachi*, Japan). Mean hydrodynamic diameters of liposomes, PAA–Dox complex particles and products of their interaction with liposomes were measured by photon correlation spectroscopy using an Autosizer IIc (*Malvern*, UK) equipped with a He-Ne-laser.

Small neutral EL liposomes (60–80 nm in diameter) as well as large negative EL/CL^{-2} binary and EL/CL^{-2}/DPPC-POE ternary liposomes (approx. 600 nm in diameter) were prepared using sonication and phase-reverse techniques.[18] Suspensions of pH-gradient small EL and EL/CL^{-2} liposomes, and pH-gradient large EL/CL^{-2}/DPPC-POE liposomes with pH 7 outside and pH 4 inside were prepared as described previously.[19]

To measure PAA concentration in the samples, the procedure based on the ability of polyacrylate anions to quench Dox fluorescence[20] was used. Briefly, increasing aliquots of PAA were mixed with a 50 µM solution of Dox and the fluorescence of Dox ($\lambda_{ex} = 490$ nm, $\lambda_{em} = 555$ nm) was measured to produce a calibration curve, which was linear up to 60 µM of PAA. To measure the concentration of PAA in the unknown sample, it was mixed with 50 µM Dox solution, and the residual fluorescence was measured under conditions identical to those used for the calibration curve. To measure PAA in the more concentrated solutions, the samples were diluted, so that the residual fluorescence fell into the range of the calibration curve. Concentrations of Dox in the samples were determined spectrophotometrically taking an extinction coefficient $\varepsilon = 10{,}500\,\mathrm{cm^{-1}M^{-1}}$.[21]

The experiments were performed in a 20 mM Hepes–Tris buffer solution, pH 7.0, at 20 °C. To prepare solutions, double-distilled water was used which had been additionally treated by passing it through Milli-Q system (*Millipore*, USA) equipped with ion-exchange and adsorption columns as well as a filter to remove large particles.

3 Results and Discussion

3.1 *Complexation of Anionic Polymer with Dox*

The pK_0 for PAA carboxylic groups is equal to 4.8, the Dox molecule (Fig. 1) contains an amino group with a pK of 8.6. Therefore, complexation of PAA to Dox was studied at pH 7 to realize electrostatic interactions between both components. The addition of increasing PAA amounts to a solution of Dox was accompanied by a decrease in Dox fluorescence. A dependence of the relative fluorescence intensity, measured at $\lambda_{em} = 555$ nm ($\lambda_{ex} = 490$ nm), on $\varphi = [\mathrm{PAA}]/[\mathrm{Dox}]$ is given in Fig. 2. Because the polyacrylate anion is not a fluorescence quencher, the observed significant decrease in Dox fluorescence intensity is apparently due to the stacking interactions of Dox molecules immobilized along PAA chains. This indicated, in turn, a formation of a PAA–Dox complex stabilized by multiple ionic bonds between the PAA chain and the Dox ensemble.

Further addition of NaCl to the PAA–Dox complex solution resulted in an increase of the Dox fluorescence intensity which indicated a release of Dox molecules from the complex species. A complete dissociation of the complex was observed at [NaCl] = 0.4 M (Fig. 3, curve 1). Thus, electrostatic PAA–Dox and stacking Dox–Dox interactions contributed to the stabilization of PAA–Dox complexes.

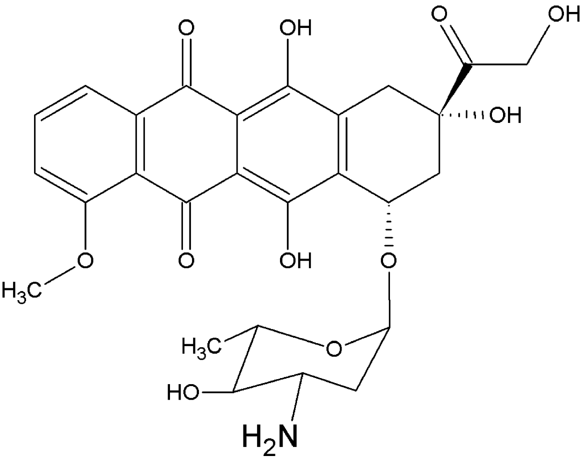

Fig. 1 Structural formula of doxorubicin

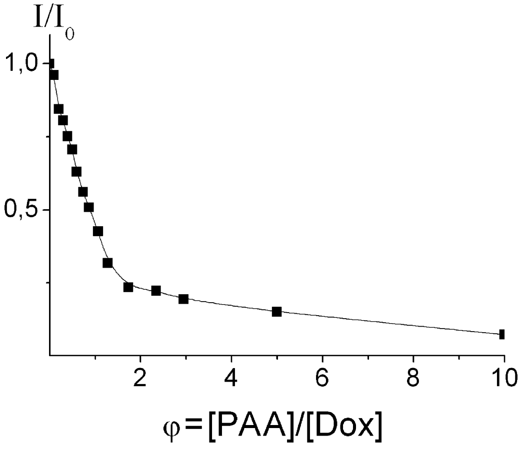

Fig. 2 Dependence of relative Dox fluorescence intensity on the PAA/Dox ratio. [Dox] = 50 μM

Using dynamic light scattering, it was found that the complexation was accompanied by the appearance of large particles. Their size fluctuated within the 600–900-nm range when changing the [PAA]/[Dox] ratio from 0.3 up to 5.

The composition of the PAA–Dox complexes was determined by ultrafiltration. Solutions containing PAA and Dox at different ratios were passed through microcentrifuge filters with 5-nm pores. Only PAA and Dox molecules passed through the filters (shown in separate experiments), but large complex particles did not. This allowed us to estimate the concentrations for PAA and Dox uninvolved in the complexation. The results are presented in Fig. 4 as dependences of $[PAA]_{unbound}$ and $[DOX]_{unbound}$ on φ. As follows from this figure, unbound PAA could be found only at $\varphi > \varphi_0$ (curve 1).

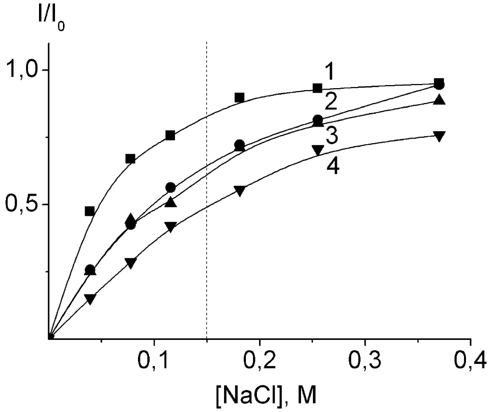

Fig. 3 Dependence of relative Dox fluorescence intensity in the presence of PAA on NaCl concentration. PAA (1), PAA-6 (2), PAA-12 (3) and PAA-18 (4); [Polyanion]/[Dox] = 3

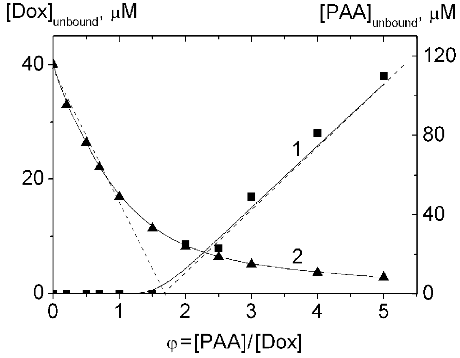

Fig. 4 Dependence of concentration of PAA (1) and Dox (2) uninvolved in the PAA–Dox complex on the PAA/Dox ratio. [Dox] = 50 μM

At the same time, an increase in the φ value resulted in a decrease in non-complexed Dox. The lowest Dox concentration in the filtrate was reached at a φ value close to φ_0 (curve 2). These results definitely showed that all added PAA was involved in the complexation in the excess of Dox. However, only a part of the Dox molecules was bound to the polyanion, a complex of ultimate (characteristic) composition φ_0 with the maximum amount of PAA–Dox salt bridges was formed. PAA-to-Dox binding was obviously accompanied by a neutralization of the PAA macromolecules' charges followed by a loss of stability and aggregation of complex species. Based on the data of Fig. 4, the φ_0 value was found to equal 1.6.

As mentioned above, the PAA–Dox complex dissociated with increasing concentration of a salt in the system. At the physiological salt concentration ([NaCl]

= 0.15 M), a fraction of Dox, complexed with PAA, was about 20% (Fig. 3, curve 1). With the purpose of increasing the stability of complexes in water-salt media, PAA was modified with pendant hexanoyl (PAA-6), dodecanoyl (PAA-12) and octadecanoyl (PAA-18) radicals. A degree of PAA modification was found to be 6% for all PAA derivatives as shown by NMR spectroscopy. Complexes of hydrophobized PAAs with Dox were indeed more stable in comparison with that formed by PAA and Dox. An increase in the length of the pendant radical favored an enhancement of stabilities for resulting complexes (Fig. 3, curves 2–4).

3.2 Interaction of Polyanion–Dox Complexes with Conventional Liposomes

It has been shown earlier that Dox, when added to a liposome suspension, incorporates in the liposomal membrane so that its part, represented by condensed aromatic rings, "bites" deeper into the hydrophobic part of the lipid bilayer, and an amino group is exposed into the surrounding water solution.[22] If Dox, precomplexed with PAA, is also able to bind to liposomes, its orientation in the liposomal membrane is most likely the same. A redistribution of Dox molecules between the PAA chain and the membrane should cause a disturbance of stacking interactions and an increase in the fluorescence intensity of the solution.

To check this prediction, a suspension of small, neutral EL liposomes was added to the PAA–Dox complex solution and the kinetics of changes in the Dox fluorescence intensity at $\lambda_{em} = 555\,nm$ was recorded (Fig. 5a). Just after component mixing, the fluorescence intensity began to rise and reached the maximum value within a few minutes, which corroborated our hypothesis about the incorporation of PAA-bound Dox into the liposomal membrane. The ultimate levels of fluorescence, obtained for different liposome concentrations, are represented in Fig. 5b. A fraction of Dox, transferred to the membrane, increased as the liposome concentration rose.

What happened with PAA macromolecules after the Dox redistribution: were they retained bound to Dox or were they released into the surrounding solution? To answer this question, the following experiment was carried out: A series of samples with the same concentration of PAA–Dox complex, but different concentrations of EL liposomes was prepared and, after equilibration, was passed through microcentrifugal filters with 5-nm pores. By using the "PAA concentration – Dox fluorescence" calibration curve (see *Experimental* part), neither PAA nor DOX was found in the filtrates. This indicated that no dissociation of the PAA–Dox complex took place when contacting with liposomes, but PAA–Dox–liposome ternary complex particles were formed.

By using photon correlation spectroscopy, a mean size of the ternary complex particles was estimated. The mean size was found to be 200 nm (at a liposome concentration of about 8 mg/mL).

Fig. 5a Time-dependence of changes in Dox fluorescence intensity after addition of 4 mg/mL EL liposome suspension to PAA–Dox mixture. [Dox] = 50 μM; [PAA] = 150 μM

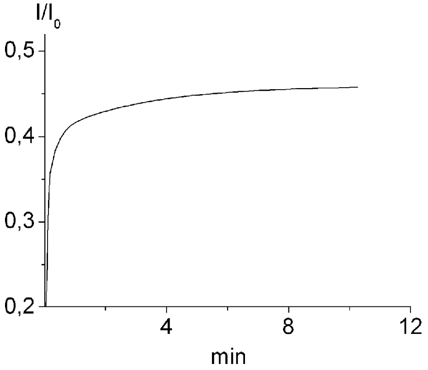

Fig. 5b Ultimate levels of Dox fluorescence recovery after addition of EL liposome suspension to PAA–Dox mixture, [Dox] = 50 μM; [PAA] = 150 μM

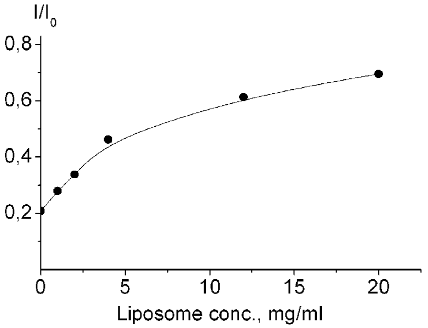

3.3 *Interaction of Polyanion–Dox Complexes with pH-Gradient Liposomes*

A driving force of intracellular Dox accumulation is its high affinity to the double-stranded DNA molecule.[23] In the present work, the membrane transport of Dox, both free and precomplexed with PAA, was arranged using a suspension of unilamellar EL liposomes with a pH 4 buffer inside vesicles and a pH 7 buffer in the surrounding solution. At pH 7, about 2.5% of Dox molecules are uncharged and can be incorporated into the outer leaflet of the liposomal membrane due to hydrophobic interactions. Then, Dox molecules diffuse to the inner leaflet and become protonated. This shifts the equilibrium

$$NH_2\,(Dox) + H^+ \leftrightarrows NH_3^+(Dox)$$

to the uncharged form of Dox in the surrounding solution, thus ensuring the transmembrane migration of a major part of the initial Dox. The inner volume of the liposomes is much smaller (approximately 1,000-fold) than the total solution volume. A substantial concentrating of Dox inside the liposomes is accompanied by the self-quenching of its fluorescence. The kinetics of this process reflects the kinetics of the transmembrane Dox permeation. This system simulates the key stages of passive permeation of low-molecular-weight compounds through biological membranes according to the partition-diffusion mechanism.

The time-dependent changes in the relative fluorescence of Dox after its addition to a suspension of the pH-gradient EL liposomes are presented in curve 1 in Fig. 6. A continuous decrease in the Dox fluorescence was observed, the whole process obeying first-order kinetics. A plateau on the kinetic curve corresponded to a transfer of the greater part of Dox molecules inside the liposomes.[24] The kinetic experiment was then repeated but the PAA–Dox complex was added to the pH-gradient liposome suspension. In this case, the two-stage kinetics for the Dox fluorescence changes was obtained (curve 2). A fast increase in the fluorescence intensity in the first stage yielded a relatively slow decrease in the second. The first stage apparently corresponded to the incorporation of Dox molecules in the outer leaflet of the liposomal membrane. This disrupted Dox stacking interactions, which might be one reason for the initial growth in Dox fluorescence intensity. The second reflected a migration of Dox molecules inside liposomes that was accompanied by the self-quenching of the Dox fluorescence.

The transformations in the PAA–Dox complex structure resulted in a release of free PAA chains to the outer solution. This was shown as follows: The PAA–Dox characteristic complex ([DOX] = 50 μM) was mixed with pH-gradient EL liposomes (lipid concentration, 2 mg/ml). After equilibration, that is, achieving the lowest level of Dox fluorescence, the mixture was passed through a microcentrifugal filter with 5-nm pores. Using the “PAA concentration – Dox fluorescence” calibration curve, we found that 70% of PAA, initially involved in complexation with Dox, were released in solution after complex–liposome interaction. Simultaneously, this

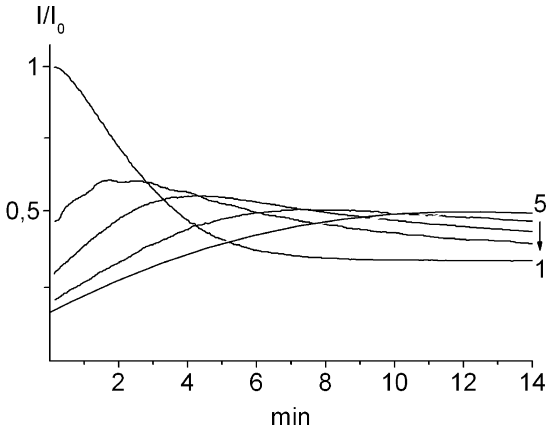

Fig. 6 Time-dependent changes in relative DOX fluorescence intensity after addition of pH-gradient EL liposome suspension to Dox solution in the absence (1) and in the presence of PAA (2–5). [DOX] = 50 μM; [PAA]/[DOX] = 1.6 (2), 3 (3), 10 (4), and 50 (5)

resulted in releasing about 70% of PAA-tied Dox which thus acquired the capability of penetrating through the liposomal membrane. The other part of Dox remained on the outer membrane leaflet and kept connected with the rest of PAA.

The mean size of the particles in the system approached that of the initial liposomes (measured by photon-correlation spectroscopy). This means that the interaction resulted in a complete desegregation of large PAA–Dox complex particles.

A rise in φ = [PAA]/[Dox] value led to an elevation of the ultimate level of Dox fluorescence, retaining the two-stage kinetics of the Dox membrane transport (Fig. 6, curves 3 and 4). However, at [PAA]/[Dox] = 50, only a permanent increase in fluorescence intensity was observed (curve 5). These changes correspond to a decrease in the amount of the penetrated Dox when PAA concentration increased.

A principal question concerns the rate of Dox permeation through the membrane of pH gradient liposomes in the absence and in the presence of PAA. The former can be easily estimated by taking into account the first-order kinetics for the fluorescence self-quenching as free Dox is added to the liposomes (Fig. 6, curve 1). However, for PAA-Dox systems, more complicated kinetic curves were obtained: with two stages (curves 2–4) or with one – only fluorescence-rising – stage (curve 5). The intricate characters of these curves did not allow for the deduction of an equation describing the membrane transport of Dox in the presence of PAA. Therefore, in order to quantify the decelerating effect of PAA, we applied a ratio of the time required for completing Dox membrane transport in the presence of PAA to that in the absence of PAA, τPAA/Dox/τDox = T. As follows from the data given in Fig. 7, the T value increased and, therefore, the rate of Dox transport decreased, when the PAA-to-Dox ratio rose. This means that the Dox transport rate could be manipulated by changing the concentration of PAA in the system.

On the basis of the above results, a mechanistic presentation for PAA-to-Dox complexation and interaction of the resulting complex with pH-gradient liposomes can be suggested (Fig. 8). Addition of PAA to Dox buffer solution results in the formation of a PAA–Dox complex of characteristic composition (PAA/Dox = 1:6 molar ratio) stabilized by electrostatic and stacking interactions (1). The complexation

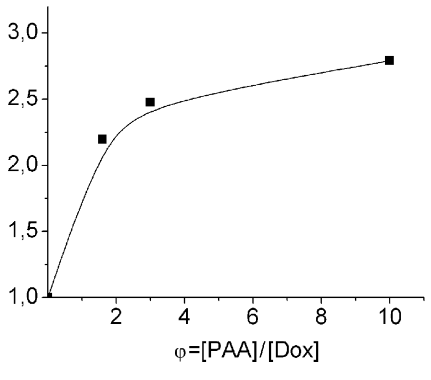

Fig. 7 Dependence of T = $\tau_{PAA/Dox}/\tau_{Dox}$ value on [PAA]/[Dox] ratio. See other conditions in the legend to Fig. 6

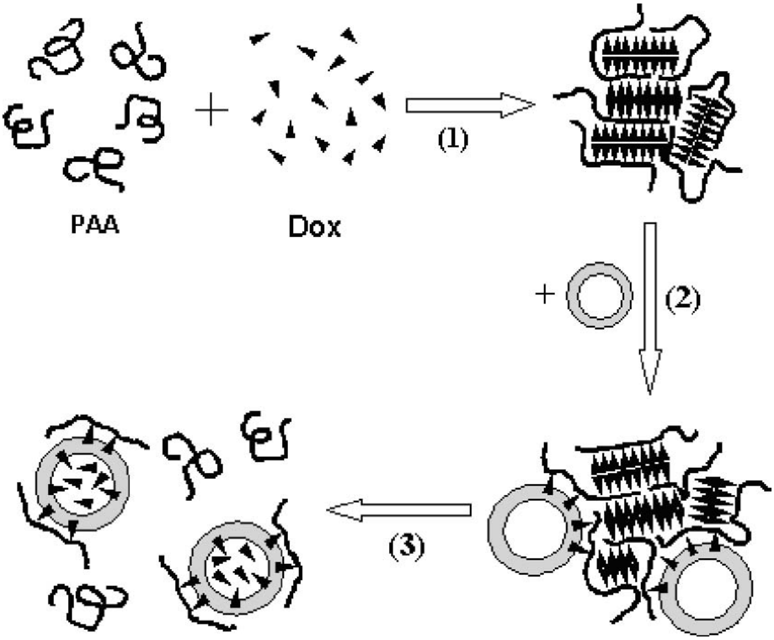

Fig. 8 The events occurring in the PAA/Dox/pH-gradient liposome system (schematic presentation)

is accompanied by the appearance of micro-sized particles. Nevertheless, the latter are able to bind to the pH-gradient liposomes (2), followed by transmembrane Dox permeation (3).

It is known that a cell membrane carries a net negative surface charge.[25] In order to examine a possible effect of the membrane charge on the Dox permeation, pH-gradient-mixed liposomes were prepared composed of neutral EL and anionic CL^{-2} (95:5 molar ratio). The addition of the characteristic PAA–Dox complex to the negative EL/CL^{-2} liposomes was also accompanied by a transmembrane migration of Dox molecules, the overall process developing in two stages. However, both τ_{Dox} and $\tau_{PAA/Dox}$ values increased in this case. This likely resulted from an electrostatic binding of cationic Dox molecules with anionic CL^{-2} molecules on the outer membrane leaflet, which complicated the Dox transfer to the inner leaflet.

The next step was to study the Dox transmembrane permeation under physiological conditions: at 0.15 M NaCl concentration plus 8 mg/ml albumin concentration. As mentioned above, at [NaCl] = 0.15 M, the fraction of Dox, involved in complexation with PAA, did not exceed 20%. A pronounced dissociation of the PAA–Dox complex was reflected in the rate of Dox permeation: it was close to the rate of permeation for free Dox. With the help of gel electrophoresis, it was shown that the electrophoretic mobility of a model bovine serum albumin (BSA) was insensitive to the addition of both PAA and PAA–Dox complex. This means that neither free

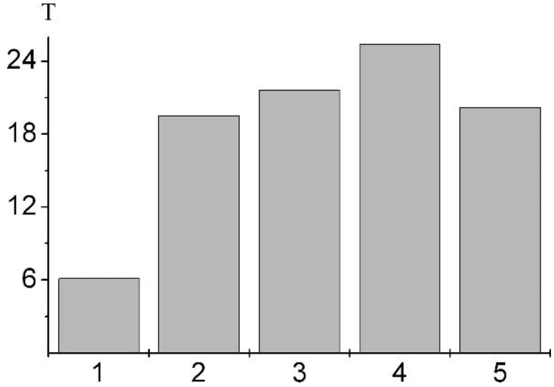

Fig. 9 $T = \tau_{PAA/Dox}/\tau_{Dox}$ values for Dox (1), PAA–Dox (2), (PAA-6)–Dox (3), (PAA-12)–Dox (4), and (PAA-18)–Dox (5). [Polyanion]/[Dox] = 3

PAA nor its complex with Dox had affinity to BSA. In a complete system, containing 0.15 M NaCl and 8 mg/ml BSA, the rate of Dox permeation was mainly determined by the salt component but only poorly affected by BSA.

As far as the hydrophobization of PAA increased the stability of its complexes with Dox complexes in water-salt media, we studied whether such modification could influence the kinetics of Dox permeation. In Fig. 9, T values for the transmembrane migration of Dox precomplexed with PAA-6 (column 1), PAA-12 (column 2) and PAA-18 (column 3) are presented. The corresponding values for free Dox (column 4) and PAA–Dox complex (column 5) are given as a control. It can be seen that the covalent modification of PAA macromolecules with hydrophobic pendant groups prolonged the Dox uptake by pH gradient liposomes, the maximum effect being observed for Dox bound to PAA-12. Complexation of Dox with PAA-18 had a weaker effect comparable to that for non-modified PAA.

3.4 Effect of Cationic Polymers on Membrane Transport of Dox

It has been shown earlier that binding of cationic polymers to small, mixed liposomes composed of negative and neutral lipids accelerates the pH-induced transport of Dox through the liposomal membrane. The rate of Dox transmembrane migration increased when the amount of bound polycation was elevated and reached its ultimate high value at the complete neutralization of the liposome surface charge.[15,26] It is known that complexation of polycations with negative liposomes induces lateral lipid segregation in the membrane as well as the formation of patches composed of negative lipid molecules neutralized by bound polycation chains.[11] Such patches and/or boundaries between them and the surrounding lipid bilayer might be responsible for the acceleration of transmembrane Dox permeation.[26]

Unlike rigid small liposomes whose shape can only be changed with difficulties, regular cells are characterized by a rather high ductility allowing them to withstand considerable deformations without being destroyed. The cell size lies usually within a micron region, i.e., it is two orders of magnitude higher than that of small liposomes. One may expect that an increase in liposome size would provide a better model to mimic cell interaction with polycations and, in particular, to study polycation-mediated membrane transport of bioactive compounds.

We prepared large pH-gradient liposomes, 600 nm in diameter, from a mixture of neutral EL and negative CL^{-2} (70/30 mol/mol). Addition of increasing amounts of PL to a suspension of EL/CL^{-2} liposomes was accompanied by a sharp enlargement of particles in the system and, finally, by phase separation and sedimentation of the PL–liposome complex. Aggregation and sedimentation of large liposomes complexed with PL, which developed within a wide range of liposome-to-Pl ratios, made the realization of kinetic experiments and the interpretation of the obtained results difficult. This caused us to abandon conventional two-component liposomes. Instead, we turned to liposomes whose surface was covered with a layer composed of polyoxyethylene (POE). The procedure was initially developed to produce liposomes which keep their stability in biological environment, in particular, when contacting with proteins (so-called "stealth" liposomes).[27,28] It was shown later that small negative liposomes with an internal POE layer remained stable after polycation binding.[29]

Based on these data, three-component liposomes, composed of EL, CL^{-2} and dipalmitoylphosphatidyletahnolamine, whose head group was covalently modified by POE with M_w = 1000 (DPPE-POE), were obtained with a 70:25:5 component molar ratio. A complete neutralization of their surface charges by adsorbed PL resulted in an only twofold increase in the size of the particles in solution. This allowed the use of the hydrophilized large liposomes in the kinetic experiments on the membrane transport of Dox in the presence of PL.

Adsorption of PL on the surface of large pH-gradient-negative liposomes resulted in a significant increase in the rate of Dox membrane transport. Importantly, the process obeyed first-order kinetics as had been the case with free Dox permeation. Therefore, the permeabilizing effect of PL was quantified by using a ratio between the rate constant in the presence of PL and the rate constant in the absence of PL, k_p/k_0. In Fig. 10, the k_p/k_0 value for the permeation of Dox through the membrane of large EL/CL^{-2}/DPPE-POE (75/25/5) liposomes is presented as a function of $Z_{+/-}$, a ratio between the number of positive PL units bound to the liposomes and the total number of CL^{2-} head groups in the system (curve 1). The maximum (nearly threefold) acceleration was achieved at $Z_{+/-} = 0.5$ and then remained unchanged up to $Z_{+/-} = 4$. For comparison, the $k_p/k_0 - Z_{+/-}$ plot for PL-mediated permeation of Dox through the membrane of small hydrophilized liposomes of the same lipid composition is given in the same figure (curve 2). Here, the acceleration of Dox permeation was also observed but with an increment of only 30%.

A possible reason for these different effects of PL on Dox transport through the membranes of small and large liposomes is the following: Interaction of PL with small negative liposomes is known to be reversible – PL can be completely removed from the liposomal membrane either by an increase in concentration of

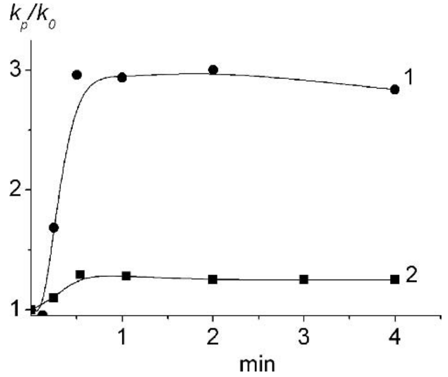

Fig. 10 Dependence of the relative rate for PL-mediated Dox permeation through the membrane of pH-gradient large (1) and small (2) EL/CL^{2-}/DPPE-POE liposomes on the $Z_{+/-}$ value. [DOX] = 50 µM

a salt in solution or by addition of a polyanion excess.[11] In contrast to this, neither salt nor polyanion can remove PL from the surface of large liposomes.[15] Moreover, PL-to-large liposome complexation causes a sharp increase in permeability of the liposomal membrane towards low-molecular-weight salts. As hypothesized earlier,[15] an increase in liposome size results in an increase in ductility of the liposomal membrane, which, in turn, makes feasible the incorporation of PL fragments, more or less expandable, into the hydrophobic part of the lipid bilayer. The same could hold true for the behavior of PL on the surface of sterically stabilized small and large liposomes. PL binding to large EL/CL^{-2}/DPPE-POE (75/25/5) liposomes could also be accompanied by the incorporation of PL fragments into the liposomal membrane and the formation of temporal defects favoring the acceleration of Dox membrane transport.

As mentioned above, in both cases, for small and large hydrophilized negative liposomes, the maximum of the Dox membrane transport was at $Z_{+/-} = 0.5$. This fact most likely means that in the membrane of both liposomes, Dox molecules were nearly uniformly distributed between the outer and inner membrane leaflet and the maximum of the Dox transmembrane permeation rate was observed at a complete neutralization of all CL^{-2} molecules from the outer leaflet.

Another important finding was a nearly threefold decrease in the Dox permeation rate for the hydrophilized negative liposomes in comparison with the conventional negative ones (transport of Dox through the membrane of the latter has been described before)[26]. The permeabilizing effect of polycations is usually related to polycation-induced lateral segregation and the formation of clusters of negative lipids in the outer membrane leaflet. If this is the case, a relative deceleration of the Dox permeation in the case of hydrophilized liposomes can point to a significant retardation or even suppression of the lateral segregation in the membrane, containing lipids with bulky hydrophilic substitutes in the polar head group region.

4 Conclusions

The binding of PAA chains to Dox molecules results in PAA–Dox complexes with characteristic composition (PAA/Dox = 1:6). Stabilization of the complex is aided by electrostatic PAA-Dox and stacking Dox–Dox interactions. The complexation causes an enlargement of particles in the system up to several hundreds of nanometers. Nevertheless, large complex particles are capable of interacting with small neutral liposomes, which is accompanied by a "destacking" of Dox and its incorporation into the outer leaflet of the liposomal membrane, retaining ionic PAA–Dox contacts. Then, the doxorubicin enters the liposome interior which has been imparted with an acidic buffer to protonate the doxorubicin. The rate of transmembrane Dox permeation decreases when elevating the polyacid-to-doxorubicin ratio. By modifying PAA with hydrophobic pendant groups, the stability of the complexes in water-salt media significantly increased. Dox, as part of complexes with hydrophobized PAAs, is able to penetrate through the membrane at physiological salt concentration and in the presence of excess protein.

A cationic PL, being coupled with negative liposomes, accelerates the membrane transport of Dox; the maximum rate is achieved at the complete neutralization of the membrane charge by the interacting PL. The effect of PL on the Dox permeation becomes more pronounced as small negative liposomes are changed to larger ones.

It is demonstrated experimentally that by the use of polyelectrolytes, the rate of membrane Dox transport can be modulated within wide limits. An opportunity thus presents itself in the manipulation of the kinetics of drug uptake by cells and thus, ultimately, for the control of the pharmaceutical action of drugs.

Acknowledgements We highly appreciate the support of some parts of this research by the Russian Foundation for Fundamental Research (grant 05-03-33033) and the Fogarty International Research Cooperation Award (grant TW05555).

References

1. H. Suzuki, D. Nakai, T. Seita, and Y. Sugiyama, Design of a drug delivery system for targeting based on pharmacokinetic consideration, *Adv. Drug Del. Rev*. 19(3), 335–357 (1996).
2. A. V. Kabanov and T. Okano, Challenges in polymer therapeutics: state of the art and prospects of polymer drugs, *Adv. Exp. Med. Biol*. 519, 1–27 (2003).
3. V. P. Torchilin, Structure and design of polymeric surfactant-based drug delivery systems, *J. Control. Release* 73(2), 137–172 (2001).
4. K. Kataoka, T. Matsumoto, M. Yokoyama, T. Okano, Y Sakurai, S. Fukushima, K. Okamoto, and G.S. Kwon, Doxorubicin-loaded poly(ethylene glycol)-poly(beta-benzyl-L-aspartate) copolymer micelles: their pharmaceutical characteristics and biological significance, *J. Control. Release* 64(1–3), 143–153 (2000).
5. L. Bromberg and V. Alakhov, Effects of polyether-modified poly(acrylic acid) microgels on doxorubicin transport in human intestinal epithelial Caco-2 cell layers, *J. Control. Release*. 88(1), 11–22 (2003).

6. B. K. Kishore, Z. Kallay, P. Lambricht, G. Laurent, and P. M. Tulkens, Mechanism of protection afforded by polyaspartic acid against gentamicin-induced phospholipidosis. I. Polyaspartic acid binds gentamicin and displaces it from negatively charged phospholipid layers in vitro, *Pharmacol. Exp. Ther.* 255(2), 867–874 (1990).
7. N. Konar and C. Kim, Drug release from drug-polyanion complex tablets: poly(acrylamido-2-methyl-1-propanesulfonate sodium -co- methyl methacrylate), *J.Control. Release* 57(2), 141–150 (1999).
8. T. Oda, F. Sato, and H. Maeda, Facilitated internalization of neocarzinostatin and its lipophilic polymer conjugate, SMANCS, into cytosol in acidic pH, *J. Natl. Cancer Inst.* 79(6), 1205–1211 (1987).
9. R. Welti and M. Glaser, Lipid domains in model and biological membranes, *Chem. Phys. Lipids* 73(1–2), 121–137 (1994).
10. P. M. Macdonald, K. J. Crowell, C. M. Franzin, P. Mitrakos, and D. J. Semchyschyn, Polyelectrolyte-induced domains in lipid bilayer membranes: the deuterium NMR perspective, *Biochem. Cell Biol.* 76(2–3), 452–464 (1998).
11. A. A. Yaroslavov, A. A. Efimova, V. I. Lobyshev, and V. A. Kabanov, Reversibility of structural rearrangements in the negative vesicular membrane upon electrostatic adsorption/desorption of the polycation, *Biochim. Biophys. Acta* 1560(1–2), 14–24 (2002).
12. A. A. Yaroslavov, V. Ye. Koulkov, A. S. Polynsky, B. A. Baibakov, and V. A. Kabanov, A polycation causes migration of negatively charged phospholipids from the inner to outer leaflet of the liposomal membrane, *FEBS Lett.* 340, 121–123 (1994).
13. S. Lee, T. Iwata, H. Oyagi, H. Aoyagi, M. Ohno, K. Anzai, Y. Kirino, and G. Sugihara, Effect of salts on conformational change of basic amphipathic peptides from beta-structure to alpha-helix in the presence of phospholipid liposomes and their channel-forming ability, *Biochim. Biophys. Acta* 1151, 76–82 (1993).
14. O. O. Glazunova, E. A. Korepanova, V. S. Efimov, A. I. Smirnov, and Yu. A.Vladimirov, A synthetic polycation, a copolymer of 1-vinyl-3-methylimidazole iodide with maleic acid diethyl ester, increases passive ionic permeability in erythrocyte membranes modified by fatty acids, *Membr. Cell Biol.* 12(3), 401–409 (1998).
15. A. A. Yaroslavov, O. Ye. Kuchenkova, I. B. Okuneva, N. S. Melik-Nubarov, N. O. Kozlova, V. I. Lobyshev, V. A. Kabanov, and F. M. Menger, Effect of polylysine on structure and permeability of negative vesicular membrane, *Biochim. Biophys. Acta* 1611(1–2), 44–54 (2003).
16. N. Oku, N. Yamaguchi, N. Yamaguchi, S. Shibamoto, F. Ito, and M. Nango, The fusogenic effect of synthetic polycations on negatively charged lipid vesicles, *J. Biochem.* 100(4), 935–944 (1986).
17. A. E. Gad, B. L. Silver, and G. D. Eytan, Polycation-induced fusion of negatively-charged vesicles, *Biochim. Biophys. Acta* 690(1), 124–132 (1982).
18. R. R. C. New, in: *Liposomes: A Practical Approach*, edited by R.R.C. New (Oxford University Press, Oxford, 1990), pp. 33–104.
19. O. O. Krylova, N. S. Melik-Nubarov, G. A. Badun, A. L. Ksenofontov, F. M. Menger, and A. A. Yaroslavov, Pluronic L61 accelerates flip-flop and transbilayer doxorubicin permeation, *Chem. Eur. J.* 9(16), 3930–3936 (2003).
20. M. V. Kitaeva, N. S. Melik-Nubarov, F. M. Menger, and A. A. Yaroslavov, Doxorubicin-poly(acrylic acid) complexes: interaction with liposomes, *Langmuir* 20(16), 6575–6579 (2004).
21. T. Soderlund, A. Jutila, P. K. Kinnunen, and A. Walter, Continuous mixing experiments allow to determine the size of binding sites for anthracyclines complexed to DNA, *Biomed. Biochim. Acta* 44(9), 1321–1327 (1985).
22. C. Heywang, M. S.-P. Chazalet, M. C. Masson, and J. Bolard, Orientation of anthracyclines in lipid monolayers and planar asymmetrical bilayers: a surface-enhanced resonance Raman scattering study, *Biophys. J.* 75(5), 2368–2381 (1998).
23. C. Cera and M. Palumbo, Anti-cancer activity of anthracycline antibiotics and DNA condensation, *Anticancer Drug Des.*5(3), 265–71 (1990).

24. P. R. Harrigan, K. F. Wong, T. E. Redelmeier, J. J. Wheeler, and P. R. Cullis, Accumulation of doxorubicin and other lipophilic amines into large unilamellar vesicles in response to transmembrane pH gradients, *Biochim. Biophys. Acta* 1149(2), 329–338 (1993).
25. J. Darnell, H. Lodish, and D. Baltimore, *Molecular Cell Biology* (Scientific American Books, New York, 1990).
26. N. O. Kozlova, I. B. Bruskovskaya, I. B. Okuneva, N. S Melik-Nubarov, A. A. Yaroslavov, V. A. Kabanov, and F. M. Menger, Interaction of a cationic polymer with negatively charged proteoliposomes, *Biochim. Biophys. Acta* 1514(1), 139–151 (2001).
27. T. M. Allen and C. Hansen, Pharmacokinetics of stealth versus conventional liposomes: effect of dose. *Biochim. Biophys. Acta* 1068(2), 133–141 (1991).
28. P. Srinath, M. C. Chary, S. P. Vyas, and P. W. Diwan, Long-circulating liposomes of indomethacin in arthritic rats – A biodisposition study, *Pharm. Acta Helv*. 74(4), 399–404 (2000).
29. A. A. Yaroslavov, E. G. Yaroslavova, A. A. Rakhnyanskaya, F. M. Menger, and V.A. Kabanov, Modulation of interaction of polycations with negative unilamellar lipid vesicles, *Colloids Surf. B* 16(1), 29–43 (1999).

Network Model of *Acetobacter Xylinum* Cellulose Intercalated by Drug Nanoparticles

Vera V. Klechkovskaya[1,*], Vladimir V. Volkov[1], Eleonora V. Shtykova[1], Natalia A. Arkharova[1], Yulia G. Baklagina[2], Albert K. Khripunov[2], Ruslan Yu. Smyslov[2], Ludmila N. Borovikova[2], and Albina A. Tkachenko[3]

Abstract It was shown that *Acetobacter xylinum* cellulose gel-films can sorb silver and selenium nanoparticles stabilized by N-poly(vinyl-2-pirrolidone). The structure of original cellulose matrix, isolated nanoparticles and cellulose with sorbed nanoparticles was characterized by electron diffraction, electron microscopy, small- and wide-angle x-ray scattering methods, and atomic force microscopy. It was found that in static culture *Acetobacter xylinum* bacterium (strain VKM B-880) may synthesize high-molecular cellulose with narrow molecular weight distribution and a considerable number of carbon sources. The structures of cellulose microfibrilles and ribbons correspond mainly to polymorphous I_β modification. We concluded from structural studies that textured cellulose films were formed. The sorption conditions of poly(vinylpyrrolidone)-Se° and poly(vinylpyrrolidone)-Ag° nanoparticles were optimized to obtain a cellulose template that can be used in medical practice.

Keywords *Acetobacter xylinum* cellulose, sorption, desorption, nanoparticles, selenium, safety medical effect

1 Introduction

A lot of the interest in the study of the sorption of nanoparticles by gel film of the cellulose *Acetobacter xylinum* (AXC) stems from the possibility of using these materials in medical applications. One of the most promising fields of using AXC gel

---

[1] Institute of Crystallography, Russian Academy of Sciences, Leninsky pr. 59, Moscow, 119333, Russia

[2] Institute of Macromolecular Compounds, Russian Academy of Sciences, Bolshoi pr. 31, St. Petersburg, 199004, Russia

[3] St. Petersburg State University, Universitetskaya nab. 7-9, St. Petersburg, 199034, Russia

[*] To whom correspondence should be addressed. E-mail: klechvv@ns.crys.ras.ru

M. Giersig and G. B. Khomutov (eds.),
Nanomaterials for Application in Medicine and Biology

films in medicine is their application as bactericidal coating and high-performance bandage material, especially for the treatment of burns and wounds. What makes AXC gel films here particularly interesting is the combination of properties they offer – they are highly elastic, provide comfort conditions for wound surfaces, and do not damage surfaces during the removal of a bandage due to low sticking.

Due to a number of specific problems, *Acetobacter xylinum* cellulose was widely investigated[1–5] within the last decade. At static cultivation, AXC forms a gel film network built from nanosized elements of supramolecular structure of AXC (AXC GF). Comprehension of the mechanisms of sorption and desorption of medical preparations in AXC GF is extremely important for the development of methods of their intercalation into gel films on the stipulation that the preparations keep their medical effects.[6]

The present article is devoted to an investigation of the structural organization of AXC macrochains (strain VKM B-880) during the synthesis of AXC and the structural characteristics of AXC synthesized in the form of gel film, both in the process of its growth and in a dry state. The structure of poly(vinylpyrrolidone)-Se^o and poly(vinylpyrrolidone)-Ag^o nanoparticles and the process of their adsorption – desorption on AXC GF was investigated. The structural studies of samples were performed by electron diffraction (a special electron diffraction camera EMR102 with acceleration voltages 75 and 100 kV, USSR), electron microscopy (FEI EM430 with the acceleration voltage 300 kV), x-ray small angle scattering (AMUR-K diffractometer, ICRAN, Moscow) and wide angle x-ray diffraction (DRON-2 diffractometer and RKV-86, Cu K_α radiation, Ni filter).

2 Results and Discussion

The performed structural study allowed us to conclude that in AXC GF (strain VKM-880) the high-crystalline cellulose is preferentially formed with polymorphic modification I_β. In order to obtain the maximum ACX yield, the composition of the nutrient medium was optimized. More detailed information on the phase composition and structure of AXC films was obtained by electron diffraction. We used the possibilities of both electron microscope (analysis of diffraction patterns obtained from a small sample area) and electron diffraction camera (high-resolution diffraction patterns from rather large areas of the film) (Fig. 1). According to the electron diffraction data, the microfibrillar ribbon represents a single-crystal formation with a width of 50–100 nm and a length of hundreds of micrometers (see Fig. 2). Dried films have an axial-plane texture in which crystal faces $\bar{1}10$ of monoclinic unit cells are aligned along the edge of the sample (Fig. 3). This structure of macrosamples of AXC is already formed at the stage of biosynthesis in microfibrillar ribbons which are oriented by the primary hydroxyl groups on the surface of the culture medium. According to the electron microscopy data,[7] they fulfill the role of a reinforcing grid which occupies a slight part of the volume of a gel film.

This feature of supramolecular organization of AXC GF allows one to use it as a template for medical preparations in which specific interactions between the cellulose crystal's primary hydroxyl groups and specific hydrogen groups take place. Such a template has a unique axial-plane texture that guarantees the preservation of high sorption and toughness performances during its purification after biosynthesis from bacterial cells and during long storage in distilled water at 5°C, as well as after sterilization at room temperature, and after saturation by different medicinal preparations.[2]

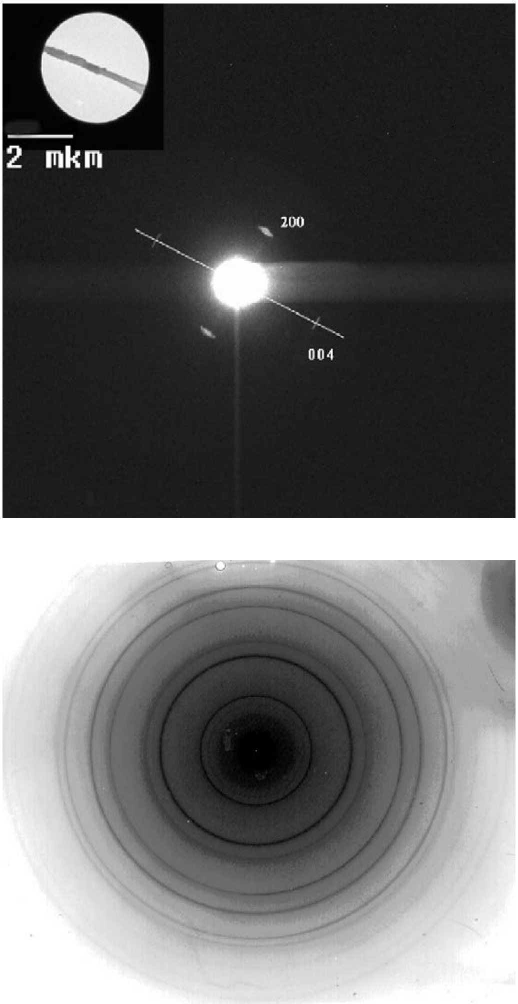

Fig. 1 Initial stages of cellulose *Acetobacter Xylinum* gel film formation: electron diffraction patterns from a portion of a microfibrille with the cross-section 50 nm (a), electron diffraction pattern of an AXC film after 24 h of its formation (b)

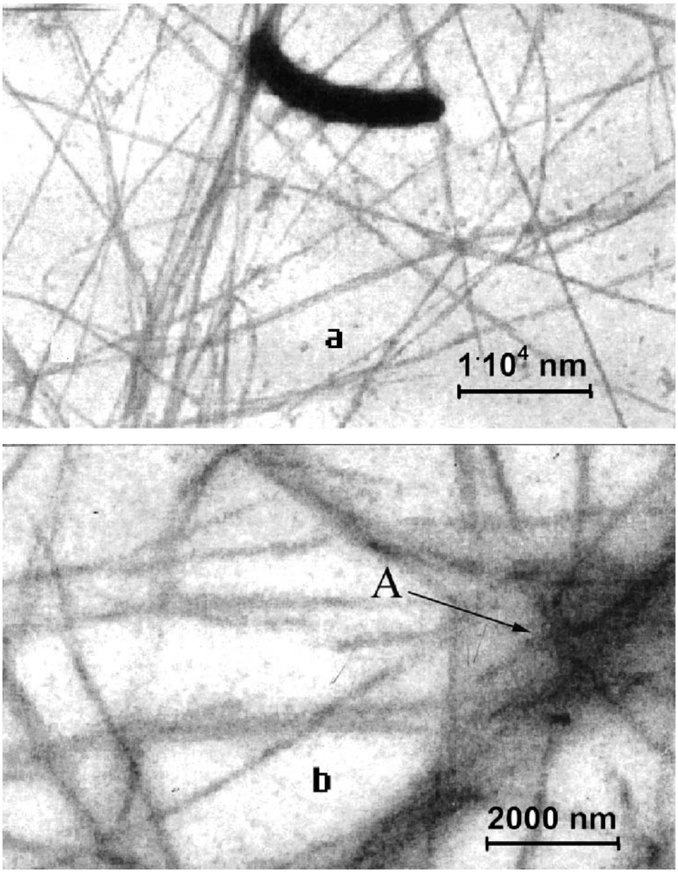

Fig. 2 Electron microscope images of *Acetobacter xylinum* shown after 3 h (a) and (b) 6 h of synthesis. Here, A is a crystal domain

With the purpose of providing antimicrobial properties to the AXC GF, the modern microbicides Povyargol and Selenopol were introduced into the AXC template. Povyargol and Selenopol are nanoparticles of zerovalent metal silver and selenium, respectively, and stabilized by poly(n-vinyl-2-pyrrolidone) (PVP). Apart from their antimicrobial activity, these drugs possess regenerative and immunostimulative properties.[8] Water-soluble composites of Ag^0 nanoparticles with PVP (PVP–nano-Ag^0) were found to possess bioactive properties; in particular, they suppress the growth of salmonella, staphyllococcus, and Pseudomonas Aeruginosa.[8]

The study of processes of sorption and desorption of nanocomplexes of PVP–nano-Ag^0 and PVP–nano-Se^0 by AXC GF is connected with earlier-obtained,[2,9] positive results concerning the possible use of AXC GF for wound coatings.

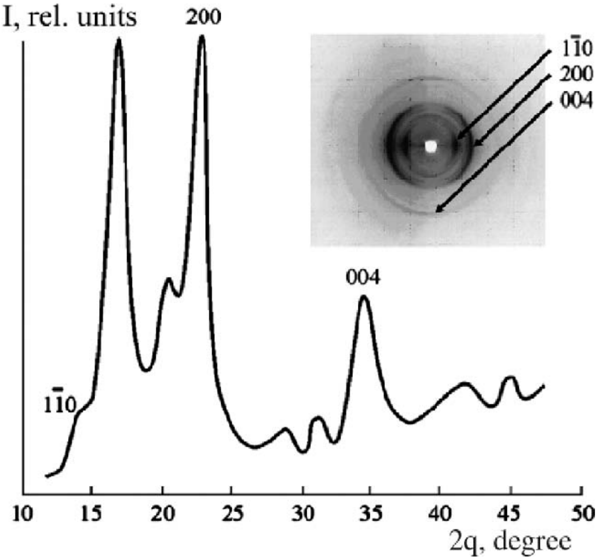

Fig. 3 Intensities of x-ray diffraction pattern measured from ACX dry film formed during seven days of biosynthesis (incident beam is orthogonal to the film surface). The x-ray diffraction pattern obtained in the butt-end geometry with the sample plane parallel to the x-ray beam is shown in the inset

To guarantee the safety of this product in medical application it is of particular importance to exactly delimit the content of amorphous Se^0 used in composites.

It was preliminarily shown by means of x-ray diffraction that the crystalline structure of AXC does not change after sorption of PVP and PVP–nano-Ag^0 and Se^0 particles. The electron microscope images of cross sections of the cellulose films modified by the PVP–nano-Ag^0 and PVP-nano-Se^0 nanocomposites are shown in Figs. 4 and 5.

Analysis of the images obtained at different magnifications (×8,000 to ×21,000) showed that the distributions of selenium and silver particles over the film surface and the film depth are nonuniform. Large spherical clusters with a diameter of 80–200 nm are located on the surface of the AXC GF-PVP-nano-Ag^0 nanocomposite (Fig. 4a and c).

Inside the matrix, silver particles are also spherical but, for the most part, their size is about 2–10 nm (Fig. 4b and d). A different situation is observed in the micrographs of the AXC gel film-PVP–Se^0 nanocomposite. Selenium crystals are seen on the surface (Fig. 5a), and elongated selenium particles, whose ratio between thickness and length is 1.5–2.0 (as shown in Fig. 5c) are observed inside the film (Fig. 5b). The data obtained by electron microscopy thus testified that Ag^0 nanoparticles having the size 2–10 nm are localized in the depth of a template and that on its surface larger Ag^0 clusters (Fig. 4) are present. At desorption of dried AXC GF–PVP–nano-Ag^0 composites by water, the PVP easily leaves the cellulose template without changing

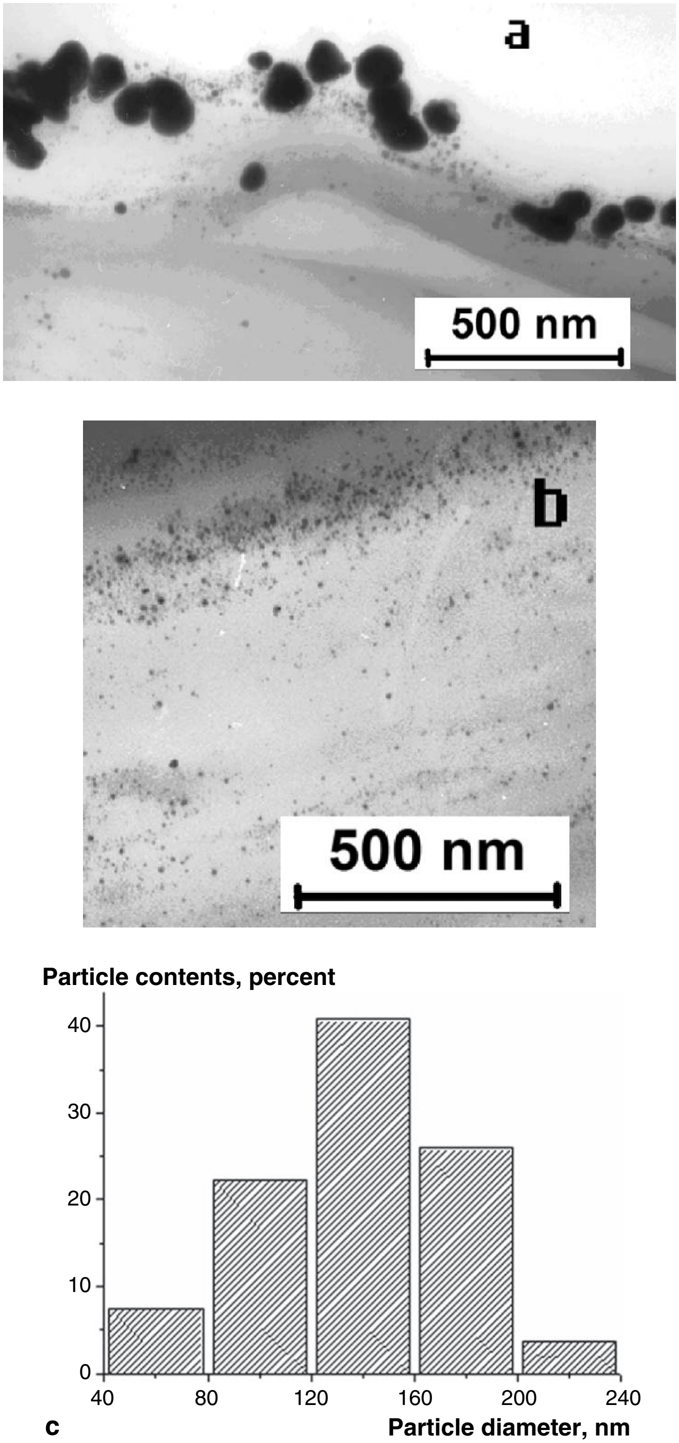

Fig. 4 (continued)

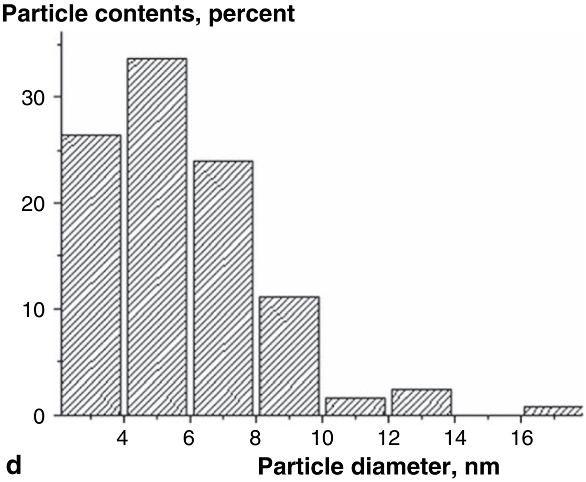

Fig. 4 Electron microscope images (a, b) and histogram of the distribution (c, d) of silver nanoparticles (a) on the surface and (b) at the depth of the cross sections of the dry sample of the bacterial cellulose gel film–Poviagrol nanocomposites

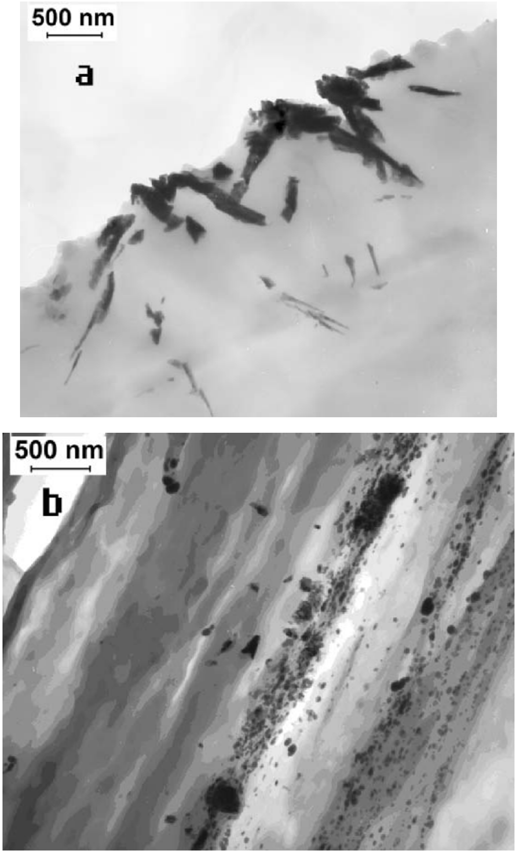

Fig. 5 (continued)

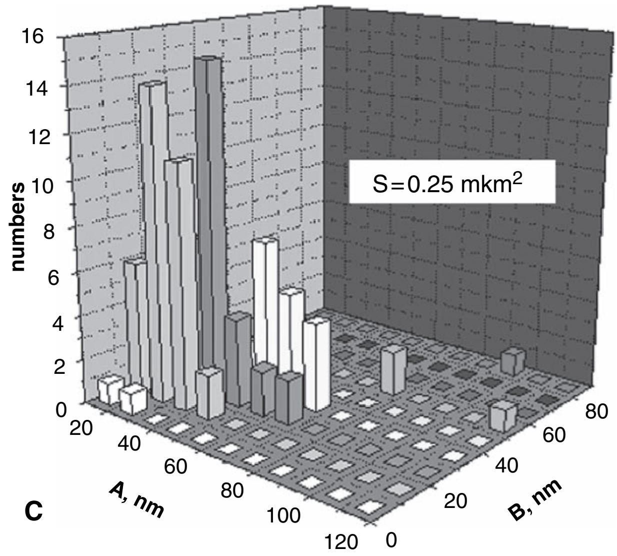

Fig. 5 Electron microscope images (a, b) and histogram of the distribution (c) of selenium nanocrystals (a) on the surface and (b) at the depth of the cross sections of the dried sample of the AXC gel film–PVP–Se^0 nanocomposite

its structural features and the amount of Ag^0 sorbed.[5] The cellulose gel films (with water) and nanocomposites were investigated by x-ray small-angle scattering (SAXS). The synchrotron radiation x-ray scattering data were collected following standard procedures using the X33 camera of the European Molecular Biology Laboratory (EMBL, Hamburg outstation) on the storage ring DORIS III of the Deutsches Elektronen Synchrotron (DESY, Hamburg). The range of momentum transfer $0.1\,\text{nm}^{-1} < s < 5\,\text{nm}^{-1}$ was covered, where $s = 4\pi\sin\theta/\lambda$, 2θ is the scattering angle and the wavelength $\lambda = 0.15\,\text{nm}$. The data were normalized to the intensity of the incident beam, averaged, and corrected for the detector response. Scattering patterns are shown in Fig. 6.

Size distributions of the Ag and Se compound clusters and nanoparticles were computed from the difference scattering profiles (scattering from pure cellulose was subtracted from SAXS profiles corresponding to cellulose with nanoparticles). Assuming that the particles are spherical, the indirect transform program GNOM[10] was used to solve the integral equation

$$I(s) = \int_0^{\infty} D_V(R) m^2(R) i_0(sR) dR,$$

where R is the radius of a sphere, R_{min} and R_{max} are the minimum and maximum radii, respectively, $i_0(x)=\{[\sin(x) - x\cos(x)]/x^3\}^2$ is the sphere form-factor and $m(R)= (4\pi/3)R^3\,\Delta\rho$, where $\Delta\rho$ is the particle scattering contrast (here 1.0). The

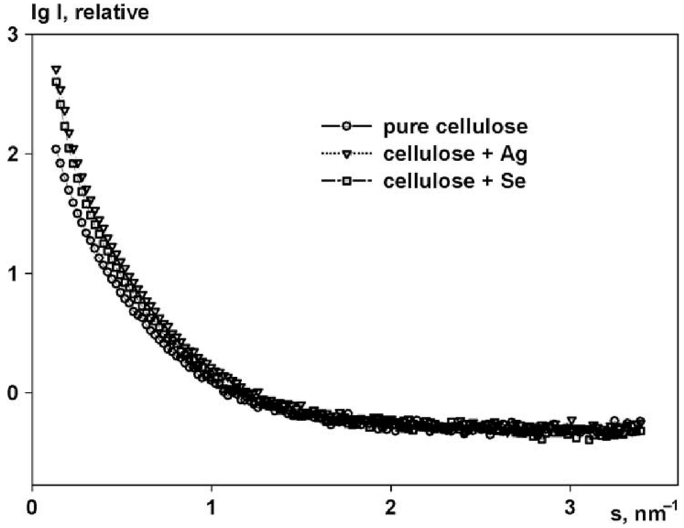

Fig. 6 X-Ray small-angle scattering profiles from cellulose samples

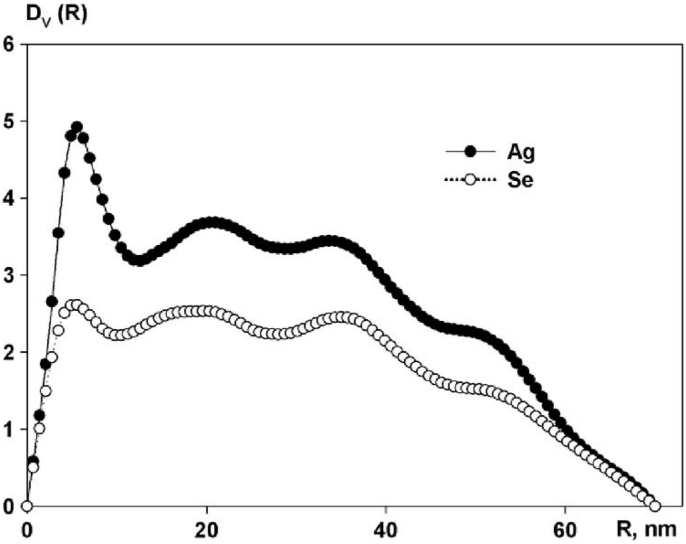

Fig. 7 Volume distributions of Ag and Se nanocomposites formed in cellulose samples

value of R_{min} was kept zero; and R_{max} was determined for each individual data set by successive runs with different values of this parameter. The calculated sizes (Fig. 7) correlate with those described before.

It is thus necessary to take into account that the never-dried gel film of AXC which is able to sorb nanoclusters of Ag^0 or Se^0, represents the frame formed by microfibrillar ribbons with a width of less than 100 nm, i.e. it is of nanolevel organization size and has an extremely developed specific surface (not less than 500 m^2 /g).

The formation of the specific structure is predominantly affected by the high surface energy of the (110) and ($\bar{1}$10) crystal faces, which contain primary hydroxyl groups. This leads to the specific interaction of the AXC matrix with the selenium and silver complexes. It seems likely that the differences in the number and sizes of silver and selenium clusters at the surface and inside the AXC matrix are associated with the preferred orientation of ribbons forming the gel film.

The investigation of biosynthesis features and the structure of the AXC made it possible to suggest that a microfibrillar ribbon in the initial never-dried gel film consists of a large number of crystalline nanofibrils formed by the (110) and ($\bar{1}$10) faces.

The distance between nanofibrils in the ribbon is most likely determined by the nature of the VKM V-880 strain of *Acetobacter xylinum* used in the synthesis, synthesis conditions, and conditions of the preparation of the synthesized gel film for the intercalation of water-soluble nanostructures. Channels between nanofibrils (nanochannels) are bounded by the (110) faces of crystallites of neighboring nanofibrils and provide the formation of a specific structure that is responsible for the intercalation of water-soluble nanocomplexes. Owing to the high surface energy of the (110) and ($\bar{1}$10) faces containing primary hydroxyl groups, nanocomplexes can very rapidly (15–30 min) penetrate into nanochannels or interact with OH groups of large faces of nanofibrils and they are located between microfibrillar ribbons without formation of selenium or silver aggregates.[4]

The adsorption of selenium on these faces is confirmed by the considerable (double) increase in the intensity of the 110 and $\bar{1}$10 reflection in the x-ray diffraction patterns obtained for the dry AXC gel films after their contact with aqueous solutions of the PVP–Se^0 nanocomposite (Fig. 9).

A similar change in intensity is observed for the 004 reflection, which is associated with the fixed periodic location of adsorbed Se^0 nanocomplexes along the polymer chain. We can assume that, in the given case, an increase in the intensity of the above reflections is caused by the increase in the contrast of the (110), ($\bar{1}$10), and (004) planes. Actually, in the x-ray diffraction patterns of cellulose Iβ, the intensity of a number of reflections, such as 200, 102, 012, and others, remains unchanged because selenium atoms do not penetrate into nanofibril crystallites and replace water molecules sorbed by primary hydroxyl groups of their walls.

3 Conclusion

It is demonstrated that the PVP—Ag^0 and PVP—Se^0 nanocomposite clusters differ in number and size upon their sorption inside the AXC gel films and on the film surface. The assumption is made that these differences can be associated with the orientation of microfibrillar ribbons, the large number of nanochannels between ribbons, and the high surface energy of the (−110) and (110) crystal faces saturated with primary hydroxyl groups.

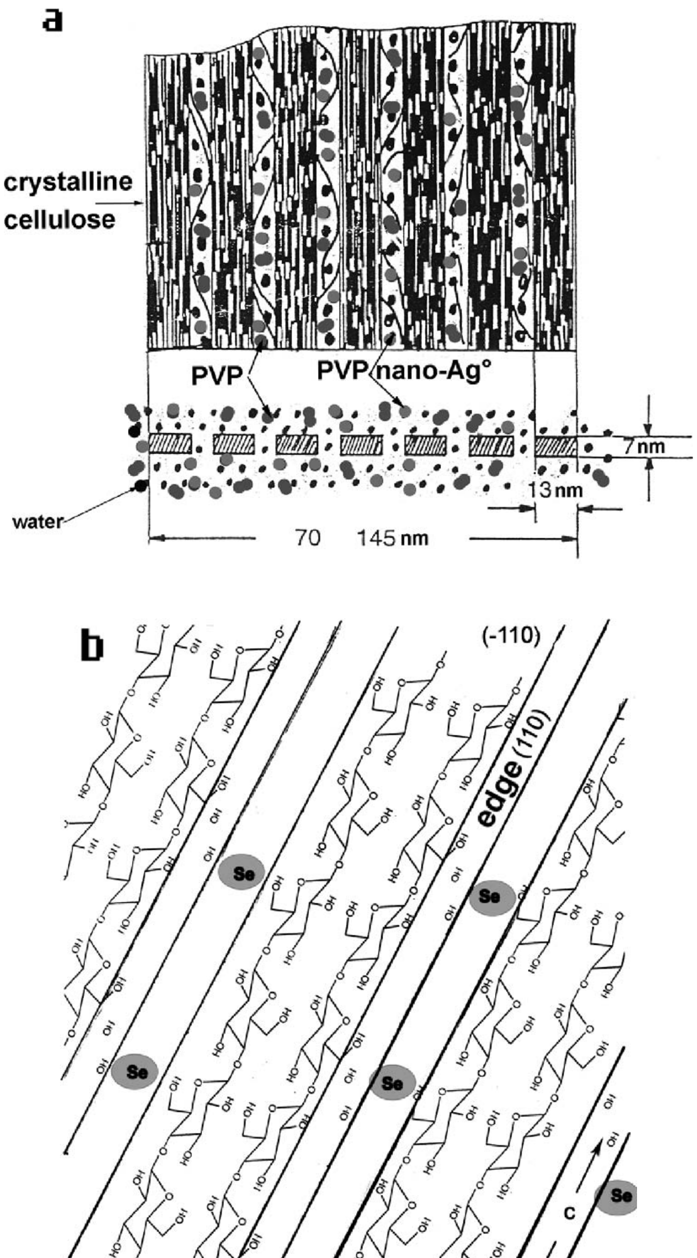

Fig. 8 Schematic diagram illustrating sorption of (a) the PVP–Ag^0 nanocomposite and (b) the PVP–Se^0 nanocomposite by the AXC gel film according to the model proposed by Fink et al.[11]

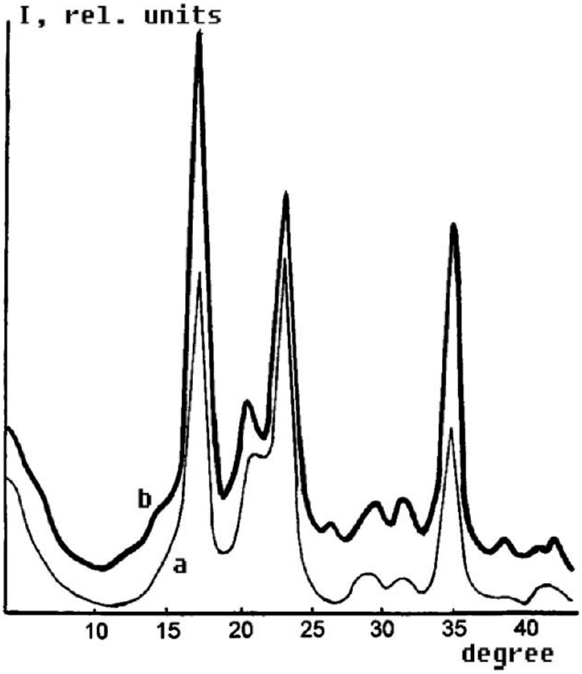

Fig. 9 X-ray diffraction patterns of the dried samples: (a) the initial AXC gel film and (b) the AXC gel film–PVP–Se^0 nanocomposite after treatment of the gel film by the 1% aqueous solution of the PVP–Se^0 nanocomposite for 15 min

According to the scheme for the sorption process, PVP—Se^0 nanocomplexes are predominantly sorbed on the (−110) and (110) faces in channels between the nanofibrils and microfibrillar ribbons. The AXC template can be used in medical practice as a safety preparation carrying stabilized amorphous selenium.

Acknowledgements This work was partially supported by RFBR grant no. 05-03-32842 and FASI contract 02.513.11.3019.

References

1. W. Czaja, A. Krystynowicz, S. Bielecki, and R. M. Brown Jr., Microbial cellulose – the natural power to heal wounds, *Biomaterials* 27, 145–151 (2006).
2. B. A. Paramonov, V. V. Kopeikin, A. A. Tkachenko, and A. K. Khripunov, Perspectives of application of wound coating obtained on the basis of cellulose produced by *Acetobacter xylinum*, in: *Proceedings of the First International Scientific and Practical Conference "Modern Polymer Materials in Medicine and Medical Engineering,"* St. Petersburg, 2005, pp. 203–205 [in Russian].

3. I. V. Gofman, A. L. Buyanov, A. K. Khripunov, L. G. Revelskaya, A. A. Tkachenko, and B. A. Paramonov, Polymer compositions based on *Acetobacter xylinum* cellulose and synthetic polymers: functional properties and prospect of medical applications, *Mater., Technol. Instruments* 11(1), 35–41 (2006).
4. Yu. G. Baklagina, A. K. Khripunov, A. A. Tkachenko, E. I. Suvorova, V. V. Klechkovskaya, L. N. Borovikova, R. Yu. Smyslov, V. K. Nilova, Ya. I. Nazarkina, V. K. Lavrent'ev, S. V. Valueva, A. I. Kipper, and V. V. Kopeikin, Interaction of Se^0 nanoparticles stabilized by poly(vinylpyrrolidone) with gel films of Acetobacter xylinum cellulose, *Crystallogr. Rep.*, 51(4), 619–626 (2006).
5. Yu. G. Baklagina, A. K. Khripunov, A. A. Tkachenko, V. V. Kopeikin, N. A. Matveeva, V. K. Lavrent'ev, V. K. Nilova, T.E. Sukhanova, R. Yu. Smyslov, I. S. Zanaveskina, V. V. Klechkovskaya, and L. A. Feigin, Sorption properties of bacterial cellulose gel films, *Russ. J. Appl. Chem.* 78(7), 1176–1181 (2005).
6. V. A. Baraboj, Biological functions, metabolism, and mechanisms of selenium effects, *Adv. Curr. Biol.*, 124(2), 157–168 (2004) [in Russian].
7. Yu. G. Baklagina, A. K. Khripunov, A. A. Tkachenko, S. V. Gladchenko, V. K. Lavrent'ev, A. Ya. Volkov, V. K. Nilova, V. M. Denisov, T.E. Sukhanova, I. S. Zanaveskina, V. V. Klechkovskaya, and L. A. Feigin, Structural parameters of cellulose produced by Acetobacter xylinum and their variation in the course of drying of gel films, *Russ. J. Appl. Chem.* 76(6), 989–996 (2003).
8. V. V. Kopeikin and E. F. Panarin, Water-soluble nanocomposites of zerovalent metallic silver with enhanced antimicrobial activity, *Dokl. Chem.* 380(4–6), 277–280 (2001).
9. A. K. Khripunov, A. A. Tkachenko, Yu. G. Baklagina, V. V. Kopeikin, M. A. Katsdze, A. G. Miroshnichenko, and E. F. Panarin, Bacterial cellulose – perspective materials for use in medical practice, in: *Proceedings of the Second International Conference "Modern Approaches to the Design of Effective Medical Dressings, Suture Materials, and Polymer Implantants,"* Moscow, November 21–22, 1995, p. 71 [in Russian].
10. D. I. Svergun, Determination of the regularization parameter in indirect-transform methods using perceptual criteria, *J. Appl.Cryst.* 25, 495–503 (1992).
11. H.-P. Fink, H. J. Purz, A. Bohn, and J. Kunze, Investigation of the supramolecular structure of never dried bacterial cellulose, *Macromol. Symp.* 120, 207–217 (1997).

This page intentionally blank

Theoretical Approaches to Nanoparticles

Krzysztof Kempa*

Abstract Nanoparticles can be viewed as wave resonators. Involved waves are, for example, carrier waves, plasmon waves, polariton waves, etc. A few examples of successful theoretical treatments that follow this approach are given. In one, an effective medium theory of a nanoparticle composite is presented. In another, plasmon polaritonic solutions allow to extend concepts of radio technology, such as an antenna and a coaxial transmission line, to the visible frequency range.

Keywords Nanoparticles, resonators, plasmons, polaritons, nanocoax

1 Introduction

Dimensions of nanoparticles are often of the order of the wavelength of various wave phenomena. This leads to resonant conditions, further enhanced by the fact that nanoparticle sizes can also be smaller than the mean free path for various de-phasing processes (e.g. phonons). Some small enough particles can resonate electron or hole waves which leads to quantum size effects. For example, the metallic or nonmetallic nature of carbon nanotubes (CNTs) is a result of the circumferential quantization of electron waves.[1] Metallic nanoparticles can resonate charge density waves (plasmons) and that is the reason for the Mie absorption,[2] for example. Nanowires (and quantum wires) can resonate electromagnetic waves or a hybrid of these and other waves (polaritons) and thus can act as nanoantennae[3] or nano transmission lines.[4] Thus, at least theoretically, nanoparticles can be viewed as a boundary value problem, and it becomes obvious that surface effects strongly affect their physical properties. This promises various detector applications. Often, cross-dimensional behavior also occurs. For example, single-wall CNTs can be viewed as rolled-up graphene layers and thus two-dimensional (2D) behavior plays an important role in their band structure

---

Department of Physics, Boston College, 140 Commonwealth Avenue, Chestnut Hill, MA 02467, USA

* To whom correspondence should be addressed. E-mail: kempa@bc.edu

M. Giersig and G. B. Khomutov (eds.),
Nanomaterials for Application in Medicine and Biology

formation.[1] Yet, the circumferential quantization restricts dimensionality further and consequently the density of states has characteristic one-dimensional (1D) peaks at the band edges (van Hove singularities).[1] Similarly, their electromagnetic response has a simple 3D character in the ultraviolet (UV) range due to bulk plasmons, but a very complex, lower dimensional nature in the infrared (IR) due to resonances of 2D and 1D plasmons.[5–6] Theoretical approaches must flexibly adapt to these different limits. In this paper, I discuss two examples of successful theoretical treatments that focus on this resonant behavior.

2 Theory of a Nanoparticle Composite

In a recent paper,[7] I have derived a generalized Maxwell-Garnet formula for a composite material consisting of conducting nanoparticles, randomly distributed in a dielectric (non-dispersive) matrix. Each nanoparticle contained a number of interacting electrons confined by a *parabolic* potential. Then, the non-parabolic contributions to the Hamiltonian do not couple to radiation with wavelengths much greater than the nanoparticle size and the inter-particle distance (long wavelength limit). Thus, the response is dominated by simple harmonic resonances of the electron density in individual nanoparticles, and therefore the formula for the dielectric function reduces to[7]

$$\varepsilon(\omega)=\varepsilon_m+\sum_{f=1}^{M}\frac{p_f\,\omega_p^2}{\omega_f^2-\omega^2-i\gamma\omega} \tag{1}$$

where ε_m is the dielectric constant of the background matrix. Eq. (1) shows that each nanoparticle behaves as a simple harmonic oscillator. M groups of different nanoparticles coexist in the composite. In the fth-group the resonance frequency is ω_f, the damping constant is ω, and the plasma frequency of the metal is $\omega_p=\sqrt{4\pi n e^2/m}$, with n and m the electron density and mass, respectively. $p_f = V_f/V$ is the volume fraction of the particles of group f, V is the total volume of the composite, and the total volume fraction is $p=\sum_{f=1}^{M}p_f$. It can be shown[7] that

$$\omega_f^2=\omega_{f0}^2-\beta p\omega_p^2 \tag{2}$$

where ω_{f0} is the resonance frequency due solely to the presence of positive ions in a given nanoparticle. β is, in general, a complicated function of the composite and the unit geometry.

For example, for a medium consisting of spherical particles $\omega_{f0}=\omega_p/\sqrt{3}$ (Mie resonance of a simple metal) and $\beta = 1/3$, the familiar Lorentz cavity factor. In the radio frequency range $\omega/\omega_p << 1$, Eq. (1) yields

$$\Delta\varepsilon(\omega)=\varepsilon(\omega)-\varepsilon_m\approx\frac{3p}{1-p}\left(1+i\frac{3\omega\gamma}{(1-p)\omega_{\mathrm{p}}^2}\right) \tag{3}$$

For a low-density composite with $p << 1$, $\Delta\varepsilon(0) << 3$. This inefficiency of doping with spherical nanoparticles has recently been observed experimentally.[8] For a high-density composite ($p \approx 1$), $\Delta\varepsilon(\omega)$ can be large. Again, this agrees with a recent experiment,[9] in which a dielectric constant of 109, with a loss tangent of 0.02, was reported for an epoxy composite heavily loaded (particle touching) with self-passivated aluminum particles, 3 µm in diameter.

For a medium consisting of elongated (e.g. cylindrical) nanoparticles ω_{f0}^2 depends on the nanoparticle elongation. For composites with a broad distribution of particle lengths, we can approximate Eq. (1) as follows

$$\varepsilon(\omega) \approx \varepsilon_m + \int_0^\infty \frac{f(x)\omega_p^2}{x - \omega^2 - i\gamma\omega} dx \tag{4}$$

where $f(x)$ is the distribution function for the various $x = \omega_f^2$, each for a given particle length. Assuming that this distribution is uniform, i.e. $f(x) = p/(x_{\max} - x_{\min})$, and for $\omega/\omega_p << 1$, Eq. (4) yields

$$\Delta\varepsilon(\omega) \approx \frac{p\omega_p^2}{(x_{\max} - x_{\min})} \ln\left(\frac{x_{\max}}{x_{\min}}\right) + \frac{p(1 - \gamma^2/2x_{\min} - \gamma^2/2x_{\max})}{x_{\min}x_{\max}} \omega_p^2\omega^2 + i\omega\omega_p^2 \frac{p\gamma}{x_{\min}x_{\max}} \tag{5}$$

Now, in contrast to the composite with spherical particles, $\mathrm{Re}[\Delta\varepsilon(0)]$ can be large even at low p, but because of the slowly varying log-function in the first term, it happens only for $x_{\min} \to 0$, i.e. only when there is a fraction of very long nanostructures in the composite.

This is in agreement with experiments,[8] as shown in Fig. 1a, for a composite made of carbon nanotubes shown in Fig. 1b (both figures taken from Kempa et al.[8]). The solid lines, which are seen to be in very good agreement with the experiment, are obtained using Eq. (5) with the following parameters: $\gamma/\omega_p = 0.5$, $x_{\min} = 3 \times 10^{-7}\,\omega_p^2$, $x_{\max} = 0.1\omega_p^2$, and $p = 0.01$, which correspond well to the experimental conditions.

In the case of a very uniform composite, made with elongated nanoparticles of the same lengths ($x_{\min} \approx x_{\max} = x$), Eq. (1) gives

$$\Delta\varepsilon(\omega) \approx \frac{p\omega_p^2}{x} + \frac{p(1 - \gamma^2/x)}{x^2}\omega_p^2\omega^2 + i\omega_p^2\omega\frac{p\gamma}{x^2} \tag{6}$$

Now, $\mathrm{Re}[\Delta\varepsilon(0)]$ can be $>> 1$ for a moderately small x. Then also $\mathrm{Im}[\Delta\varepsilon(\omega)]$ can be small even at large frequencies. In addition, for $x \approx \gamma^2$ one can ensure that the coefficient of the ω^2 term is slightly positive, and can therefore extend the large value of $\mathrm{Re}[\Delta\varepsilon(\omega)] \approx p\omega_p^2/\gamma^2$ to large frequencies. It is useful to note that for properly chosen structures $\gamma << \omega_p$ in the radio-THz frequency range. Thus, for such a very uniform composite, by imposing the condition for nanostructure uniformity, real part of the dielectric function is maximized while the imaginary is minimized, in a large frequency range. Such a composite has not been fabricated yet.

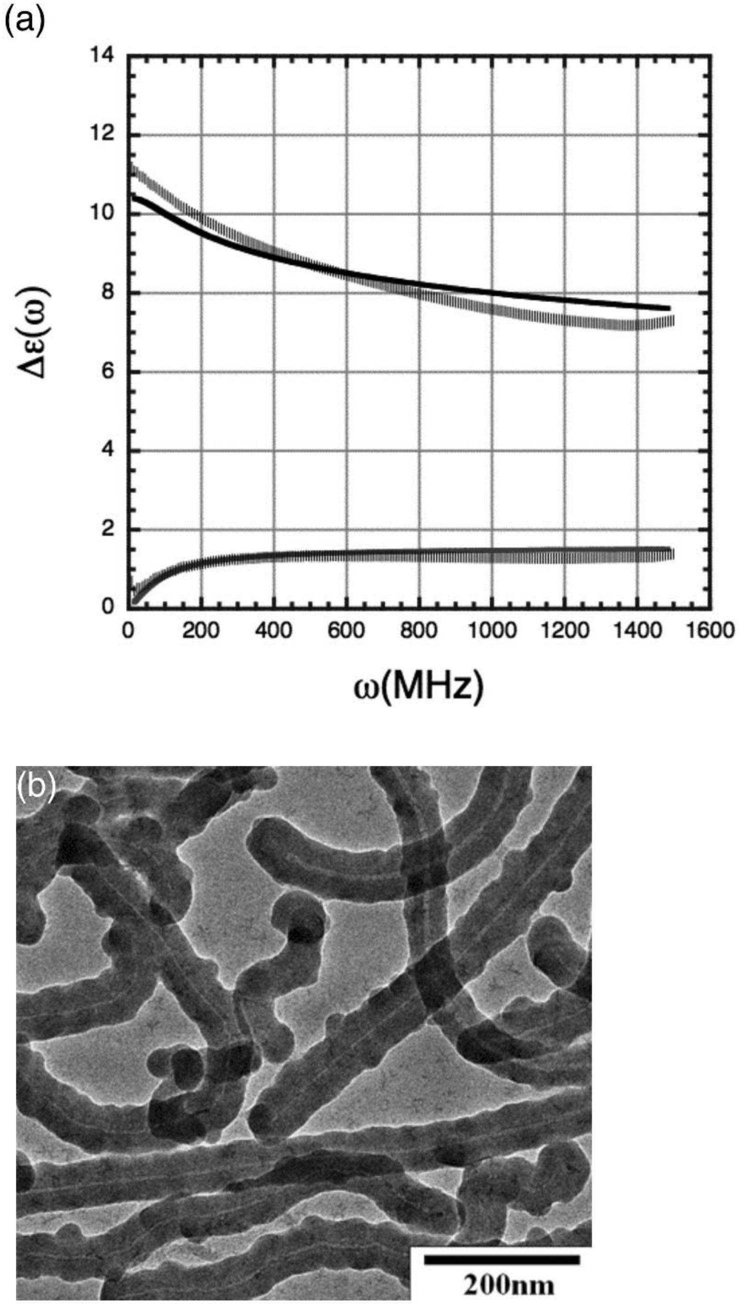

Fig. 1 (a) Theory (Eq. 5, solid lines) and measurements (data points accompanied by vertical error bars) of CNT-PMMA type I composite. Upper and lower curves correspond to Re[Δε(ω)] and Im[Δε(ω)], respectively. (b) SEM picture of SiO_2-coated CNTs. (Figures 1a and b are taken from Kempa et al.[8] Reprinted with permission from American Institute of Physics)

3 Radio Technology in the Visible: Nanoantennae and Nanocoaxial Transmission Lines

In recent papers it was demonstrated that straight multi-wall CNTs can act as nanoantennae for visible light.[3,10] An antenna is an external resonator of the electromagnetic radiation: reflections at antennae ends cause an electromagnetic wave propagating along antenna sides to become a standing wave. Thus, a resonance develops when the antenna length equals the integer multiple of the half-wavelength of the radiation outside the antenna: $L = \mathrm{n}\lambda/2$. In the visible frequency range, conventional antenna theory must be modified because of plasma effects. Typically, metals have their plasmon resonances (bulk and surface) in the visible or UV frequency ranges. Interaction of these resonances with transmission line modes (photon modes) leads to new modes, plasmon polariton modes. Any metal-dielectric interface supports a plasmon polariton.

To illustrate this, consider a single, planar interface between a metal with a dielectric function ε_1, and a uniform dielectric with the dielectric constant ε_2. Solving this simple problem involves matching plane wave solutions of Maxwell's equations in each region across the interface, using standard boundary conditions. To describe the metallic region, one can use the simple, yet accurate Drude dielectric function $\varepsilon_1 = \varepsilon_b - \omega_p^2/(\omega^2 + i\omega\gamma)$, where ε_b is the contribution from bound electrons in the metal. The resulting eigenmode of the system (plasmon polariton) has the dispersion (for $\gamma \to 0$) shown in Fig. 2.

The topology and meaning of this dispersion relation is clear: the "light-line" ($\omega = ck_x/\sqrt{\varepsilon_2}$) crosses with the surface ($\omega_{sp} = \omega_p/\sqrt{\varepsilon_2 + \varepsilon_b}$) and bulk ($\omega_{rp} = \omega_p/\sqrt{\varepsilon_b}$)

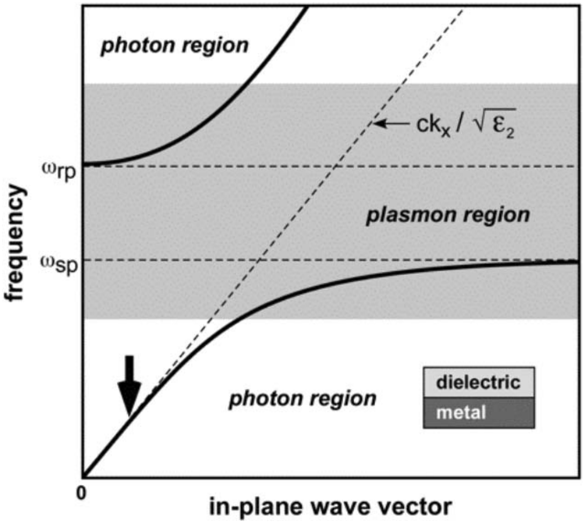

Fig. 2 Plasmon polariton at the metal dielectric interface

plasmon resonances, and this anti-crossing results in the two-branch structure of the plasmon polariton. It is important to note that for small k_x the lower branch asymptotically approaches the "light-line" (see the arrow in Fig. 2), and this strongly suggests that then the plasmon polariton becomes identical with the free-space TEM photon mode. In the plasma frequency range, on the other hand, there is a drastic departure from the simple free-space plane wave behavior: a gap opens in the spectrum, and the plasmon polariton acquires "mass" at the renormalized bulk plasmon frequency.

Elements of this mode structure prevail in the cylindrical geometry.[11] In particular, the main conclusions regarding the low-frequency solution ($\omega << \omega_p$), are essentially the same as above, as long as $2r > d_c = c / \omega_p$, where r is the radius of the cylindrical antenna. These conditions are satisfied for multi-wall CNTs ($r \approx 50\,nm$, $\hbar\omega_p \approx 6eV$) in the visible range and this allows for using the standard radio antenna theory (and standard numerical antenna codes) for CNT nanoantennae, as demonstrated in Refs. 3 and 10. Figure 3 (taken from Kempa et al.[10]) shows that an excellent agreement can indeed be achieved between the calculated and the measured directional multi-lobe emission patterns from a CNT nanoantenna, operating in the visible range.

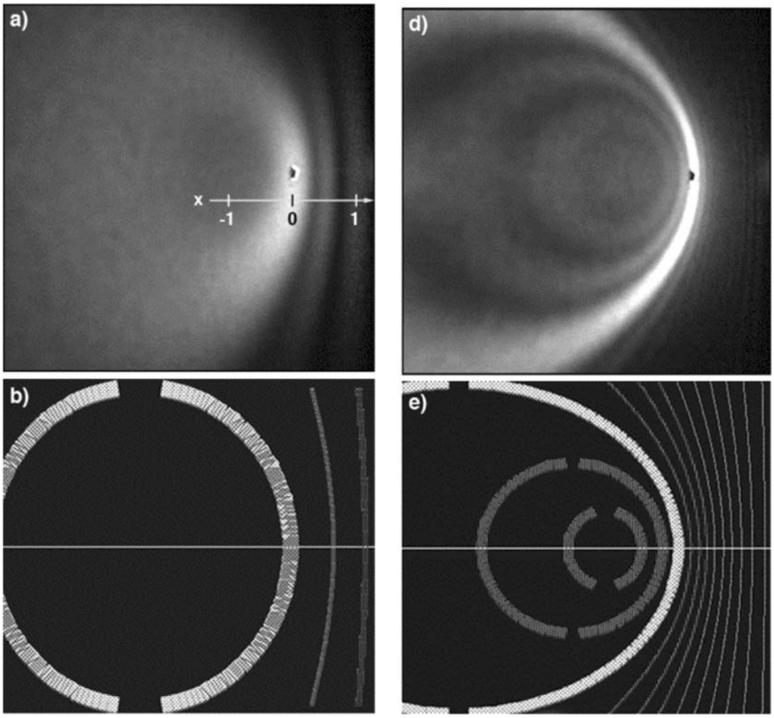

Fig. 3 Measured (a, d) and calculated (b, e) maps of projected emission patterns from CNT nanoantennae of two lengths: 850 nm (a, b) and 3,500 nm (d, e). (Figure 3 taken from Kempa et al.[10] Reproduced with permission)

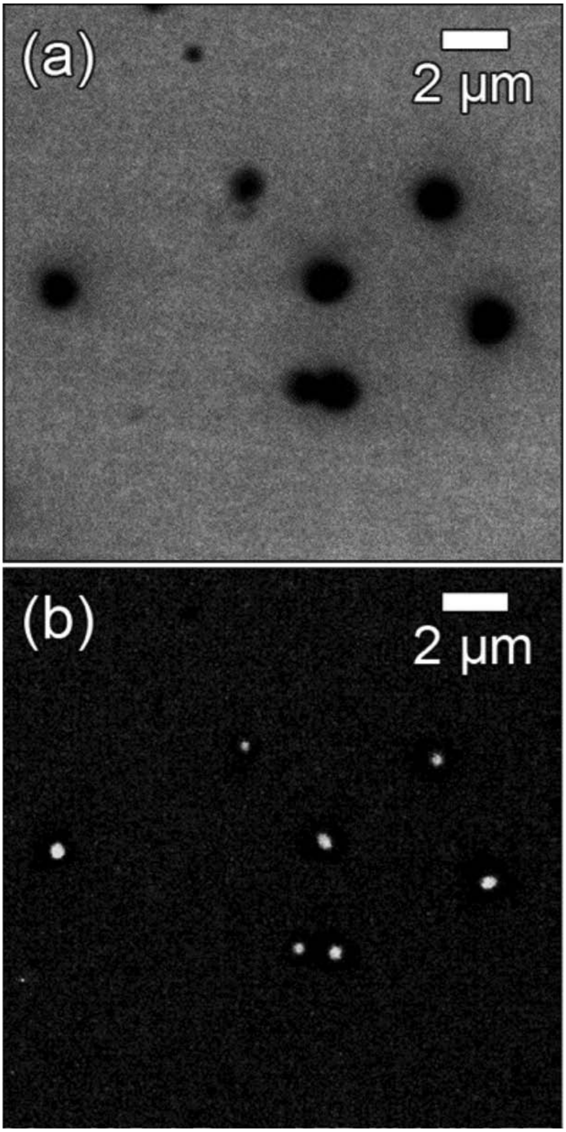

Fig. 4 High resolution optical microscope images of light reflected from (a) and transmitted through (b) CNT-based nanocoaxes. (Figures 4a and b taken from Rybczynski et al.[4] Reprinted with permission from American Institute of Physics)

For the same reason, i.e. the reduction of the plasmon polariton to the conventional TEM mode in the low frequency limit, the conventional radio theory can be applied also to nanotransmission lines in the visible range. It has been shown very recently,[4] that a nanoscopic analog of the conventional coaxial transmission line, the nanocoax, can be built based on CNTs. It has all the properties of its conventional cousin, but most importantly the basic transmitted mode, while technically plasmon polariton, is essentially a transverse electromagnetic (TEM). Since there is no cut of frequency for this mode, the subwavelength propagation is allowed. Figure 4 (taken from Rybczynski et al.[4]) shows high resolution optical microscope (top-view) images of 7 nanocoaxes based on optically long CNTs (6 micron long >> wavelength of visible light) as central electrodes. The CNTs were covered by an optically thin (100 nm thick << wavelength of visible light) film of alumina, followed by a thick layer of metal (Cr) as the outer electrode. Tops of the nanocaoxes were exposed by polishing so that light could pass only through the narrow inter-electrode spacing filled with the transparent alumina. Thus, each nanocoax is an optical subwavelength transmission line. Figure 4a shows white light reflected from the top side of the nanocoax sample, with dark spots representing light scattered from the nanocoax tips. Figure 4b shows the same area illuminated from the other side, with light emerging through top ends. The transmission shows no sign of frequency cut-off (light remains white), as expected.

4 Conclusion

I discussed two examples of a successful theoretical approach to the electromagnetic response of nanostructures based on the idea of wave resonances. First was the effective medium theory of a nanoparticle composite, in which the intra-particle resonances dominate the response. The second example discusses the external electromagnetic wave resonances coupled to the plasmon response in a nanoscopic wire. The resulting wave quantum is the plasmon polariton, which for sufficiently low frequencies reduces to the weakly retarded solution resembling the conventional TEM transmission line modes in wires and coaxial cables.

Acknowledgements This work was supported in part by the Fall 2005 Technology Investigation Award from the Massachusetts Technology Transfer Center, and by the Grant from the US Army Natick Soldier Systems Center under the grant DAAD16-02-C-0037.

References

1. R. Saito, G. Dresselhaus, and M. S. Dresselhaus, *Physical Properties of Carbon Nanotubes*, (Imperial College Press, London, 1999).
2. U. Kreibig and M. Vollmer, *Optical properties of metal clusters* (Springer, Berlin, 1995).
3. Y. Wang, K. Kempa, B. Kimball, J. B. Carlson, G. Benham, W. Z. Li, T. Kempa, J. Rybczynski, A. Herczynski, and Z. F. Ren, Receiving and transmitting light-like radio waves: antenna effect in arrays of aligned carbon nanotubes, *Appl. Phys. Lett.* 85(13), 2607–2609 (2004).

4. J. Rybczynski, K. Kempa, A. Herczynski, Y. Wang, M. J. Naughton, Z. F. Ren, Z. P. Huang, D. Cai, and M. Giersig, Subwavelength waveguide for visible light, *Appl. Phys. Lett.* 90, 021104 (2007).
5. K. Kempa, Gapless plasmons in carbon nanotubes, *Phys. Rev. B* 66(19), 195406 (2002).
6. K. Kempa and R. Chura, Plasmons in Carbon Nanotubes, in: *Low-dimensional systems: theory, preparation, and some applications*, L. M. Liz-Marzan and M. Giersig (eds.) (Kluwer Academic Publishers, Dordrecht, 2003), pp. 37–43.
7. K. Kempa, Dielectric function of media based on conductive particles, *Phys. Rev. B* 74, 033411 (2006).
8. T. Kempa, D. Carnahan, M. Olek, M. Correa, M. Giersig, M. Cross, G. Benham, M. Sennett, Z. F. Ren, and K. Kempa, Dielectric media based on isolated metallic nanostructures, *J. Appl. Phys.* 98, 034310 (2005).
9. J. Xu and C. P. Wong, in: *Proceedings of the 9th International Symposium on Advanced Packaging Materials: Processes, Properties and Interfaces*, Atlanta, GA, USA, Mar. 24–26, 2004; (Institute of Electrical and Electronics Engineers, New York, 2004), pp. 158–170.
10. K. Kempa, J. Rybczynski, Z. P. Huang, K. Gregorczyk, A. Vidan, B. Kimball, J. Carlson, G. Benham, Y. Wang, A. Herczynski, and Z. F. Ren, Carbon nanotubes as optical antennae, *Adv. Mater.* 19(3), 421–426 (2007).
11. X. Wang and K. Kempa, Plasmon polaritons in slot waveguides: Simple model calculations and a full nonlocal quantum mechanical treatment, *Phys. Rev. B* 75, 245426 (2007).